

AFIT/GAE/ENY/91D-2

AD-A243 868



1

DTIC
ELECTE
JAN 03 1992
S D

OPTIMIZATION OF TANGENTIAL MASS
INJECTION FOR MINIMIZING FLOW
SEPARATION IN A SCRAMJET INLET

THESIS

Richard J. Kacik
Captain, USAF

AFIT/GAE/ENY/91D-2

92-00043



Approved for public release; distribution unlimited

92-00043

AFIT/GAE/ENY/91D-2

OPTIMIZATION OF TANGENTIAL MASS INJECTION FOR
MINIMIZING FLOW SEPARATION IN A SCRAMJET INLET

THESIS

Presented to the Faculty of the School of Engineering
of the Air Force Institute of Technology

Air University

In Partial Fulfillment of the
Requirements for the Degree of

Master of Science in Aeronautical Engineering



Approved for	
Date	
By	
Date	
Approved for	
Dist	Approved for
A-1	

Richard J. Kacik, B.S.

Captain, USAF

December 1991

Approved for public release; distribution unlimited

Preface

This research project was an investigation of a current design problem in hypersonic propulsion - where to position an injection slot for controlling shock-induced flow separation in a scramjet inlet. Parametrics were gathered with a variable geometry model tested in a Mach 6 wind tunnel. Over eight hours of test time and 62 runs indicated that the optimum slot location was 5-6 slot heights upstream of the shoulder depending on the undetermined ideal shock position.

The experimental tests were sponsored by the Air Force Wright Laboratory's Flight Dynamics Directorate (WL/FI) with oversight from the National Aerospace Plane (NASP) Joint Program Office. This effort was undertaken with the hopes of contributing to the design process of the NASP and other future air-breathing hypersonic vehicles.

Many individuals were involved in this undertaking - perhaps as many as 25. I wish to particularly thank John Brohas of the AFIT Model Shop for crafting such a complex model, John Leugers of the Wright Laboratory for his advice on structural design and instrumentation, and Norm Scaggs, Max Hillsamer, and other FI staff for their support in wind tunnel operation. Thanks to my faculty advisor, Dr. William Elrod, and committee members: Lt Col Paul King (ret.), Ken Stetson, and Lt Col Gerald Hasen. Most importantly, a special thanks goes to my sponsor, Don Stava, for originally proposing this project and guiding me throughout.

Table of Contents

	Page
Preface	ii
List of Figures	v
List of Tables	xv
List of Nomenclature	xvi
Abstract	xix
I. Introduction	1
Background	1
Summary of Current Knowledge	2
Problem	9
Objectives	11
Scope	12
II. Theory	16
Injection Mixing Analysis Model	17
Stream Growth Rates	20
Computer Results	22
III. Experimental Set-Up	27
Model	27
Instrumentation	31
Facility	34
Installation	38
IV. Experimental Procedure	40
Test Program	40
Test Objectives	44
General Approach	45
Measurements	46
V. Results	49
Checkout Tests	49
Blockage	49
Injection	51
Flow Characterization Tests	51
Determination of Inlet Flow Conditions	51
Wall Static Pressure Distributions	53
Pitot Pressure Profiles	61
Schlieren Photos	66

Parametric Tests	67
Characteristics of Separation	69
Incipient Separation Criteria	71
Determination of Controlling TMI Rates	78
Trend Analysis	85
Flow Oddities	95
Inlet Unstarts	96
Rapid Flow Switches	97
Comparisons	98
Theory	93
Other Experimental Data	100
VI. Summary	103
Conclusions	103
Recommendations	106
Bibliography	110
Appendix A: Separation Analysis	115
Appendix B: Control Volume Analysis	121
Appendix C: Derivation of Mass Flux Profiles	124
Appendix D: Program Listing for MASS FLUX PROFILES .	131
Appendix E: Program Listing for OPTIMAL SLOT LOCATION	134
Appendix F: Schlieren Photographs	137
Appendix G: C/L Static Pressure Distribution Plots .	164
Appendix H: Pitot Pressure Profile Plots	210
Appendix I: Pitot Pressure vs TMI Pressure Plots . .	257
Vita	273

List of Figures

Figure	Page
1. Flow Separation at the Inlet Shoulder of a Typical Hypersonic Vehicle	3
2. Velocity Profiles for a) Slot too Close to Shock, b) Slot too Far from Shock	6
3. Location of TMI Slot for Effective Control (Ref. 24)	8
4. Effect of Shock Impingement Location (Ref. 26) .	10
5. Side View of Model and Flow Structure with Variables	13
6. Overview of Theoretical Analysis	16
7. Theoretical Optimum Slot-to-Shoulder Distance .	18
8. Freestream and Jet Stream Models	19
9. Calculated Mass Flux Profiles in the Mixing Region for $p_{o1}=500$ psia, $p_{oj}=17$ psia	23
10. Calculated Mass Flux Profiles in the Mixing Region for $p_{o1}=500$ psia, $p_{oj}=35$ psia	23
11. Close-up of Mass Flux Profiles in the Mixing Region for $p_{o1}=200$ psia, $p_{oj}=7$ psia	24
12. Mass Flux Along the Line $y=0$ for $p_{o1}=200$ psia, $p_{oj}=7$ psia	25
13. Mass Flux Along the Line $y=0$ for $p_{o1}=500$ psia, $p_{oj}=35$ psia	25
14. Theoretical Optimum Slot Location for $M_1=5.76$, $M_j=3$, $T_{o1}=1000^\circ\text{R}$, $T_{oj}=530^\circ\text{R}$	26
15. Scramjet Inlet Model with TMI Slot	28
16. Multiple Model Pieces	28
17. Tangential Mass Injection Piece Diagram	30
18. Model Instrumentation Diagram	32
19. Test Cabin with Model in the Injected Position .	36

20.	Test Cabin with the Door Closed	36
21.	Schematic Diagram of WL Mach 6 High Reynolds Number Facility (Ref. 37)	37
22.	Run 3 Pitot Pressure Survey at X=12.1 in, Z=0.1 in, p_{o1} = 0 psia, p_{o1} = 9 psia	52
23.	Run 4 Pitot Pressure Profile at X=11.8 in	54
24.	Run 3 Pitot Pressure Profile at X=11.8 in, p_{o1} = 500 psia	54
25.	Run 46 Total Temperature Profile at X=12.1 in, p_{o1} = 19 psia	55
26.	Run 47 Total Temperature Profile at X=12.1 in, p_{o1} = 46 psia	55
27.	Run 3 C/L Static Pressure Distribution at p_{o1} = 500 psia, p_{o1} = 0 psia	59
28.	Run 5 C/L Static Pressure Distribution at p_{o1} = 18 psia	59
29.	Run 8 C/L Static Pressure Distribution at p_{o1} = 46 psia	59
30.	Run 10 C/L Static Pressure Distribution at p_{o1} = 0 psia	60
31.	Run 14 C/L Static Pressure Distribution at p_{o1} = 45 psia	60
32.	Comparison of Boundary Layer Profiles	61
33.	Pitot Pressure Profiles at X=16.5 in for a) Run 9 at p_{o1} =0 psia, b) Run 11 at p_{o1} =7 psia, c) Run 12 at p_{o1} = 15 psia	63
34.	Pitot Pressure Profiles at X=16.5 in for a) Run 10 at p_{o1} =0 psia, b) Run 13 at p_{o1} =25 psia, c) Run 14 at p_{o1} = 45 psia	64
35.	Pitot Pressure Profiles at X=14 in for a) Run 51 at p_{o1} =0 psia, b) Run 52 at p_{o1} =10 psia, c) Run 52 at p_{o1} = 20 psia	65
36.	Close-up Diagram of the Model and Flow Field	67
37.	Run 26 Schlieren Photo at p_{o1} = 0 psia	68
38.	Run 27 Schlieren Photo at p_{o1} = 23 psia	68

39.	Schematic Diagram of Shock Wave-Boundary Layer Interaction on a Flat Surface <u>With</u> Separation (Ref. 16)	70
40.	Schematic Diagram of Shock Wave-Boundary Layer Interaction on a Flat Surface <u>Without</u> Separation (Ref. 16)	70
41.	Velocity Profiles for a) Separated Flow, b) Incipient Separation, c) Attached Boundary Layer	71
42.	Run 19 C/L Static Pressure Distributions	73
43.	Run 35 C/L Static Pressure Distributions for $p_{o_i} = 21-47$ psia	74
44.	Run 32 C/L Static Pressure Distributions	76
45.	Run 32 Schlieren Photo at $p_{o_i} = 0$ psia	77
46.	Run 32 Schlieren Photo at $p_{o_i} = 6$ psia	77
47.	Run 58 Pitot Pressure vs. Injection Pressure	79
48.	Run 38 Pitot Pressure Profile at $X=12.6$ in, $p_{o_i} = 6.2$ psia	80
49.	Controlling Mass Injection Ratio vs. Slot Location for Shock on Shoulder, $\alpha = \beta = 15^\circ$	87
50.	Controlling Mass Injection Ratio vs. Shock Location for $L_{SHR} = 5$ in, $\alpha = \beta = 15^\circ$	88
51.	Controlling Mass Injection Ratio vs. Shock Location for $L_{SHR} = 2$ in, $\alpha = \beta = 15^\circ$	89
52.	Controlling Mass Injection Ratio vs. Shock Location for $L_{SHR} = 2$ in, $\alpha = \beta = 12^\circ$	90
53.	Controlling Mass Injection Ratio vs. Shock Location for $L_{SHK} = 2$ in, $\delta = 0.26$ in	91
54.	Controlling Mass Injection Ratio vs. Shock Location for $L_{SHR} = 2$ in, $\delta = 0.20$ in	92
55.	Experimental (Ramp-Induced) Incipient Separation Limit (Ref. 16)	116
56.	Boundary Layer Separation Induced by a) Compression Ramp, b) Incident Shock Wave	117
57.	Cowl Deflection Angle for Incipient Separation	118

58.	Diagram of Control Volume	122
59.	Diagram of Flow Parameters Used for Mass Flux Profiles	124
60.	Comparison of Edge Mass Flux Boundary Conditions	129
61.	Schlieren Photo of Initial TMI Jet Checkout at $p_{o1} = 0$ psi , $p_{oj} = 38$ psia	138
62.	Schlieren Photo of TMI Jet Checkout at $p_{o1} = 0$ psi, $p_{oj} = 50$ psia After TMI Corners Welded and TMI Supply Line Enlarged	138
63.	Run 1 Schlieren Photo with $p_{oj} = 0$ psia	139
64.	Run 2 Schlieren Photo with $p_{oj} = 0$ psia	139
65.	Run 5 Schlieren Photo at $p_{oj} = 18$ psia	140
66.	Run 6 Schlieren Photo at $p_{oj} = 46$ psia	140
67.	Run 9 Schlieren Photo at $p_{oj} = 0$ psia	141
68.	Run 10 Schlieren Photo at $p_{oj} = 0$ psia	141
69.	Run 11 Schlieren Photo at $p_{oj} = 7$ psia	142
70.	Run 12 Schlieren Photo at $p_{oj} = 15$ psia	142
71.	Run 13 Schlieren Photo at $p_{oj} = 25$ psia	143
72.	Run 14 Schlieren Photo at $p_{oj} = 45$ psia	143
73.	Run 15 Schlieren Photo at $p_{oj} = 10$ psia	144
74.	Run 17 Schlieren Photo at $p_{oj} = 18$ psia	145
75.	Run 17 Schlieren Photo at $p_{oj} = 26$ psia	145
76.	Run 18 Schlieren Photo at $p_{oj} = 14$ psia	146
77.	Run 19 Schlieren Photo at $p_{oj} = 30$ psia	146
78.	Run 20 Schlieren Photo at $p_{oj} = 10$ psia	147
79.	Run 56 Schlieren Photo at $p_{oj} = 32$ psia	147
80.	Run 21 Schlieren Photo at $p_{oj} = 11$ psia	148
81.	Run 57 Schlieren Photo at $p_{oj} = 46$ psia	148
82.	Run 22 Schlieren Photo at $p_{oj} = 0$ psia	149

83.	Run 22	Schlieren Photo at $p_{o,j} = 10$ psia	149
84.	Run 23	Schlieren Photo at $p_{o,j} = 0$ psia	150
85.	Run 23	Schlieren Photo at $p_{o,j} = 35$ psia	150
86.	Run 25	Schlieren Photo at $p_{o,j} = 0$ psia	151
87.	Run 25	Schlieren Photo at $p_{o,j} = 18$ psia	151
88.	Run 28	Schlieren Photo at $p_{o,j} = 18$ psia	152
89.	Run 58	Schlieren Photo at $p_{o,j} = 7.7$ psia	153
90.	Run 58	Schlieren Photo at $p_{o,j} = 12$ psia	153
91.	Run 30	Schlieren Photo at $p_{o,j} = 0$ psia	154
92.	Run 30	Schlieren Photo at $p_{o,j} = 12$ psia	154
93.	Run 30	Schlieren Photo at $p_{o,j} = 24$ psia	155
94.	Run 59	Schlieren Photo at $p_{o,j} = 8.6$ psia	155
95.	Run 33	Schlieren Photo at $p_{o,j} = 17$ psia	156
96.	Run 34	Schlieren Photo at $p_{o,j} = 6$ psia	157
97.	Run 61	Schlieren Photo at $p_{o,j} = 10.4$ psia	157
98.	Run 35	Schlieren Photo at $p_{o,j} = 15$ psia	158
99.	Run 37	Schlieren Photo at $p_{o,j} = 23$ psia	158
100.	Run 38	Schlieren Photo at $p_{o,j} = 23$ psia	159
101.	Run 39	Schlieren Photo at $p_{o,j} = 23$ psia	159
102.	Run 40	Schlieren Photo at $p_{o,j} = 46$ psia	160
103.	Run 41	Schlieren Photo at $p_{o,j} = 26$ psia	160
104.	Run 42	Schlieren Photo at $p_{o,j} = 40$ psia	161
105.	Run 43	Schlieren Photo at $p_{o,j} = 8$ psia	161
106.	Run 44	Schlieren Photo at $p_{o,j} = 24$ psia	162
107.	Run 45	Schlieren Photo at $p_{o,j} = 20$ psia	162
108.	Run 51	Schlieren Photo at $p_{o,j} = 0$ psia	163
109.	Runs 9,11,12	C/L Static Pressure Distributions	165

110.	Runs 10,13,14	C/L Static Pressure Distributions	166
111.	Run 15	C/L Static Pressure Distributions . . .	167
112.	Run 16	C/L Static Pressure Distributions . . .	168
113.	Run 17	C/L Static Pressure Distributions . . .	169
114.	Run 18	C/L Static Pressure Distributions . . .	170
115.	Run 20	C/L Static Pressure Distributions . . .	171
116.	Run 56	C/L Static Pressure Distributions . . .	172
117.	Run 21	C/L Static Pressure Distributions . . .	173
118.	Run 57	C/L Static Pressure Distributions . . .	174
119.	Run 22	C/L Static Pressure Distributions . . .	175
120.	Run 23	C/L Static Pressure Distributions . . .	176
121.	Run 24	C/L Static Pressure Distributions . . .	177
122.	Run 25	C/L Static Pressure Distributions . . .	178
123.	Run 27	C/L Static Pressure Distributions . . .	179
124.	Run 28	C/L Static Pressure Distributions for $p_{o,j} = 0-10$ psia	180
125.	Run 28	C/L Static Pressure Distributions for $p_{o,j} = 14-30$ psia	181
126.	Run 58	C/L Static Pressure Distributions for $p_{o,j} = 0-10$ psia	182
127.	Run 58	C/L Static Pressure Distributions for $p_{o,j} = 11-15$ psia	183
128.	Run 29	C/L Static Pressure Distributions . . .	184
129.	Run 30	C/L Static Pressure Distributions for $p_{o,j} = 0-15$ psia	185
130.	Run 30	C/L Static Pressure Distributions for $p_{o,j} = 18-24$ psia	186
131.	Run 59	C/L Static Pressure Distributions . . .	187
132.	Run 31	C/L Static Pressure Distributions . . .	188
133.	Run 60	C/L Static Pressure Distributions . . .	189

134.	Run 33	C/L Static Pressure Distributions . . .	190
135.	Run 34	C/L Static Pressure Distributions . . .	191
136.	Run 61	C/L Static Pressure Distributions for $p_{o,j} = 0-10$ psia	192
137.	Run 61	C/L Static Pressure Distributions for $p_{o,j} = 10-46$ psia	193
138.	Run 35	C/L Static Pressure Distributions for $p_{o,j} = 0-18$ psia	194
139.	Run 62	C/L Static Pressure Distributions . . .	195
140.	Run 36	C/L Static Pressure Distributions . . .	196
141.	Run 37	C/L Static Pressure Distributions . . .	197
142.	Run 38	C/L Static Pressure Distributions . . .	198
143.	Run 39	C/L Static Pressure Distributions . . .	199
144.	Run 40	C/L Static Pressure Distributions . . .	200
145.	Run 41	C/L Static Pressure Distributions for $p_{o,j} = 0-23$ psia	201
146.	Run 41	C/L Static Pressure Distributions for $p_{o,j} = 27-40$ psia	202
147.	Run 42	C/L Static Pressure Distributions . . .	203
148.	Run 43	C/L Static Pressure Distributions . . .	204
149.	Run 44	C/L Static Pressure Distributions for $p_{o,j} = 0-17$ psia	205
150.	Run 44	C/L Static Pressure Distributions for $p_{o,j} = 20-41$ psia	206
151.	Run 54	C/L Static Pressure Distributions . . .	207
152.	Run 45	C/L Static Pressure Distributions . . .	208
153.	Run 55	C/L Static Pressure Distributions . . .	209
154.	Run 5	Pitot Pressure Profile at $X=12.1$ in, $p_{o,j} = 18$ psia	211
155.	Run 8	Pitot Pressure Profile at $X=12.1$ in, $p_{o,j} = 46$ psia	212

156.	Run 15 Pitot Pressure Profile at X=17.3 in, p _{o,j} = 0 psia	213
157.	Run 16 Pitot Pressure Profile at X=17.3 in, p _{o,j} = 0 psia	214
158.	Run 17 Pitot Pressure Profile at X=15.5 in, p _{o,j} = 0 psia	215
159.	Run 18 Pitot Pressure Profile at X=15 in, p _{o,j} = 0 psia	216
160.	Run 19 Pitot Pressure Profile at X=15 in, p _{o,j} = 0 psia	217
161.	Run 20 Pitot Pressure Profile at X=15 in, p _{o,j} = 0 psia	218
162.	Run 56 Pitot Pressure Profile at X=15 in, p _{o,j} = 36 psia	219
163.	Run 21 Pitot Pressure Profile at X=15 in, p _{o,j} = 0 psia	220
164.	Run 22 Pitot Pressure Profile at X=14 in, p _{o,j} = 0 psia	221
165.	Run 23 Pitot Pressure Profile at X=14 in, p _{o,j} = 0 psia	222
166.	Run 24 Pitot Pressure Profile at X=13 in, p _{o,j} = 0 psia	223
167.	Run 25 Pitot Pressure Profile at X=13 in, p _{o,j} = 18 psia	224
168.	Run 25 Pitot Pressure Profile at X=13.5 in, p _{o,j} = 18 psia	225
169.	Run 26 Pitot Pressure Profile at X=13 in, p _{o,j} = 0 psia	226
170.	Run 27 Pitot Pressure Profile at X=13.5 in, p _{o,j} = 23 psia	227
171.	Run 28 Pitot Pressure Profile at X=14.4 in, p _{o,j} = 0 psia	228
172.	Run 28 Pitot Pressure Profile at X=14.4 in, p _{o,j} = 10 psia	229
173.	Run 58 Pitot Pressure Profile at X=14.2 in, p _{o,j} = 7.6 psia	230

174.	Run 29 Pitot Pressure Profile at X=14.4 in, p _{o,j} = 26 psia	231
175.	Run 30 Pitot Pressure Profile at X=13 in, p _{o,j} = 0 psia	232
176.	Run 30 Pitot Pressure Profile at X=13 in, p _{o,j} = 18 psia	233
177.	Run 59 Pitot Pressure Profile at X=12.9 in, p _{o,j} = 6.3 psia	234
178.	Run 59 Pitot Pressure Profile at X=12.9 in, p _{o,j} = 8.6 psia	235
179.	Run 31 Pitot Pressure Profile at X=13 in, p _{o,j} = 15 psia	236
180.	Run 32 Pitot Pressure Profile at X=13.5 in, p _{o,j} = 0 psia	237
181.	Run 33 Pitot Pressure Profile at X=13 in, p _{o,j} = 0 psia	238
182.	Run 34 Pitot Pressure Profile at X=13.5 in, p _{o,j} = 7.6 psia	239
183.	Run 61 Pitot Pressure Profile at X=13.5 in, p _{o,j} = 7.4 psia	240
184.	Run 61 Pitot Pressure Profile at X=13.5 in, p _{o,j} = 10 psia	241
185.	Run 62 Pitot Pressure Profile at X=13.5 in, p _{o,j} = 19 psia	242
186.	Run 36 Pitot Pressure Profile at X=14.2 in, p _{o,j} = 10 psia	243
187.	Run 37 Pitot Pressure Profile at X=14.2 in, p _{o,j} = 11 psia	244
188.	Run 39 Pitot Pressure Profile at X=12.6 in, p _{o,j} = 6.2 psia	245
189.	Run 41 Pitot Pressure Profile at X=14.5 in, p _{o,j} = 27 psia	246
190.	Run 43 Pitot Pressure Profile at X=13.5 in, p _{o,j} = 7.9 psia	247
191.	Run 44 Pitot Pressure Profile at X=15.5 in, p _{o,j} = 24 psia	248

192.	Run 54 Pitot Pressure Profile at X=15.3 in, p _{oj} = 46 psia	249
193.	Run 55 Pitot Pressure Profile at X=15.3 in, p _{oj} = 46 psia	250
194.	Run 51 Pitot Pressure Profile at X=10.5 in, p _{oj} = 0 psia	251
195.	Run 51 Pitot Pressure Profile at X=11.5 in, p _{oj} = 0 psia	252
196.	Run 53 Pitot Pressure Profile at X=11.5 in, p _{oj} = 0 psia	253
197.	Run 53 Pitot Pressure Profile at X=14 in, p _{oj} = 0 psia	254
198.	Run 53 Pitot Pressure Profile at X=14 in, p _{oj} = 10 psia	255
199.	Run 53 Pitot Pressure Profile at X=14 in, p _{oj} = 20 psia	256
200.	Run 15 Pitot Pressure vs. TMI Pressure	258
201.	Run 16 Pitot Pressure vs. TMI Pressure	259
202.	Run 17 Pitot Pressure vs. TMI Pressure	260
203.	Run 18 Pitot Pressure vs. TMI Pressure	261
204.	Run 19 Pitot Pressure vs. TMI Pressure	262
205.	Run 20 Pitot Pressure vs. TMI Pressure	263
206.	Run 56 Pitot Pressure vs. TMI Pressure	264
207.	Run 57 Pitot Pressure vs. TMI Pressure	265
208.	Run 59 Pitot Pressure vs. TMI Pressure	266
209.	Run 60 Pitot Pressure vs. TMI Pressure	267
210.	Run 61 Pitot Pressure vs. TMI Pressure	268
211.	Run 62 Pitot Pressure vs. TMI Pressure	269
212.	Run 40 Pitot Pressure vs. TMI Pressure	270
213.	Run 54 Pitot Pressure vs. TMI Pressure	271
214.	Run 55 Pitot Pressure vs. TMI Pressure	272

List of Tables

Table	Page
1. Pressure Port Locations	33
2. Thermocouple Locations	33
3. Parameter to Configuration Map	41
4. Shock Location Map	41
5. TMI Inlet Model Test Matrix	42
6. Differences in Wall and Freestream Pressure . .	56
7. Differences in Wall and Jet Pressures Behind the Slot	57
8. Location of Recompression Shock Impingement . .	58
9. Determination of s_1 Values	66
10. Controlling Mass Injection Ratios	81

List of Nomenclature

- a - speed of sound, ft/sec
A - area, in²
b - jet half width, in
c - cowl height, in; jet growth rate parameter
C_f - skin friction coefficient
g_c - gravitational constant, ft/sec²
h - slot height, in
H - boundary layer shape factor, δ^*/θ
L - axial distance measured from slot, in
m - 2-D mass flow rate, lb_m/ft·sec
M - Mach number, u/a
p - pressure, lb_f/in²
Q - heat transfer rate, ft·lb_f/sec
R - gas constant, ft²/sec²·°R
Re - Reynolds number, $\rho u \delta / \mu$
s₁ - boundary layer growth rate or line
s₂ - entrainment rate or line
s₃ - jet growth rate or line
s₄ - jet centerline growth rate or line
T - temperature, °R
u - axial velocity, ft/sec
w - viscous dissipation work, ft·lb_f
x - axial distance measured from slot, in
X - axial distance measured from the model leading edge, in
y - normal distance measured from top of slot, in
Y - lateral distance from model centerline, in
Z - vertical distance from model surface, in

Greek Symbols

α - flow turning angle at the shoulder, compression ramp angle
 β - cowl deflection angle
 γ - ratio of specific heat coefficients
 δ - velocity boundary layer thickness, in
 δ^* - displacement thickness, in
 δ_H - enthalpy thickness, in
 δ_T - thermal boundary layer thickness, in
 θ - cowl shock angle; momentum thickness, in
 λ - velocity defect parameter
 μ - dynamic viscosity, lb_m/ft·sec
 ρ - density, lb_m/ft³
 τ - shear stress, lb_f/in²
 ϕ - model pitch angle

Subscripts

0 - incoming tunnel freestream, stagnation
1, 1a - x station just upstream of slot
1b - x station just upstream of cowl shock
2 - x station just downstream of cowl shock
aw12 - $\alpha=12^\circ$ aft wedge piece
aw15 - $\alpha=15^\circ$ aft wedge piece
BL - freestream boundary layer flow
c - jet centerline
CAP - inlet capture
cowl - cowl lip
cw - cowl wedge piece

e - boundary layer edge
fp- front plate piece
I - incipient
i1 - 1 in insert piece
i2 - 2 in insert piece
j,TMI - jet or tangential mass injection exit
JET - jet stream flow
max - maximum
min - minimum
SHK - inviscid cowl shock impingement
SHR - shoulder
T - pitot
w - wall

Superscripts

* - throat

Abstract

With the reemergence of interest in air-breathing hypersonic propulsion, scramjet inlet efficiency has become an area of concern. The impingement of the engine cowl shock near the shoulder (expansion corner between forebody and combustor) may cause boundary layer separation which reduces inlet efficiency. Tangential mass injection (TMI) upstream of the shoulder has recently been tested to control this separation but without much parametric evaluation. To resolve this deficiency, a 2-D scramjet inlet model with variable length, cowl, and TMI was built and tested in the WL Mach 6 High Reynolds Number Facility. Parameters varied were boundary layer thickness, TMI flow rate, cowl position, cowl and shoulder angle, and slot to shoulder distance. The optimum slot location was determined by finding the minimum injection flow rate required to eliminate separation for each configuration and analyzing the trends. The test results, along with a simplified mixing theory based on maximizing the jet/freestream wake mass flux, indicated that the optimum slot location was 5-6 slot heights upstream of the shoulder. However, this result was somewhat obscured by the observation that, when the cowl shock impinged closer to (but downstream of) the slot or aft of the shoulder, less mass injection was required to eliminate separation. A typical TMI rate for controlling the shock-induced separation in these regions was 3-6% of the inlet captured mass flow.

OPTIMIZATION OF TANGENTIAL MASS INJECTION FOR MINIMIZING FLOW SEPARATION IN A SCRAMJET INLET

I. INTRODUCTION

When a shock wave interacts with a boundary layer, often the result is flow separation from the body. This is a source of turbulence and buffeting on wings with transonic flow regions. In supersonic and hypersonic engine inlets, it can be the cause of inlet buzz, inlet unstart, or even engine flameout. Thus, a method to suppress separation and its undesirable effects is required for efficient operation.

Background

Many methods have been proposed to control this boundary layer separation. They fall into two categories (1:211). Some, such as wall cooling, vortex generators, boundary layer bleed, and tangential mass injection, act on the boundary layer upstream of the shock interaction region. Others, including wall transpiration, passive suction/injection, and boundary layer removal, act in the shock impingement/separation zone. The most common technique used in supersonic inlets has been boundary layer bleed.

The hot, thick boundary layer characteristic of a hypersonic vehicle renders many of these techniques

impractical for controlling the cowl shock-induced separation in a scramjet inlet (see Figure 1). For instance, boundary layer bleed is inappropriate as the high temperature and large volume required for bleed ducts simply cannot be afforded in terms of cooling, space, and weight (2:1). In fact, other ingestion techniques (i.e. passive suction/injection and boundary layer removal) are not feasible for the same reason. Likewise, vortex generators are susceptible to high heating effects and have been found to have little effect in controlling shock-induced separation (3:15). Although wall cooling and transpiration will likely be used for hypersonic vehicle thermal protection, neither shows great promise for reducing flow separation in a scramjet inlet (4). This leaves tangential mass injection (also known as tangential slot injection, upstream wall jet blowing, and boundary layer energization) as the most logical choice for hypersonic shock-viscous control.

Summary of Current Knowledge

Numerous applications have been identified for tangential mass injection (TMI) into an external stream: thermal protection, fuel injection, skin friction reduction, and boundary layer control (5:1). TMI has been widely used in the form of film cooling in combustors, afterburners, and rocket nozzles (6:981). Consideration has been given to injecting hydrogen fuel on the ramp of a scramjet inlet for premixing in order to reduce the combustor length. Heilala found that

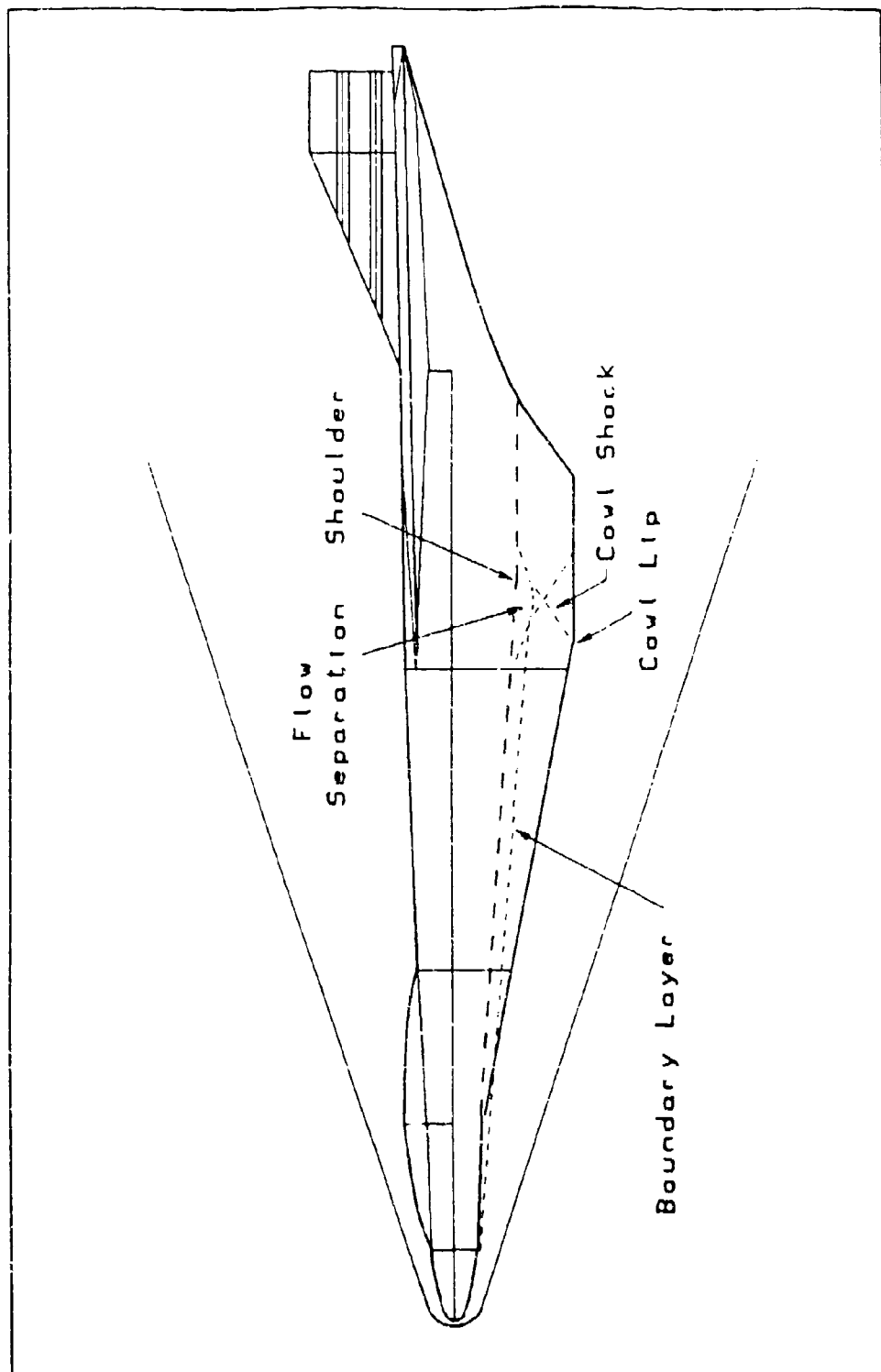


Figure 1. Flow Separation at the Inlet Shoulder of a Typical Hypersonic Vehicle

injecting helium (as a hydrogen substitute) at an angle of 5° - 20° from the tangential produced the best mixing and inlet performance efficiencies (7:viii). TMI has also been used on the wings of supersonic aircraft to reduce friction and separation, thus allowing higher angles of attack and greater lift (8:380, 9:725).

With so many applications, TMI has been the subject of numerous studies. Gilreath and Schetz found that, for supersonic injection, certain mixing zone properties and wave patterns can be predicted by simple inviscid theory without accounting for the viscous effects near the wall (10:610). Schetz also concluded that whether the flow is subsonic or supersonic is not an important factor in mixing analysis (11:183), but that the boundary layer shape does have a strong influence (12:41). Schetz, et al speculated that the injection kinetic energy need not be greater than that of the freestream to reduce separation downstream, as long as the post-injection boundary layer was turbulent where without injection it was laminar (12:37). Finally, Schetz, et al developed a computer model for TMI in a hypersonic flow which accounts for the effects of pressure mismatch, turbulent mixing, skin friction, and heat transfer (13:1).

The area of shock wave/boundary layer interaction has also received a great deal of attention. Holden has compiled a vast number of experimental results showing that the extent of separation induced by a compression corner ramp is roughly similar to that induced by an incident-reflecting oblique

shock given the same degree of total flow turning (14:18-19). Holden noted that the incipient separation point of a turbulent boundary layer is difficult to pin down due to the unsteadiness of the flow (14:4). Delery and Marvin recognized that the separation extent is reduced by

- 1) increasing the Mach number,
- 2) decreasing the shock angle, or
- 3) decreasing the Reynolds number of the flow based on

boundary layer thickness, Re_δ , when it is less than 10^6 (15:75). Delery also pointed out a stronger incident shock is needed to separate a turbulent boundary layer than a laminar boundary layer (16:9-11).

Many have also investigated the combination of TMI used to control shock wave/boundary layer interaction, such as Alzner and Zakkay (17), Grin and Zakharov (18), and Lakshminantha, et al (19). However, these studies were for ramp induced separation not typical of a scramjet inlet.

Some have even attempted to optimize the location of TMI for reducing separation - albeit for low supersonic speeds and again for geometries not typical of a scramjet inlet. Peake conducted a Mach 1.8 experiment with an oblique shock impinging on a flat surface (20:7-8). He found that the optimum length between the TMI slot and the impinging shock was bounded by the two extremes shown in Figure 2. If the slot was too close to the shock, then a "wake flow reversal" or "bursting" occurred between the external and injection streams causing a drastic increase in turbulence. On the

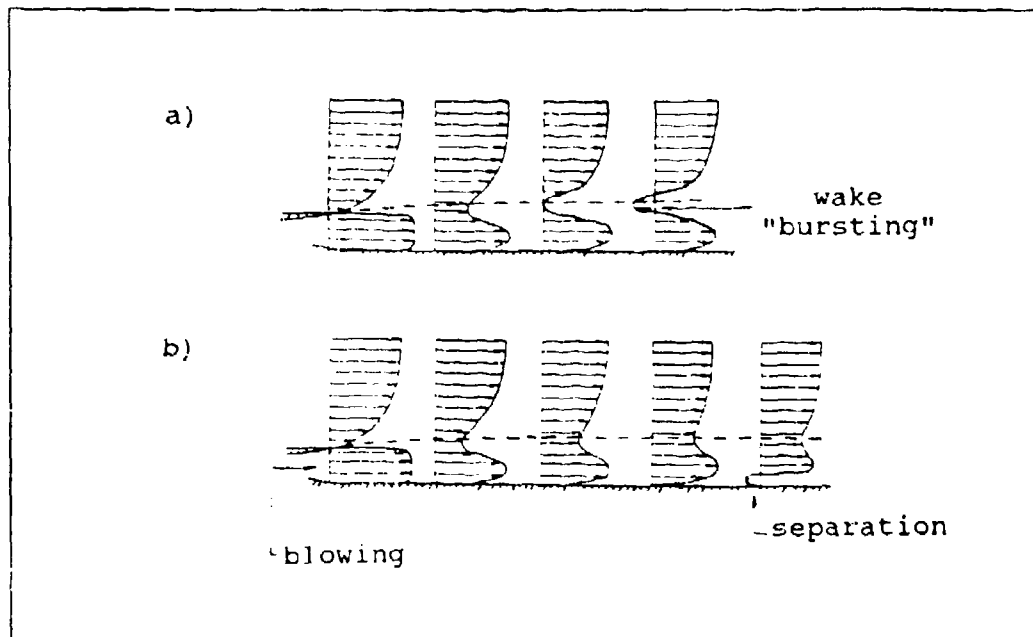


Figure 2. Velocity Profiles for a) Slot too Close to Shock, b) Slot too Far from Shock (Ref. 1)

other hand, if the slot was too far from the shock, a new boundary layer formed between the jet and the wall which eventually separated upon reaching the shock. Peake found that the optimum position for the slot was six times the initial boundary layer thickness upstream of the shock impingement. In a later experiment, Viswanath, et al determined that TMI was more effective if placed in the separated region (21:726). However, this was based on ramp-induced separation.

Despite an earlier investigation by Soviets Ogorodnikov, et al (22), only recently has serious consideration been given to applying TMI for a scramjet inlet geometry with an impinging shock wave in the vicinity of an expansion corner

(or shoulder). Under the sponsorship of the National Aerospace Plane (NASP) Joint Program Office, White, et al conducted two experiments with a 2-D scramjet inlet model (2,24). In the first series of tests, White observed that blowing was effective if the slot was positioned upstream of the separation (see Figure 3) but that downstream or "shock foot" blowing was ineffective (23). Indeed this is just the opposite result that Viswanath, et al (21) found for ramp-induced separation. White, et al also determined that an injection mass flow rate of 4% to 5% of the inlet captured mass flow would eliminate separation in the shoulder region for freestream Mach numbers of 4 and 5 (2:5), but they ran into inlet starting problems due to the contraction ratio at Mach 3 (2:8). The second experiment, performed jointly with General Dynamics, covered Mach numbers of 6, 8, and 10 (24:1). At Mach 6, White discovered that a minimum injection rate of 2.5% of inlet mass capture was needed to avoid inlet unstart (24:1-8). Injection improved not only the separation effects but also inlet starting, maximum contraction ratio, pressure recovery, and stability of the terminal shock system past the shoulder. However, at Mach 8 and 10, TMI had little effect on separation or other performance parameters (24:1). White speculated the natural boundary layer momentum was high enough to overcome any adverse pressure gradients at this high freestream Mach regime. Neither of these two experiments involved variation of the TMI to shoulder distance. However, White, et al did make the following conclusion:

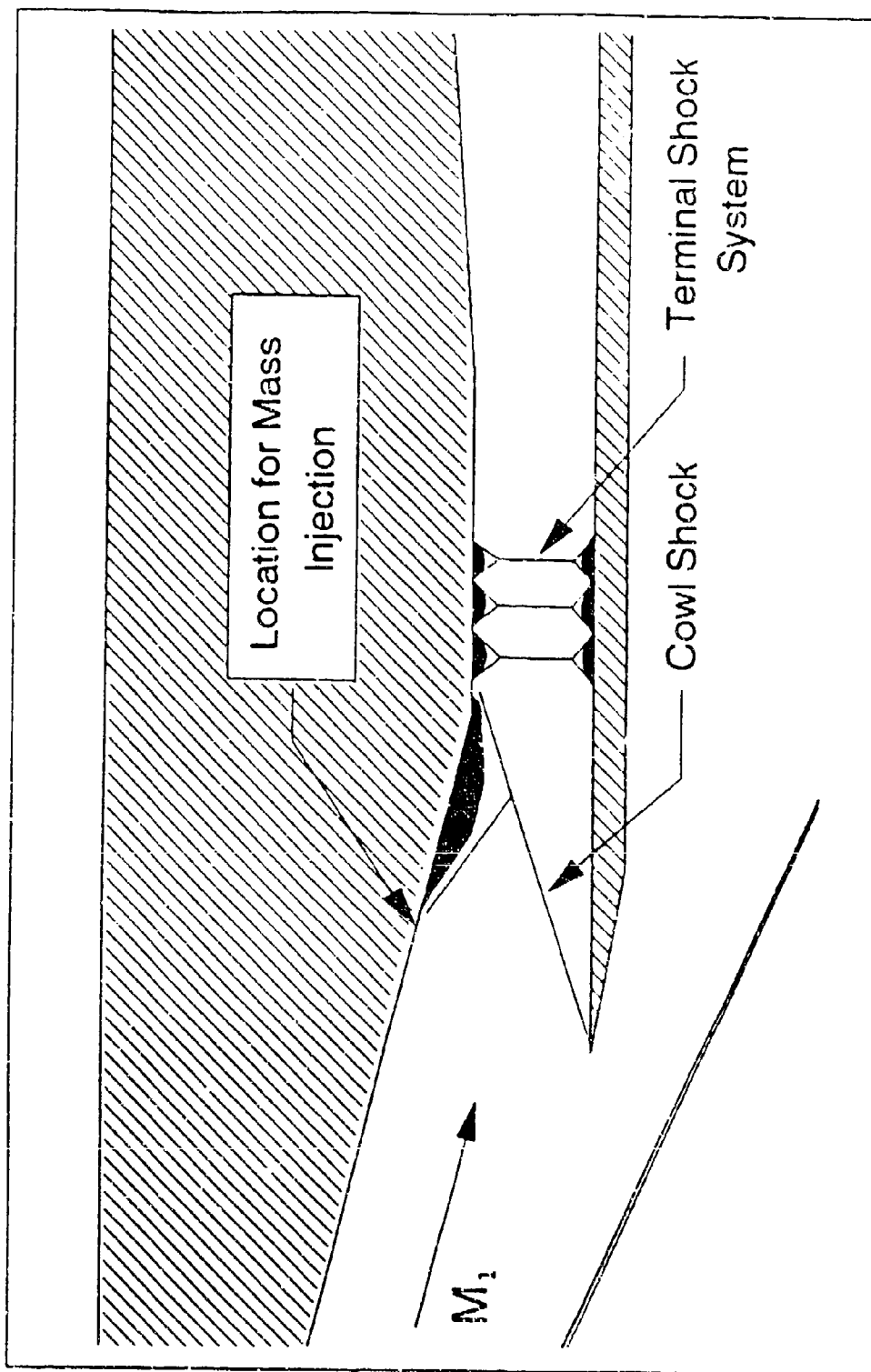


Figure 3. Location of TMI Slot for Effective Control (Ref. 24)

An experimental test program complemented by numerical investigations indicate that the position of the injector with respect to the boundary layer separation point is an important factor in the effectiveness of the injection. (2:8)

Problem

There are several problems associated with shock-induced separation in a scramjet inlet. First, it can cause the inlet to unstart and lead to flameout. If an unstart occurs at the higher flight Mach numbers, severe structural damage to the engine or vehicle could result (25:23). Second, separation can reduce the effective engine intake area and, thus, available mass flow. With less mass captured, scramjet performance is degraded. Another problem is that the separated flow may never reattach. Separated flow is certainly undesirable for fuel injection mixing in the combustor. If the boundary layer does reattach, the local wall heat transfer rate can be severe (16:9-3). Perhaps, the root of the problem with separation is the shock/expansion waves it creates (26). These effects are detrimental to the shock system stability and efficiency of a scramjet inlet. Figure 4 illustrates that when the cowl shock hits forward or aft of the shoulder, separation may result. Theoretically, there is no separation for "shock on the shoulder" (i.e. exact wave cancellation exists). A movable cowl lip may be employed to produce this nominal condition; however, any disturbance would cause the shock impingement to miss the shoulder. A momentary drop in thrust may result as the response time of

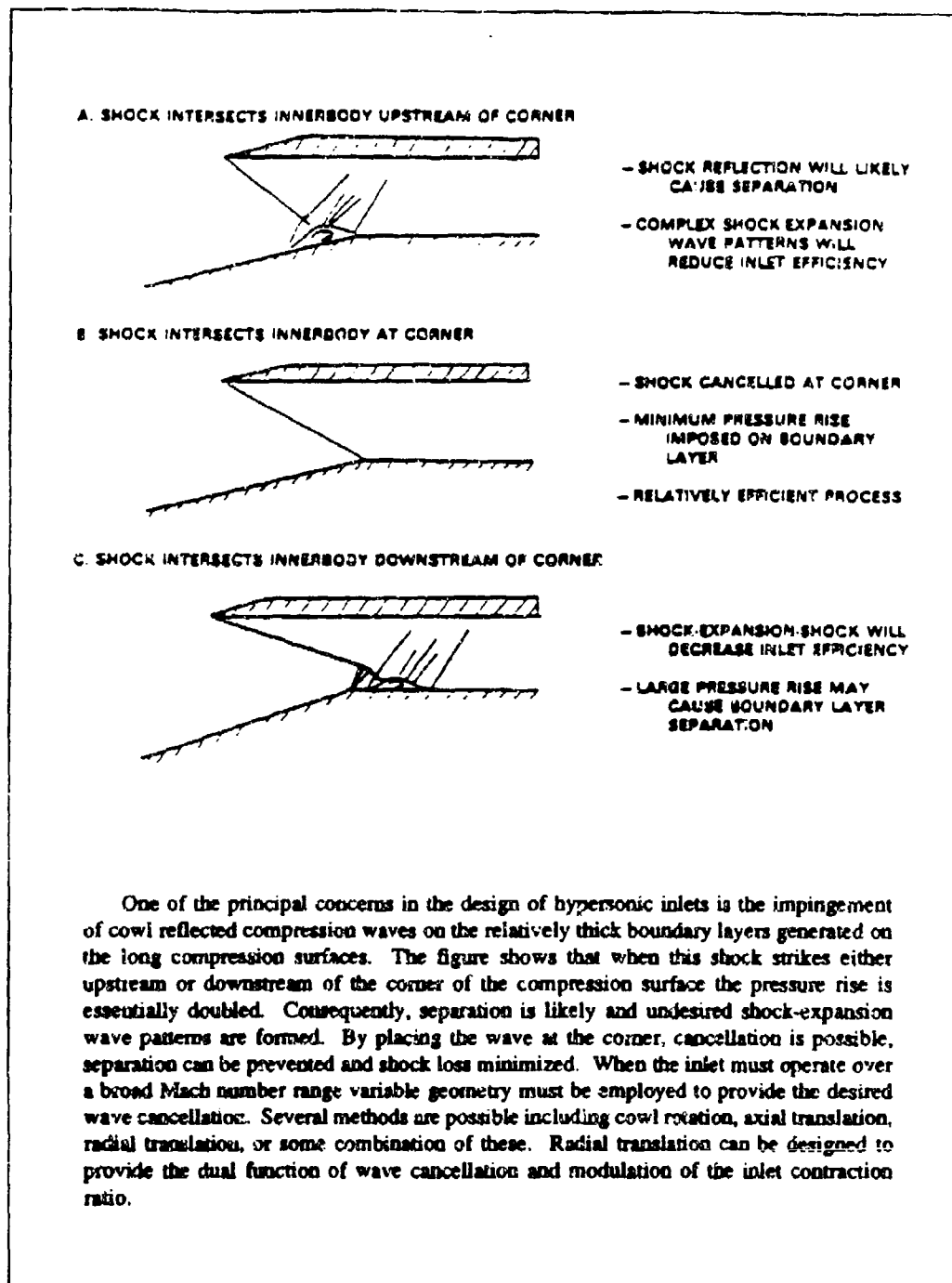


Figure 4. Effect of Shock Impingement Location (Ref. 26)

the cowl can never be zero. Thus, a method is sought by which separation can be eliminated for such off-design conditions.

If TMI is to be used, the primary issue involves the location of the tangential injection slot. Since this would most likely have a fixed position on the vehicle, it would have to be chosen based on its effectiveness over the entire range of the flight envelope. This range entails different Mach numbers, altitudes, and angles of attack. Roughly speaking, the different altitudes correspond to different Reynolds numbers and, thus, boundary layer thicknesses. In addition, the different Mach numbers and angles of attack correspond to various cowl shock angles and impingement locations.

Another issue is the magnitude of mass injection required to eliminate the separation. Of course, this would vary depending on the extent and location of separation present at any particular instant. The solution to this problem would be integrated into the design of the computer-controlled valve regulating the TMI flow and the total amount of injectant fluid a vehicle would need to carry for a given mission.

Objectives

The primary objective of this experimental investigation was the determination of the optimum TMI location for an inlet Mach number of 6. This corresponded to a flight Mach number of approximately 8 for the 12°-15° range of inlet ramp angles tested. Parameters varied were boundary layer thickness, δ ,

cowl deflection angle, β , flow turning angle at the shoulder, α , slot-to-shock impingement distance, L_{SHK} , slot-to-shoulder distance, L_{SHR} , and TMI flow rate, m_{TMI} (see Figure 5). The optimum slot distance upstream of the shoulder was determined based solely on minimizing the separation area with the smallest quantity of TMI flow rate. Other factors which may influence the actual design location include optimization over the flight envelope, limits of cowl scheduling response, and fuel injection/thermal protection considerations.

A secondary objective was to determine the optimum TMI flow rate for each test condition. The optimum was deemed as the minimum blowing rate (or controlling mass injection rate) necessary to eliminate separation. Operating at the controlling mass injection rate minimizes the amount of secondary fluid injectant that a vehicle would need to carry while maximizing engine performance. By determining values of this TMI flow rate under various test conditions, trends were identified for boundary layer thickness, cowl deflection angle, and cowl shock impingement position.

Scope

The parameters investigated in this project were varied over a range of values that could be related to actual flight conditions and vehicle configurations. The boundary layer thickness was varied by adjusting the freestream stagnation pressure of the wind tunnel, and the δ range corresponded to an altitude range of 80,000 to 100,000 ft. The cowl shock



Figure 5. Side View of Model and Flow Structure with Variables

angle range provided for a 3° variation in angle of attack. The flow turning angle at the shoulder was tested at 12° and 15° . The shock position was varied from $L_{SHK}/L_{SHR}=0.5$ to 1.05. The slot-to-shoulder distance range was 10-25 slot heights (2 in to 5 in). Finally, the TMI flow rate was varied from 0 to 15% of the inlet captured mass flow rate.

Other factors that may influence the extent and control of the separation, their values in the present experiment, and the reason they were not varied in this effort include:

- 1) freestream Mach number, $M_\infty=6$ - tunnel had fixed geometry throat and nozzle,
- 2) injection Mach number, $M_j=3$ - TMI nozzle not variable,
- 3) freestream total temperature, $T_\infty=1000^\circ\text{R}$ - varied slightly during some runs but was not totally controllable and had a relatively small range for tunnel operation,
- 4) injection total temperature, $T_{oj}=530^\circ\text{R}$ - heater/cooler not available for TMI fluid supply,
- 5) TMI fluid, air - easier to compare with other experiments and no other fluid supply readily available,
- 6) TMI slot height, $h=0.20$ in - TMI nozzle not variable,
- 7) cowl height, $c=2.0$ in - probably not an independent factor (contraction ratio was varied from 1.3 to 1.6),
- 8) impingement zone wall temperature, $T_w\approx 700^\circ\text{R}$ - difficult to control; varied during run as model heated up, and
- 9) wall skin friction, $C_f=?$ - perceived as only a minor influence on separation and very difficult to measure or vary.

Additionally, this project did not model the inlet throat/combustor interface or sometimes called the isolator duct. In order to avoid tunnel blockage and facilitate inlet self-starting, the cowl length was reduced and, therefore, did not extend past the throat. As a result, its function became that of a shock generator. This isolator section is thought to only have a secondary effect on the separation.

The wind tunnel model was also limited to 2-D. Sidewalls would only have increased the tunnel blockage and added complexity to the flow analysis. Likewise, no pre-compression ramp was used to keep blockage to a minimum.

Finally, no effort was made to determine inlet efficiency (in terms of either kinetic energy or pressure recovery). This would have required delicate and expensive instrumentation and may not have yielded realistic results since the throat section was not properly modelled.

II. THEORY

Three separate analyses were considered from a theoretical standpoint (see Figure 6). First, a method based on experimental ramp-induced incipient separation data was developed to determine the extent of separation for a given flow condition and inlet geometry. Then a control volume analysis would be iteratively applied to determine what jet total pressure, p_{oj} , was required to just eliminate separation. Finally, for the controlling p_{oj} an injection mixing analysis would be employed to determine the optimum location of the

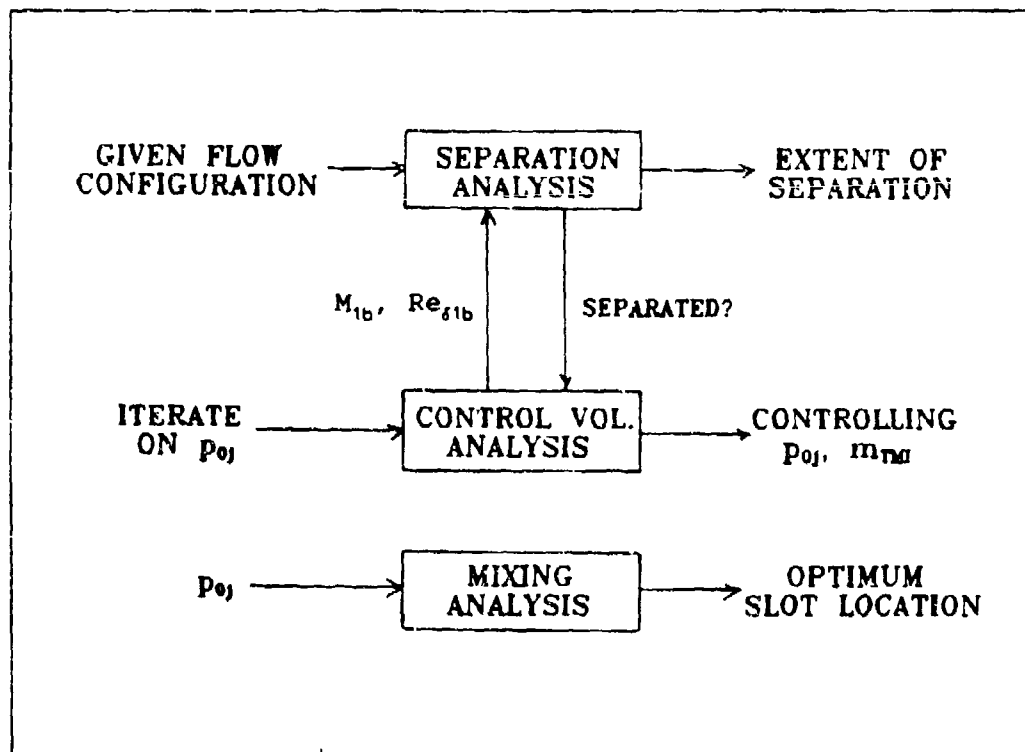


Figure 6. Overview of Theoretical Analysis

slot with respect to the shoulder. In the end, the first two analyses had to be abandoned due to the inability to account for boundary layer shape factor, H_{1b} , changes. Nevertheless, these two sections are included as Appendices A and B with the hope that future researchers will be able to utilize them once shape factor influence is known.

Injection Mixing Analysis Model

With the abandonment of the separation and control volume analyses, this mixing analysis was performed for a range of injection total pressures instead of the controlling p_{oj} . As it turned out, the optimum slot location as theorized here remained fairly constant with varying p_{oj} , so the other two analyses were not critical for determining slot location.

Based on the bounds suggested by Peake (20), it is proposed that the optimum distance of the slot from the shock impingement is the downstream length required for the mass flux of the wake flow from the slot's top nozzle surface to become maximized. Figure 7 shows that this distance best avoids the wake bursting phenomenon while keeping the new boundary layer growth of the jet to a minimum. Now since the shock is nominally expected to impinge on the shoulder, this length is chosen as the optimum slot-to-shoulder distance, L_{SHR} .

To model the mixing of the freestream boundary layer and the jet stream, a superposition method proposed by Carriere and Eichelbrenner (27:209-213) was investigated. They

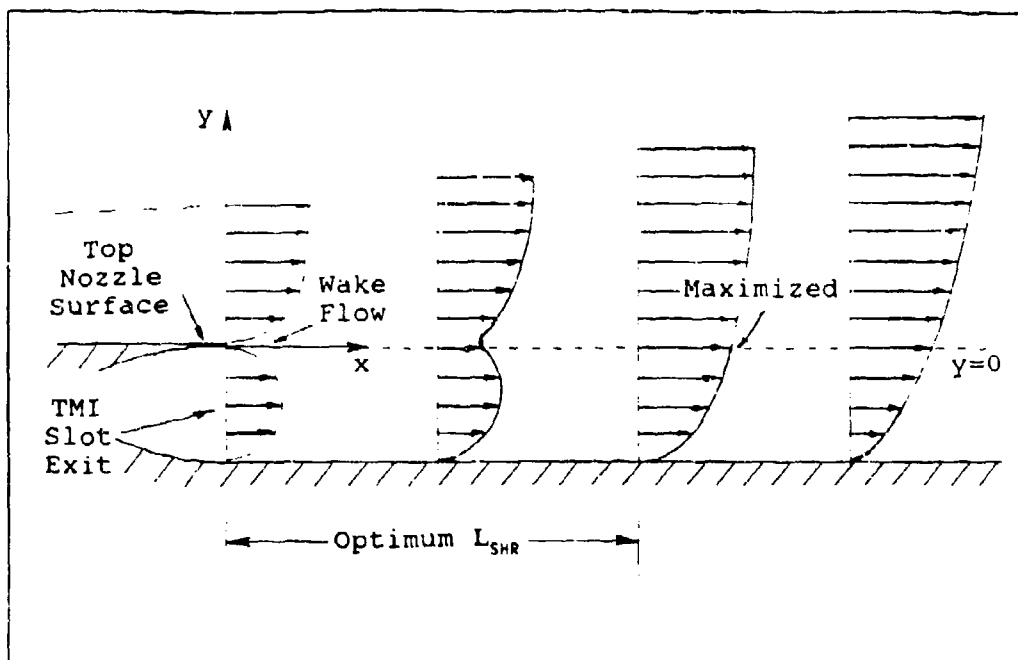


Figure 7. Theoretical Optimum Slot-to-Shoulder Distance

considered the velocity profiles of the two streams as if they acted independently, maintaining their shape downstream, but expanding at growth rates observed experimentally with both streams present. Then, they simply added the two profiles to obtain the flow velocity at any x, y position.

This approach was adapted for compressibility by using mass flux (ρu) profiles instead of velocity profiles. This better satisfies the conservation of mass, especially for supersonic/hypersonic velocities. Another adaption was the incorporation of a boundary layer entrainment into the jet flow as proposed by Schetz, et al (13). Figure 8 displays the freestream and jet stream models used in the present analysis.

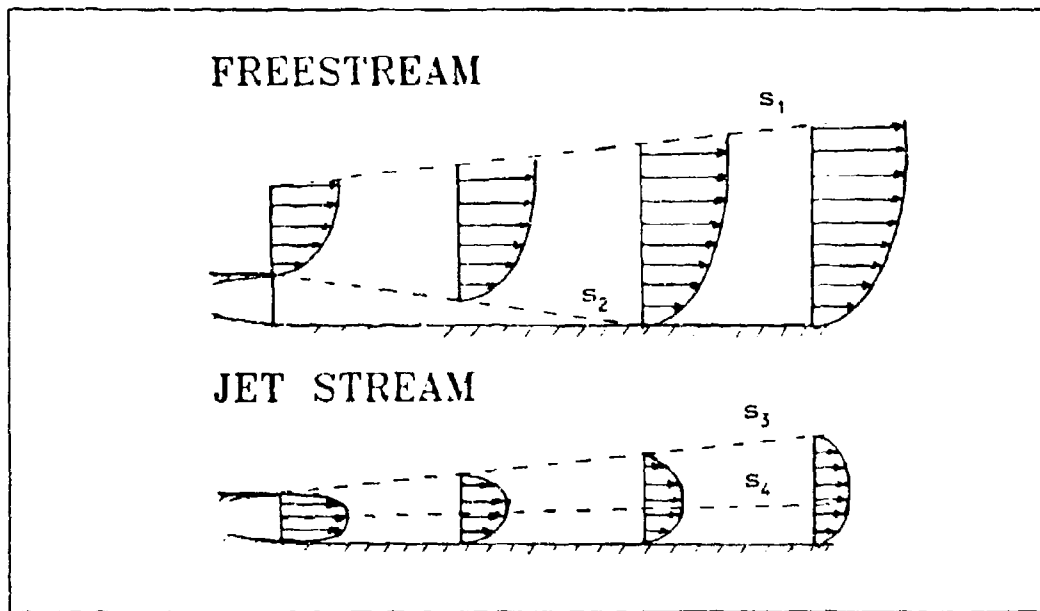


Figure 8. Freestream and Jet Stream Models

Turbulent flow was assumed for both streams. The common velocity profile of the form

$$\frac{u}{u_1} = \left(\frac{y}{\delta}\right)^{1/7} \quad (1)$$

was used for the freestream boundary layer and the top and bottom halves of the jet. Previous experimental data for hypersonic flow over a flat plate (28) indicated that the density profile through a boundary layer could be approximated by

$$\frac{\rho}{\rho_1} = \frac{T_1}{T_w} + \left(1 - \frac{T_1}{T_w}\right) \left(\frac{y}{\delta}\right) \quad (2)$$

which was also adapted for the top and bottom parts of the jet as shown in the Appendix C Assumed Profiles section. From

Figure 8 and Equation (2) it is realized that fictitious walls should be considered for temperature along the lines labelled s_1 and s_2 . As a first order approximation, the new T_w was assumed to be the temperature of the opposite stream that the slope line was cutting through. This temperature was derived by assuming constant pressure through the boundary layer and by combining the equation of state and Equation (2) to give the general form of

$$T = \frac{T_1}{\frac{T_1}{T_w} + (1 - \frac{T_1}{T_w}) (\frac{Y}{\delta})} \quad (3)$$

Now, by the conservation of mass

$$m_{BL} = \rho_1 u_1 \int (\frac{\rho}{\rho_1}) (\frac{u}{u_1}) dy = \text{constant} \quad (4)$$

for any x station of the freestream. See Appendix C for the equivalent jet stream development.

Stream Growth Rates

To integrate these equations, appropriate assumptions must be made about the growth rates or limits of each stream. It is commonly accepted that the growth rates for turbulent 2-D mixing zones and planar jets are linear with x (29:512). Several investigators have reported values for these slopes. Carriere and Eichelbrenner found that the boundary layer grows at the same rate as the wall jet with $s_1=s_3=0.1$ and $s_4=0.01$ (27:211). Walker, et al observed that $s_2=-0.067$ for $\delta \approx h$ and slight overexpansion (5:13), while Gilreath and Schetz

observed $s_2 = -0.071$ (10:2153). Some have found that the jet growth rate is equal to the boundary layer entrainment rate for mixing zones, such as Reichardt's $-s_2 = s_3 = 0.111$ (29:509) and Albertson's $-s_2 = s_3 = 0.132$ (29:509). Abramovich suggested that these rates depend on a velocity defect parameter,

$$\lambda = \frac{u_{max} - u_{min}}{u_{max} + u_{min}} \quad (5)$$

where $-s_2 = s_3 = b/x = c\lambda$ and c was experimentally determined to be in the range 0.2-0.3 (30:153). For the present set of experiments, $u_{max} = 2230$ ft/sec and $u_{min} = 2020$ ft/sec giving $-s_2 = s_3 = 0.046-0.069$. Schetz, et al found that this matches well for supersonic conditions (12:29). Pai described an analysis by Kuethe that depended on the velocity ratio between two mixing streams and yielded different growth rates (31:109). Again for the present case, $u_2/u_1 = 0.625$ and from Pai's graphs and equations $s_2 = -0.085$ and $s_3 = 0.068$. Based on all this data, the growth rates used in this analysis were

$$\begin{aligned} s_1 &= 0.07 & s_3 &= 0.07 \\ s_2 &= -0.07 & s_4 &= 0.01 \end{aligned}$$

Now upon integrating the m_{BL} and m_{JET} equations and solving for ρu for each stream as a function of x and y , the two streams are superimposed to get

$$(\rho u)(x, y) = (\rho u)_{BL}(x, y) + (\rho u)_{JET}(x, y) \quad (6)$$

Computer Results

Appendix C shows the derivation of the mass flux equations for any x, y position. A computer program was written in BASIC incorporating these equations. Appendix D contains the listing for the "MASS FLUX PROFILES" program which was used to generate Figures 9, 10, and 11 for visualization of the mixing zone. One may notice from these figures that the initial mass flux profiles are nearly linear. This comes from the initially assumed profiles for p and u ; when combined pu varies as $(y/\delta)^{8/7}$. It is also worth noting that the initial wake between the two streams (at $y=0$) diffuses and mixes out rather quickly and then gradually diminishes as the jet expands downstream.

From the criterion proposed earlier, the optimum slot-to-shoulder distance is the L where pu is maximized along the line $y=0$. Figures 12 and 13 show this mass flux as a function of x . The computer program was modified to calculate the L_{SHK} where pu is maximized over a range of TMI rates. The "OPTIMUM SLOT LOCATION" program is listed in Appendix E, and Figure 14 shows the computed results. It is clear that for inputs corresponding to the actual test conditions, the optimum L_{SHK} was fairly independent of the blowing rate and was approximately 1 in, five to six slot heights, or, equivalently, 5-66.

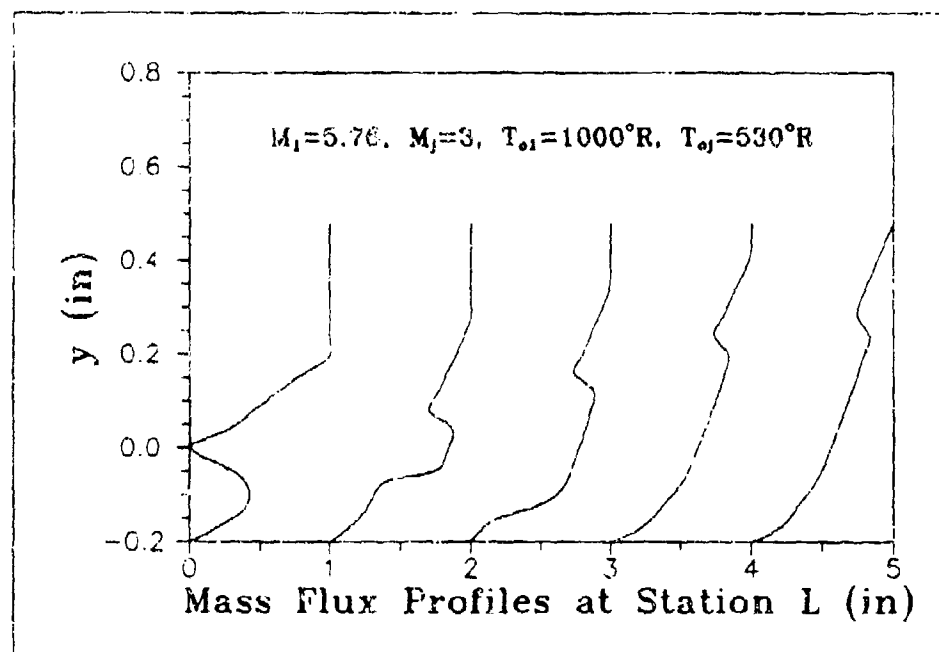


Figure 9. Calculated Mass Flux Profiles in the Mixing Region for $p_{01}=500$ psia, $p_{02}=17$ psia

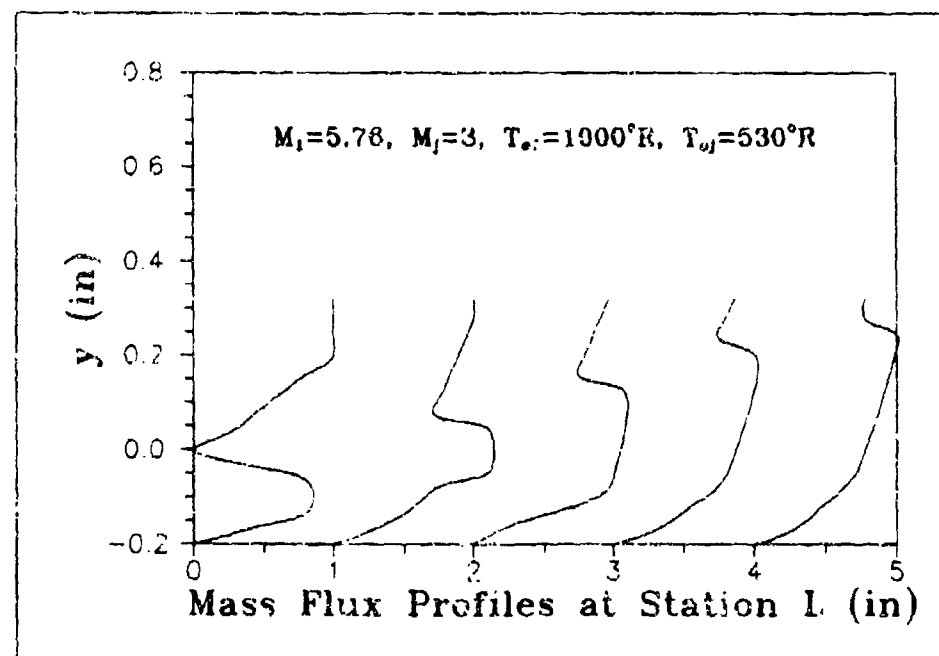


Figure 10. Calculated Mass Flux Profiles in the Mixing Region for $p_{01}=500$ psia, $p_{02}=35$ psia

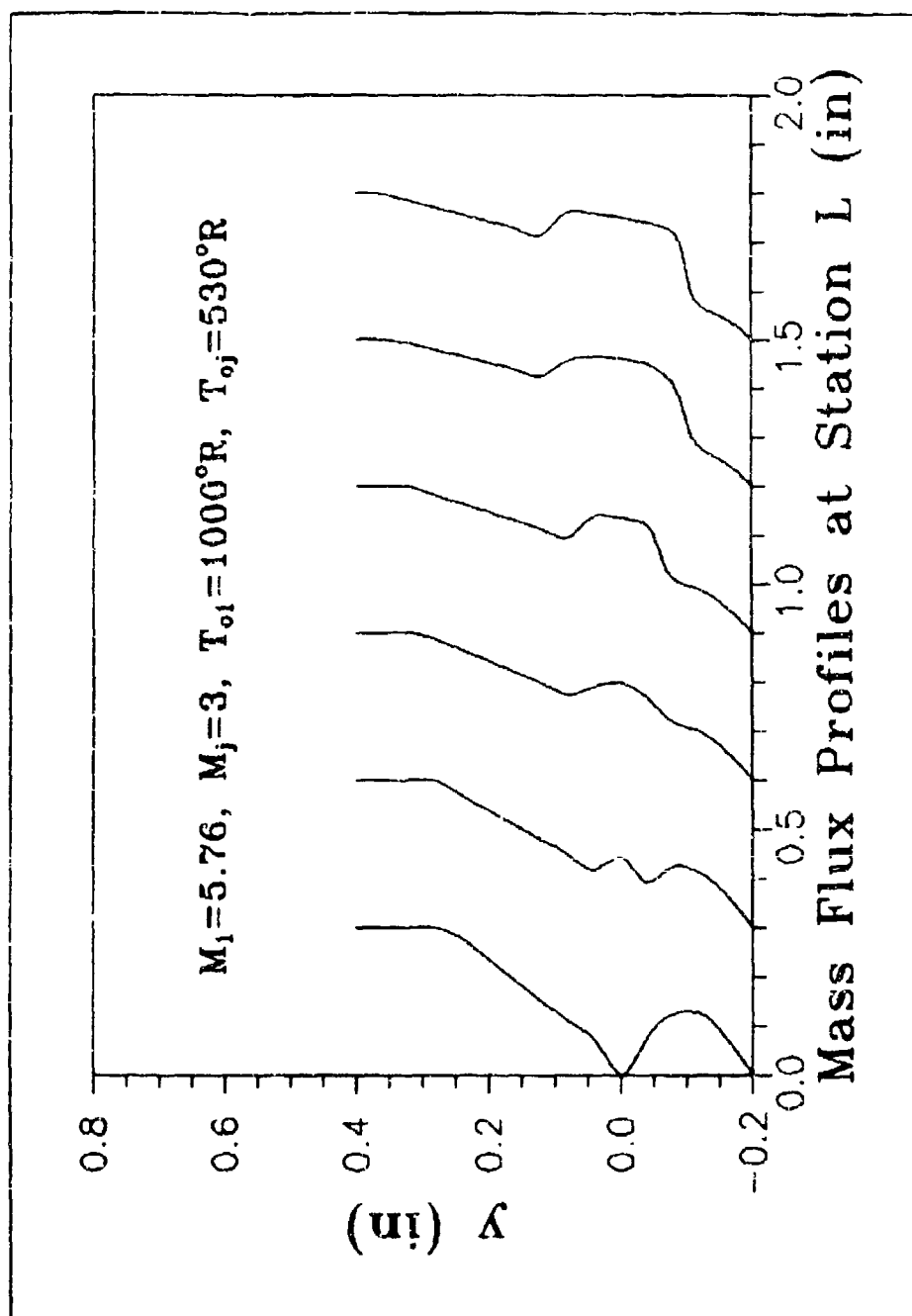


Figure 11. Close-up of Mass Flux Profiles in the Mixing Region for $p_{01}=200$ psia, $p_{0j}=7$ psia

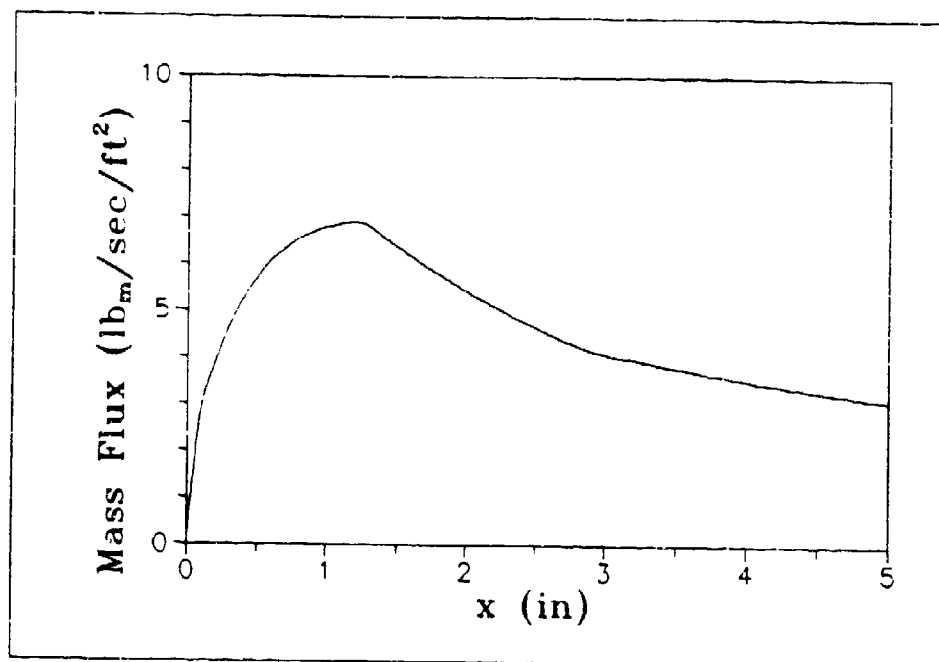


Figure 12. Mass Flux Along the Line $y=0$
for $p_{o1}=200$ psia, $p_{o2}=7$ psia

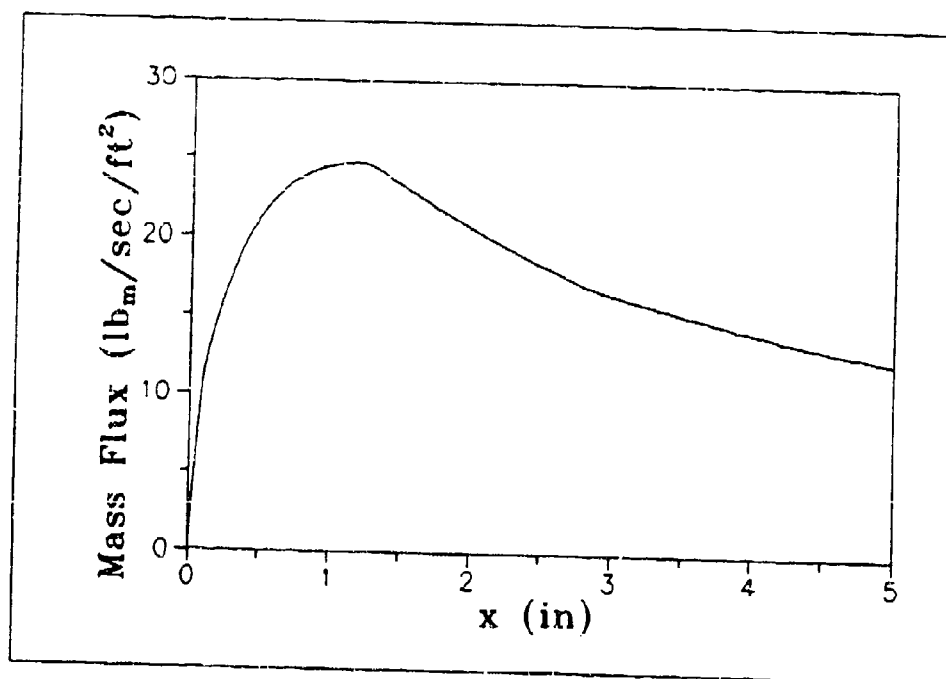


Figure 13. Mass Flux Along the Line $y=0$
for $p_{o1}=500$ psia, $p_{o2}=35$ psia

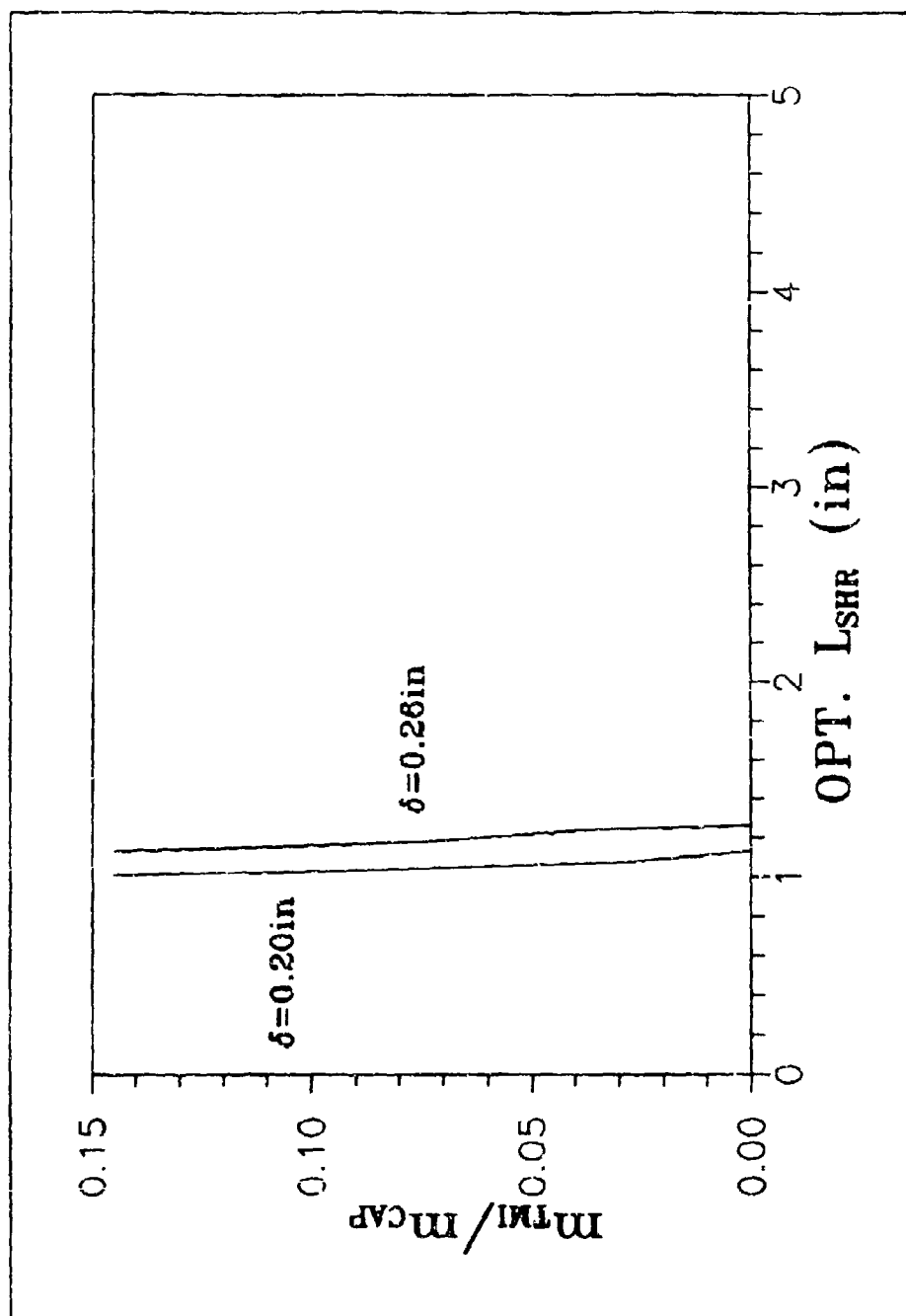


Figure 14. Theoretical Optimum Slot Location for $M_1=5.76$, $M_j=3$, $T_{o1}=1000^\circ R$, $T_{oj}=530^\circ R$

III. EXPERIMENTAL SET-UP

This chapter describes the equipment used in the experiments, which consisted of a multi-piece model, a wind tunnel facility, instrumentation, and struts and piping for the model-facility interface.

Model

The scramjet TMI inlet model used in the experiments is shown in Figure 15. The model was designed with consideration of the project goals, aerodynamic loads, and wind tunnel requirements. It was based on the Scaggs/Galassi flat plate model (32: Fig. 1) which was built for the same facility. Their basic design was modified to provide for tangential mass injection, variable length inserts, interchangeable aft wedges, and an adjustable cowl. The material chosen for the model was Stainless Steel 17-4 for its low thermal expansion qualities. Figure 16 is a picture of the multiple model pieces. The overall maximum dimensions (L x W x H) were 19.51 x 16.00 x 3.38 in (including the cowl).

The front plate was slightly different than the Scaggs/Galassi plate. Originally, normal mass injection was considered for this piece to thicken the boundary layer as proposed by Clausen (33). However, Stava suggested that a rough plate surface and low tunnel reservoir pressure could reasonably duplicate the expected NASP inlet condition - a

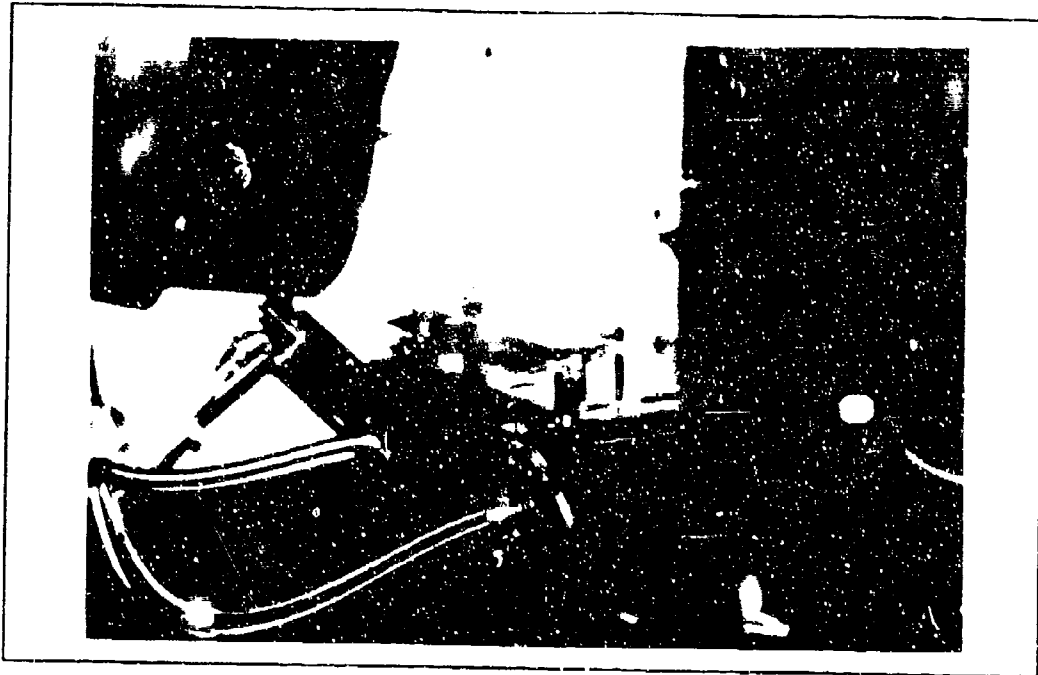


Figure 15. Scramjet Inlet Model with TMI Slot

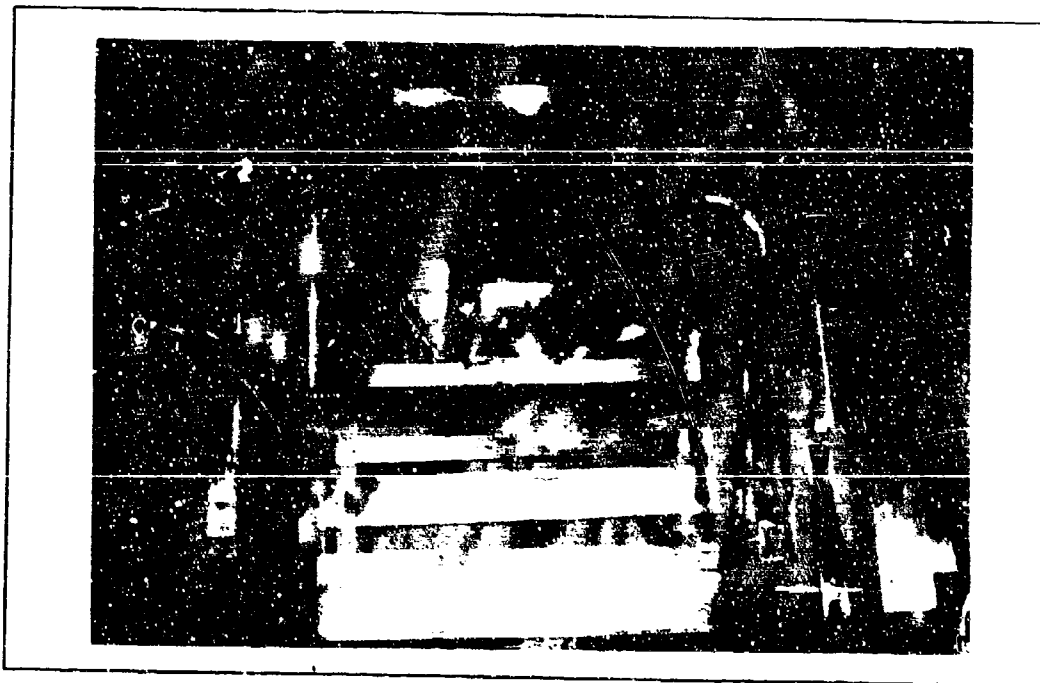


Figure 16. Multiple Model Pieces

boundary layer thickness approximately 25% of the cowl height (4). Therefore, the plate surface was not as polished as the Scaggs/Galassi plate. Also, the leading edge was modified to ensure that the weak bow shock/Mach wave would not impact the cowl shock. This required at least a 16° wave angle as opposed to the 12° angle experienced by Scaggs and Galassi (34). The 10° wedge on the underside of the leading edge was maintained as well as the 9.5 in leading edge width to ensure that the corner Mach lines did not infringe on the model centerline downstream.

The tangential mass injection piece (see Figure 17) was the most complex part of the model. An injection Mach number of 3 was chosen for comparison with White's experiments (2,24). Also, any higher Mach number may have caused the TMI air flow to liquefy since it was not heated. The Mach 3 air nozzle was scaled from Merz's drawings (35:3) to obtain a 0.20 in slot injection height. Merz's nozzle was designed using the method of characteristics and was tested to have minimal shock interference patterns (36). Considerations for minimizing tunnel blockage and maintaining low subsonic flow in the TMI ducts led to a design of TMI air supply from both sides of the model. Flexible stainless steel supply pipes that connect to L-shaped attachments underneath the model outside of the "core flow" are visible in Figure 15. O-rings were used to seal the ducts. Additionally, a flow turning vane and porous plate were installed upstream of the throat to provide a uniform velocity distribution across the 4 in

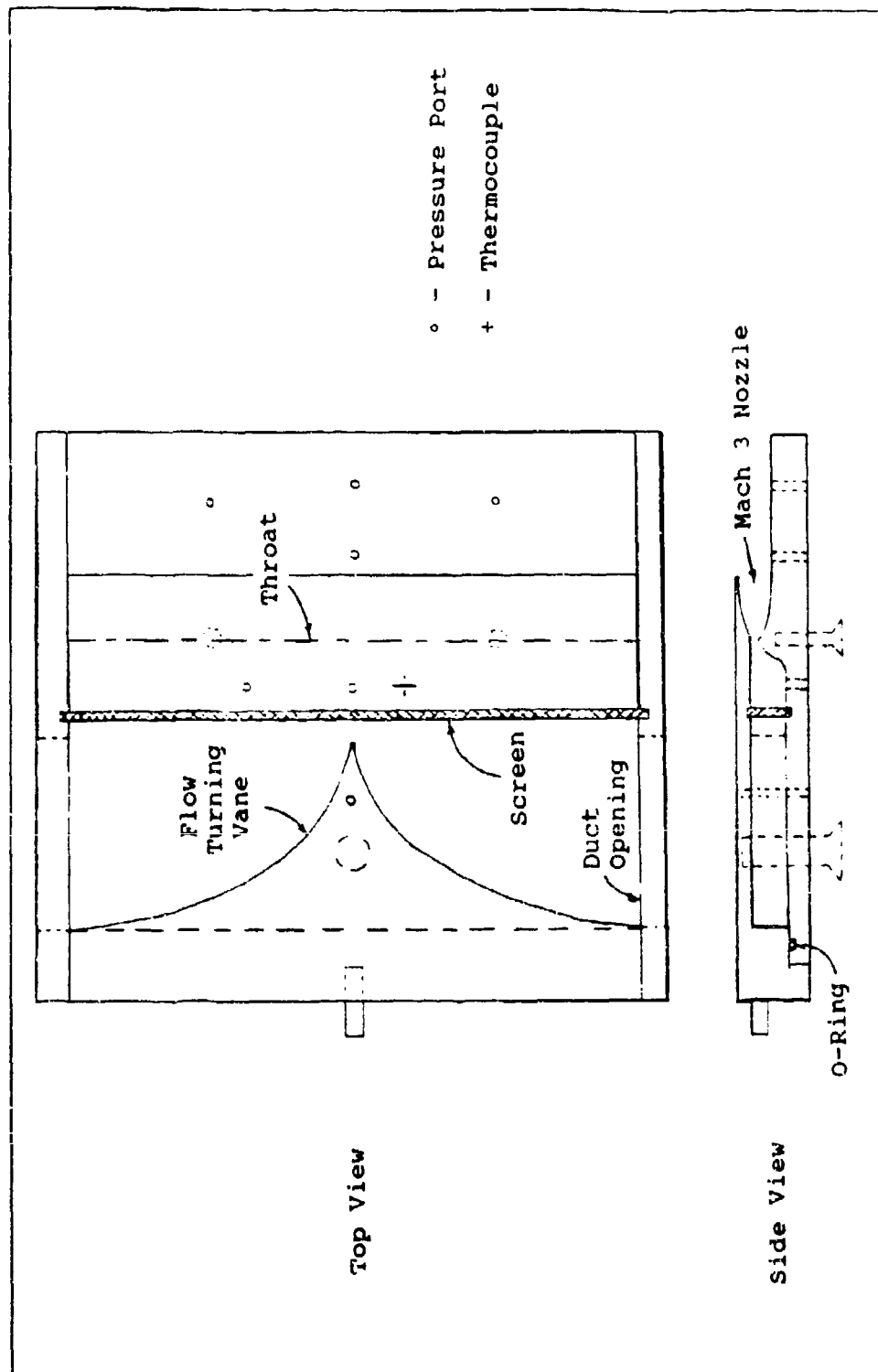


Figure 17. Tangential Mass Injection Piece Diagram

opening which was located 12 in from the model leading edge.

The other pieces were designed to permit a variety of inlet model geometries. The 1 in and 2 in spacer strips could be inserted between the slot and aft wedge to allow four configurations of TMI-to-shoulder lengths to be tested. The 2 to 5 in range was selected on Stava's advice that a proper mixing length was on the order of 10 to 25 times the boundary layer thickness (4). The flow turning angle at the shoulder could be chosen by selecting either the 12° or the 15° angle aft wedge piece. Although the cowl lip height was fixed at 2 in, the cowl deflection angle could be adjusted to either 12° or 15° through different holes in the rear cowl supports. Usually, the flow turning angle and cowl angle were matched. The diamond-shaped cowl was designed for inlet self-starting even at the maximum contraction ratio using the Kantrowitz starting limit (4). Finally, the shock impingement location (nominally at the shoulder) was adjustable by sliding the cowl and clamp assembly forward or aft. The clamp slots were designed to provide shock impingements over a 4.8 in range upstream, on, and downstream of the shoulder for all possible slot-to-shoulder lengths.

Instrumentation

The model was fitted with 39 static pressure ports although only a maximum of 29 were in use at any one time. Additionally, seven thermocouples were attached with only as many as five in use for any given run. Figure 18 and Tables 1 and 2 show the locations of the pressure taps and thermo-

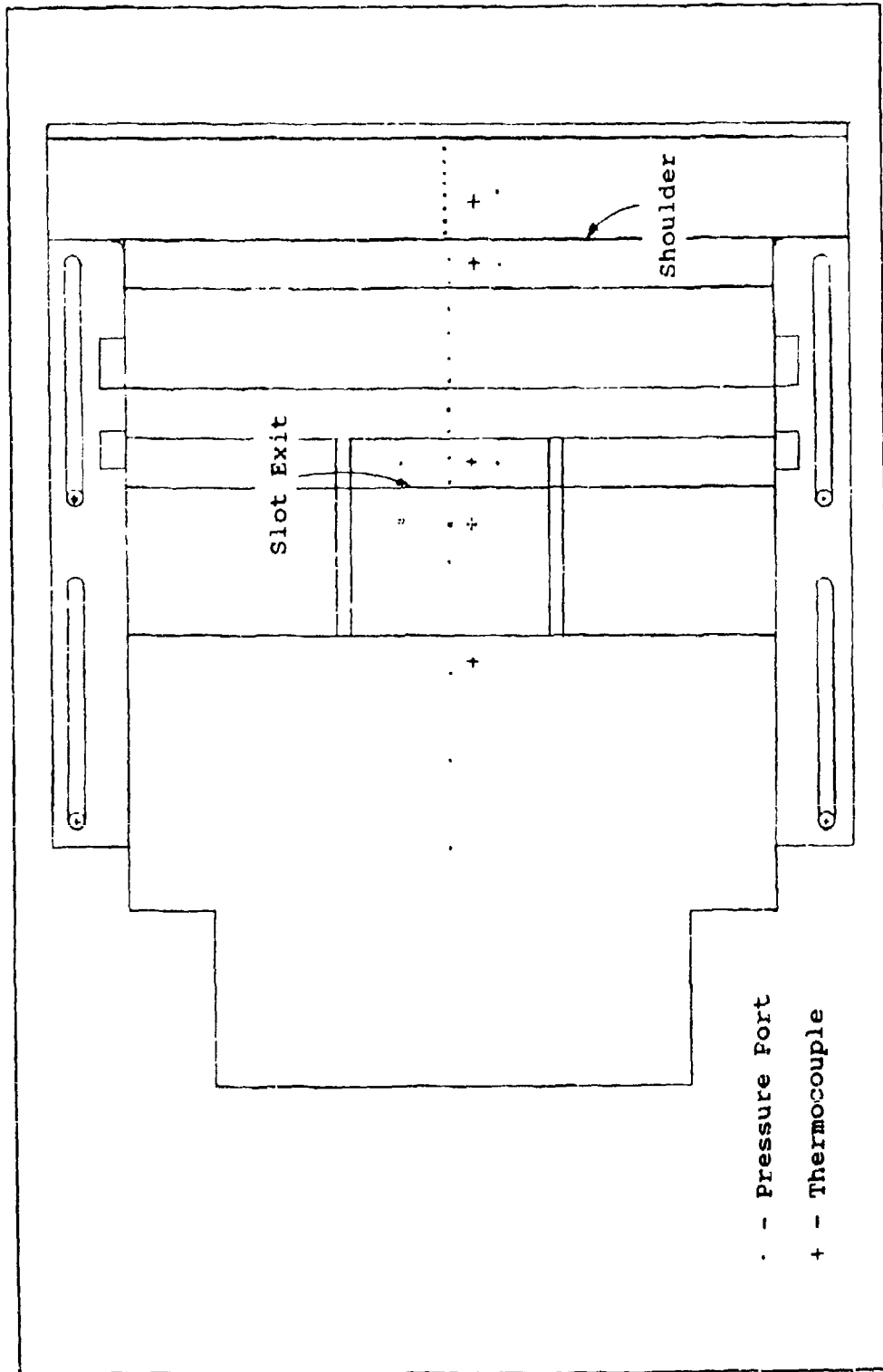


Figure 18. Model Instrumentation Diagram

TABLE 1

Pressure Port Locations

Port	X (in)	Y (in)	Port	X (in)	Y (in)	Port	X (in)	Y (in)
P _{fp} -1	4.750	0	P _{aw12} -1	.125	0	P _{aw15} -1	.125	0
P _{fp} -2	6.500	0	P _{aw12} -2	.500	1.0	P _{aw15} -2	.500	1.0
P _{fp} -3	8.250	0	P _{aw12} -3	.625	0	P _{aw15} -3	.625	0
P _{fp} -4	10.500	0	P _{aw12} -4	1.125	0	P _{aw15} -4	1.125	0
P _{THI} -1	11.235	0	P _{aw12} -5	1.375	0	P _{aw15} -5	1.375	0
P _{THI} -2	11.235	-1.0	P _{aw12} -6	1.625	0	P _{aw15} -6	1.625	0
P _{fp} -5	12.125	0	P _{aw12} -7	1.875	0	P _{aw15} -7	1.875	0
P _{fp} -6	12.50	-1.0	P _{aw12} -8	2.125	0	P _{aw15} -8	2.125	0
P _{fp} -7	12.50	1.0	P _{aw12} -9	2.250	1.0	P _{aw15} -9	2.250	1.0
P _{fp} -8	12.625	0	P _{aw12} -10	2.375	0	P _{aw15} -10	2.375	0
			P _{aw12} -11	2.625	0			
P _{i1} -1	.125	0						
P _{i1} -2	.625	0						
P _{i2} -1	.125	0						
P _{i2} -2	.625	0						
P _{i2} -3	1.125	0						
P _{i2} -4	1.625	0						
P _{cw} -1	2.00	0						
P _{cw} -2	4.00	0						

TABLE 2

Thermocouple Locations

Thermocouple	X (in)	Y (in)
T _{fp} -1	8.500	0.50
T _{THI} -1	11.235	0.50
T _{fp} -2	12.500	0.50
T _{aw12} -1	0.50	0.50
T _{aw12} -2	2.00	0.50
T _{aw15} -1	0.50	0.50
T _{aw15} -2	2.00	0.50

NOTE: For Tables 1 and 2, X is measured from the leading edge of an unattached piece (e.g. front plate, 1 in/2 in insert, 12°/15° aft wedge, cowl wedge)

couples. Channels for the 1/16 in diameter pressure tubing and thermocouple wiring were carved out of the bottom of the main flat plate pieces and out of the top of the cowl. Access panels 0.1 in thick covered these channels. The stainless steel pressure tubes were soldered to the taps. The thermocouples were installed 0.030 in beneath the surface where the static temperature was to be measured. Notice that two pressure ports and one thermocouple were positioned in the TMI plenum chamber for calculation of the TMI flow rate. They measured virtually stagnation conditions of the jet stream.

The facility instrumentation included a traversing probe, laser velocimetry (LV), and the schlieren photo system. The traversing probe could be equipped to measure pitot pressure or total temperature. LV was planned to obtain velocity profiles at several x locations. The schlieren photo/video system was set-up when the LV system was not in use. It was used for flow visualization of the shocks, boundary layer, and separation occurring in the region at the rear 6 in of the model.

Facility

The model was tested in the Wright Laboratory Mach 6 High Reynolds Number Facility located at Wright-Patterson AFB OH. Its test section is an open air, circular jet as shown in Figure 19. Once tunnel flow is established, the model is injected into the stream. The diameter of the exit nozzle is 12.35 in, but the effective core diameter is only 9-10 in due

to an annular shear layer (34). The capture cone is positioned to capture any shocks from the model and collect the exhaust flow. The freestream Mach number varies slightly with temperature, pressure, and position; but an average centerline value is 5.76 (37:26). Figure 20 is a more distant view of the test cabin with the door closed. Also visible in this picture are 1) the pressure transducer bank, 2) the exhaust duct, 3) the throat section, and 4) the secondary mirror of the schlieren system.

A schematic diagram of the facility is shown in Figure 21. A cylinder tank farm provides a total pressure range of 100-2100 psia. The pebble bed storage heater raises the total temperature of the air to between 900°R and 1100°R. This combination allows a Reynolds number per foot range of 1.5×10^6 to 30×10^6 in the test section. The flow exhausts to the 100,000 cubic foot vacuum sphere for the low pressure runs ($p_o < 700$ psi). The present set of experiments was performed at p_o 's of 200 and 500 psia with $T_o = 1000^\circ\text{R}$. This produced Re/ft values of about 3×10^6 and 7.2×10^6 .

The facility also contained a control room from which the experiments were conducted. Control stations provided for operation of the probe drive system, tunnel flow conditions, and position/injection of the model platform. A headphone-microphone intercom system allowed for communication with the operator controlling the TMI flow regulator located outside of the control room. Several monitors were used to get readings of selected parameters, and some (T_o , p_o , and p_i) were plotted

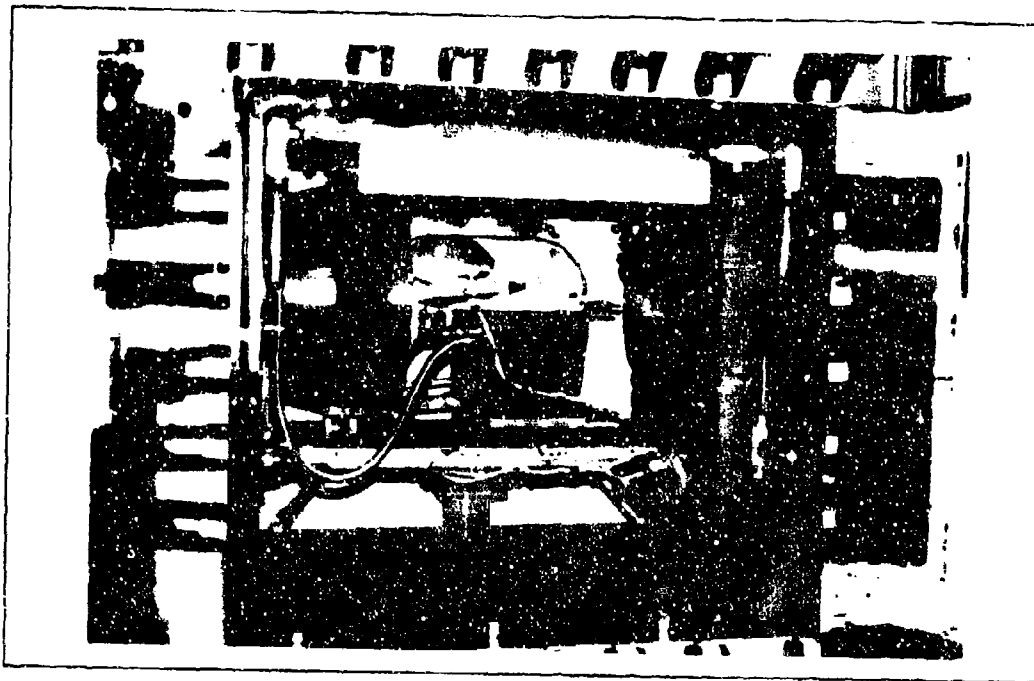


Figure 19. Test Cabin with Model in the Injected Position

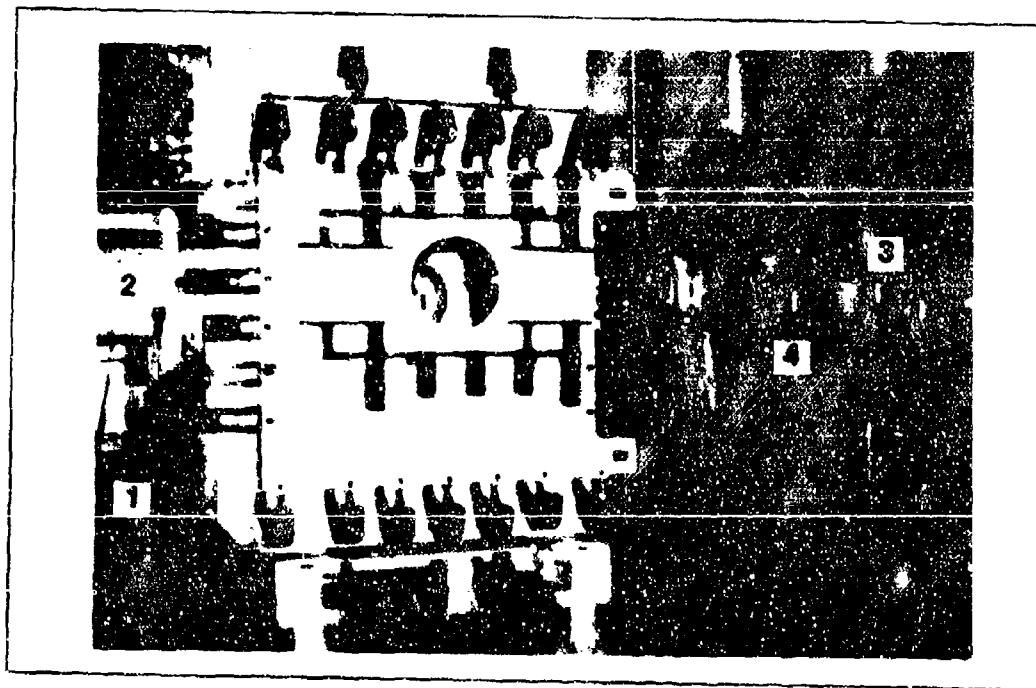


Figure 20. Test Cabin with the Door Closed

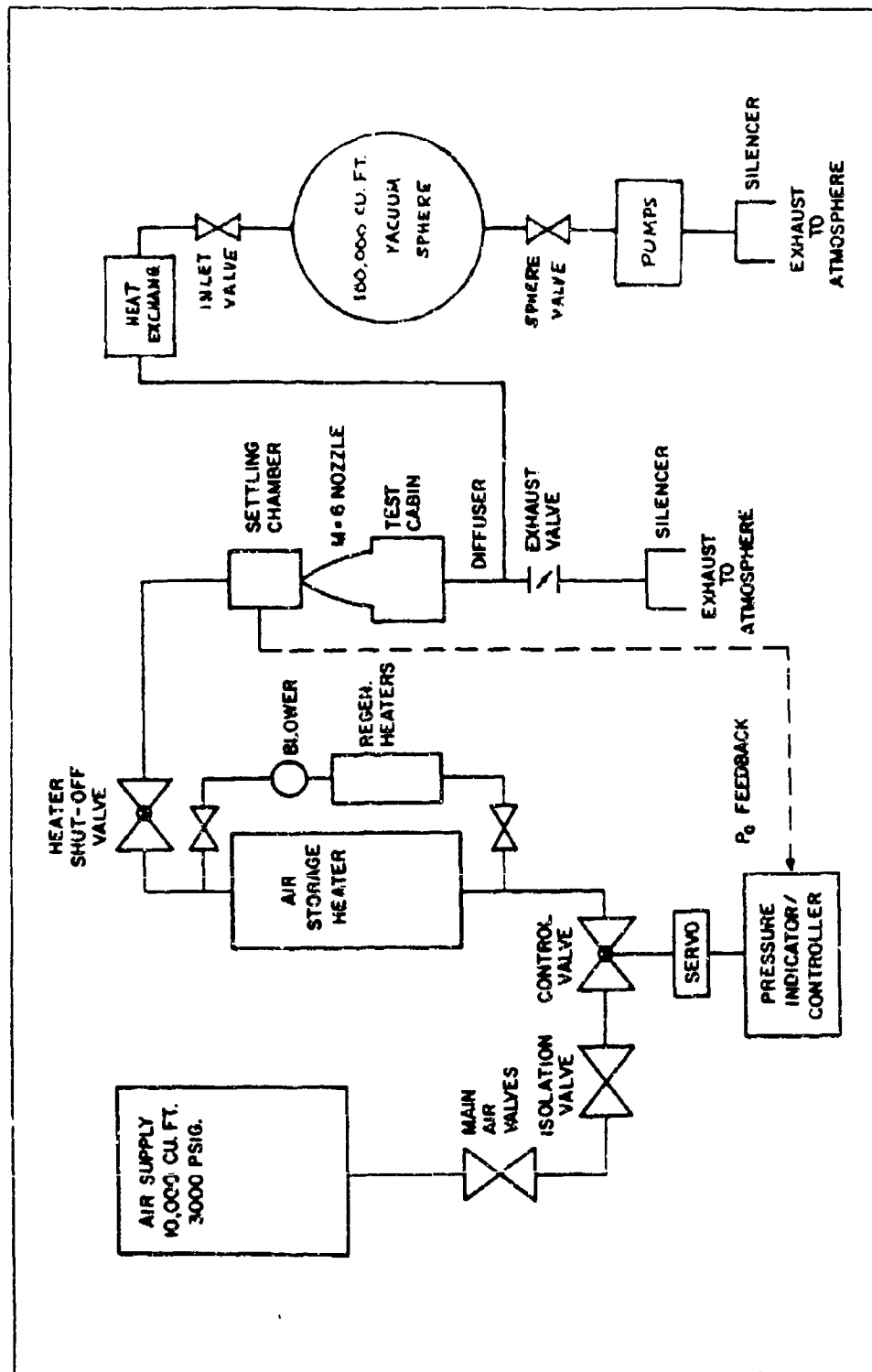


Figure 21. Schematic Diagram of WL Mach 6 High Re Facility (Ref. 37)

in real-time. The data acquisition unit was a Hewlett-Packard 3852 which was connected to a Digital Equipment Corporation Microvax 3 for data processing, storage, and graphing.

Installation

A hook-up for the injection flow was made. Two separate pipes, each with a diameter of 0.75 in, were attached to the underside of the model spaced about 11 in apart and 10 in from the leading edge. The pipes had to be flexible for the model to be injected or removed from the core flow, yet be heat resistant. The pipes had a common source reservoir, which was ambient temperature air with a maximum stagnation pressure of 50 psia. The injection mass flow rate was adjustable during a test run through a dome pressure regulator.

The model was mounted on the platform support system with dual vertical struts. The struts had four 3/8 in diameter bolt holes with centers spaced 6.5 in apart and 15 in from strut to strut. The platform support system could be hydraulically raised to inject the model into the flow.

With the model on its struts the pressure tubing was threaded through ports in the test cabin and connected to transducers just outside. Similarly, the thermocouple wiring was threaded through and connected to amplifiers. Then the instrumentation was calibrated. For each transducer, a multiple point calibration was performed resulting in a first order least squares curve fit. The thermocouples were calibrated with a ninth order curve fit since they were not as

linear. Most of the pressure transducers were rated at 20 psia, except for the two connected to the TMI chamber which were rated at 50 psia. Both the pressure and temperature readings were accurate to within 0.5%.

Configuration changes were made without removing the model from the tunnel. Typically, all that was required was the loosening of the four main bolts and sliding of the cowl assembly. To add or remove an insert, the cowl assembly was moved all the way forward and the insert either bolted to or unbolted from the bottom clamps. Changing the aft wedge piece was more involved because the limited number of transducers required pressure tube switching and recalibration.

IV. EXPERIMENTAL PROCEDURE

Three different categories of tests were conducted - checkout, flow characterization, and parametric. During the initial checkout tests only the schlieren system and a TMI plenum pressure port were used. Additionally, for flow characterization, pitot pressure surveys were made and wall static pressure distributions were collected for various amounts of blowing. An attempt to measure velocity profiles with LV failed. Parametric testing utilized the pitot probe, wall pressure ports, and the schlieren system.

Test Program

The test program was the plan for how the parameters were to be varied and in what order. Tables 3 and 4 show the planned parameter values and their mapping to model/facility configuration. The cowl lip position, X_{cowl} , values in Table 4 were derived with the aid of an oblique shock chart (38) - the condition, $M_1=5.76$, and cowl deflection angles, $\beta=12^\circ$ and 15° , yielded cowl shock angles, $\theta=20^\circ$ and 23° , respectively. The test matrix in Table 5 shows the actual configurations, measurements, and sequence for the runs. A blank entry in this table indicates that the value above it still applies. In general, this sequence was established on the basis of doing the most difficult configuration changes the fewest number of times. Some tests had to be rerun due to problems

TABLE 3

Parameter to Configuration Map

Parameter	Value	Configuration
L_{SHR}	2 in	No inserts
	3 in	Only 1 in insert
	4 in	Only 2 in insert
	5 in	Both inserts
L_{SHK}	$.8L_{SHR}$	X_{cowl} depends on L_{SHR} and β (See Table 4)
	L_{SHR}	
	$1.1L_{SHR}$	
α	12°	12° aft wedge piece
	15°	15° aft wedge piece
β	12°	12° cowl angle hole
	15°	15° cowl angle hole
ϕ	0°	Wedge shims out
	2°	2° wedge shims in
δ_1	0.50 in	Tunnel $p_o=200$ psia $=500$ psia
	0.25 in	
m_{TMI}	$0.05m_{CAP}$	At $p_o=200$ psia $p_{oi}=7$ psia
		$=500$ psia $=17$ psia
	$0.10m_{CAP}$	At $p_o=200$ psia $p_{oi}=14$ psia
		$=500$ psia $=35$ psia

TABLE 4

Shock Location Map

β	L_{SHR} (in)	X_{cowl} (in) for $L_{SHK} =$		
		$.8L_{SHR}$	L_{SHR}	$1.1L_{SHR}$
12°	2	8.0	8.4	8.7
	3	8.8	9.4	9.7
	4	9.6	10.4	10.8
	5	10.4	11.4	11.9
15°	2	8.3	8.7	9.1
	3	9.1	9.7	10.0
	4	9.9	10.7	11.1
	5	10.7	11.7	12.2

TABLE 5

TMI Inlet Model Test Matrix

Test Mat. Run	Tunnel Runs	Configuration					Measurements			
		α	β	ϕ	Inserts	X_{cowl} (in)	P_o (psia)	P_{qj} (psia)	Type	X(in)
1	1	15°	15°	0°	Both	11.7	200	0	-	-
2	2						500	0	-	-
3	3			2°		rmv	500	0	P_T	11.8
4	4						200	0		
5	5						200	18.4		12.1
6	6, 7, 8						500	46		
7	9					11.7	200	0		16.5
8	10						500	0		
9	11						200	7.4		
10	12						200	15.6		
11	13						500	25		
12	14						500	45		
13	15					12.2	200	0-22		17.3
14	16						500	0-15		
15	17					10.7	200	0-30		15.5
	18							0-38		15.0
16	19						500	0-29		
17	20				2"	10.7	200	0-30		15.0
	56	12°						0-36		
18	21	15°					500	0-30		
	57	12°						0-46		-
19	22	15°			1"	9.7	200	0-30		14.0
20	23						500	0-35		
21	24				None	8.7	200	0		13.0
	25							0-18		13.0
								18-30		13.5
22	26						500	0		13.0
	27							0-23		13.5
23	28					9.1	200	0-30		14.4
	58	12°						0-15		14.2
24	29	15°					500	0-26		
25	30					8.3	200	0-24		13.0
	59	12°						0-16		12.9
26	31	15°					500	0-15		13.0
	60	12°						0-15		12.9
27	32	12°	12°	2°	None	7.8	200	0-22		13.5
28	33						500	0-23		13.0
29	34					8.4	200	0-8		13.5
	61					8.3		0-10		
30	35					8.4	500	0-47		-
	62					8.3		0-46		13.5
31	36					8.7	200	0-15		14.2
32	37						500	0-30		
33	38					7.4	200	0-23		12.6
34	39			0°				0-23		

TABLE 5
TMI Inlet Model Test Matrix
(continued)

Test		Configuration						Measurements	
Mat. Run	Tunnel Runs	α	β	ϕ	Inserts	X_{cowl} (in)	p_p (psia)	p_{qj} (psia)	Type X(in)
35	40	12°	12°	0°	None	7.4	500	0-46	p_r 12.6
36	41			2°	1"	9.4	200	0-40	
37	42						500	0-46	
38	43					8.3	200	0-24	13.6
39	44				2"	10.4	200	0-41	15.5
	54					10.3		20-46	15.3
40	45					10.4	500	0-46	-
	55					10.3		0-46	15.3
41	46					rmv	200	18	T_r 12.1
42	47						500	46	
43	48						200	0	LV 11.0
44	49						500		
45	50						200		LLS 11-18
46	51							0	p_r 11.5 10.5 14.0
47	52							10 20	14.0
48	53			0°				0 0 10 20	11.5 14.0

NOTE: $T_0=1000^\circ\text{R}$, rmv= cowl removed, LLS= laser light sheet

with the tunnel or inconclusive results; thus, a test matrix run number may have several different (tunnel) run numbers.

If all possible parameter combinations were tested, it would have required 48 runs. The coverage was reduced to 29 runs due to the tight facility schedule. The off-design conditions of the cowl shock impinging forward or aft of the shoulder were tested only at the extreme values of $L_{\text{SHR}}=2$ in and 5 in. Additionally, as the $\beta=15^\circ$ results indicated that

TMI was ineffective for the larger L_{SHR} configurations, the $L_{SHR}=5$ in test runs were eliminated for $\beta=12^\circ$ and two runs were added with $L_{SHK}=1$ in.

Test Objectives

The objectives of the checkout test were as follows:

- 1) determine the minimum tunnel total pressure without the model causing tunnel unstart (blockage test),
- 2) check for inlet self-starting,
- 3) check for undesirable flow patterns (e.g. the bow shock impacting the cowl, corner Mach lines crossing the centerline downstream),
- 4) characterize the boundary layer thickness,
- 5) ensure the supply pipes can provide 50 psia to the TMI plenum and the model can withstand the pressure loading,
- 6) check the 2-D quality of the jet flow, and
- 7) ensure general model compatibility with the facility.

The objectives of the flow characterization tests were to obtain velocity profiles at several locations and wall static pressure distributions. These were desired for several different rates of TMI to permit a trend analysis.

The objectives of the parametric testing were to determine the TMI rate required to eliminate separation for each configuration and to determine the optimum slot location. The controlling TMI rate data would be used to discern trends in the various parameters so that an ideal vehicle configuration and TMI rate control system could be established.

General Approach

The general steps followed during a test run were as follows:

- 1) zero full-scale set the pressure transducers (only the first run of each day),
- 2) establish the model and facility configuration,
- 3) pump down the vacuum sphere,
- 4) conduct a pre-test readiness check and countdown,
- 5) start the tunnel and video schlieren VCR; fine tune p_o ,
- 6) inject the model and wait for stability,
- 7) take a pitot pressure survey for $m_{TMI}=0$ (selected runs),
- 8) take a schlieren photo for $m_{TMI}=0$ (selected runs),
- 9) position the pitot probe in the separation bubble just off the surface (selected runs),
- 10) begin increasing the TMI flow rate incrementally,
- 11) perform pitot pressure survey(s) near the suspected controlling m_{TMI} ,
- 12) take a schlieren photo,
- 13) continue increasing the TMI flow rate up to 10-15% of the inlet captured flow rate,
- 14) turn off TMI, eject the model, and stop the tunnel flow,
- 15) bring the test cabin pressure up to atmospheric, and
- 16) print out the data and graphs.

Run times were limited to 30 min for $p_o=200$ psia and 10 min for $p_o=500$ psia due to the filling of the vacuum sphere. Only four or five runs per day could be performed before depleting the heat capacity of the storage heater.

Measurements

The traversing probe was used for pitot pressure and total temperature profiles. Surveys went out to a maximum of 0.72 in above the surface in 0.020-0.060 in increments. The probe would be brought down to the model surface and the Z position indicator zeroed. The pressure or temperature reading typically took 5-10 sec to steady out for each step. Once it leveled off at each step, a computer keystroke stored all test data at that particular instant. Each test point is differentiated by a unique test point number (TPN). Pitot pressure surveys were used to determine δ , separation height, velocity profiles, controlling m_{TMI} , and the jet 2-D qualities. Total temperature surveys provided an indication of δ_1 .

Perhaps one of the most important parameters to measure was TMI mass flow rate. Since an adequate mass flow meter was not available, m_{TMI} had to be calculated from the plenum pressure and temperature readings (there were two pressure ports in the plenum just in case one developed a leak or got blocked). The following equation was used (with $\gamma=1.4$)

$$m_{TMI} = \frac{\sqrt{\frac{\gamma}{R} \left(\frac{2}{\gamma+1} \right)^{\frac{\gamma+1}{\gamma-1}} g_c} P_{oj} A^*}{\sqrt{T_{oj}}} = \frac{0.532 P_{oj} A^*}{\sqrt{T_{oj}}} \quad (7)$$

which is equivalent to the method shown in Appendix C.

The static pressure tap measurements were used to determine the separation length and incipient separation point. Static temperatures on the model surface were not

important for this investigation but may be useful for any follow-on CFD analyses.

Contrary to the original thinking, incipient separation could not be determined in real-time. This forced a slight change in the procedure for detecting it. Rather than increasing the TMI flow directly up to the incipient separation point, it had to be increased incrementally taking test data points over a range. The wall static pressure data would be graphed after the test and the controlling mass injection rate found by interpolation of the curves based on several criteria.

Another method used for determining the controlling TMI rate was to position the pitot probe just off the model surface in the separated region while the TMI flow was increased. If separation was still present, the pitot pressure in the "bubble" would remain virtually the same, but once the bubble was eliminated there would be a sharp increase in p_t .

A unique approach to making LV measurements in a hypersonic wind tunnel was attempted. The procedure involved firing four laser beams at slightly different angles through the test cabin window and detecting the back scatter light from the seeded air (most LV set-ups use the precision demanding forward scatter technique). This effort failed to provide velocity profiles due to a lack of laser power and a lack of seed in the boundary layer. Also, since the TMI flow was not seeded, the only data that could have been obtained

were velocity profiles upstream of the slot and perhaps data for s_1 and s_3 . However, LV did provide a good indication of the freestream velocity and flow visualization of the tangential mass injection (the latter in the form of a laser light sheet video).

The schlieren system consisted of a light source, two primary mirrors (one on each side of the movable test cabin window), an instant-developing camera with adjustable knife edge and view-through ground glass, and a video camera. Both the light source and the still camera had secondary mirrors aimed at opposite primary mirrors. The still camera provided 3.5 x 5 in photographs with negatives. Taking a schlieren photo momentarily interrupted the schlieren video which was recorded on a VHS VCR.

V. RESULTS

As mentioned previously, the experimental tests were categorized as either checkout, flow characterization, or parametric. The checkout test results indicated that a few minor changes were necessary for proper operation; these were made prior to any further testing. The results of the flow characterization showed that certain trends in wall and pitot pressure occurred when the TMI flow rate was increased. These trends helped to identify criteria that could be used to determine the incipient separation point. The criteria were applied to the parametric test results to find the controlling TMI flow rate for each test condition. When plotted, these rates indicated that the optimum slot-to-shoulder length was approximately five slot heights with a corresponding controlling TMI rate ratio (normalized to the inlet captured mass flow) of around 5%. These values compared favorably to the theory and previous experimental results.

Checkout Tests

The checkout test series consisted of tunnel blockage and injection tests. The blockage tests were conducted as Runs 1 and 2. The injection tests usually did not require running the tunnel and so were not labelled as runs; although, part of Run 3 and Run 50 were considered to be injection tests.

Blockage. Run 1 verified that the model with cowl caused no tunnel blockage at a reservoir pressure of 200 psia, the

lowest selected value. The schlieren video indicated that the inlet self-started. The incoming boundary layer thickness at $X=12$ in was estimated to be 0.3 in from the schlieren photo - less than the 0.5 in desired for the 25% cowl height condition, but it was deemed satisfactory since little could be done to increase δ without jeopardizing the natural profile shape of the boundary layer. Modelling the boundary layer growth of a scramjet inlet is a problem common to many hypersonic wind tunnel facilities (33:1-2). Run 2 was with $p_0=500$ psia, and it also passed the blockage and inlet self-starting checks. The incoming boundary layer thickness for this condition was estimated to be 0.25 in.

Both runs showed that the bow shock angle was less than the 16° needed and that the bow shock may deflect the cowl shock in future runs. Dorrance suggests that this flat plate bow shock is caused by the boundary layer's displacement thickness growth rate at the leading edge (39:145-6). Stava proposed pitching the entire model at -2° angle of attack to partially negate the δ^+ growth and, thus, weaken the bow shock (4). This approach would also lower the cowl lip with respect to the bow shock, further mitigating any interference. Hence, 2° wedge shims were fabricated and placed on the top and bottom of the end clamps on both sides of the model for the majority of the remaining runs. Apparently, that solved the problem as no cowl shock deflection was observed in subsequent runs (see Figures 73, 86, 87, and 88 in Appendix F).

Injection. These tests ensured that the secondary air supply could provide the desired maximum $p_{o,j}$ and that the jet retained 2-D characteristics, especially along the model centerline. Initially, the top half of the TMI nozzle raised up with injection (especially at the corners) allowing a maximum $p_{o,j}$ of only 38 psia. To resolve this deficiency, the TMI nozzle corners and TMI assembly leading edge were heliarc welded to the front plate providing the design $p_{o,j}$ of 50 psia. The TMI assembly and ducts still leaked in several places causing undesirable shocks in the flow field. These were patched with high temperature resin.

The porous screen was blown out in early tests leading to concerns about the 2-D qualities of the jet. However, a pitot pressure survey just behind the slot exit in Run 3 verified it still had good 2-D flow across its 4 in width (see Figure 22). Later, in Run 50, a laser light sheet test showed that the jet flow maintained its two dimensionality well downstream.

Flow Characterization Tests

The purpose of these tests was to deduce values for M_1 , δ , and δ_1 and trends for wall static pressures, pitot pressure profiles, and general flow structure. They were conducted in Runs 3-14, 39, and 46-53.

Determination of Inlet Flow Conditions. With the model at zero pitch angle, the incoming Mach number, M_1 , would have been reduced from $M_o=5.76$ by the bow shock. In fact, with a 12° bow shock angle, oblique shock tables and a Prandtl-Meyer

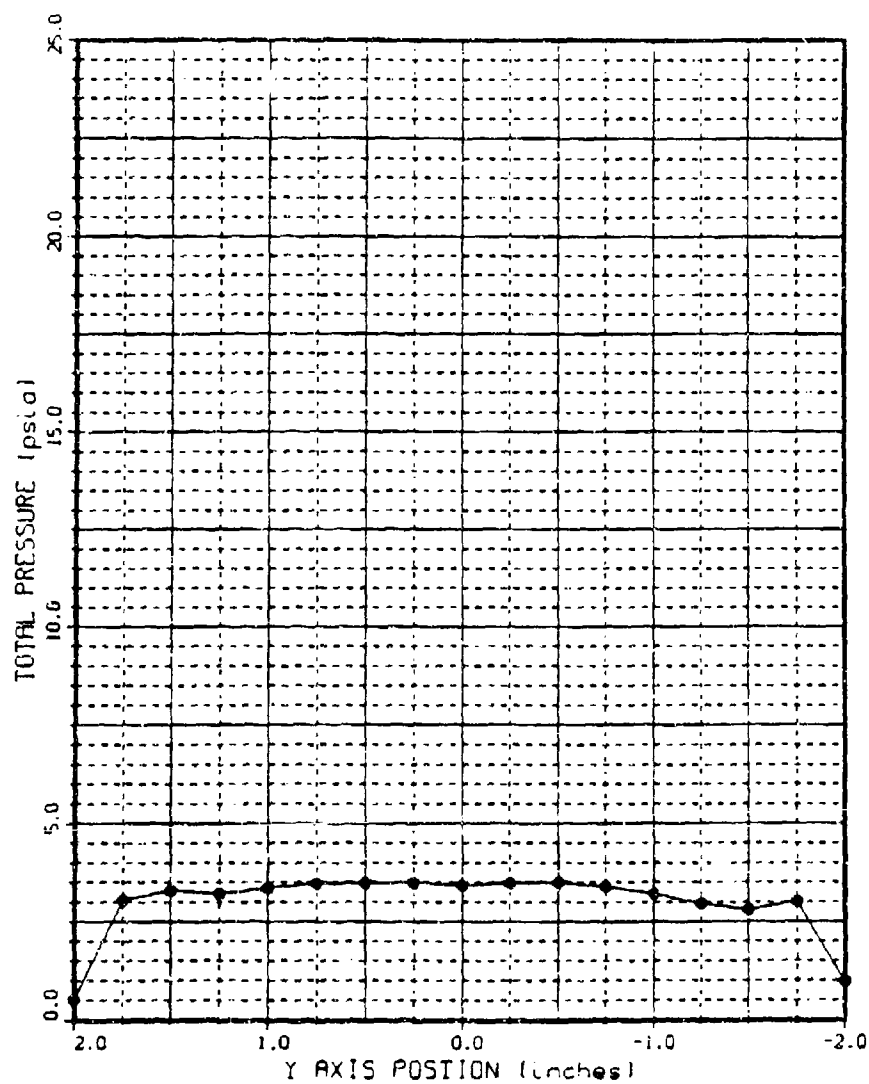


Figure 22. Run 3 Pitot Pressure Survey at $X=12.1$ in, $Z=0.1$ in, $p_{o1}=0$ psia, $p_{o1}=9$ psia

expansion calculation (38) gave $M_1=5.5$. However, with the model pitched to weaken the bow shock one could assume $M_0=M_1=5.76$. An LV measurement confirmed that the freestream velocity, u_1 , was 3230 ft/sec. The isentropic temperature relation and Mach number equation with $T_{01}=1000^\circ\text{R}$ and $M_1=5.76$ yield the same result.

Assuming the static pressure through the boundary layer is constant, the pitot pressure profiles are representative of the velocity profiles. The boundary layer thickness was determined by locating the point where the local pitot pressure was 99% of the edge pitot pressure. From Figure 23, $\delta=0.26$ in for the $p_0=200$ psia runs, and from Figure 24, $\delta=0.20$ in for the $p_0=500$ psia runs. Note that in Figure 23, the $Z=0$ pitot pressure measurement was approximately twice that of the above two Z positions, indicating that the probe tip was entirely within the subsonic region of the boundary layer where no shock would be generated to reduce the total pressure. Refer to the Pitot Pressure Profiles section for further discussion on the boundary layer shapes.

Figures 25 and 26 indicate that δ_r has virtually the same value as the respective δ . Note that the total temperatures were measured just behind and from the bottom of the slot.

Wall Static Pressure Distributions. The measured values of p_w ranged from 0.16 psia to 4 psia, with the smaller values occurring on the front plate upstream of the slot and the higher values downstream at the cowl shock impingement. This section will address the wall pressures ahead of the slot,

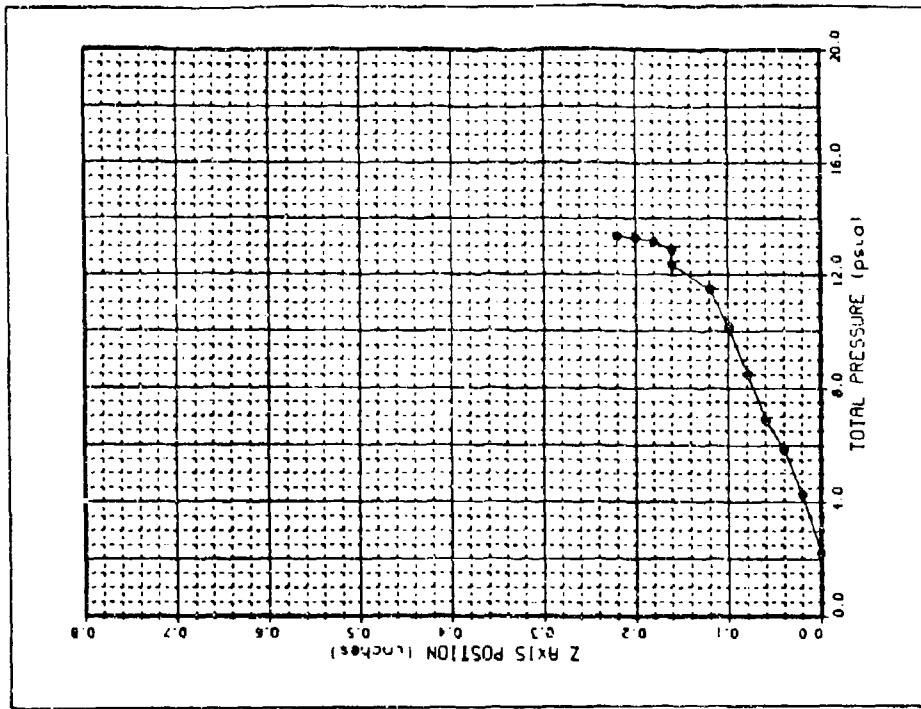


Figure 23. Run 4 Pitot Pressure Profile at $X=11.8$ in, $P_{01}=500$ psia

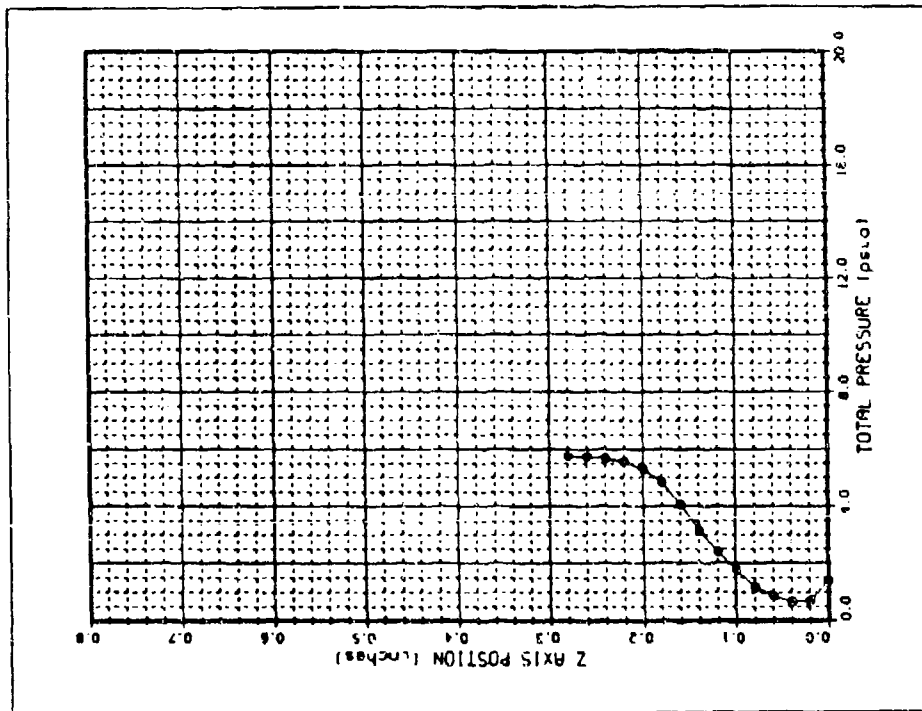


Figure 24. Run 3 Pitot Pressure Profile at $X=11.8$ in, $P_{01}=500$ psia

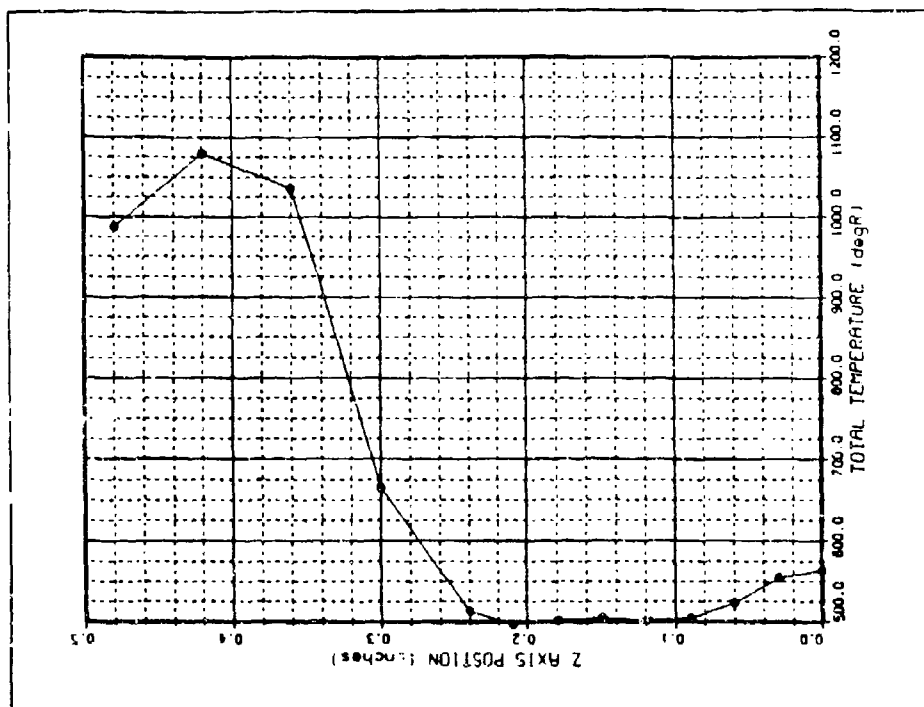


Figure 25. Run 46 Total Temperature Profile at $X=12.1$ in, $P_{01}=19$ psia

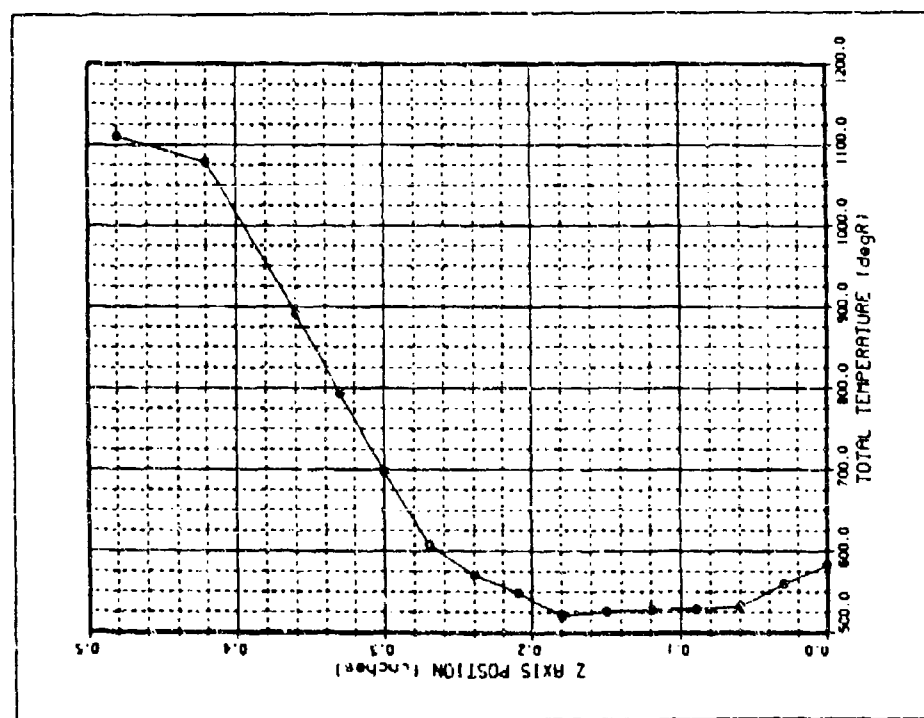


Figure 26. Run 47 Total Temperature Profile at $X=12.1$ in, $P_{01}=46$ psia

just behind the slot, and downstream of the slot with and without the cowl.

A critical issue with the wall static pressure upstream of the slot is how well it represents the freestream static pressure. Peake found them to match for $M \approx 2$ within 10% difference, even in the mixing region (20:8). Assuming isentropic flow upstream of the slot (even a 12° bow shock reduces p_0 only ~1%), the freestream static pressure can be calculated by

$$p = p_0 \left(1 + \frac{\gamma - 1}{2} M^2 \right)^{-\frac{\gamma}{\gamma - 1}} \quad (8)$$

For the present set of experiments with $\gamma = 1.4$ and $M_1 = 5.76$, the equation above gives about a 15% difference when compared to the measured wall pressures as shown in Table 6.

TABLE 6
Differences in Wall and Freestream Pressure

p_0 (psia)	Avg. Measured p_w (psia)	Calculated p_1 (psia)	% Difference
200	0.18	0.16	12
500	0.34	0.40	16

It is worth mentioning that pressure port p_{fp-4} , located atop the TMI assembly at $x = 10.5$ in, was observed to have leakage at its solder joint. This caused its readings to err on the high side at high injection pressures. No effect was observed at low values of p_{oj} .

As expected, the wall pressure just behind the slot (p_{tp-5}) was dependent on p_{oj} . However, its measured values did not match the calculated jet static pressure as closely as did the upstream wall and the calculated freestream pressures. Equation (8) was utilized again with $\gamma=1.4$ and two different values of M_j to form Table 7.

TABLE 7
Differences in Wall and Jet Pressures Behind Slot

p_{oj} (psia)	Avg. Measured p_w (psia)	$M_j=3.0$		$M_j=2.6$	
		Calculated p_j (psia)	% Diff.	Calculated p_j (psia)	% Diff.
10	0.50	0.27	60	0.50	0
20	0.95	0.54	55	1.00	5
30	1.50	0.82	59	1.50	0
40	2.10	1.09	63	2.00	5

Two possible explanations for the large difference with $M_j=3$ are offered. Some bowing of the nozzle top surface (an estimated 0.020-0.030 in at the centerline) was observed at the higher jet total pressures. This would cause a lower jet Mach number as the area ratio would be smaller:

$$\frac{A_j}{A^*} = \frac{0.20 \text{ in} + 0.025 \text{ in}}{0.047 \text{ in} + 0.025 \text{ in}} = 3.125$$

which from NACA Report 1135 (38) yields $M_j=2.68$. Another observation was that the jet formed a potential core which lengthened with increasing p_{oj} . Thus, p_{tp-5} was probably behind a shock wave emanating from the wall at the slot exit.

This would increase the wall static pressure beyond that of the jet stream core. Most likely, a combination of these two factors occurred.

With the cowl removed, a recompression shock impinged downstream of the slot causing a pressure rise as shown in Figures 27-29. This shock impingement moved downstream with increasing p_{0j} as indicated in Table 8. This would suggest that s_2 from the theory increases with injection rate; however, this was not reinvestigated in the theory.

TABLE 8
Location of Recompression Shock Impingement

p_{01} (psia)	p_{0j} (psia)	L (in)	s_2
500	0	2	-0.100
200	18	3.5	-0.057
500	46	4	-0.050

With the cowl attached, the generated shock created a pressure peak at the point of impingement. As shown in Figure 30, the case of no injection results in a gradual rise in pressure to the peak starting 3.5 in upstream of the impingement. With injection, the peak went higher and became more distinct as shown in Figure 31. The beginning of the pressure rise was delayed by at least 2 in. Expansion waves from the bottom of the reduced cowl wedge, together with the expansion past the shoulder, most likely caused the pressure drop after the impingement point.

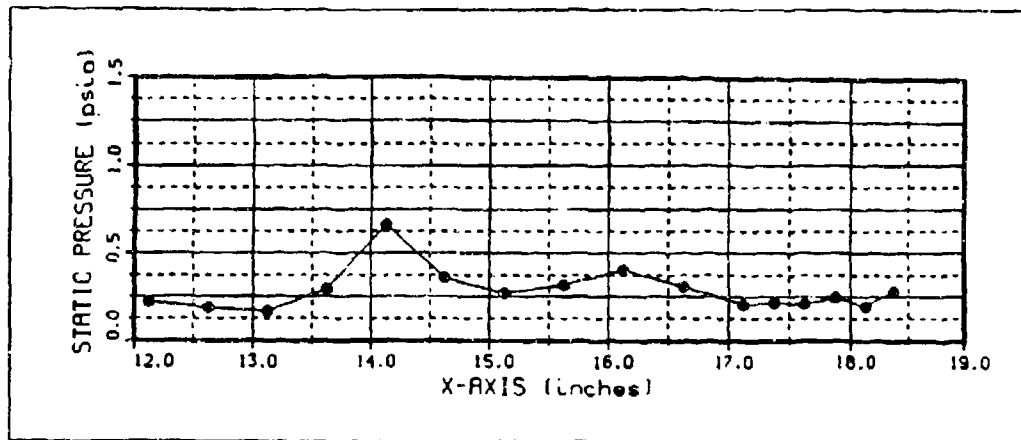


Figure 27. Run 3 C/L Static Pressure Distribution at $p_{o1} = 500$ psia, $p_{oj} = 0$ psia

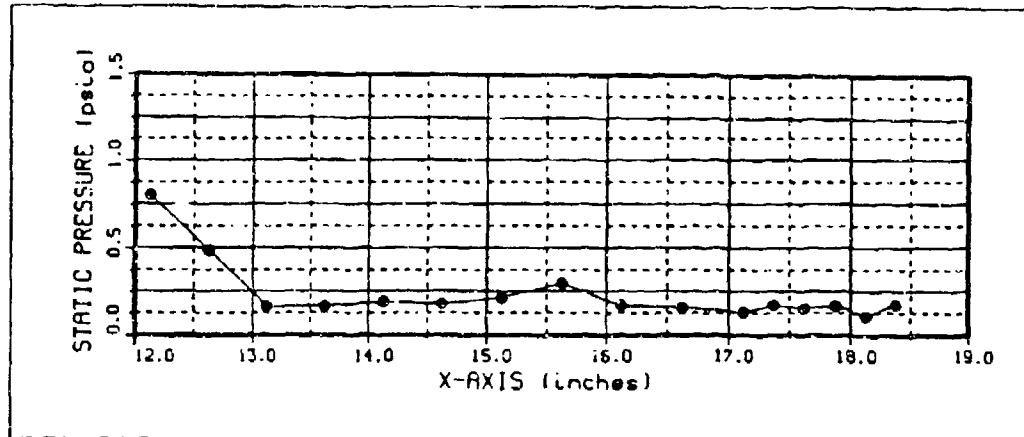


Figure 28. Run 5 C/L Static Pressure Distrib. at $p_{oj} = 18$ psia

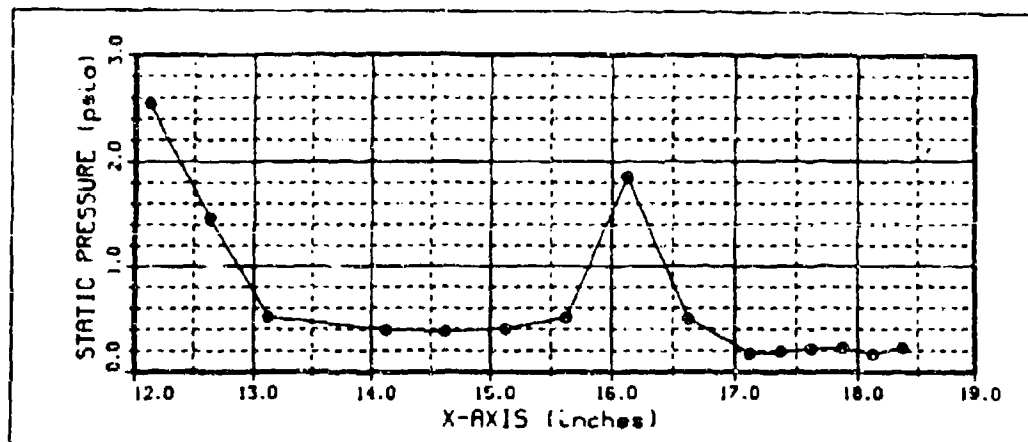


Figure 29. Run 8 C/L Static Pressure Distrib. at $p_{oj} = 46$ psia

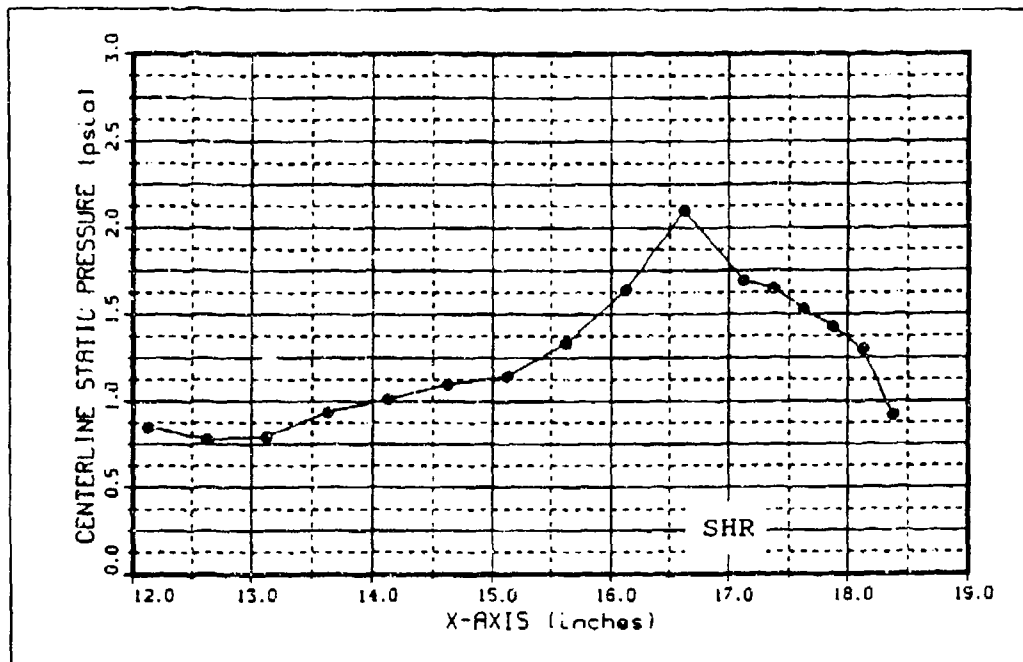


Figure 30. Run 10 C/L Static Pressure Distrib. at $p_{oj} = 0$ psia

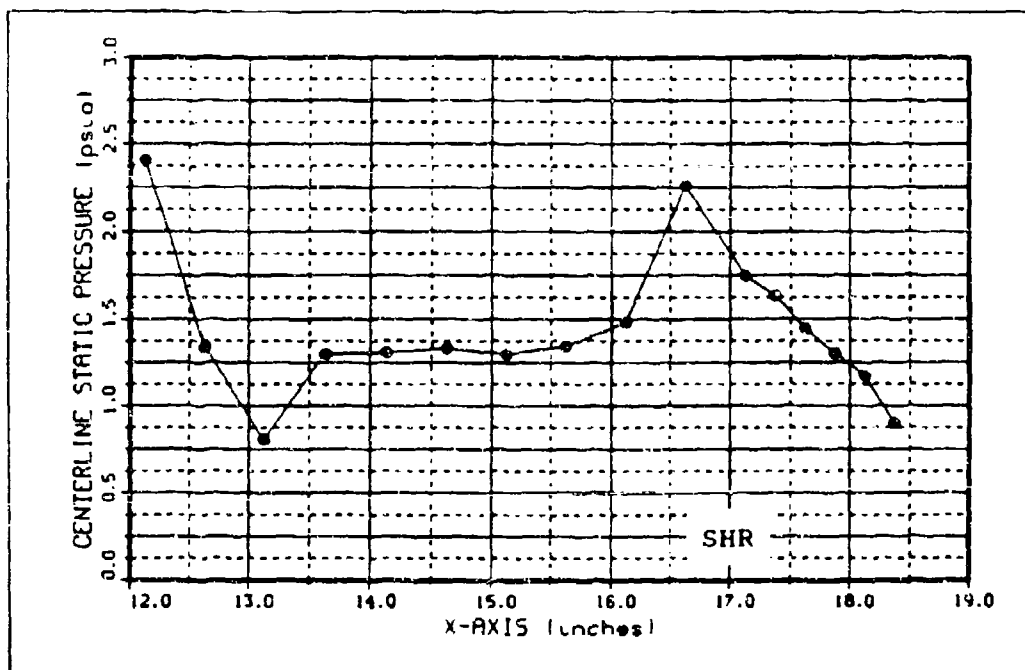


Figure 31. Run 14 C/L Static Pressure Distrib. at $p_{oj} = 45$ psia

Pitot Pressure Profiles. These surveys provided an indication of incoming boundary layer shape, separation height, and values for s_1 . Since LV measurements could not provide velocity profiles, the pitot pressure profiles were deemed an adequate substitute.

Recall that Figure 23 was a graph of the pitot pressure through the incoming boundary layer at $p_o=200$ psia. The shape at the bottom of the curve lead to concern that the boundary layer was already separated, perhaps due to the 2° model pitch. This survey was repeated in Run 51 with little change, and another survey was made with no model pitch in Run 53. The results are compared in Figure 32 along with the profile for $p_o=500$ psia. The model pitch apparently did have some influence, but the boundary layer just before the slot at

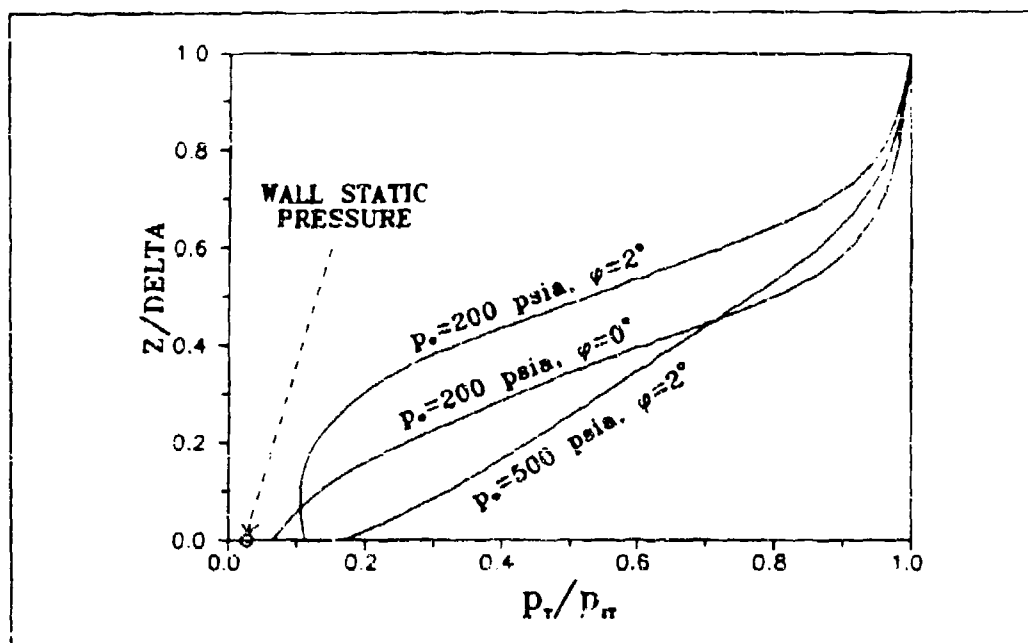


Figure 32. Comparison of Boundary Layer Profiles

$p_o=200$ psia never appeared to be turbulent. At the other extreme, concern of separation was alleviated when it was noted that the smallest pitot pressure was at least twice the wall static pressure. Furthermore, Stetson pointed out that the "elbow-shaped" profile in Figure 23 is a common consequence of probe-wall interference and is typical of a pitot pressure profile for a laminar boundary layer (40). It was concluded that the incoming flow was laminar for $p_o=200$ psia and turbulent for $p_o=500$ psia.

When probing in a separation bubble, the pitot pressure was observed to be constant and roughly equal to the peak wall static pressure. The separation height could be determined from the point at which the pitot pressure began to increase. Figures 33 and 34 indicate that the separation height was reduced as injection was increased. From Figure 33c), separation was nearly eliminated at the highest TMI flow rate tested for that configuration.

The boundary layer growth rate in the mixing region was measured for $p_o=200$ psia at several different TMI rates. Pitot pressure surveys were taken 2 in downstream of the slot for $p_{o,i}=0, 10$ and 20 psia as shown in Figure 35. Note that the surveys for $p_{o,i}=10$ and 20 psia were cut just short of the boundary layer edge, but one can extrapolate that they occur at $z=0.64$ in and 0.75 in, respectively. With $\delta_i=0.26$ in, $h=0.20$ in, and $L=2.0$ in, values for s_i were calculated and are displayed in Table 9.

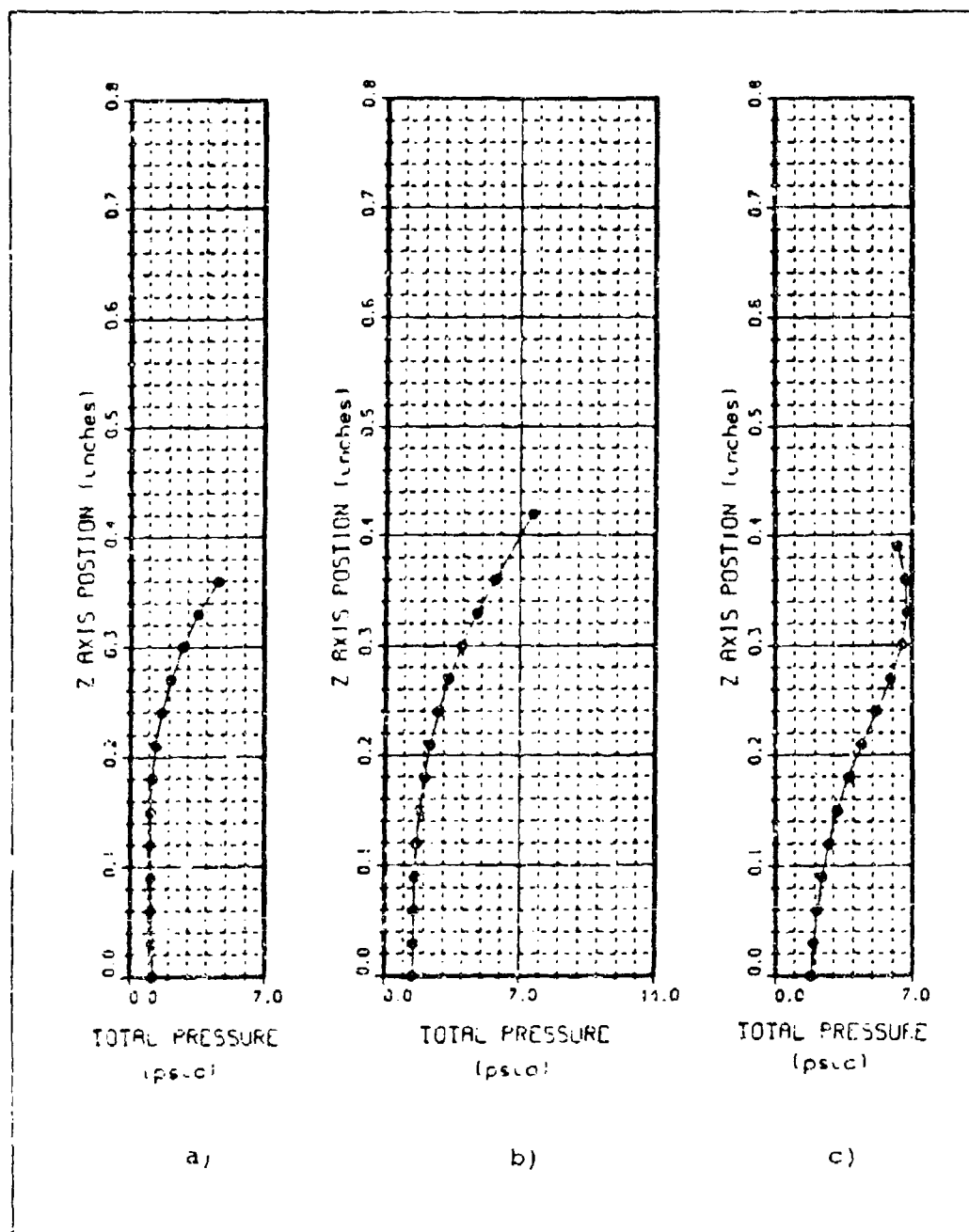


Figure 33. Pitot Pressure Profiles at $X=16.5$ in for a) Run 9 at $p_{0j} = 0$ psia, b) Run 11 at $p_{0j} = 7$ psia, c) Run 12 at $p_{0j} = 15$ psia

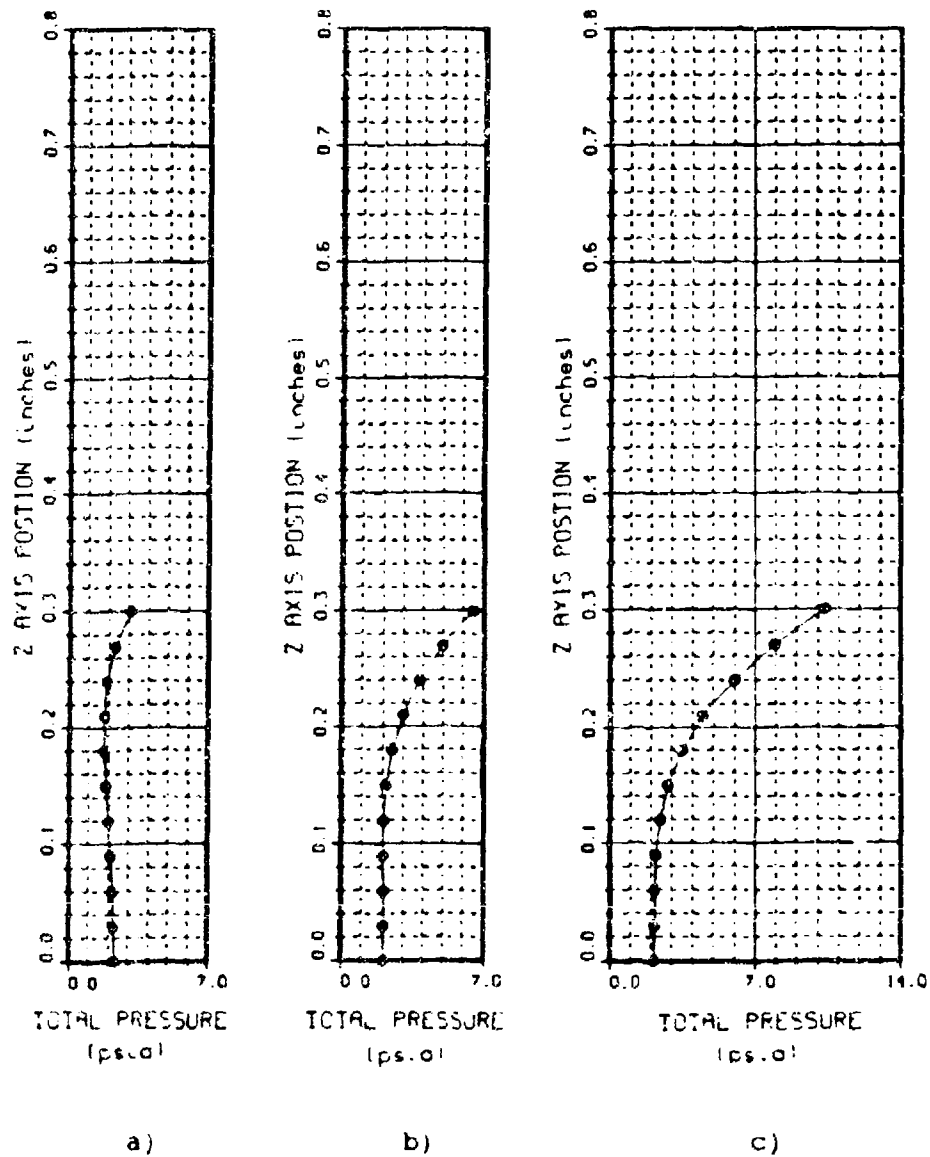


Figure 34. Pitot Pressure Profiles at $X=16.5$ in for a) Run 10 at $p_{0i} = 0$ psia, b) Run 13 at $p_{0i} = 25$ psia, c) Run 14 at $p_{0i} = 45$ psia

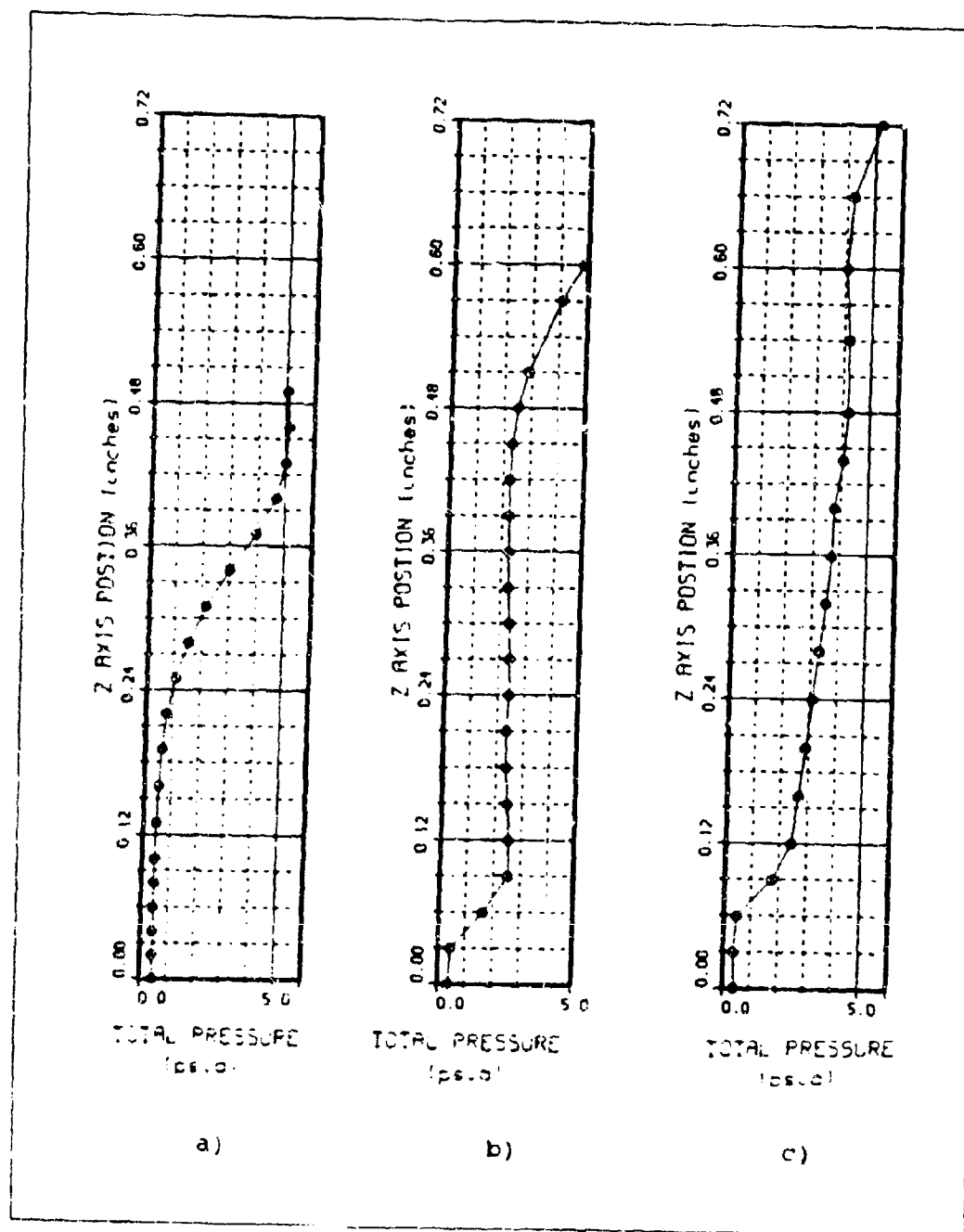


Figure 35. Pitot Pressure Profiles at $X=14$ in for a) Run 51 at $p_{0j} = 0$ psia, b) Run 52 at $p_{0j} = 10$ psia, c) Run 52 at $p_{0j} = 20$ psia

TABLE 9

Determination of s_1 Values

$p_{o,j}$ (psia)	$\delta+h+s_1 L$ (in)	s_1
0	0.46	0
10	0.64	0.09
20	0.75	0.14

Schlieren Photos. These photos provided a valuable visual aid in identifying the shocks and separation. The schlieren videotapes were also valuable in establishing trends with increasing TMI flow as well as capturing several flow oddities (see the Flow Oddities section).

Figure 36 is a diagram identifying the various features visible in the schlieren photographs. The freestream flow is from the right, and the slot exit is just below the bolt and washer and, in this case, just behind the back of the rear cowl support. The cowl is supported by two vertical columns on each side and is presently positioned to generate a shock impinging near the shoulder. Figures 37 and 38 show the general flow structure for the same configuration without and with injection respectively. A separation bubble appears in Figure 37 from the slot exit to the cowl shock. In Figure 38, this zone is filled by the shock structure of the expanding jet. A small bubble is visible in the impingement zone, but this is most likely separation occurring off to the sides of the 4 in slot since the corresponding pitot pressure profile indicated no separation. Also, the incoming (station 1) flow

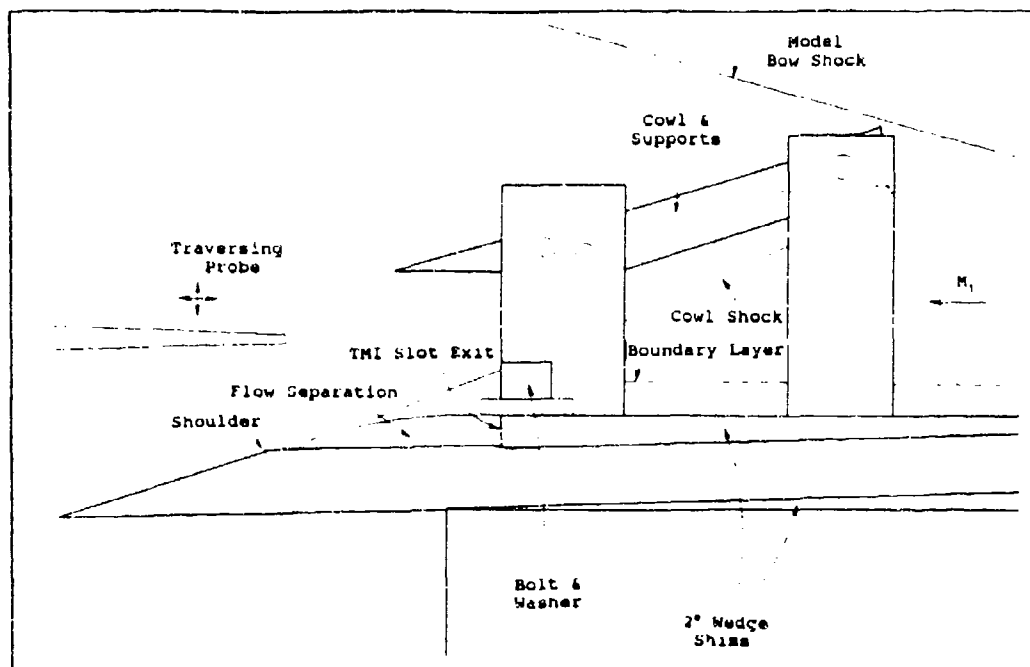


Figure 36. Close-up Diagram of the Model and Flow Field

seems cleaner for the case with TMI as the "white triangle" above the slot exit is bigger. There does appear to be some leakage around the TMI assembly for the "jet on" case, but this was believed to be on the sides away from the centerline.

Parametric Tests

During this series of tests, the parameters α , β , L_{SHR} , L_{SHK} , δ , and p_{o1} were varied to determine their optimum values for minimizing the p_{o1} required to eliminate separation. Incipient separation criteria were identified and used to determine the controlling p_{o1} for each test condition. From there, the corresponding m_{TMI}/m_{CAP} values were calculated and

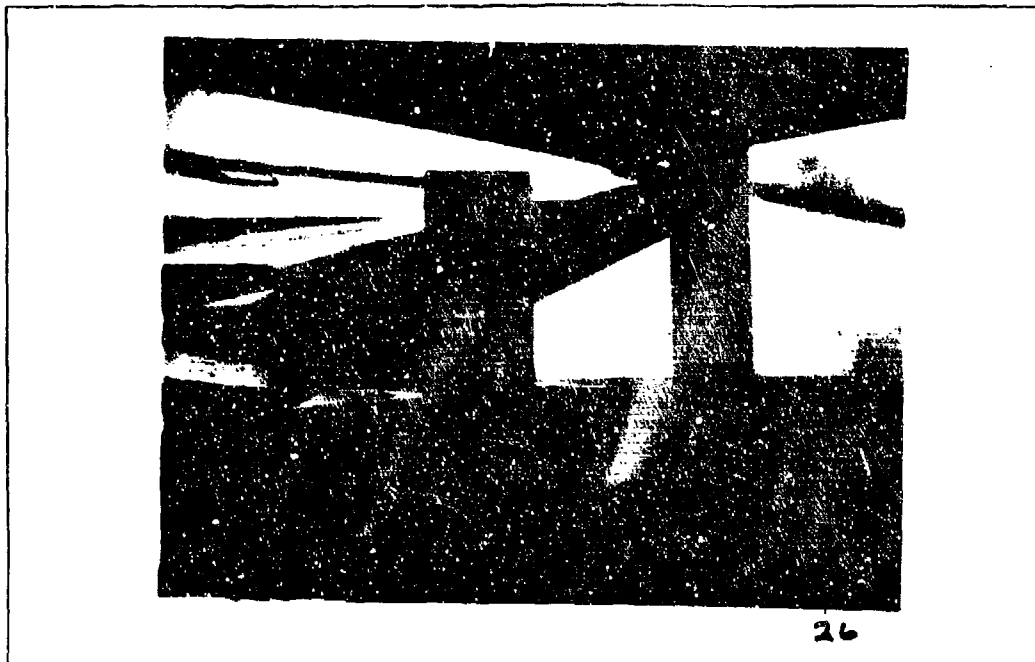


Figure 37. Run 26 Schlieren Photo at $p_{oj} = 0$ psia



Figure 38. Run 27 Schlieren Photo at $p_{oj} = 23$ psia

plotted versus the other parameters which permitted a trend analysis. The parametric tests were conducted in Runs 9-38, 40-45, and 54-62.

Characteristics of Separation. Figures 39 and 40 are schematic diagrams of the shock-boundary layer interaction on a flat surface with and without separation, respectively. In both cases, the incident shock only penetrates down to the sonic line of the boundary layer. In the subsonic region along the wall, the higher pressure behind the shock feeds upstream of the impingement to some extent. Figure 39 shows a separation bubble which is bounded by a separation point, S; a reattachment point, R; and a dividing streamline, DSL. The bubble of reversed, nearly stagnant flow generates a separation shock well forward of the incident shock impingement. Without separation, a "sonic line bubble" still exists as shown in Figure 40 causing compression and a reflected shock just ahead of the impingement. However, this compression is much closer to the impingement than for the case with separation. Also, the flow field with separation is much more complex with a separation shock, expansion, recompression, and a slip line whereas without separation there is essentially only a reflected shock.

Incipient separation is defined as the onset of reversed flow near the wall. Figure 41 shows that it occurs at the point where the velocity gradient at the wall in the normal direction is zero. This is also the point where there is no skin friction stress since $C_f \sim \tau_w \sim \partial u / \partial y|_w$.

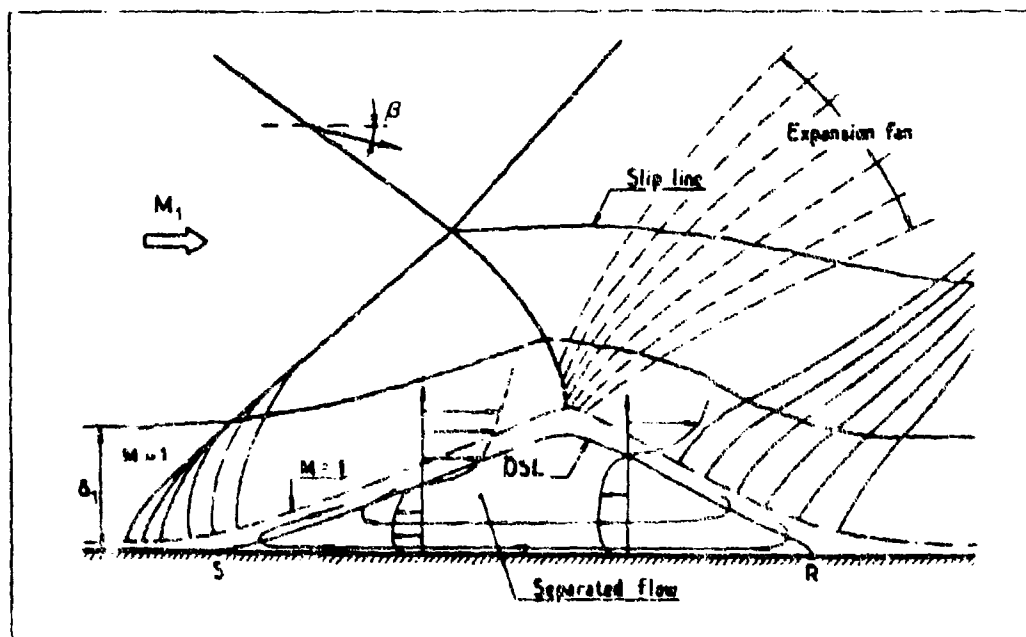


Figure 39. Schematic Diagram of Shock Wave-Boundary Layer Interaction on a Flat Surface With Separation (Ref. 16)

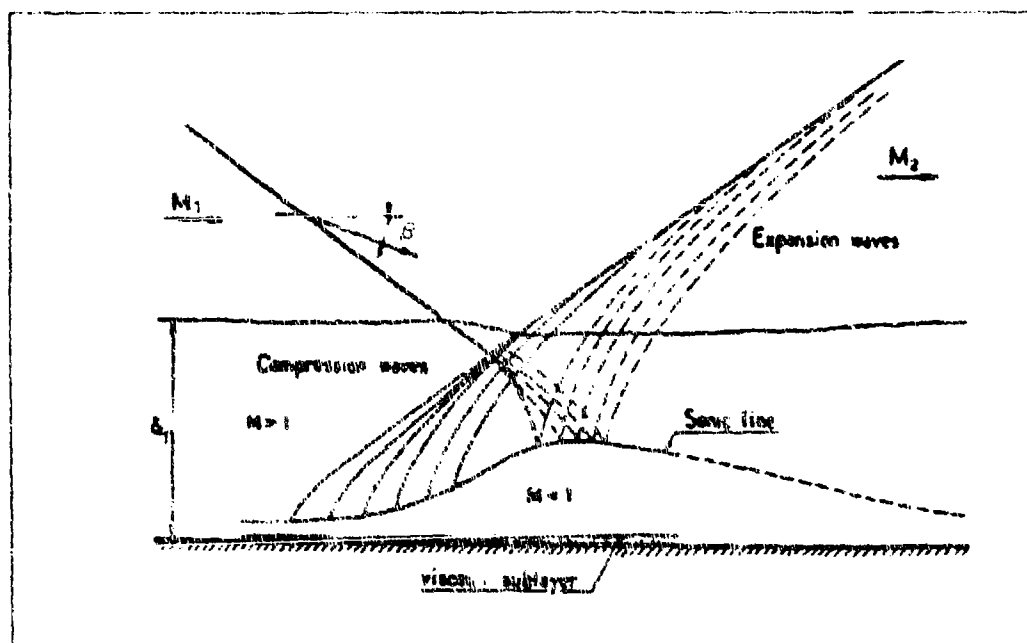


Figure 40. Schematic Diagram of Shock Wave-Boundary Layer Interaction on a Flat Surface Without Separation (Ref. 16)

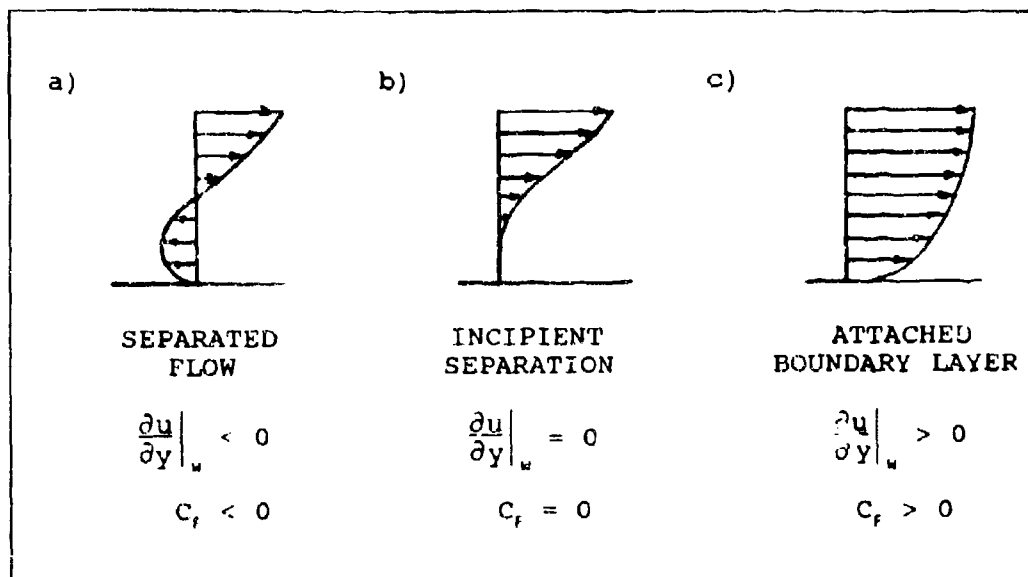


Figure 41. Velocity Profiles for a) Separated Flow, b) Incipient Separation, and c) Attached Boundary Layer

Holden attempted to determine incipient separation points by measuring skin friction but failed due to the turbulent flow unsteadiness (14:4). Other investigators have tried a variety of techniques, including inspection of wall pressure distributions, pitot pressure probing, and flow visualization (e.g. schlieren, shadowgraph, and holographic interferometry). These have met with limited success as the results always contained a certain degree of ambiguity (15:73-75). Delery and Marvin suggested that laser doppler velocimetry (LDV) may provide more definitive data (15:75).

Incipient Separation Criteria. Six criteria were identified and used in this effort. Three of them involved the wall (centerline static) pressure distributions, two used pitot pressure probing, and one was the inspection of the

schlieren photos/videotape. They are listed below in the order thought to be the least definitive to the most definitive.

1) Zero Slope - the point where the static pressure distribution has a zero slope just prior to the sharp rise corresponding to shock impingement. This would indicate that on a gross scale, the high pressure behind the shock is no longer feeding upstream along the wall and that separation has been eliminated. Figure 42 is a representative example where separation was eliminated at $p_{0j}=29$ psia.

2) Inflection Elimination the point where an inflection (if present) along the rise to the peak in the centerline static pressure distribution is eliminated. A compression along the wall prior to the shock impingement will always occur whether caused by a separation or sonic line bubble. If separation is present, the wall pressure will be somewhat constant in that zone. This causes an inflection or plateau as the "leveling-off" is then followed by a rise corresponding to the impingement. When the initial bubble merges with the impingement rise, separation is eliminated. This has been the most popular technique used in previous efforts (15:74), however, for the current effort this occurrence seemed undependable and was not observed for every run - perhaps due to insufficient pressure ports. Figure 43 is a representative example where separation was eliminated between $p_{0j}=36$ psia and 47 psia.

3) Unchanging Pressure - the point where the centerline static pressure just before the impingement rise (usually the

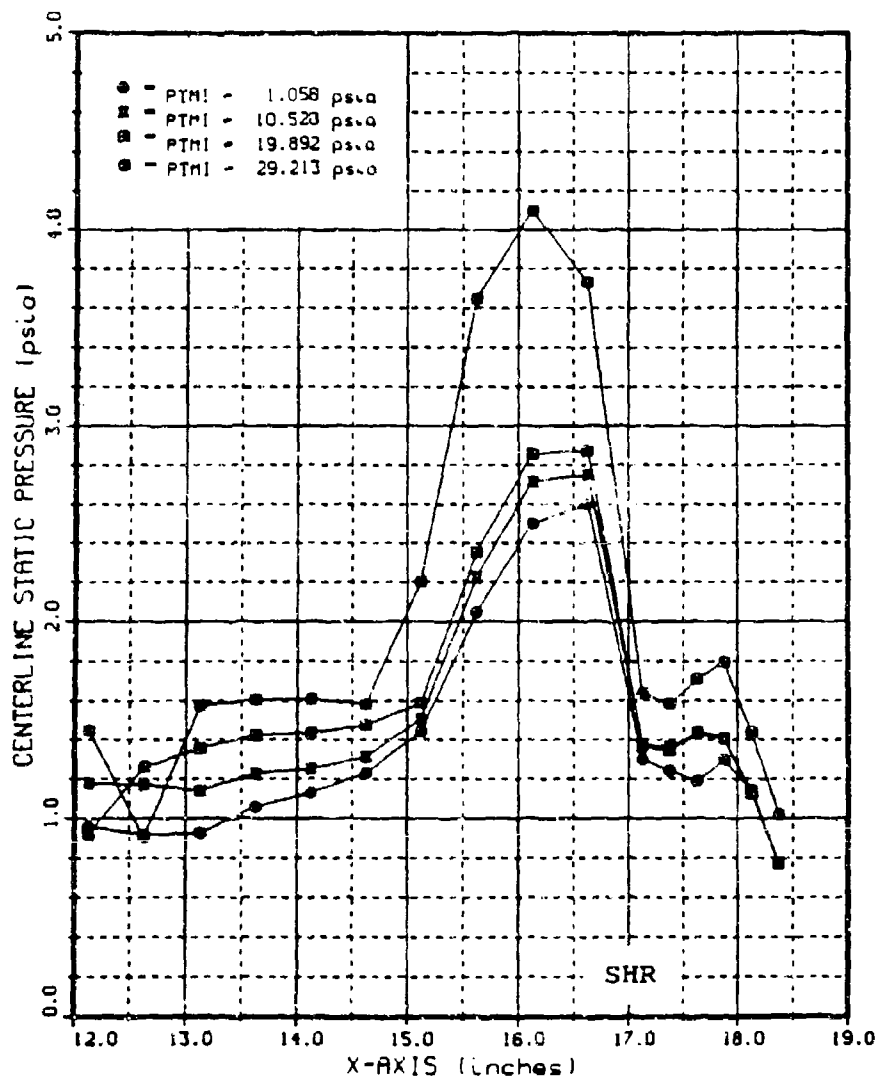


Figure 42. Run 19 C/L Static Pressure Distributions

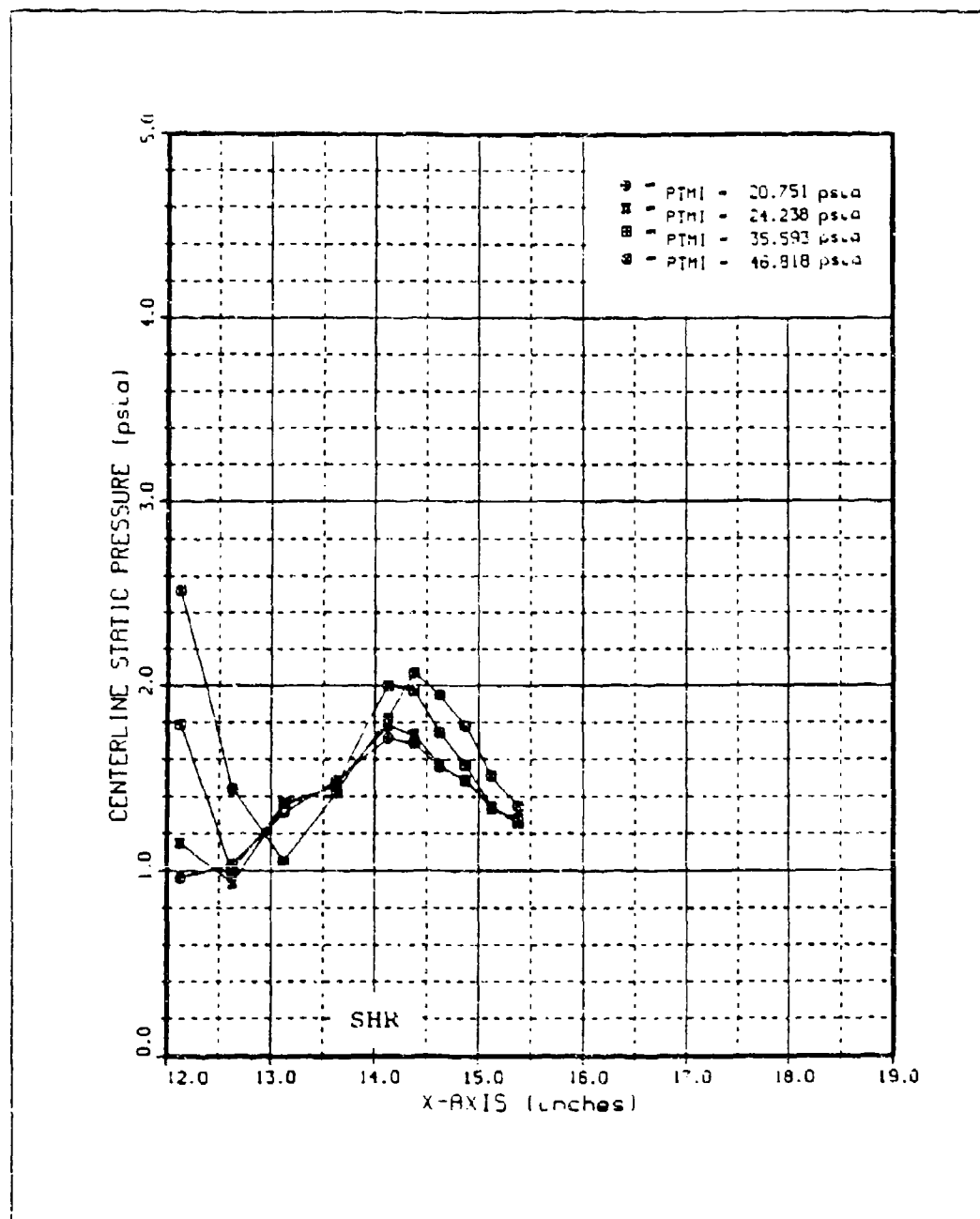


Figure 43. Run 35 C/L Static Pressure Distributions. for $p_{o1}=21-47$ psia

port prior to the peak) no longer changes with increasing TMI rate. This criterion is a modification of the first since the pressure slope may never reach zero if the bubble rise zone is large or if the shock impinges close to the TMI slot. Increasing the injection rate reduces the forward extent of the separation bubble until the sonic line bubble is reached. Further increasing TMI has no effect on the pressure here, and separation is considered to be eliminated. An example of this is shown in Figure 44 where the controlling p_{oj} per this criterion is 18 psia.

4) Bubble Elimination - the point where the separation bubble is eliminated as evidenced by the schlieren photos and videotape. The changing shock patterns in the videotape permitted identification of the separation. Occasionally, a near instantaneous flow switch gave a clear indication of when the incipient separation point was reached as TMI flow was increased. The schlieren photos provided a closer and cleaner view of the impingement zone; however, both the photos and video were obscured by the side effects, since the injection slot was only 4 in wide in the center of the model while the shock generator was 13 in wide. The cowl supports, lighting, focus, data correlation (videotape only), and run time also led to problems in applying this criterion. Run 32 is a good example of how this criterion was applied in selecting the controlling p_{oj} of 6 psia. Figure 46 is a schlieren photo that was taken just after a rapid flow switch, and the apparent separation in the $p_{oj}=0$ psia photo (Figure 45) is filled by a perfectly expanded jet.

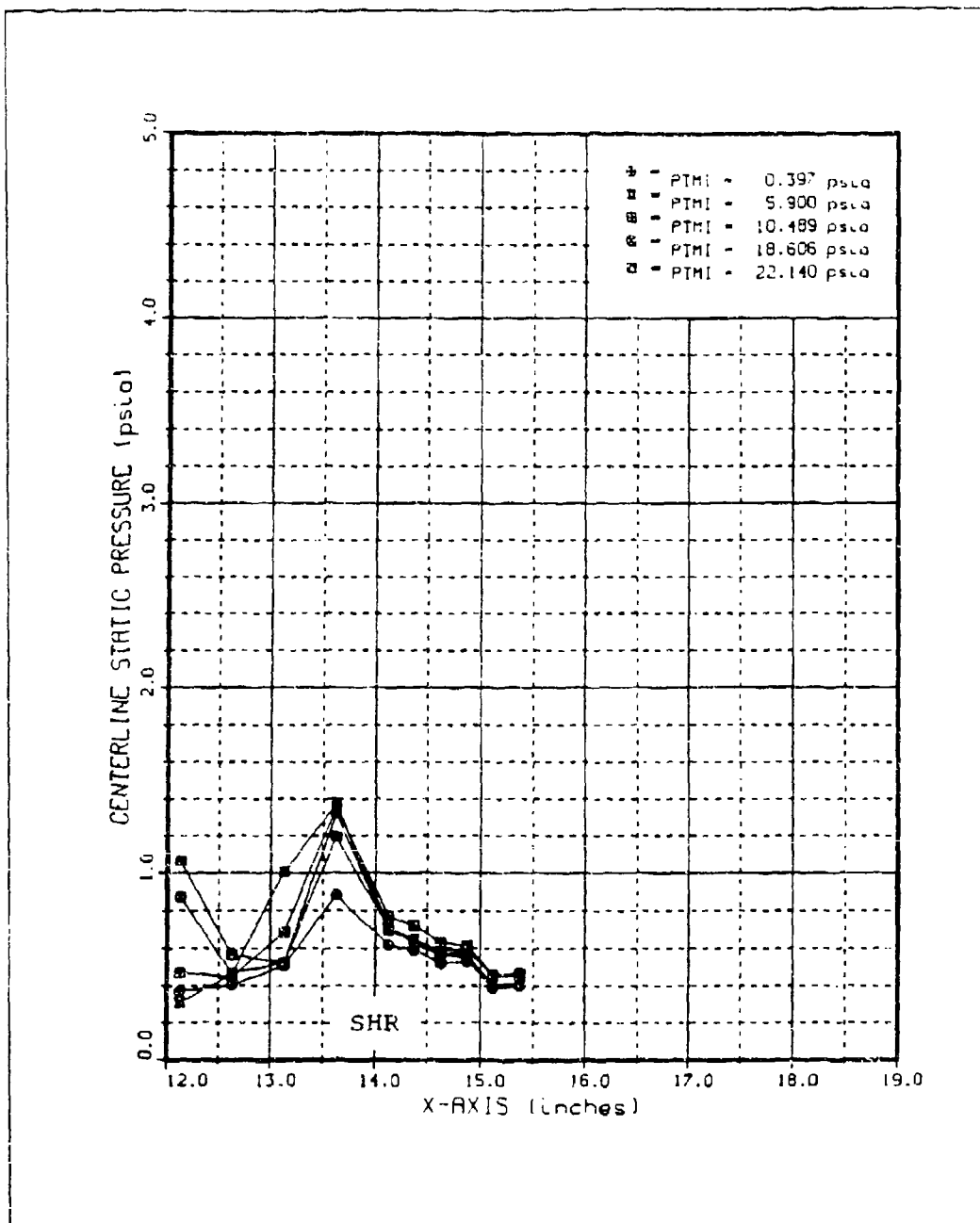


Figure 44. Run 32 C/L Static Pressure Distributions

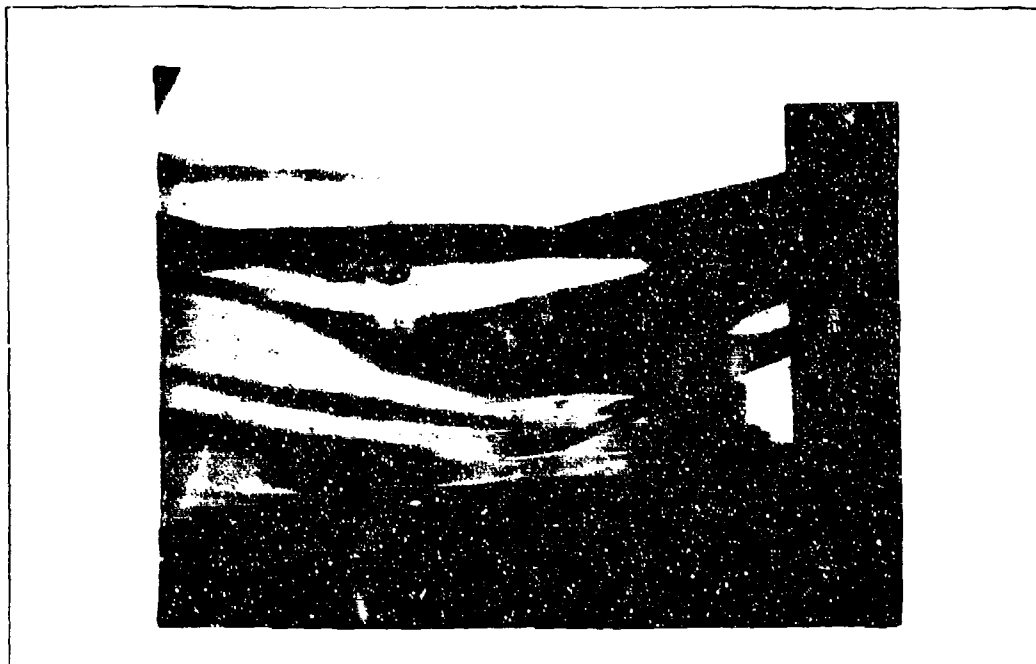


Figure 45. Run 32 Schlieren Photo at $p_{oj}=0$ psia

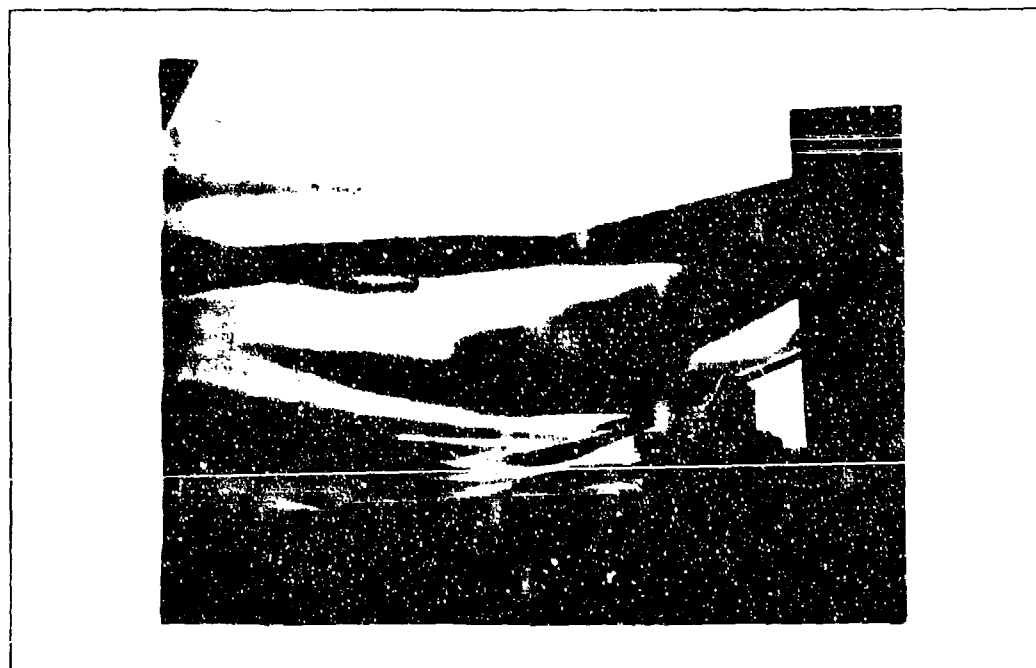


Figure 46. Run 32 Schlieren Photo at $p_{oj}=6$ psia

5) Sharp Rise - the point where a sharp rise in impingement pitot pressure (with the probe in the middle of the separated region just off the surface) was observed as TMI total pressure was increased. The sharp rise indicates that the separation shock was eliminated and, thus, separation as well. This method was only applied to a limited set of runs as the probe appeared to interfere with the centerline static pressure port readings. Figure 47 is a representative example where the separation was eliminated at $p_{oj}=7.7$ psia.

6) Positive Slope - the point where a positive slope is first detected in the impingement pitot pressure profile near the wall (i.e. $\partial p_t / \partial z|_{z=0} > 0$ which implies $\partial u / \partial z|_{w} > 0$). As shown in Figure 41, this is perhaps the best physical description for incipient separation. However, only several (if any) surveys to obtain profiles could be made per run due to run time limitations. Figure 48 is an example of a pitot pressure profile at the point of incipient separation.

Determination of Controlling TMI Rate. Table 10 shows how each criterion was used in determining the controlling p_{oj} , which directly led to the controlling mass injection ratio for each test matrix run (TMK). "X's" indicate criteria that were used to arrive at the specific controlling p_{oj} value. "M's" imply the chosen p_{oj} met the criteria, but did not help in selecting its value. A blank means the criterion could not be applied either due to insufficient data or no clear match to the criterion. A "C" suggests that the criterion conflicted with the chosen p_{oj} , but insufficient data precluded choosing

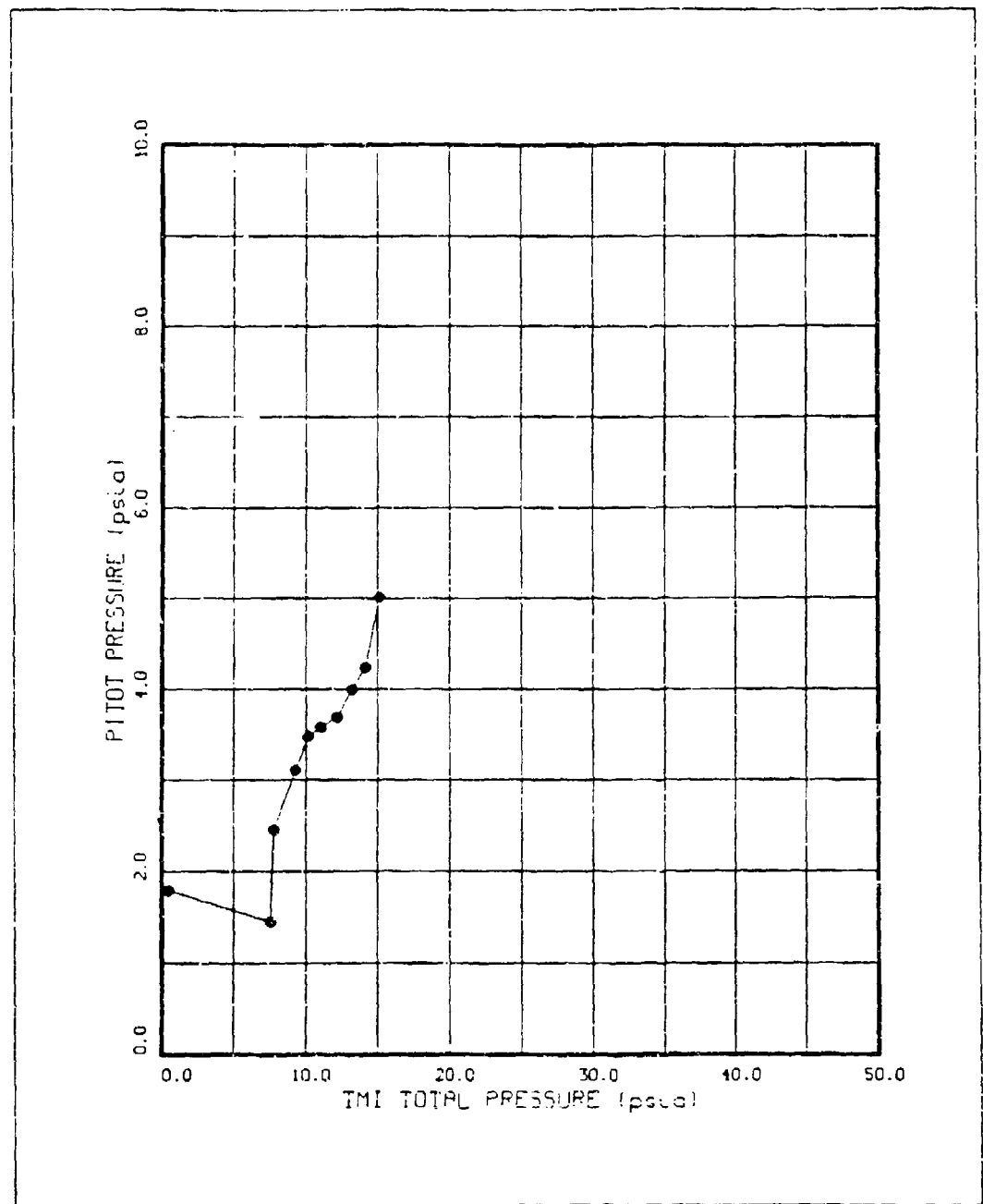


Figure 47. Run 58 Pitot Pressure vs. Injection Pressure

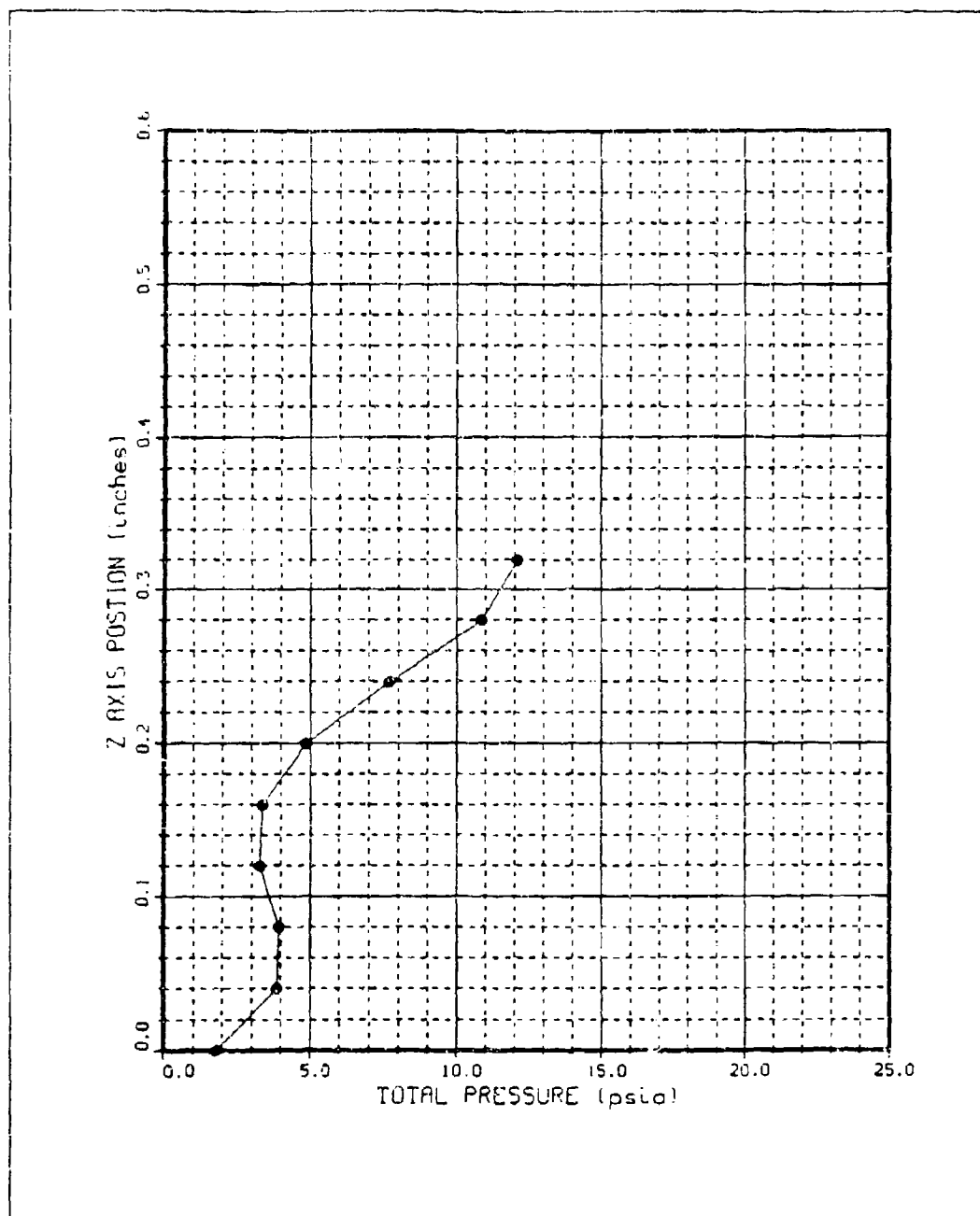


Figure 48. Run 38 Pitot Pressure Profile at X=12.6 in,
 $p_{0j} = 6.2$ psia

TABLE 10

Controlling Mass Injection Ratios

TMR	Runs	Parameter Values				Criteria Usage						CONTROLLING			
		$\frac{\alpha, \beta}{15^\circ}$	$\frac{L_{SMR}(in)}{5}$	$\frac{L_{SMR}(in)}{4.6}$	$\frac{\delta(in)}{.26}$	1	2	3	4	5	6	$p_{o,j}$ (psia)	UNC	$\frac{m_{MI}}{m_{CAP}}$	UNC
10	9,11,12				.26			X	X		X	>16		>.116	
12	10,13,14				.20			X	X		X	>45		.150e	
13	15			5.1	.26			X	X		X	10	+5	.073	$\pm .036$
14	16				.20				C			15e	+10	.044e	$\pm .029$
15	17,18			3.6	.26			26	X	X		>38		>.276	
16	19				.20			X				29	+7	.084	$\pm .020$
17	20,56		4	3.6	.26			24			X	>36		>.261	
18	21,57				.20				M	X	X	>46		>.133	
19	22		3	2.6	.26			X	X	>30		18	+4	.131	$\pm .029$
20	23				.20			X		C		36	+8	.104	$\pm .023$
21	24,25		2	1.6	.26			X				12e	+6	.087e	$\pm .044$
22	26,27				.20			30e	X		X	23	+8	.067	$\pm .023$
23	28,58			2.1	.26			X	X		X	7.7	+5	.056	$\pm .004$
24	29				.20			X	X		X	20	+5	.058	$\pm .015$
25	30,59			1.2	.26			13	12	28e	X	8	+1.5	.058	$\pm .011$
26	31,60				.20			X	X		X	14	+1.5	.041	$\pm .004$
27	32	12°	2	1.4	.26			20	X	18	X	6	+4	.044	$\pm .029$
28	33				.20			X	30e		X	12	+8	.035	$\pm .023$
29	34,61			1.8	.26			X	40	6	X	11	+2	.080	$\pm .015$
30	35,62				.20			M	X		M	40	+5	.116	$\pm .015$
31	36			2.1	.26			14	X		X	10	+3	.073	$\pm .022$
32	37				.20			X	X		M	16	+6	.046	$\pm .017$
33	38			1.0	.26			13			M	5	+3	.036	$\pm .022$
35	40				.20			25	43		M	10	+7	.029	$\pm .020$
36	41		3	3.0	.26			X			X	>40		>.290	
37	42				.20			20	X		X	>40		>.116	
38	43			1.9	.26			30	X		X	16	+6	.116	$\pm .044$
39	44,54		4	4.0	.26			X	X	25e	X	>46		>.334	
40	45,55				.20			X	X		X	>46		>.133	

GENERAL NOTES: all TMRs had $\phi=2^\circ$ except TMR 35, Runs 56-60 had $\alpha=12^\circ$ & $\beta=15^\circ$, e-estimated
 CRITERIA NOTES: X-used, M-met, blank-N/A, C-conflicts, #-controlling $p_{o,j}$ per criterion

a new value. A number suggests that the criterion conflicted with the chosen p_{oj} and the new value it indicates. An "e" denotes that the value was estimated, usually by extrapolating the existing data. Appendices F-I contain the charts and photographs to which the criteria were applied and from which the controlling values were selected.

Not all of the criteria were always met as shown in Table 10. In fact, there was not a single instance where all six criteria indicated the same controlling p_{oj} , and only once were five of the six criteria consistent (TMR 23). In all, 19 of the 29 parametric test runs had at least one criterion that conflicted with the others. This conflict was just one source of ambiguity. The other was interpolation between the p_{oj} test points in applying the criteria to the graphs and photos. These two factors were used to estimate an uncertainty for the controlling p_{oj} for each TMR. This led to a potential error band on each controlling mass injection ratio data point.

Although the criteria 1-6 were arranged from least definitive to most definitive, the most definitive criteria were not always used to select the controlling p_{oj} . Occasionally, the data was suspect or did not exactly match the more definitive criteria. For instance, in Run 23 the schlieren photo for $p_{oj}=35$ psia appeared to show shock-induced separation, but this may have been off to the sides of the 4 in slot. Since criterion 1 was almost exactly satisfied at $p_{oj}=36$ psia, it was used to select the controlling p_{oj} . Another condition under which the most definitive applicable

criterion was not used occurred when several less definitive criteria supported a common controlling injection pressure. TMRs 19, 30, and 38 were examples of this situation.

Another problem in applying the criteria arose for the runs where the cowl shock impinged downstream of the shoulder. For these cases, separation was apparently present both forward and aft of the shoulder. A decision was made to identify the controlling $p_{o,j}$ with elimination of only the separation aft of the shoulder, since that is the entrance to the combustor where non-separated flow is more important. Thus, all pitot surveys and criteria applications were made in this region for the particular runs with $L_{SHK}/L_{SHR} > 1$.

Once the controlling $p_{o,j}$ was determined, the controlling mass injection ratio (m_{TMI}/m_{CAP}) was calculated using the approach in the Appendix C Calculation of Intermediate Variables section. With the inputs

$$\begin{array}{ll} \gamma_1 = 1.4 & \gamma_j = 1.4 \\ M_1 = 5.76 & M_j = 3 \\ T_{o1} = 1000^\circ R & T_{o,j} = 530^\circ R \end{array}$$

the following variables were calculated:

jet conditions

$$\begin{array}{l} T_j = 189.3^\circ R \\ p_j = 0.02722 p_{o,j} \\ \rho_j = 0.0003883 p_{o,j} \text{ lb}_m/\text{ft}^3 \cdot \text{psia} \\ u_j = 2023 \text{ ft/s} \\ m_{TMI} = 0.01309 p_{o,j} \text{ lb}_m/\text{ft} \cdot \text{s} \cdot \text{psia} \end{array}$$

inlet conditions

$$T_1 = 131.0 \text{ } ^\circ\text{R}$$

$$u_1 = 3230 \text{ ft/s}$$

$$p_{o1} = 200 \text{ psia } (\delta = 0.26 \text{ in})$$

$$p_{o1} = 500 \text{ psia } (\delta = 0.20 \text{ in})$$

$$p_1 = 0.1626 \text{ psia}$$

$$p_1 = 0.4065 \text{ psia}$$

$$\rho_1 = 0.003352 \text{ lb}_m/\text{ft}^3$$

$$\rho_1 = 0.008379 \text{ lb}_m/\text{ft}^3$$

$$\dot{m}_{CAP} = 1.804 \text{ lb}_m/\text{ft}\cdot\text{s}$$

$$\dot{m}_{CAP} = 4.511 \text{ lb}_m/\text{ft}\cdot\text{s}$$

$$\frac{\dot{m}_{TMI}}{\dot{m}_{CAP}} = 0.007256 \frac{p_{oj}}{\text{psia}}$$

$$\frac{\dot{m}_{TMI}}{\dot{m}_{CAP}} = 0.002902 \frac{p_{oj}}{\text{psia}}$$

Thus, the controlling mass injection ratios depended solely on p_{o1} and p_{oj} since none of the other associated parameters were varied.

Other items to note from Table 10 include the L_{SHK} , ϕ , α , and β values and the TMRs where the controlling p_{oj} was never reached. The slot to theoretical (inviscid) shock impingement distances were not exactly $0.8L_{SHR}$, L_{SHR} , and $1.1L_{SHR}$ as originally planned but more like $0.7L_{SHR}$, $0.9L_{SHR}$, and $1.05L_{SHR}$. However, since the boundary layer separation tended to push the actual shock impingement slightly downstream, the X_{cowl} schedule from Table 5 was deemed satisfactory. Adjustments were made, however, to have $L_{SHK} = L_{SHR}$ for TMRs 36, 37, 39, and 40. Another item to note is that all of the parametric runs had $\phi = 2^\circ$, except TMR 35 or Run 40 which was accidentally left at $\phi = 0^\circ$ after the flow characterization test of Run 39. The difference was deemed insignificant. Also, Runs 56-60, which were repeat runs to clarify some previously ambiguous data,

were made with the 12° aft wedge piece ($\alpha=12^\circ$) while the cowl was set for a 15° deflection ($\beta=15^\circ$). Ideally, the 15° aft wedge should have been used for good comparison with the corresponding previous runs, but this would have required several days of work in pressure tube switching which could not be afforded in the facility schedule. Upon inspection of the pressure distributions, close agreement was found between the repeat and previous runs despite the difference in α . Even in the most affected case (TMR 23, where the shock impinged past the shoulder) the graphs indicated the same general controlling p_{o_j} . The last item to note from Table 10 is the nine TMRs for which separation could not be eliminated with any amount of TMI tested. Uncertainties were not estimated for these cases since the controlling p_{o_j} was never reached (although it had to be greater than the upper limit tested). Also note that an extrapolation was made for TMR 12 in going from p_{o_j} to m_{TMI}/m_{CAP} so that the curve in Figure 50 could be more easily represented.

Trend Analysis. As stated before, the primary objective of this project was to determine the optimum L_{SHR} for the given freestream and jet conditions. The secondary and necessary intermediate objective was to determine the controlling m_{TMI} under various inlet geometries. Although the average uncertainty in determining this rate was $\pm 35\%$, trends were discerned. The test results indicate that certain values of L_{SHK} , δ , α , and β led to a smaller injection rate for control of separation but had no apparent affect on the optimum slot

location. The trends for all six of these parameters are presented in Figures 49-54. In these figures, the x-axis (L_{SHR} or L_{SHK}) is normalized to the slot height ($h=0.20$ in) and the y-axis (m_{TMI}) is normalized to the captured inlet mass flow rate (m_{CAF}). The curves were drawn by the GRAPHER program with either a cubic spline or a second-order polynomial fit of the data points. The uncertainty bands from Table 10 were left off of the figures for purposes of clarity.

As alluded to earlier, the optimum relative slot/shoulder location was considered to be the point at which the controlling mass injection rate was minimized. The results would have been surprising at the time that the model was designed (with a $L_{SHR}=2-5$ in range) but were exactly as expected after a theory was derived. From Figure 49, the downward trend of the curves indicates that the optimum L_{SHR} lies between 0 and 10 slot heights and probably reaches a minimum midway in between, although this region was not actually tested. Figure 52 further indicates that the best L_{SHK} value for minimizing TMI is 5-6h, and if "shock on shoulder" is indeed the ideal condition, then perhaps the optimum L_{SHR} is 5-6h. One should note that the data points in Figure 49 had L_{SHK}/L_{SHR} values that ranged from 0.8-0.92 but were considered to be "shock on shoulder" as explained in the previous section. A graph similar to Figure 49 could not be made for $\alpha=\beta=12^\circ$ since each δ curve had only one valid data point (at $L_{SHR}=2$ in). In fact, there is some evidence from the schlieren video that the controlling p_{o_j} was never reached for

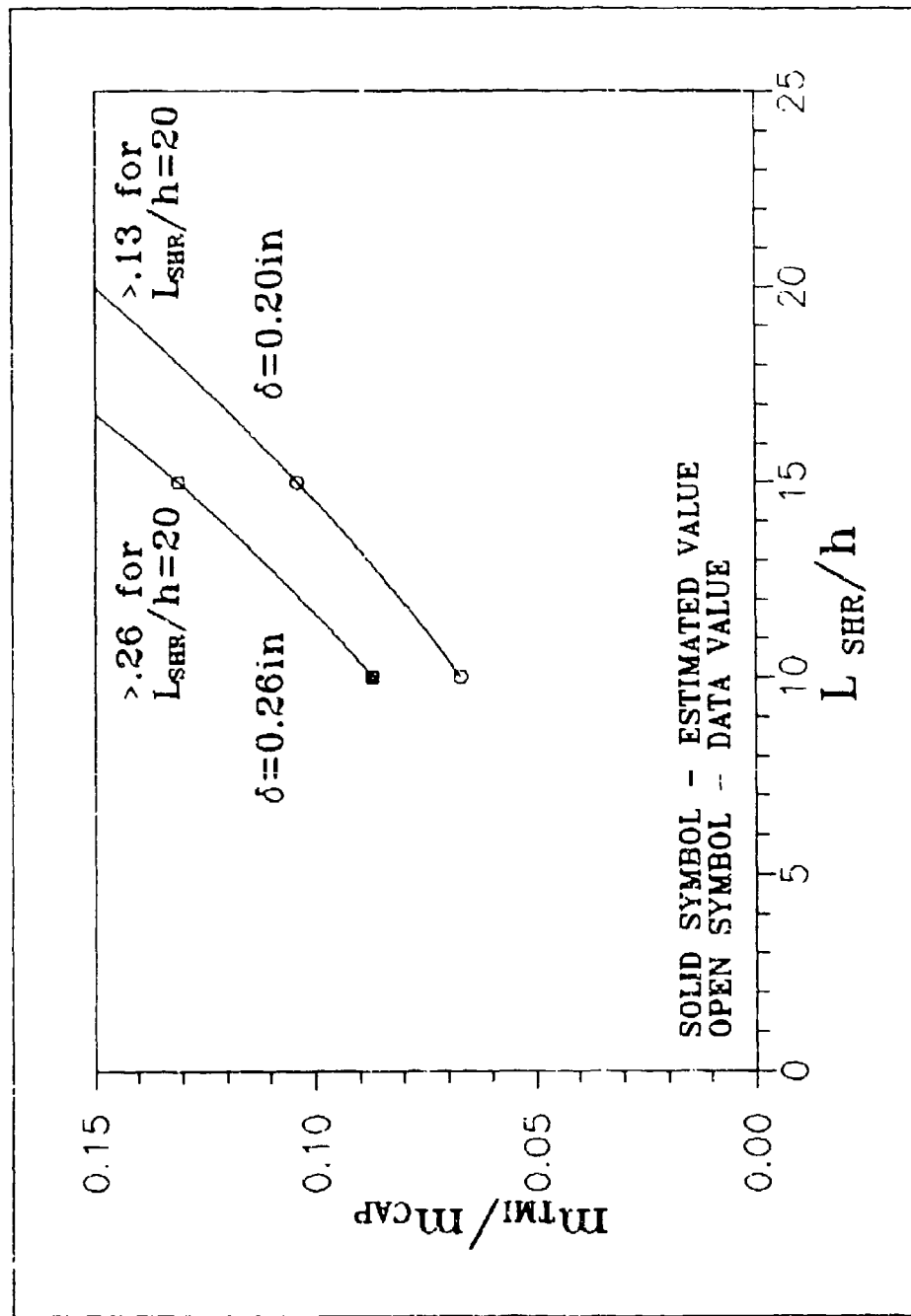


Figure 49. Controlling Mass Injection Ratio vs. Slot Location for Shock on Shoulder, $\alpha = \beta = 15^\circ$

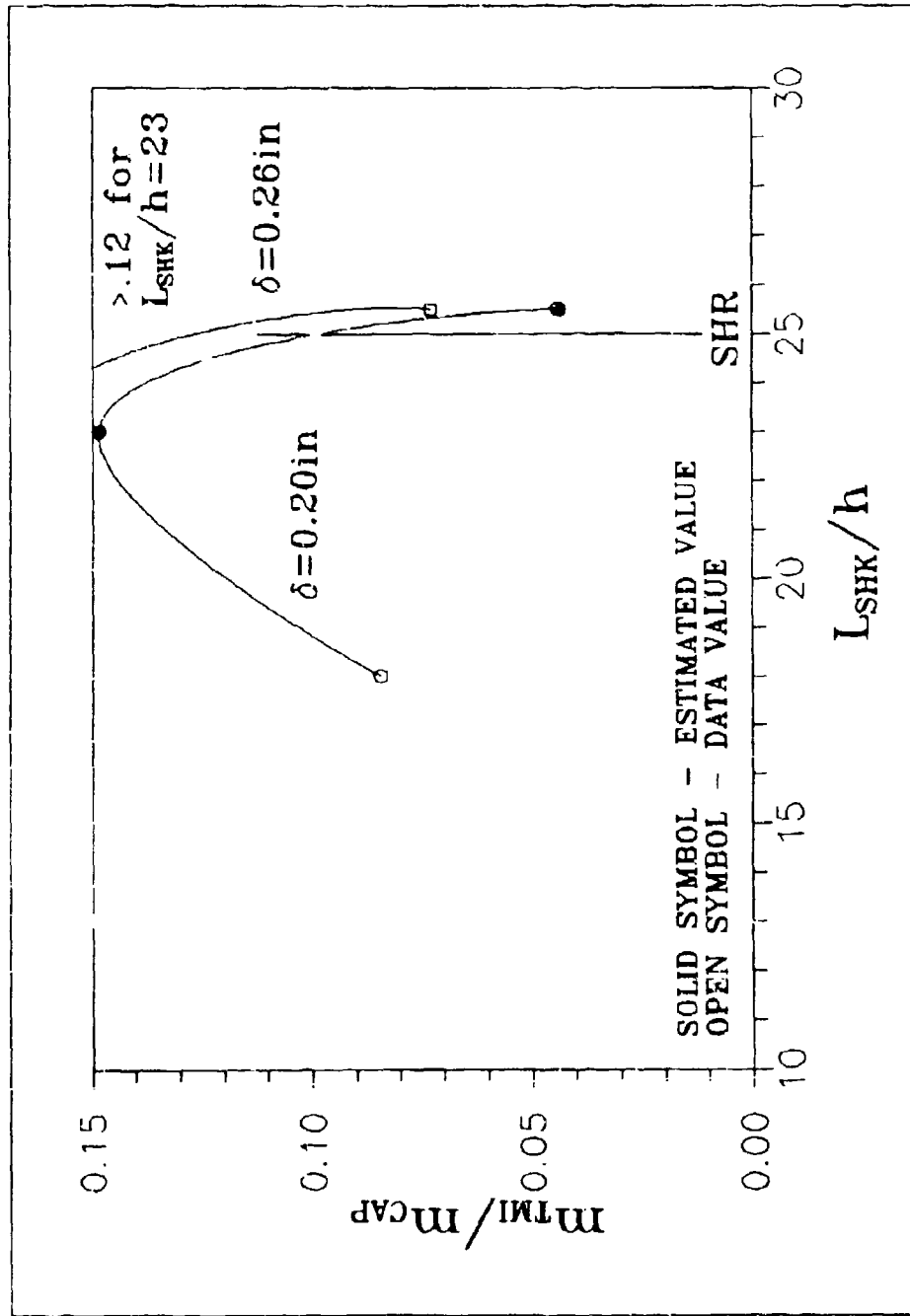


Figure 50. Controlling Mass Injection Ratio vs. Shock Location for $L_{SHR}=5$ in, $\alpha=\beta=15^\circ$

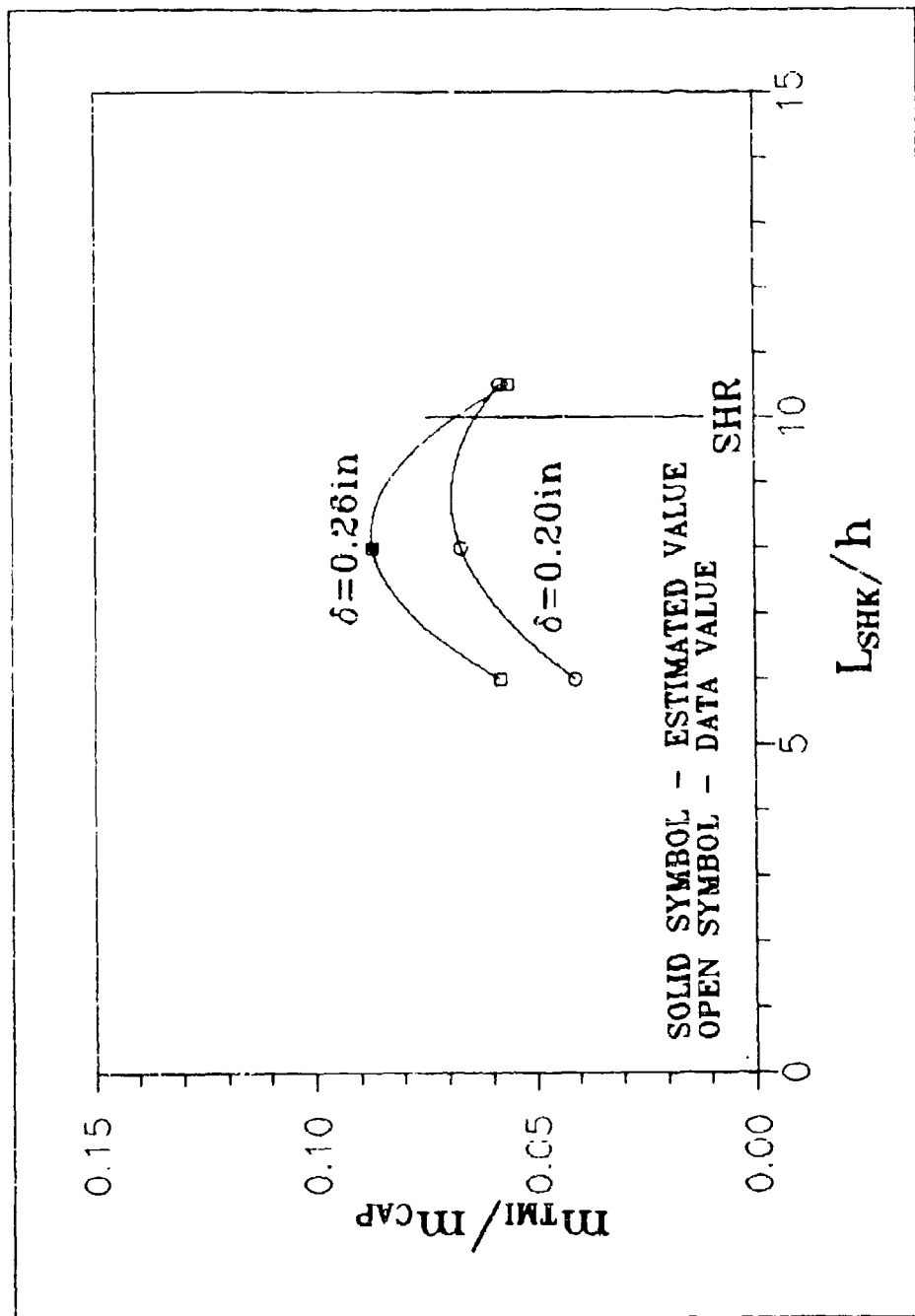


Figure 51. Controlling Mass Injection Ratio vs. Shock Location for $L_{SHR}=2$ in, $\alpha=\beta=15^\circ$

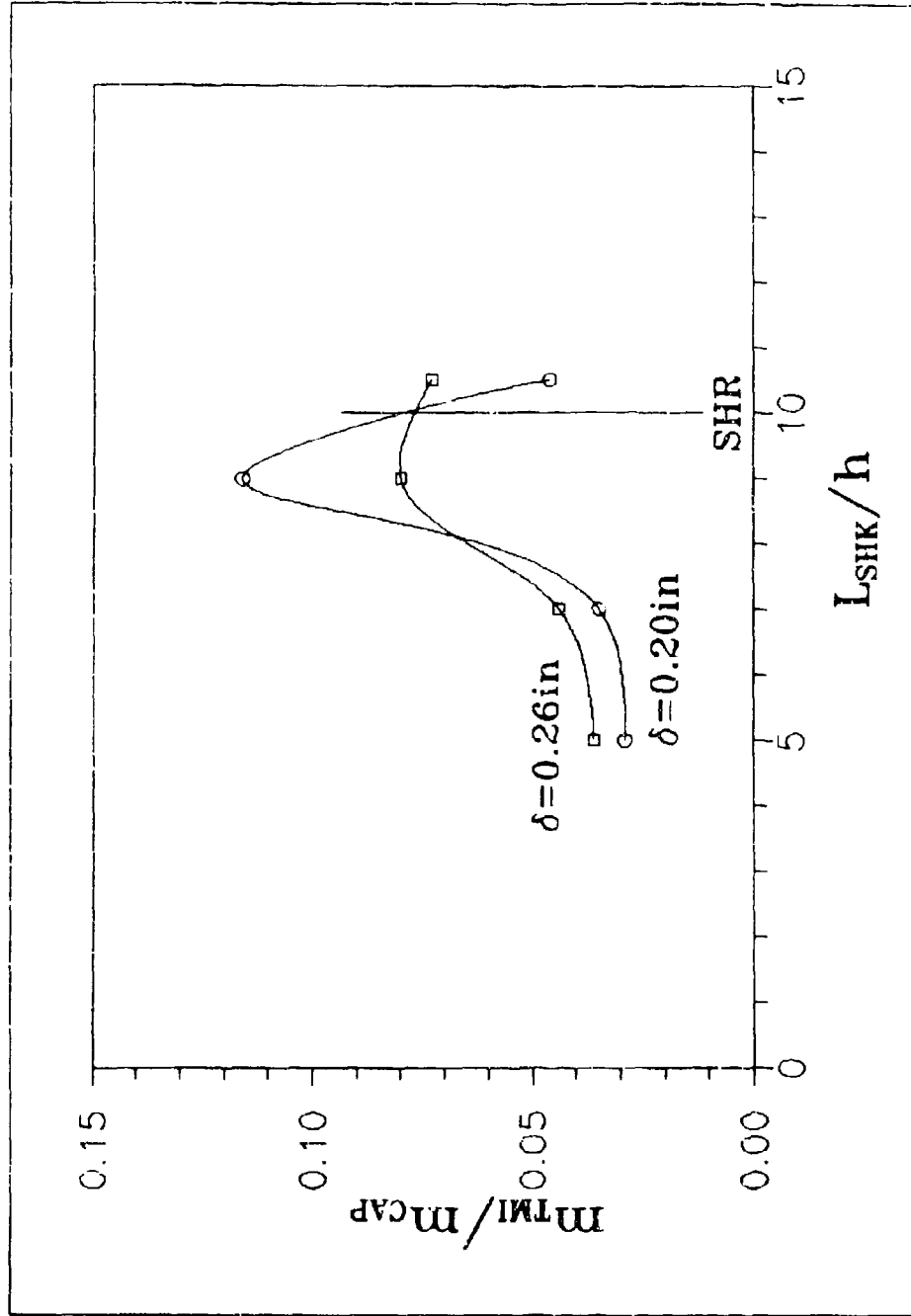


Figure 52. Controlling Mass Injection Ratio vs. Shock Location for $L_{SHR}=2\text{in}$, $\alpha=\beta=12^\circ$

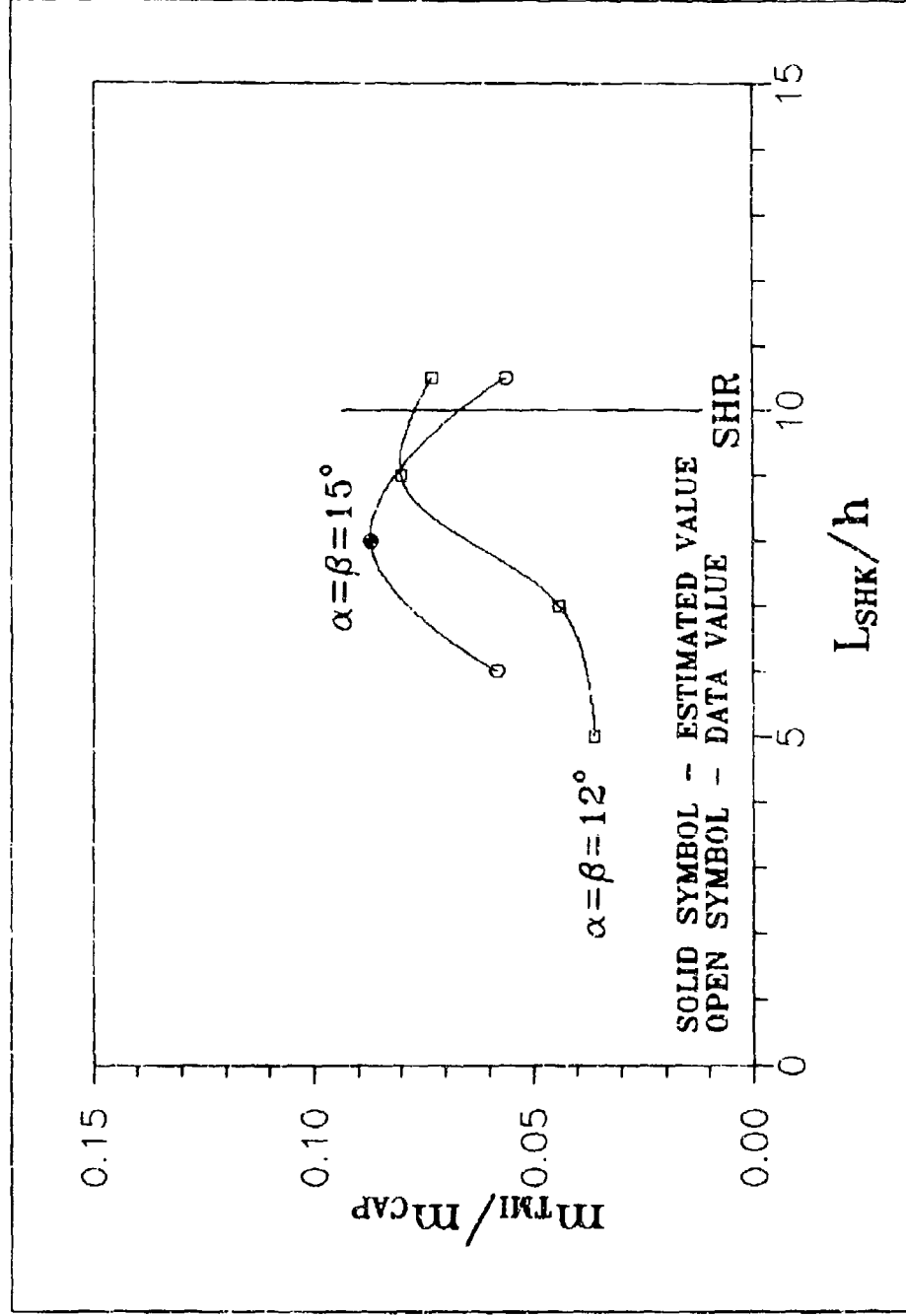


Figure 53. Controlling Mass Injection Ratio vs. Shock Location for $L_{SHR}=2in$, $\delta=0.26in$

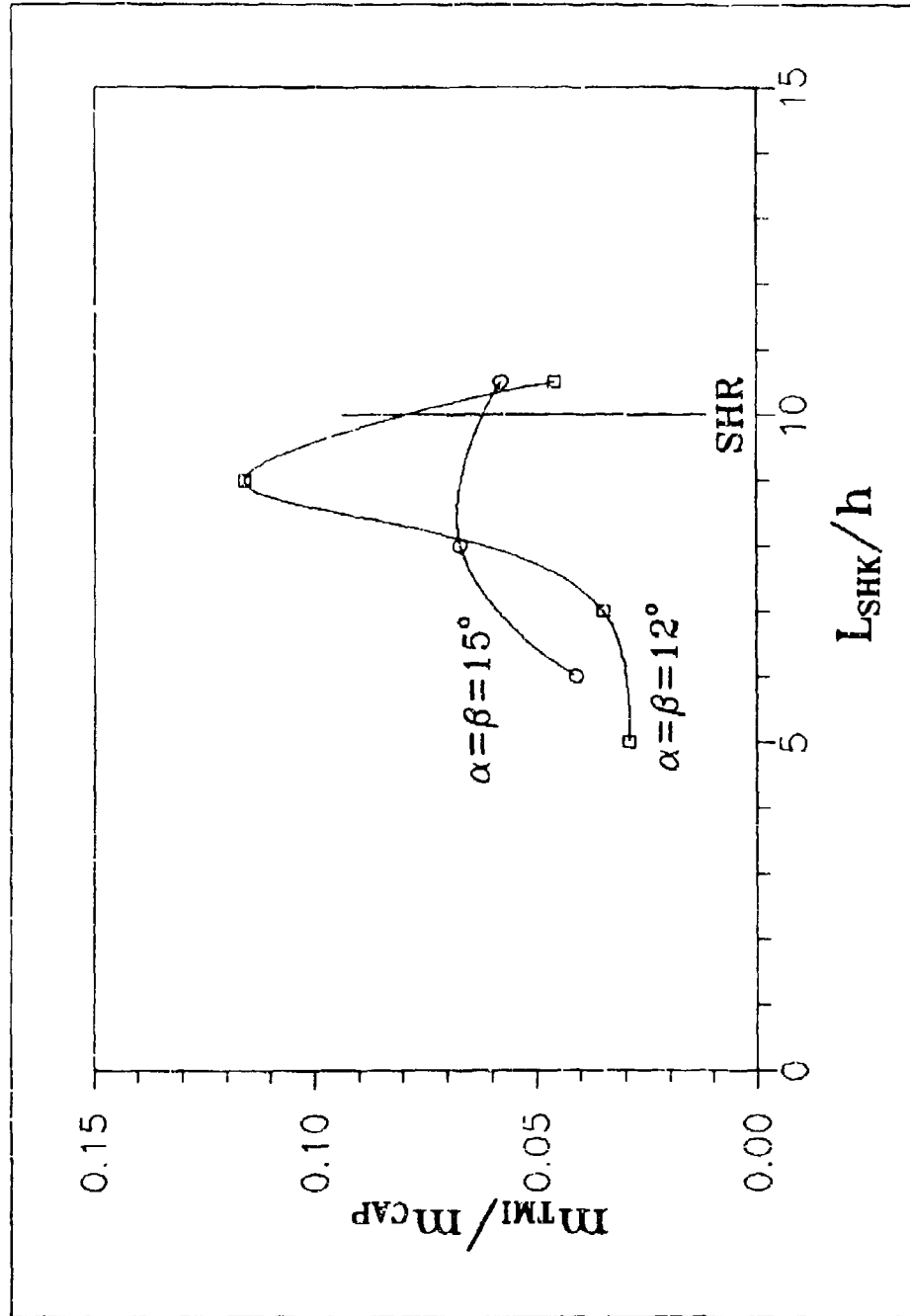


Figure 54. Controlling Mass Injection Ratio vs. Shock Location for $L_{SHR}=2\text{in}$, $\delta=0.20\text{in}$

$\alpha=\beta=15^\circ$ at $L_{SHR}=3$ in for both δ cases (Runs 22 and 23). Despite these complications, it is clear that the optimum L_{SHR} for minimizing the TMI required to eliminate separation was less than 10h and most likely 5-6h regardless of the α , β , δ , and L_{SHK} values.

From the equations and calculations used in the previous section, one can find that the values $m_{TMI}/m_{CAP}=0.043$, 0.100, and 0.160 correspond to the conditions of matching static pressures ($p_i=p_j$), matching mass fluxes ($\rho_i u_i = \rho_j u_j$), and matching momentum fluxes ($\rho_i u_i^2 = \rho_j u_j^2$), respectively. Thus, roughly speaking, the lines $m_{TMI}/m_{CAP}=0.05$, 0.10, and 0.15 in the graphs have some physical significance. From the test results and Table 10, the smallest value of the controlling m_{TMI}/m_{CAP} was 0.029 (TMR 35/Run 40). This corresponded to the conditions $L_{SHR}=10h$, $L_{SHK}=5h$, $\delta=h$, and $\alpha=\beta=12^\circ$ which were the smallest values tested for all parameters. This is a good indication of what the three remaining trends will be. Most of the lower controlling m_{TMI}/m_{CAP} values hovered around 0.043. Operationally, this suggests that when the parameters mentioned above are near their optimal values, running the TMI at a matching pressures condition is appropriate. This is rather fortunate since no slot lip shock would be created, thus, avoiding a potential source of inlet inefficiency.

The results for shock impingement position relative to the shoulder provided the biggest surprise of the whole project. They indicate that "shock on the shoulder" may not lead to shock wave cancellation (with no flow separation) nor

to even the smallest controlling TMI rate. Figures 50-52 suggest that shocks impinging in the range $L_{SHK}/L_{SHR}=0.75-1.02$ required the most injection to control the separation while shocks impinging closer to the slot or aft of the shoulder were easier to control. This finding impacts both the theoretical and experimental optimal L_{SHR} determination, which presumed that the ideal flow geometry was the cowl shock hitting on or near the shoulder. Indeed this may still be the ideal condition for inlet efficiency, but it is apparently not so for minimizing TMI to eliminate separation. Also, although a shock hitting past the shoulder would have a smaller effective β and less separation, a shock hitting closer to the slot seemed to require slightly less injection for control. Since no data was collected on inlet efficiency or on whether a shock impingement closer to the slot or aft of the shoulder was more effective, no further modification could be made to the optimal L_{SHR} - theoretical or experimental. Also, no tests were conducted for $L_{SHK}/L_{SHR}<0.5$ or >1.05 , which from the trends may have offered at least as small or even smaller controlling mass injection ratios.

The incoming boundary layer thickness had an influence on the controlling mass injection rate. The smaller thickness ($\delta=0.20$ in) almost always required the smaller TMI rate to control. This was expected since the smaller δ has less momentum/energy deficit that needs to be filled by the TMI. The assessment that the $\delta=0.20$ in case was turbulent, whereas the $\delta=0.26$ in case was laminar, may also have been a factor as

indicated by Schetz, et al (12:37). Another observation that was a little more surprising was that the δ curves of Figures 50-52 seemed to converge just aft of the shoulder. Perhaps, the initial upstream boundary layer no longer matters once the corner is turned, since δ_{10} is bounded more by the cowl shock impinging past the shoulder.

The influence of the flow turning angle, α , and cowl deflection angle, β , are shown in Figures 53 and 54. The data curves for these are taken directly from Figures 51 and 52 so that the variation of α and β can be compared. As mentioned in the previous section, the 3° variation of α had little influence; thus, it is believed that β was the prime factor in Figures 53 and 54. These graphs indicate that the smaller β leads to a smaller controlling TMI rate for $L_{SHK}/h < 7.5$ or $L_{SHK}/L_{SHR} < 0.75$. This was expected since a smaller cowl shock angle implies a smaller extent of shock-induced separation on a flat surface, which requires less injection to eliminate. The crossover of the curves just forward of the shoulder may be due to the greater relief offered by $\alpha=15^\circ$ as the separation begins to straddle the shoulder. However, more than likely, the $\beta=15^\circ$ curves (drawn with a second order polynomial fit) suffer from a lack of data in the $L_{SHK}/h=8-10.5$ range. Further testing may reveal the same trends as for the $\beta=12^\circ$ curves (see Figure 52).

Flow Oddities

During the course of wind tunnel testing several flow

oddities were observed and recorded on the schlieren videotape - five inlet unstarts and eight rapid flow "switches". The unstarts were likely attributable to facility and inlet geometry problems. Meanwhile, the flow switches were probably a good indication that a separation bubble was eliminated.

Inlet Unstart. Inlet unstart was encountered in Runs 19, 24, 25, 44, and 58. In Runs 19 and 44, the unstarts occurred near the end of the tests as the vacuum sphere back pressure built up to a point where the flow and shock waves became unsteady. In the case of Run 44, the instant that the TMI was reduced the inlet unstated; while in Run 19, the entire tunnel flow appeared to unstart once the sphere pressure got too high. For Runs 24, 25, and 58, the inlet appeared to unstart with the initiation of TMI flow. In all three cases, the test conditions were nearly the same with $L_{SHR}=2$ in, $\delta=0.26$ in, and $\beta=15^\circ$. The only differences were that Runs 24 and 25 had $L_{SHK}=1.6$ in and Run 58 had $L_{SHK}=2.1$ in and $\alpha=12^\circ$. Recall that the cowl was "cut-off" to reduce tunnel blockage; the combination of L_{SHR} and L_{SHK} values in these runs meant that the x location of this cowl cut-off point nearly coincided with that of the TMI slot. With $\beta=15^\circ$ these runs had the maximum contraction ratio of 1.6, which was right at the limit for inlet self-starting. The rearward facing step probably provided some relief, but once TMI was turned on, that relief was partially eliminated causing unstart. The presumed laminar flow of the $\delta=0.26$ in runs may also have been a factor.

In Run 24, the inlet did not restart when TMI was cut off but did start when the model was ejected and re-injected into the tunnel flow. However, once again the inlet unstated upon TMI initiation. It was hypothesized that since this was the first run at $L_{SHR}=2$ in, perhaps the capture cone was not capturing all of the shocks and flow. Thus, the entire model was moved back 2 in in the tunnel for Run 25. Apparently, this solved the problem and two pitot surveys were made with TMI on. However, later review of the videotape indicated that indeed the inlet had unstated at about the time of TMI turn-on, albeit in a more subtle manner. In Run 58, the unstart was apparently caused by a rapid TMI increase to $p_{oj} \approx 10$ psia (an accidental overshoot of the starting target of 6 psia). A second attempt was made this time gradually increasing the injection pressure. After a rapid flow switch at $p_{oj}=7.7$ psia, the pressure was increased 1 psia at a time up to 15 psia without inlet unstart.

Rapid Flow Switches. Rapid flow switches in the separation region occurred in Runs 28, 31, 32, 34, 38, 58, 59, and 60. These near instantaneous changes in shock structure were believed to correspond to the elimination of separation as the p_{oj} at the time of the switch appeared to match the results of the other criteria for incipient separation. It is also interesting to note that L_{SHR} was 2 in for all of these runs and $\delta=0.26$ in for all but Runs 31 and 60 (TMR 26). This combination was present for the three unstarts apparently caused by TMI initiation. Perhaps, these conditions created

an unstable flow, but more than likely the shock impingement was close enough to the slot such that when the jet stream static pressure rose higher than the separation bubble pressure the separation shock was eliminated and, hence, separation also eliminated.

Comparisons

The test results matched the theory and experimental results from other projects quite well. The experimental optimum slot location and other trends were compared to the theoretical results and the results of other projects whose principal investigators were Peake, Ogrodnikov, and White.

Theory. The optimum slot-to-shoulder distance predicted by the superposition mixing, maximum wake theory was $5-6\delta$, while the experimental results indicated $5-6h$. These two are identical for the $\delta=h$ case and reasonably close for the $\delta=1.3h$ case. Actually, L_{SHR} was not tested at less than $10h$, and it was only speculated that its optimum was not dependent on δ based on Figure 52 (where the two δ curves for shock position appeared to bottom out at the same L_{SHR}). Thus, experimentally, there may have been a variation of the optimum L_{SHR} due to δ . On the other hand, the theory could also have been manipulated to yield no δ dependency. Had the freestream boundary condition $\rho_e u_e = \rho_i u_i$ been used to derive the optimum slot location as described in Appendix C, Figure 14 would have had a single vertical line between $5h$ and $6h$. At this point, the evidence is inconclusive as to whether or not the optimum

L_{SHR} has a δ dependency, so the theoretical and experimental results were left as is but still relatively close.

The optimal values for the other parameters also matched the theoretical expectations, except for shock position. The experimental results suggested that the "shock on the shoulder" condition may not be the ideal condition, at least for minimizing the controlling TMI flow rate. From a theoretical (inviscid) viewpoint, shock on the shoulder would lead to wave cancellation and maximum pressure recovery. The situation that actually appears to dominate is that the jet becomes less and less effective at maintaining attached flow as the shock is moved downstream (explained by Figures 2, 12, and 13); then, as the forward extent of the separation (just ahead of shock impingement) begins to occupy the relief aft of the shoulder, the required injection rate to eliminate it is reduced. The optimal shock position was not determined, but it certainly did not appear to be in the range $L_{SHK}/L_{SHR}=0.75-1.02$ for minimizing TMI. Regardless of where the optimal shock position is, the optimal L_{SHR} from theory and experiment which presumed shock on shoulder would be adjusted equally. The boundary layer thickness trend matched the theoretical prediction - a thicker initial boundary layer required more mass injection to eliminate separation. Similarly, the steeper cowl deflection angle and greater inlet-combustor flow turning angle created a larger separation zone and required more TMI to control, just as predicted.

Other Experimental Data. Recall from the introduction chapter, that Peake (20) found the optimum distance between the injection slot and shock impingement to be 6δ . In essence, the results of the current project are the same with $5-6h$ and $h \approx \delta$. Since shock on the shoulder was presumed, this also turned out to be the optimum slot-to-shoulder distance. The closeness of these results is remarkable considering that Peake's conditions were $M_1=1.8$ and $M_j=2.37$, whereas the present conditions were $M_1=5.76$ and $M_j=3$. It suggests that an injection slot can be positioned at a fixed location on a scramjet inlet and be effective in eliminating separation over a relatively large flight Mach number range.

Results from the optimum (controlling) mass injection rate also closely matched those of other projects. For the favored conditions of $L_{SHK}/L_{SHR}=0.5-0.6$ and $L_{SHR}=10h$ in the present set of experiments, the controlling mass injection rate ranged from 3 to 6% of the captured mass flow, depending on the values of δ and β (the smaller values of $\delta=0.20$ in and $\beta=12^\circ$ gave 3%, and the higher values of $\delta=0.26$ in and $\beta=15^\circ$ gave 6%) . A Soviet team led by Ogorodnikov tested an axisymmetric inlet model and found that the controlling mass injection rate ratio was 3% for virtually the same freestream and jet Mach numbers and $\beta=10^\circ$ (22:10). Apparently, the type of inlet - planar versus axisymmetric - does not make much difference in the amount of injection required to eliminate the cowl shock induced separation. Two experiments led by

White with planar models incorporating Mach 3 air injection also were in close agreement with the current injection rates. In the first experiment, White found that a TMI flow rate 4-5% of the captured flow rate eliminated separation for freestream flows of $M_1=4$ and 5 and with $\beta=10^\circ$ (2:6). In the second series of tests with $\beta=11^\circ$, he found that the controlling mass injection ratio was 2-3% for $M_1=6$ (23,24:1-10) and 0% for $M_1=8$ and 10 (24:1-8). Furthermore, for $M_1=6$, White found that by increasing the TMI ratio to 6%, the static pressure recovery of the inlet was improved 25% (24:1-21). Thus, all applicable data appears to fall within the 3-6% range.

There were other similarities to White's experimental observations. White observed a sudden, dramatic change in the inlet flow field leading to steady shocks in the isolator duct which were associated with the elimination of separation (2:5). This is likely the same rapid flow switching phenomenon encountered in the present project. Another similarity is that hysteresis was not observed in the separation extent or the incipient separation point as the TMI flow was increased and subsequently decreased (2:5). Furthermore, White noted during his Mach 6 runs that when the cowl shock impinged at or near the shoulder, more injection was required to eliminate separation than when the shock impinged halfway between the slot and shoulder (23). This confirms the current finding that the optimal shock position for minimal TMI may not be shock on the shoulder.

The only incongruity found between these results was that White's second experiment had $L_{SHR}=44.2h$ and demonstrated TMI effectiveness at $M_1=6$, while the present results indicate that TMI is only economically effective for $L_{SHR}<20h$ (see Figure 49). This suggests that the optimum L_{SHR} may in fact be more dependent on δ than on h . However, since White's L_{SHR} in terms of δ is still at or above the high end of the present effectivity range, the optimum L_{SHR} is likely dependent on some combination of factors that are not readily apparent. Without a definitive dependence, the experimental result for optimum L_{SHR} was left in terms of slot heights.

VI. SUMMARY

This chapter presents the conclusions and recommendations resulting from this project. The conclusions address the primary objective of determining the optimal slot location and the secondary objective of defining trends in the controlling mass injection rate. The recommendations cover areas that require further study/investigation and specific advice for follow-on work with the same or similar model/facility set-up used here.

Conclusions

The primary objective of this project was to determine the optimum slot location for using tangential mass injection to eliminate the flow separation induced by the cowl shock impingement in a scramjet inlet. Prior to starting, the best guess for the optimum slot location was 10-25 times the initial boundary layer thickness upstream of the shoulder. It was thought to vary not only with boundary layer thickness but also with shock impingement position, cowl deflection angle, inlet flow turning angle, and perhaps several other parameters not tested here. The background research and theoretical development suggested an optimum value of 5-6 δ , varying only with boundary layer thickness and presuming shock on the shoulder. The actual test results on a 2-D model at a flight Mach number of 8 (inlet Mach 5.8) and injection Mach number of 3 indicated an optimum slot-to-shoulder distance of 5-6 slot

heights (where $h \approx \delta$) with no dependencies except possibly on shock position. Although no tradeoff on overall inlet performance was done, it seemed that the "shock on shoulder" condition required a higher TMI flow rate to control the separation. Therefore, if an inlet is designed for minimizing the TMI flow and, thus, for the cowl shock to nominally impinge either well forward or aft of the shoulder, then the slot-to-shoulder distance should be adjusted to keep the slot-to-shock impingement distance at 5-6h.

There are several shortcomings in this finding. First, although the slot-to-shock distance of 5-6h with the shock well forward of the shoulder was tested rather thoroughly, the slot-to-shoulder distance of 5-6h or lower was never tested. Secondly, h was just a convenient constant ($h=0.20$ in) used to normalize these distances and may not, in fact, be a factor. If a different slot height is chosen, there is no guarantee that these optimum distances will be 5-6h. And lastly, the optimum slot-to-shoulder distance proposed here is relatively short and does not allow much flexibility or variation for shock impingement position. Operationally, this means that for a shorter L_{SHR} there is a higher probability that the cowl shock will hit upstream of the slot, which White claims is ineffective (23) and, therefore, will require a very responsive cowl positioning system.

The secondary objective of this project was to define trends in the controlling mass injection rate (that required to just eliminate separation) for various values of slot-to-

shoulder and slot-to-shock distances, boundary layer thickness, and cowl deflection and inlet flow turning angles. A controlling TMI rate ratio (normalized to the captured inlet flow rate) was determined for each condition by applying six separate criteria to the wall static pressure, schlieren photo, and pitot pressure data and then making calculations based on the injection total pressure measurement. The controlling TMI rate was minimized when the smallest values of all the parameters stated above were tested - namely $L_{SHR}=10h$, $L_{SHK}=5h$, $\delta=h$, and $\beta=\alpha=12^\circ$. For this case, the controlling TMI rate was 3% of the captured inlet flow rate and ranged up to 6% for the other δ , β , and α values ($\delta=1.3h$ and $\beta=\alpha=15^\circ$) at the same shock and shoulder distances. These values center on the 4.3% condition of matching freestream and jet static pressures. For relative shock impingement positions in the range of $L_{SHK}/L_{SHR}=0.75-1.02$ and slot-to-shoulder distances of $L_{SHR}>10h$, the controlling mass injection ratios were always higher. In some cases, separation was never totally eliminated even with a mass injection ratio of 30%. Thus, the slot location and shock impingement position with respect to the shoulder were extremely important factors in how much tangential mass injection was required to eliminate separation.

The test results compared favorably to the theory developed for the optimum slot location and to other experimental results. The theory presumed shock on the shoulder and was based on avoiding Peake's two extremes: wake

bursting and boundary layer reversal (20:7-8). The downstream distance it took to maximize the mass flux of the initial wake between the freestream and jet flows seemed a satisfactory midpoint between the two extremes and a good position for shoulder placement. The superposition of streams concept by Carriere and Eichelbrenner (27) was adapted for compressibility and entrainment. The optimum slot-to-shoulder distance from this approach was 5-6 δ for the given test configuration and was relatively independent of the TMI flow rate. This matched well with the 5-6h from the test results and Peake's 6 δ for slot-to-shock distance (20). The controlling TMI ratio range of 3-6% for the smaller shock and shoulder distances also agreed well with the results of an experiment by Ogorodnikov (22) and two led by White (2,24).

Recommendations

Recommendations are provided for further research on this topic and for follow-on work based on the present experimental set-up. Of course, the primary recommendation would be to further definitize the optimal slot location. The $L_{SHR}=5-6h$ result found in the present experiment was somewhat ambiguous for three reasons: the ideal shock impingement position (initially thought to be the shoulder) was not determined, the $L_{SHR}=5-6h$ condition was not actually tested, and the experiment was performed for only one flight Mach number. Thus, recommendations 1)a., 1)b., 3)a., and 4)b. are perhaps slightly more worthy of consideration.

- 1) More parametrics
 - a. Try other values of M_1 , M_j , T_{o1} , T_{oj} , δ/c , and h/c .
 - b. Probe the $L_{SHR}/h=2-10$ range.
 - c. Extend the range of shock positions to $L_{SHK}/L_{SHR}=0.2-1.5$ and do a more detailed survey.
- 2) More detailed flow analyses
 - a. Begin filling in the experimental database on the specific effect of boundary layer shape factor, H , on the incipient separation point in terms of Reynolds number based on δ , Re_δ , and the total flow turning angle (due to ramp or incident-reflecting shock), α_1 .
 - b. Modify the computer programs listed in Appendices D and E to assess other freestream and jet conditions and to account for changing stream growth rates with varying TMI (which should be better defined experimentally). Find a more representative pu boundary condition for the edge of the boundary layer (s_1).
 - c. Improve the theoretical analysis by accounting for the effects of turbulence, convective Mach number, pressure mismatch, boundary layer shape factor, etc. Perform a CFD analysis based on the work of Cebecci and Bradshaw (41), Delery and Marvin (15), and Schetz, et al (13).
 - d. Refine and collate the incipient separation criteria to reduce the uncertainty in determining controlling mass injection rates.

3) Inlet efficiency tradeoffs

- a. Perform a tradeoff of shock on shoulder versus shock off shoulder measuring inlet efficiency (total pressure recovery and kinetic energy efficiency) and controlling TMI rate.
- b. Perform a tradeoff analysis for the case where the controlling mass injection flow is underexpanded; determine whether the best inlet performance is provided by optimum expansion of the jet (no slot lip shock) or by the controlling mass injection (no separation shock).

4) Further optimization of slot location

- a. Determine the optimal L_{SHR} and controlling TMI rates using helium as the tangential mass injectant to simulate hydrogen and compare to the results for air.
- b. If the cowl is designed so that its lip shock always impinges aft of the shoulder, determine if an injection slot placed at the shoulder and jet flow tangential to the combustor body surface is superior to the present inlet geometry with TMI slot forward of the shoulder.
- c. Determine the optimal slot location and optimum TMI flow rate for film cooling of the shoulder, fuel injection, and/or in combination with reducing boundary layer separation. Define trends for peak inlet-combustor performance.
- d. Determine optimal slot location for a given flight

envelope or mission (not just a few particular points) and find the optimum TMI flow rate over the envelope for a given L_{SHR} .

5) Pre X-30 considerations

- a. Investigate an active cooling system for the wall/shoulder for reducing separation and test in conjunction with TMI.
- b. Prior to X-30 final design, wind tunnel test an automated cowl scheduling system and automated TMI plenum pressure regulator interactively with appropriate sensors and under dynamic simulated flight conditions.
- c. Study the 3-D effects of TMI for both inlet vane/sidewall interaction and an axisymmetric inlet.

6) Model/Facility Enhancements

- a. Roughen or extend the front plate, round the model leading edge, increase ϕ , decrease p_{01} , add a trip strip, and/or a second mass injection (normal or tangential) on the front plate upstream of the primary slot to obtain a thicker boundary layer, δ_1 . Should also assess the validity of its profile shape.
- b. Build a new aft wedge piece to test the $L_{SHR}=5h$ case and a new 0.5 in insert strip for a more detailed survey.
- c. Obtain/install a static pressure probe to measure pressure recovery, pressure rise, and kinetic energy efficiency.

Bibliography

1. Delery, J. M. "Shock Wave/Turbulent Boundary Layer Interaction and its Control," Progress in Aerospace Sciences, Vol. 22, No. 4, 1985, pp. 209-280.
2. White, M. E., et al. "Tangential Mass Addition for the Control of Shock Wave/Boundary Layer Interactions in Scramjet Inlets," Proceedings of the Ninth International Symposium on Air-Breathing Engines. Washington: American Institute of Aeronautics and Astronautics, September 1989.
3. Kohut, 1st Lt Orest L. Investigation of a Rectangular Inlet for a Low Speed Fixed Geometry Scramjet. MS Thesis, GA/ME/69-2. School of Engineering, Air Force Institute of Technology (AU), Wright-Patterson AFB OH, March 1969.
4. Stava, Donald, National Aerospace Plane Team Inlet Leader. Personal correspondence. Flight Dynamics Directorate, Wright Laboratory, WL/FIMM, Wright-Patterson AFB OH, January-December 1990.
5. Walker, D. A., et al. "Turbulence Measurement for Slot Injection in Supersonic Flow," AIAA 88-0123, presented at the AIAA 26th Aerospace Sciences Meeting, Reno NV, 11-14 January 1988.
6. Goldstein, R. J., et al. "Film Cooling with Air and Helium Injection Through a Rearward-Facing Slot," AIAA Journal, Vol. 4 No. 6, 1966, pp. 981-985.
7. Heilala, Capt Gary A. The Effect of External Fuel Injection on the Fuel-Air Mixing Efficiency and Inlet Performance of a Supersonic Combustion Ramjet. MS Thesis, GA/AE/67-1. School of Engineering, Air Force Institute of Technology (AU), Wright-Patterson AFB OH, March 1967.
8. Schlichting, Hermann. Boundary-Layer Theory (Seventh Ed.). New York: McGraw-Hill Book Company, 1979.
9. Chang, Paul K. Separation of Flow. New York: Pergamon Press, 1970.
10. Gilreath, H. E. and J. A. Schetz. "Transition and Mixing in the Shear Layer Produced by Tangential Injection in Supersonic Flow," Journal of Basic Engineering, December 1971, pp. 610-618.

11. Schetz, Joseph A. Injection and Mixing in Turbulent Flow. Volume 68 of Progress in Aeronautics and Astronautics. New York: American Institute of Aeronautics and Astronautics, 1980.
12. Schetz, Joseph A., et al. Research on Slot Injection into a Supersonic Air Stream, June 1967-August 1968. Contract F33(615)-67-C-1805. Wright-Patterson AFB OH: Air Force Aero Propulsion Laboratory, September 1968 (AFAPL-TR-68-97).
13. Schetz, J. A., et al. "Effects of Pressure Mismatch on Slot Injection in Supersonic Flow," AIAA-90-0092, presented at the 28th Aerospace Sciences Meeting, Reno NV, 8-11 January 1990.
14. Holden, M. S. "Shock Wave-Turbulent Boundary Layer Interaction in Hypersonic Flow," AIAA Paper No. 72-74, presented at the 10th Aerospace Sciences Meeting, San Diego CA, 17-19 January 1972.
15. Delery, J. M. and J. G. Marvin. "Shock-Wave Boundary Layer Interactions," AGARDograph No. 280, February 1986.
16. Delery, J. "Shock/Shock and Shock-Wave/Boundary-Layer Interactions in Hypersonic Flows," AGARD Report No. 761, June 1989, pp. 9-1 to 9-51.
17. Alzner, E. and V. Zakkay. "Turbulent Boundary-Layer Shock Interaction with and without Injection," AIAA Journal, Vol. 9, No. 9, September 1971, pp. 1769-1776.
18. Grin, V. T. and N. N. Zakharov. "Experimental Investigation of Effect of Tangential Blowing and Wall Cooling on Flow with Separation," Fluid Dynamics, Vol. 6, 1974, pp. 1035-1039.
19. Lakshmikantha, H., et al. "Effect of Fluid Injection on Shock Wave Boundary Layer Interaction," Department of Aerospace Engineering, Indian Institute of Science, Bangalore, Report 69FM7, November 1969.
20. Peake, D. J. "The Use of Air Injection to Prevent Separation of the Turbulent Boundary Layer in Supersonic Flow," British Ministry of Aviation, Aeronautical Research Counsel C.P. 890, 1966.
21. Viswanath, P. R., et al. "Injection Slot Location for Boundary-Layer Control in Shock-Induced Separation," Journal of Aircraft, Vol. 20, No. 8, August 1983, pp. 726-732.

22. Ogorodnikov, D. A., et al. "Controlling the Boundary Layer in Hypersonic Air Intakes," FTD-HT-23-1349-72, presented at the 1st International Symposium on Air-Breathing Engines, Marseille, France, 19-23 June 1972.
23. White, Michael E., JHU/APL Deputy Program Manager. Telephone interviews. National Aerospace Plane Program, John Hopkins University Applied Physics Laboratory, Baltimore MD, 17 May 1990 & 3 June 1991.
24. White, M. E. "Shock Wave/Boundary Layer Interaction with Mass Addition for a Generic Hypersonic Inlet - Cooperative General Dynamics/TMP Test Program," Quarterly Technical Reports for the National Aerospace Plane Program, John Hopkins University Applied Physics Laboratory, Laurel MD, NASP CR 1099, January-March 1990.
25. Birch, Stuart and James H. Brahney (editors). "Technology Update - NASP Engine Inlet Design," Aerospace Engineering, Vol. 11, No. 8, August 1991, p.23.
26. Heppenheimer, Thomas A. Lecture notes from Hypersonic Technologies seminar. University of California, Irvine, Costa Mesa CA, 21-22 October 1988.
27. Carriere, P. and E. A. Eichelbrenner. "Theory of Flow Reattachment by a Tangential Jet Discharging Against a Strong Adverse Pressure Gradient," Boundary Layer and Flow Control, Volume 1. Edited by G. V. Lachmann. New York: Pergamon Press, 1961, pp. 209-231.
28. Galassi, Capt Lello, Project Engineer. Personal correspondence. Flight Dynamics Laboratory, WRDC/FIMG, Wright-Patterson AFB OH, September 1990.
29. White, Frank M. Viscous Fluid Flow. New York: McGraw-Hill Book Company, 1974.
30. Abramovich, Genrikh N. The Theory of Turbulent Jets. Cambridge MA: The M.I.T. Press, 1963.
31. Pai, Shih-I. Fluid Dynamics of Jets. New York: D. Van Nostrand Company, 1954.
32. Scaggs, Norman and Lello Galassi. "Skin Friction and Heat Transfer Measurements at Mach 6." Test Plan. Flight Dynamics Laboratory, WRDC/FIMG, April 1990.
33. Clausen, Capt Robert D. A Computational Model for Thickening Boundary Layers with Mass Addition for Hypersonic Engine Inlet Testing. MS Thesis, AFIT/GAE/ENY/89D-04. School of Engineering, Air Force Institute of Technology (AU), Wright-Patterson AFB OH, December 1989.

34. Scaggs, Norman, High Speed Aerodynamics Group Leader. Personal correspondence. Flight Dynamics Directorate, Wright Laboratory, WL/FIMG, Wright-Patterson AFB OH, March-May 1990.
35. Merz, Richard A., Associate Professor. Letter to Dr. William Elrod. Lafayette College, Department of Mechanical Engineering, Easton PA, 9 April 1987.
36. Elrod, William C., Professor. Personal correspondence. Air Force Institute of Technology, AFIT/ENY, Wright-Patterson AFB OH, March 1990.
37. Molten, Randy G. "Expansion of the Aerodynamic Simulation Capabilities of the Air Force WRDC Mach 6 High Reynolds Number Facility." Flight Dynamics Laboratory, Wright-Patterson AFB OH, 1989.
38. Ames Research Staff. "Equations, Tables, and Charts for Compressible Flow," NACA Report 1135. Ames Aeronautical Laboratory, Moffett Field CA, 1958.
39. Dorrance, William H. Viscous Hypersonic Flow. New York: McGraw-Hill, 1962.
40. Stetson, Kenneth F., Senior Research Engineer. Personal correspondence. Flight Dynamics Directorate, Wright Laboratory, WL/FIMG, Wright-Patterson AFB OH, September 1991.
41. Cebeci, Turner and Peter Bradshaw. Physical and Computational Aspects of Convective Heat Transfer. New York: Springer-Verlag, 1984.
42. Settles, G.S. An Experimental Study of Compressible Turbulent Boundary-Layer Separation at High Reynolds Number. PhD Thesis. Princeton University, Princeton NJ, September 1975.
43. Spaid, F.W. and J.C. Frishett. "Incipient Separation of a Supersonic, Turbulent Boundary-Layer, Including Effects of Heat Transfer," AIAA Journal, Vol. 10, No. 7, July 1972, pp. 915-922.
44. Kuehn, D.M. "Experimental Investigation of the Pressure Rise Required for the Incipient Separation of Turbulent Boundary-Layers in Two-Dimensional Supersonic Flow," NASA Memo 1-21-59A, February 1959.

45. Roshko, A. and G.J. Thomke. "Supersonic, Turbulent Boundary Layer Interaction with a Compression Corner at Very High Reynolds Numbers," Proceedings of the Symposium on Viscous Interaction Phenomenon in Supersonic and Hypersonic Flow. Hypersonic Research Laboratory, Aerospace Research Laboratory, 7-8 May 1969.
46. Law, C.H. "Supersonic, Turbulent Boundary-Layer Separation," AIAA Journal, Vol. 12, No. 6, June 1974, pp. 794-797.
47. Holman, Jack P. Heat Transfer (Seventh Edition). New York: McGraw-Hill Publishing Company, 1990.
48. Schetz, Joseph A. Foundations of Boundary Layer Theory for Momentum, Heat, and Mass Transfer. Englewood Cliffs NJ: Prentice-Hall, Inc., 1984.

Appendix A

Separation Analysis

A number of experiments (14,42-46) have been performed to determine the compression corner angle for which ramp-induced separation of a turbulent boundary layer is first detected, α_1 . Data from these experiments have been correlated and plotted versus Reynolds number based on the incoming boundary layer thickness, Re_δ , and as a function of Mach number, M (see Figure 55). Holden found that, given the same Re_δ and M , incipient separation occurred at roughly the same total flow turning angle regardless of the mechanism inducing the separation - ramp or incident shock (14) as shown in Figure 56. The total flow turning angle is α for the ramp and 2β for the incident-reflecting shock. Now the incipient wedge angle, β_1 , can be cross-plotted versus M for various Re_δ values as shown in Figure 57. If the actual β point fell above the corresponding curve, then separation would be present and its distance from the curve would be an indicator of the separation extent. Similarly, if the point was below the curve there would be no separation.

Consider the following example from the present experiment:

$$\beta = 15^\circ \quad M = 5.76 \quad \delta_1 = 0.26 \text{ in} \quad h = 0.20 \text{ in}$$

$$\rho_1 = 0.0034 \text{ lb}_m/\text{ft}^3 \quad u_1 = 3230 \text{ ft/s} \quad T_1 = 131^\circ\text{R}$$

Now for no blowing assume $\delta_{1b} = \delta_1 + h$ just before the shock and $\rho_{1b} = \rho_1$, $u_{1b} = u_1$, $T_{1b} = T_1$. The dynamic viscosity of the air is just

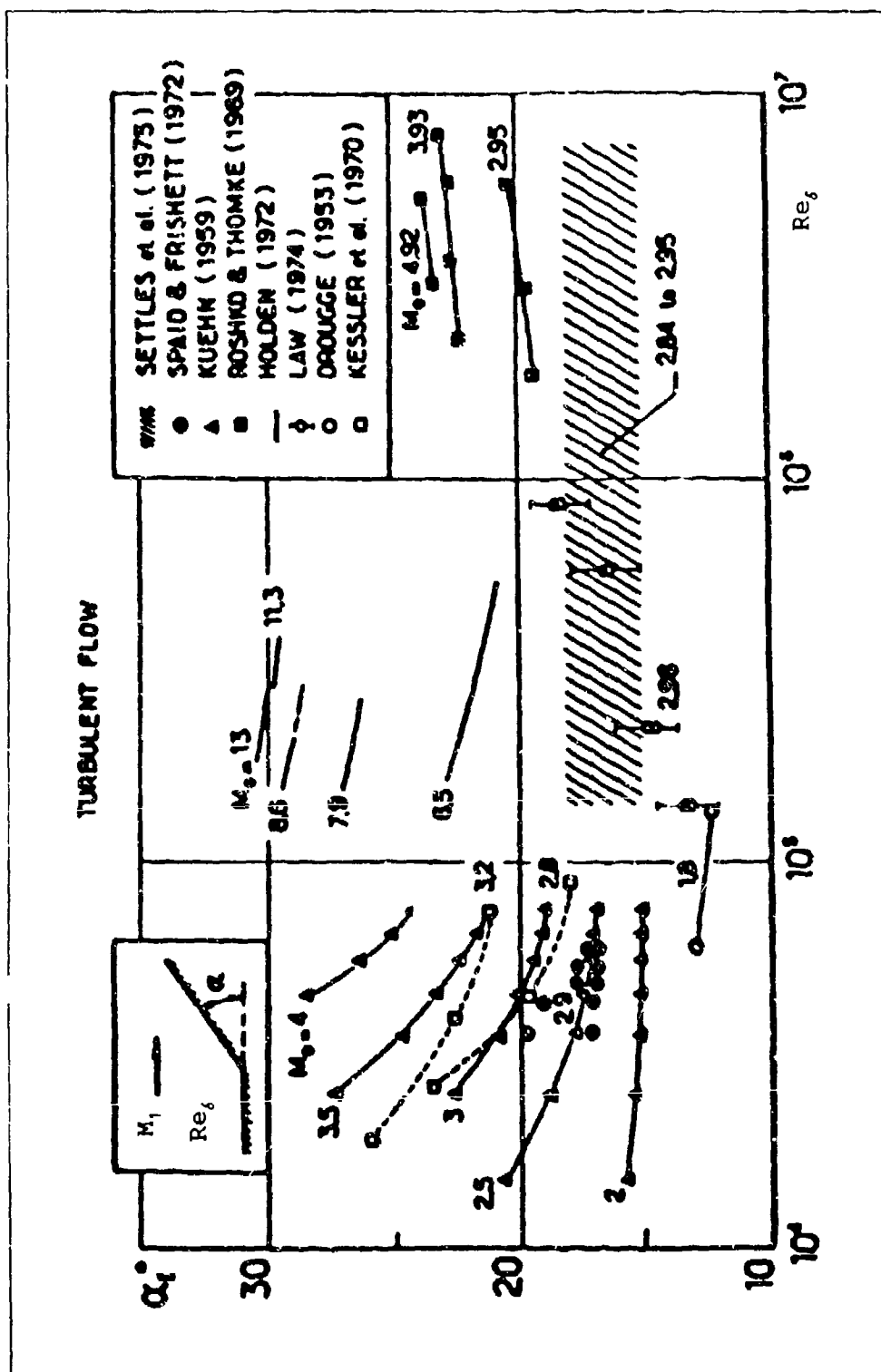


Figure 55. Experimental (Ramp-Induced) Incipient Separation Limit (Ref. 16)

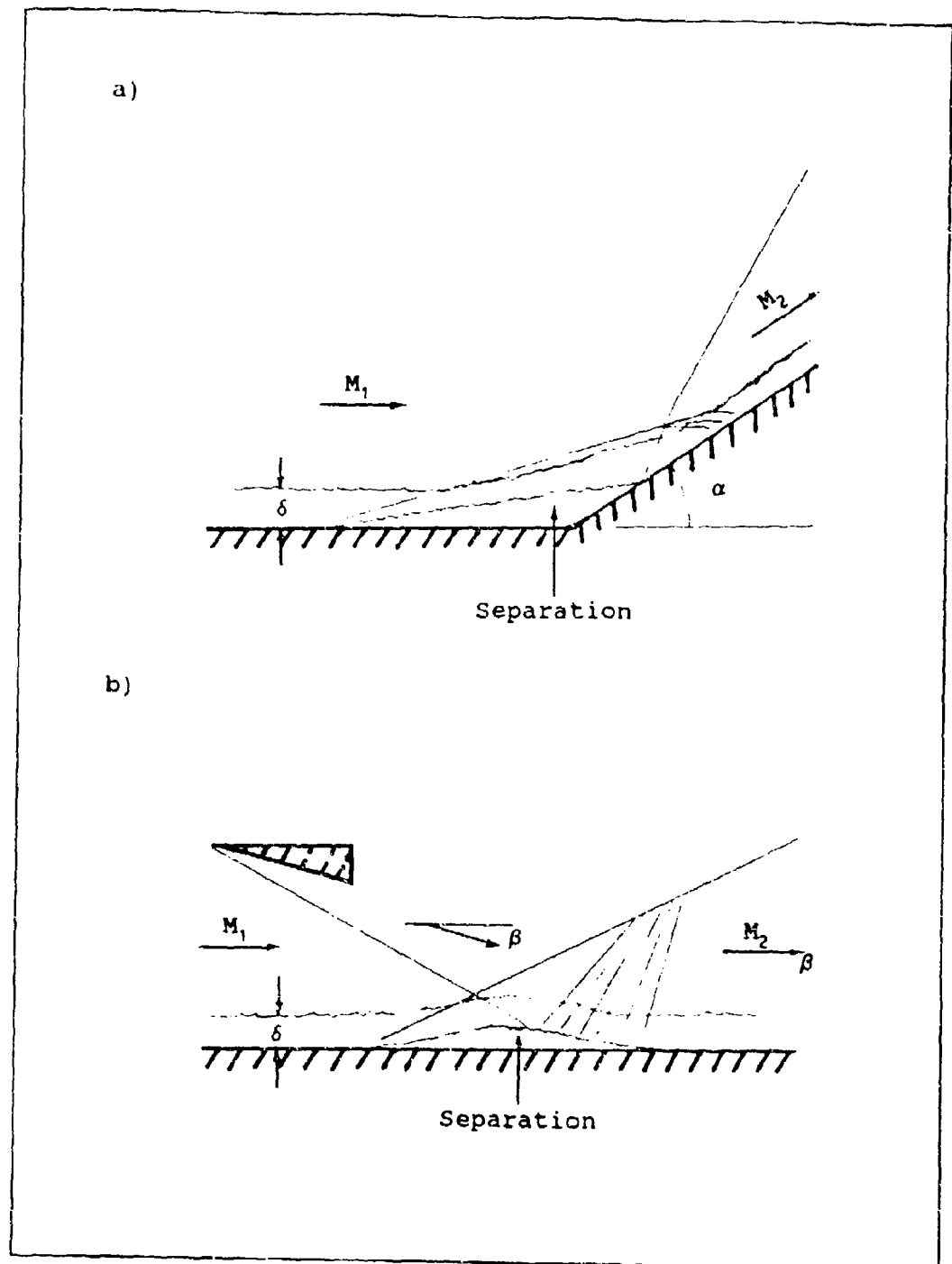


Figure 56. Boundary Layer Separation Induced by a) Compression Ramp, b) Incident Shock Wave

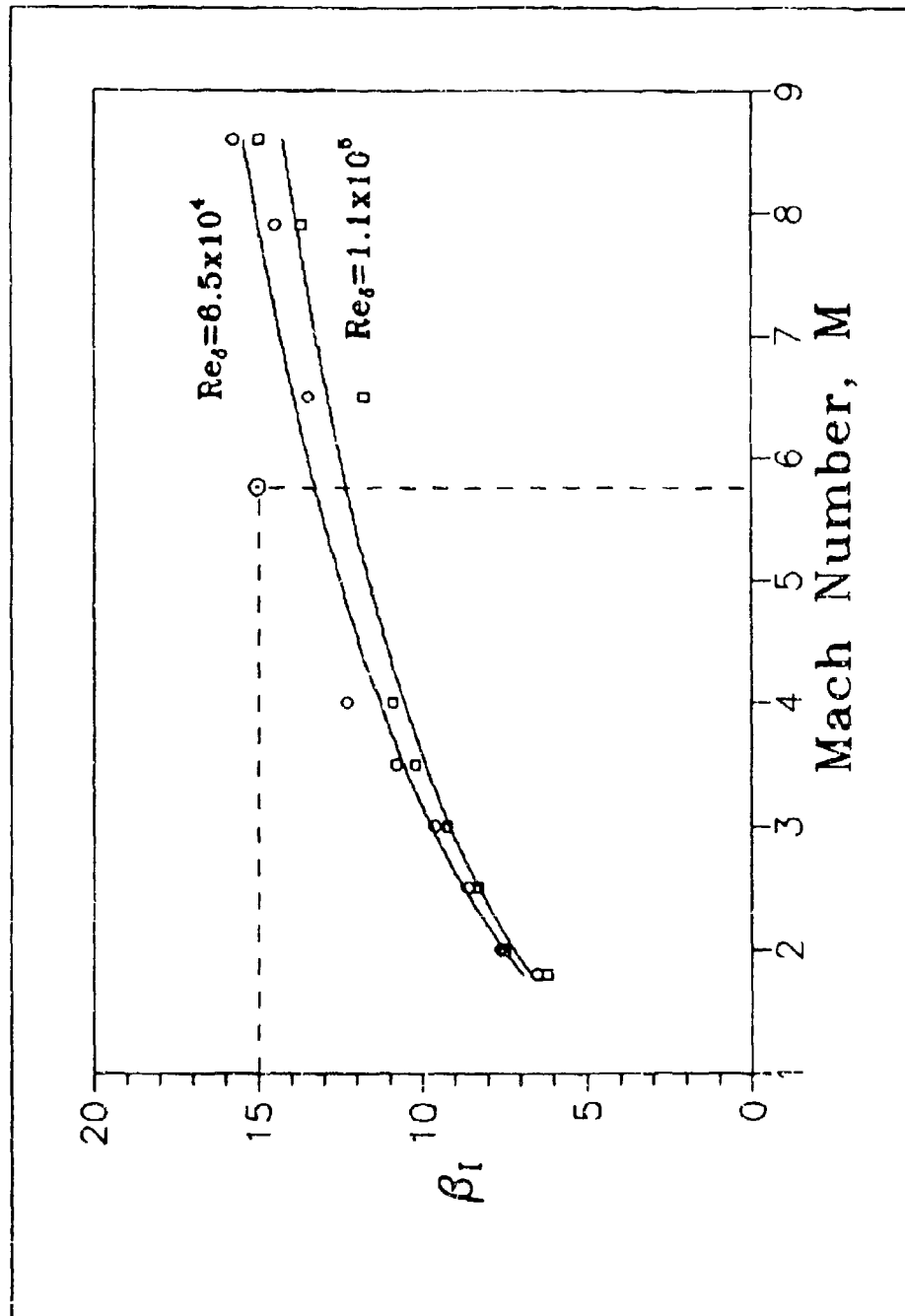


Figure 57. Cowl Deflection Angle for Incipient Separation

a function of the temperature and was found to be $\mu_{1b}=3.7 \times 10^{-6}$ lb_m/ft·sec (47:661). Then

$$Re_{\delta_{1b}} = \frac{\rho_{1b} u_{1b} \delta_{1b}}{\mu_{1b}} = 1.1 \times 10^5 \quad (9)$$

From Figure 57, this point lies above the incipient line and is thus in the separated zone. Mass injection does not alter β , but does affect M_{1b} and $Re_{\delta_{1b}}$. Increasing the TMI rate would increase M_{1b} by forcing more mass into the same space and increasing the flow velocity. This would move the point closer to the incipient line but not nearly enough. Increasing TMI also increases δ_{1b} (see the Chapter II Stream Growth Rates section) which would lead to higher values of $Re_{\delta_{1b}}$. This trend is in the wrong direction since the higher $Re_{\delta_{1b}}$ establishes a lower incipient separation curve. Since White, et al have shown that TMI can reduce and eliminate separation (2), this approach must be flawed. What Figure 57 does not account for is that TMI makes the boundary layer profile fuller - reducing the shape factor,

$$H = \frac{\delta^*}{\theta} \quad (10)$$

where

$$\delta^* = \int_0^{\delta} \left(1 - \frac{\rho u}{\rho_{1b} u_{1b}}\right) dy \quad (11)$$

$$\theta = \int_0^{\delta} \frac{\rho u}{\rho_{1b} u_{1b}} \left(1 - \frac{u}{u_{1b}}\right) dy \quad (12)$$

according to Schlichting (8:354). Delery makes note that a reduction in H_{1b} tends to move the incipient separation curve upward, but the exact influence was not reported or varied in the previous experiments (1:264). Attempts at defining a smaller effective δ_{1b} were unsuccessful.

This analysis is limited to separation wholly forward or aft of the shoulder. For the latter, new effective values of β , M_{1b} , and $Re_{\delta_{1b}}$ must be calculated to account for the expansion. If the separation straddles the shoulder this analysis may be invalid as the experimental data is only for a compression ramp or an incident shock impinging on a flat surface. As White observed, very little data is available for an oblique shock impinging at an expansion corner (2:2).

Appendix B

Control Volume Analysis

In order to relate the separation back to the TMI rate required to eliminate it, a control volume analysis was considered. For a given set of freestream and jet parameters, the conservation laws of momentum, mass, and energy can be applied to yield the M_{1b} and $Re_{\delta_{1b}}$ downstream of the slot just before the cowl shock. These could be iteratively fed back into the separation analysis to identify which jet total pressure, p_{0j} , caused the incipient separation curve to coincide with the actual β and M point in Figure 57. This would then yield the "controlling" mass injection rate as shown in the Appendix C Calculation of Intermediate Variables section.

A control volume is selected such that the entrance plane coincides with the slot exit and the exit plane is just before the cowl shock as shown in Figure 58. The control volume then has length L_{SK} . The height is chosen so that the jet growth downstream of the slot is totally contained by the control volume. The cowl height may be a convenient choice. The cowl shock is ignored since only freestream conditions in front of the shock are desired.

The momentum equation can be solved for $\rho_{1b} u_{1b}^2$ by making appropriate assumptions about the momentum thickness, θ , of the incoming boundary layer and jet profiles, the pressure just before the shock, p_{1b} , and the shear stress at the wall, τ_w .

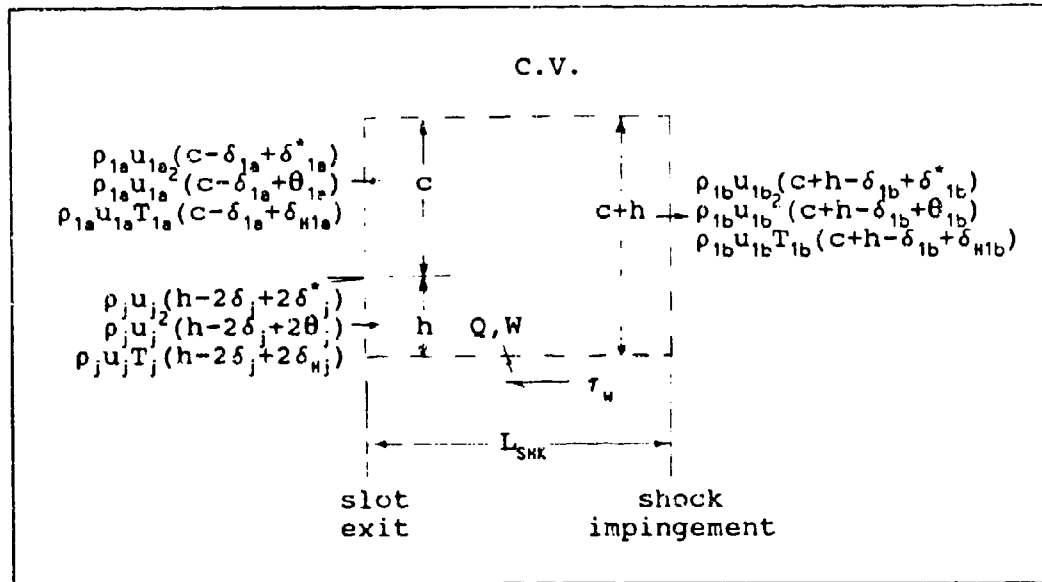


Figure 58. Diagram of Control Volume

Similarly, the continuity equation can be solved for $\rho_{1b} u_{1b}$ by assuming a displacement thickness, δ^* , for the boundary layer and jet. Together these two yield u_{1b} . The energy equation can be used to get T_{1b} with assumptions for the enthalpy thickness, δ_H , of the two incoming streams, the heat transfer rate, Q , and the viscous dissipation, W . For appropriate assumptions, the texts of Schlichting (8), Holman (47), and Schetz (48) are recommended. Then for a non-reacting flow,

$$M_{1b} = \frac{u_{1b}}{a_{1b}} = \frac{u_{1b}}{\sqrt{\gamma R T_{1b}}} \quad (13)$$

Obtaining Reynolds number based on boundary layer thickness, $Re_{\delta_{1b}}$, is only slightly more difficult. The mass flux, $\rho_{1b} u_{1b}$, was already derived from continuity, and the dynamic viscosity, μ_{1b} can be determined as a function of T_{1b} .

However, δ_{1b} cannot be easily arrived at analytically. There are actually two boundary layers present - the original inlet ramp boundary layer and the new one that starts at the slot exit and grows along the stepped down wall. The appropriate one to use is the original one since the new one just affects the shape factor. As shown in the Chapter II Stream Growth Rates section, the original boundary layer grows with mass injection and can be approximated given the slot to shock length, L_{SHK} . Then $Re_{\delta_{1b}}$ can be estimated as in Equation (9).

To complete the iterative loop process, a calculation of H_{1b} would be required. From Equations (10)-(12) the shape factor is dependent on the velocity profile and mass flux profile which can be assumed, measured, or computed with an appropriate numerical scheme. Although mass flux profiles were computed in the Chapter II Computer Results section, no further effort was made to obtain H_{1b} since no data is available as to its influence on incipient separation.

Appendix C

Derivation of Mass Flux Profiles

Given: $M_1, M_j, T_{01}, T_{0j}, p_{01}, p_{0j}, \delta, c, h, \gamma_1, \gamma_j, R, T_w$

Goal: Obtain equation for $(\rho u)(x, y)$

Assumptions:

- compressible, turbulent, isentropic, non-reacting flow
- constant shape ρ and u profiles for each stream
- $T_w = \text{constant with } x$
- fictitious T_w 's are temperature of stream passed through
- $\delta_T = \delta$
- $T_e(x) = T_1$ and $T_c(x) = T_j$

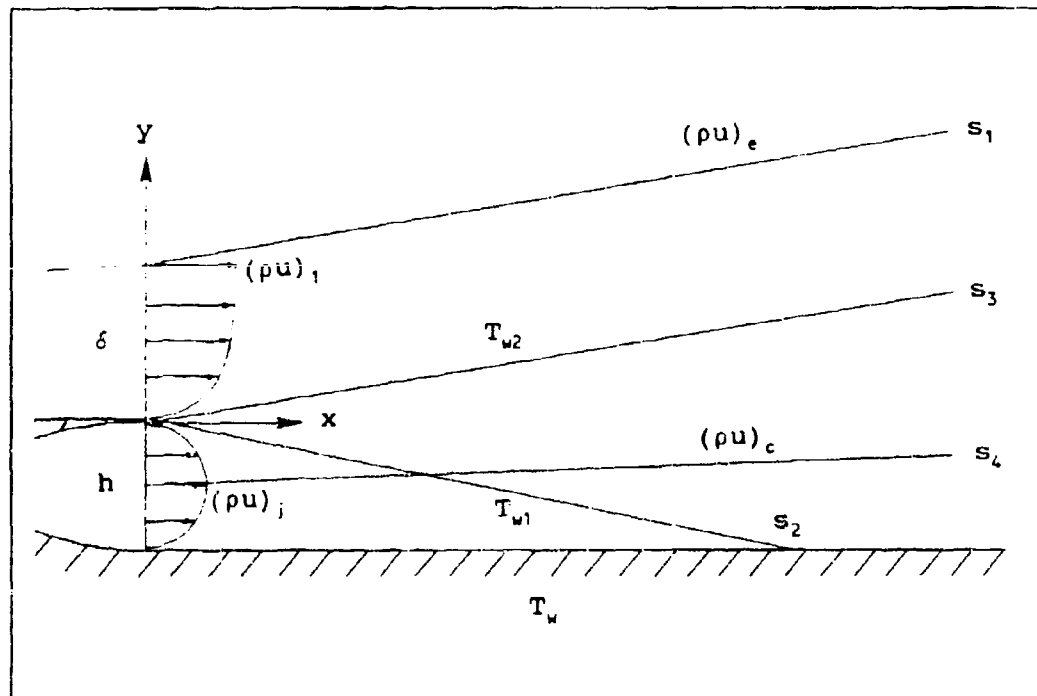


Figure 59. Diagram of Flow Parameters Used for Mass Flux Profiles

Calculation of Intermediate Variables

$$T_1 = T_{01} \left(1 + \frac{\gamma_1 - 1}{2} M_1^2 \right)^{-1}$$

$$T_j = T_{0j} \left(1 + \frac{\gamma_j - 1}{2} M_j^2 \right)^{-1}$$

$$P_1 = P_{01} \left(1 + \frac{\gamma_1 - 1}{2} M_1^2 \right)^{-\frac{\gamma_1}{\gamma_1 - 1}}$$

$$P_j = P_{0j} \left(1 + \frac{\gamma_j - 1}{2} M_j^2 \right)^{-\frac{\gamma_j}{\gamma_j - 1}}$$

$$\rho_1 = \frac{P_1}{RT_1}$$

$$\rho_j = \frac{P_j}{RT_j}$$

$$u_1 = M_1 \sqrt{\gamma_1 R T_1}$$

$$u_j = M_j \sqrt{\gamma_j R T_j}$$

$$m_{CAP} = \rho_1 u_1 C$$

$$m_{THI} = \rho_j u_j h$$

Assumed Profiles

Adapting Equations (1) & (2) to specific streams/regions

Freestream

Velocity

Density

$$\left(\text{for } x < -\frac{h}{s_2} \right) \quad \frac{u}{u_e} = \left(\frac{y - s_2 x}{\delta + s_1 x - s_2 x} \right)^{\frac{1}{7}} \quad \frac{\rho}{\rho_e} = \frac{T_e}{T_{w1}} + \left(1 - \frac{T_e}{T_{w1}} \right) \left(\frac{y - s_2 x}{\delta + s_1 x - s_2 x} \right)$$

$$\left(\text{for } x > -\frac{h}{s_2} \right) \quad \frac{u}{u_e} = \left(\frac{y + h}{\delta + h + s_1 x} \right)^{\frac{1}{7}} \quad \frac{\rho}{\rho_e} = \frac{T_e}{T_w} + \left(1 - \frac{T_e}{T_w} \right) \left(\frac{y + h}{\delta + h + s_1 x} \right)$$

Jet Stream

$$\text{(top)} \quad \frac{u}{u_c} = \left(\frac{s_3 x - y}{\frac{h}{2} + s_3 x - s_4 x} \right)^{\frac{1}{7}} \quad \frac{\rho}{\rho_c} = \frac{T_c}{T_{w2}} + \left(1 - \frac{T_c}{T_{w2}} \right) \left(\frac{s_3 x - y}{\frac{h}{2} + s_3 x - s_4 x} \right)$$

$$\text{(bottom)} \quad \frac{u}{u_c} = \left(\frac{y + h}{\frac{h}{2} + s_4 x} \right)^{\frac{1}{7}} \quad \frac{\rho}{\rho_c} = \frac{T_c}{T_w} + \left(1 - \frac{T_c}{T_w} \right) \left(\frac{y + h}{\frac{h}{2} + s_4 x} \right)$$

Fictitious Wall Temperatures

Adapting Equation (3) for the entrainment (s_2) line

$$\text{(from } s_3 \text{ to } s_4) \quad T_{w1} = \frac{T_c}{\frac{T_c}{T_w} + (1 - \frac{T_c}{T_w}) (\frac{s_3 x - s_2 x}{\frac{h}{2} + s_3 x - s_4 x})} \quad (14)$$

$$\text{(from } s_4 \text{ to } y = -h) \quad T_{w1} = \frac{T_c}{\frac{T_c}{T_w} + (1 - \frac{T_c}{T_w}) (\frac{h + s_2 x}{\frac{h}{2} + s_4 x})} \quad (15)$$

and for the jet growth line (along s_3)

$$\text{(for } x < -\frac{h}{s_2}) \quad T_{w2} = \frac{T_e}{\frac{T_e}{T_w} + (1 - \frac{T_e}{T_w}) (\frac{s_3 x - s_2 x}{\delta + s_1 x - s_2 x})} \quad (16)$$

$$\text{(for } x > -\frac{h}{s_2}) \quad T_{w2} = \frac{T_e}{\frac{T_e}{T_w} + (1 - \frac{T_e}{T_w}) (\frac{h + s_3 x}{\delta + h + s_1 x})} \quad (17)$$

Edge and Centerline Mass Fluxes

There are two possibilities for a simple calculation of $(\rho u)_e$. First, one could assume

$$(\rho u)_e = \rho_1 u_1 \quad (18)$$

which would mean that sufficient mass flow must cross s_1 to fill the boundary layer as the area expands. Or alternatively, one could assume no mass flow crosses s_1 , causing $(\rho u)_e$ to decrease proportionately with the expansion downstream. For the latter case, $(\rho u)_e$ can be derived as follows. The mass flow rate through the incoming boundary layer is

$$m_{BL}(x=0) = \rho_1 u_1 \int_0^\delta \frac{\rho u}{\rho_1 u_1} dy = \rho_1 u_1 \int_0^\delta \frac{T_1}{T_w} \left(\frac{y}{\delta} \right)^{\frac{1}{7}} + \left(1 - \frac{T_1}{T_w} \right) \left(\frac{y}{\delta} \right)^{\frac{8}{7}} dy$$

$$= \rho_1 u_1 \left[\frac{T_1}{T_w} \frac{7}{8 \delta^{1/7}} y^{\frac{8}{7}} + \left(1 - \frac{T_1}{T_w} \right) \frac{7}{15 \delta^{8/7}} y^{\frac{15}{7}} \right]_0^\delta$$

$$m_{BL}(x=0) = \rho_1 u_1 \left[\frac{7}{8} \delta \frac{T_1}{T_w} + \frac{7}{15} \delta \left(1 - \frac{T_1}{T_w} \right) \right] = \rho_1 u_1 \delta \left(\frac{7}{15} + \frac{49}{120} \frac{T_1}{T_w} \right)$$

This mass flow expands downstream and is bounded by lines s_1 and s_2 . For $x < -h/s_2$,

$$m_{BL}(x) = \rho_e u_e \int_{s_2 x}^{\delta + s_1 x} \frac{\rho u}{\rho_e u_e} dy$$

$$= \rho_e u_e \int_{s_2 x}^{\delta + s_1 x} \frac{T_e}{T_{w1}} \left(\frac{y - s_2 x}{\delta + s_1 x - s_2 x} \right)^{\frac{1}{7}} + \left(1 - \frac{T_e}{T_{w1}} \right) \left(\frac{y - s_2 x}{\delta + s_1 x - s_2 x} \right)^{\frac{8}{7}} dy$$

Letting $y' = y - s_2 x$, $dy' = dy$

$$= \rho_e u_e \int_0^{\delta + s_1 x - s_2 x} \frac{T_e}{T_{w1}} \left(\frac{y'}{\delta + s_1 x - s_2 x} \right)^{\frac{1}{7}} + \left(1 - \frac{T_e}{T_{w1}} \right) \left(\frac{y'}{\delta + s_1 x - s_2 x} \right)^{\frac{8}{7}} dy'$$

$$= \rho_e u_e \left[\frac{T_e}{T_{w1}} \frac{7}{8 (\delta + s_1 x - s_2 x)^{1/7}} (y')^{\frac{8}{7}} \right.$$

$$\left. + \left(1 - \frac{T_e}{T_{w1}} \right) \frac{7}{15 (\delta + s_1 x - s_2 x)^{8/7}} (y')^{\frac{15}{7}} \right]_0^{\delta + s_1 x - s_2 x}$$

$$m_{BL}(x) = \rho_e u_e (\delta + s_1 x - s_2 x) \left(\frac{7}{15} + \frac{49}{120} \frac{T_e}{T_{w1}} \right)$$

Now setting $m_{BL}(x=0) = m_{BL}(x)$ and solving for $(\rho u)_e$

$$(\rho u)_e = \left(\frac{\delta}{\delta + s_1 x - s_2 x} \right) \frac{\left(\frac{7}{15} + \frac{49}{120} \frac{T_1}{T_w} \right)}{\left(\frac{7}{15} + \frac{49}{120} \frac{T_e}{T_{w1}} \right)} \rho_1 u_1$$

The temperature ratio has little effect, so simplifying

$$\left(\text{for } x < -\frac{h}{s_2} \right) \quad (\rho u)_e = \left(\frac{\delta}{\delta + s_1 x - s_2 x} \right) \rho_1 u_1 \quad (19)$$

Similarly,

$$\left(\text{for } x > -\frac{h}{s_2} \right) \quad (\rho u)_e = \left(\frac{\delta}{\delta + h + s_1 x} \right) \rho_1 u_1 \quad (20)$$

In actuality, a proper $(\rho u)_e$ probably lies somewhere in between the two extremes of a constant edge mass flux and a proportionately reduced edge mass flux. It would seem logical that there would be no discontinuity in mass flux at the boundary layer edge; however, for $(\rho u)_e = \rho_1 u_1$ and the same 1/7 power law shape, mass flow would have to be added to the profile all the way to the bottom as shown in Figure 60. Mass flow crossing s_1 could not possibly make it down that far. More than likely, the boundary layer profile changes shape as it expands. To keep the analysis simple a constant shape was assumed using $(\rho u)_e = \rho_1 u_1$ for the mass flux profile plots and using the reduced edge mass flux [Equations (19) and (20)] for the optimum location figures as these gave the best representations respectively. Optimum slot location did not vary significantly using the other boundary condition.

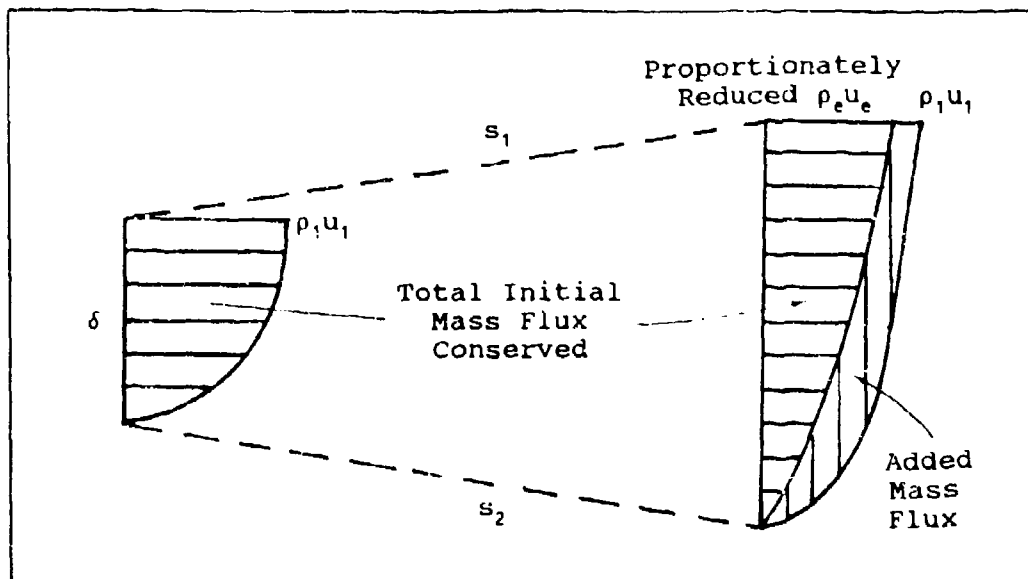


Figure 60. Comparison of Edge Mass Flux Boundary Conditions

The jet centerline (or more precisely, jet peak line since $s_4 = s_3/2$) mass flux is much less ambiguous. By the conservation of mass a linear expansion of the jet and constant ρu shapes give

$$m_{JET}(x=0) = \rho_j u_j h \left(\frac{7}{15} + \frac{49}{120} \frac{T_j}{T_w} \right)$$

$$m_{JET}(x) = \rho_c u_c \left[\left(\frac{h}{2} + s_3 x - s_4 x \right) \left(\frac{7}{15} + \frac{49}{120} \frac{T_c}{T_w} \right) + \left(\frac{h}{2} + s_4 x \right) \left(\frac{7}{15} + \frac{49}{120} \frac{T_c}{T_w} \right) \right]$$

Equating the above two equations and again ignoring the temperature ratio influence

$$(\rho u)_c = \left(\frac{h}{h + s_3 x} \right) \rho_j u_j \quad (21)$$

Mass Flux Profiles

With the edge and centerline mass fluxes for any x station found, the freestream and jet stream mass fluxes at any x, y location are obtained by appending the y position fraction (enclosed in []).

Freestream

(for $x < -h/s_2$)

$$(\rho u)_{BL} = (\rho u)_e \left[\frac{T_e}{T_{w1}} \left(\frac{y - s_2 x}{\delta + s_1 x - s_2 x} \right)^{\frac{1}{7}} + \left(1 - \frac{T_e}{T_{w1}} \right) \left(\frac{y - s_2 x}{\delta + s_1 x - s_2 x} \right)^{\frac{8}{7}} \right]$$

(for $x > -h/s_2$)

$$(\rho u)_{BL} = (\rho u)_e \left[\frac{T_e}{T_w} \left(\frac{y + h}{\delta + h + s_1 x} \right)^{\frac{1}{7}} + \left(1 - \frac{T_e}{T_w} \right) \left(\frac{y + h}{\delta + h + s_1 x} \right)^{\frac{8}{7}} \right]$$

Jet Stream

(top - between s_4 and s_3)

$$(\rho u)_{JET} = (\rho u)_c \left[\frac{T_c}{T_{w2}} \left(\frac{s_3 x - y}{\frac{h}{2} + s_3 x - s_4 x} \right)^{\frac{1}{7}} + \left(1 - \frac{T_c}{T_{w2}} \right) \left(\frac{s_3 x - y}{\frac{h}{2} + s_3 x - s_4 x} \right)^{\frac{8}{7}} \right]$$

(bottom - between $y = -h$ and s_4)

$$(\rho u)_{JET} = (\rho u)_c \left[\frac{T_c}{T_w} \left(\frac{y + h}{\frac{h}{2} + s_4 x} \right)^{\frac{1}{7}} + \left(1 - \frac{T_c}{T_w} \right) \left(\frac{y + h}{\frac{h}{2} + s_4 x} \right)^{\frac{8}{7}} \right]$$

where $(\rho u)_e$, $(\rho u)_c$, T_{w1} , and T_{w2} have previously been defined in Equations (14)-(21). Finally, the net mass flux is

$$(\rho u)(x, y) = (\rho u)_{BL} + (\rho u)_{JET} \quad (6)$$

Appendix E

Program Listing for MASS FLUX PROFILES

As written, this GW BASIC program will create an array in the file CASE1.DAT of six mass flux profiles for the $\delta=0.26$ in case. To generate the profiles for the $\delta=0.20$ in case the following changes must be made:

```
130 P01=500
190 D=0.20
480 OPEN "O", #1, "A:CASE2.DAT"
```

The 0.3 value in lines 526 and 960 can also be modified to give different close-up factors.

```

100 REM
110 REM      INPUTS
120 REM
130      P01=200
140      T01=1000
150      M1=5.75
160      P0J=0
170      T0J=500
180      MJ=0
190      D=.20
200      H=.2
205      GAM1=1.4
207      GAMJ=1.4
209      R=53.34
210      TW=700
220 REM
230      S1=.07
240      S2=-.07
250      S3=.07
260      S4=.01
270 REM
280      Y=0
290 REM
300 REM      CALCULATE INTERMEDIATE VARIABLES
310 REM
320      T1=T01/(1+(GAM1-1)/2*M1**2)
330      TJ=T0J/(1+(GAMJ-1)/2*MJ**2)
340      P1=P01/(1+(GAM1-1)/2*M1**2) * (GAM1/(GAM1-1))
350      PJ=P0J/(1+(GAMJ-1)/2*MJ**2) * (GAMJ/(GAMJ-1))
360      RHO1=144*P1/R/T1
370      RHOJ=144*PJ/R/TJ
380      U1=M1*(GAM1*32.17*R*T1)**.5
390      UJ=MJ*(GAMJ*32.17*R*TJ)**.5
400 REM
410 REM      ASSUMPTIONS
420 REM
430      TE=T1
440      TC=TJ
450 REM
460 REM      CONSERVATION OF MASS ANALYSIS
470 REM
480      DIM KUT(6)
490      OPEN "O",#1,"A:CASE1.DAT"
500      FOR Y=-H TO D+2*S1 STEP .04
510      FOR XC=0 TO 5
520          X=.1*XC
530 REM

```

```

540 REM      FREESTREAM MODEL
550 REM
555     IF Y = S2*X THEN 720
558     IF Y = D+S1*X THEN 740
560     IF X = -H/S2 THEN 660
570     IF X = H/2/(S4-S2) THEN 600
580     TW1=TC/(TC/TW+(1-TC/TW)*((S3-S2)*X/(D+S1*X-S4*X)))
590     GOTU 610
600     TW1=TC/(TC/TW+(1-TC/TW)*(H+S2*X)/(H/2+S4*X))
610 REM
620     YFOS=(Y-S2*X)/(D+S1*X-S2*X)
630     PROF=TE/TW1*YFOS*(1/7)+(1-TE/TW1)*YFOS*(8/7)
640     KUCL=RH01*U1*PROF
650     GOTU 750
660 REM
670     TW1=TW
680     YFOS=(Y+H)/(D+H+S1*X)
690     PROF=TE/TW1*YFOS*(1/7)+(1-TE/TW1)*YFOS*(8/7)
700     KUCL=RH01*U1*PROF
710     GOTU 750
720     KUCL=0
730     GOTU 750
740     KUCL=RH01*U1
750 REM
760 REM      JETSTREAM MODEL
770 REM
775     IF Y = S3*X THEN 915
778     IF Y = S4*X-H/2 THEN 880
780     IF X = -H/S2 THEN 610
790     TW2=TE/(TE/TW+(1-TE/TW)*((S1-S2)*X/(D+S1*X-S2*X)))
800     GOTU 820
810     TW2=TE/(TE/TW+(1-TE/TW)*((S1*X+H)/(D+H+S1*X)))
820 REM
825 REM      - TOP PART
830 REM
840     YFOS=(S3*X-Y)/(H/2+S1*X-S4*X)
850     PROF=TC/TW2*YFOS*(1/7)+(1-TC/TW2)*YFOS*(8/7)
860     KUJET=RH0J*UJ*H/(H+S3*X)*PROF
870     GOTU 920
880 REM
885 REM      - BOTTOM PART
890 REM
890     YFOS=(Y+H)/(H/2+S4*X)
900     PROF=TC/TW*YFOS*(1/7)+(1-TC/TW)*YFOS*(8/7)
910     KUJET=RH0J*UJ*H/(H+S3*X)*PROF
915     GOTU 920
920 REM
930 REM      SUPERPOSITION OF TWO STREAMS
940 REM
950     KU=KUCL+KUJET
960     ROT(XC)=.5*KU/RH01/U1+X
965     NEXT XC
970     WRITE #1,Y,ROT(0),ROT(1),ROT(2),ROT(3),ROT(4),ROT(5)
980     NEXT Y
990 END

```

Appendix E

Program Listing for OPTIMAL SLOT LOCATION

As written, this GW BASIC program will create an array in the file CASE6.DAT of optimum L_{SHR} values over a range of controlling mass injection ratios for the $\delta=0.20$ in case. To generate the file for the $\delta=0.26$ in case the following changes must be made:

```
130  P01=200
190  D=0.26
480  OPEN "O",#1,"A:CASE5.DAT"
515  FOR POJ=0 TO 20 STEP 4
```

```

100 REM
110 REM      INPUTS
120 REM
130      P01=500
140      T01=1000
150      M1=5.76
170      T0J=530
180      MJ=3
190      D=.2
200      H=.2
201      C=2
205      GAM1=1.4
207      GAMJ=1.4
209      R=53.34
210      TW=700
220 REM
230      S1=.07
240      S2=-.07
250      S3=.07
260      C4=.01
270 REM
280      Y=0
290 REM
300 REM      CALCULATE INTERMEDIATE VARIABLES
310 REM
320      T1=T01/(1+(GAM1-1)/2*M1**2)
330      TJ=T0J/(1+(GAMJ-1)/2*MJ**2)
340      P1=P01/(1+(GAM1-1)/2*M1**2) * (GAM1/(GAM1-1))
360      RHO1=144*P1/R/T1
380      U1=M1*(GAM1*32.17*R*T1)**.5
390      UJ=MJ*(GAMJ*32.17*R*TJ)**.5
395      MCAF=RHO1*U1*C/12
400 REM
410 REM      ASSUMPTIONS
420 REM
430      TE=T1
440      TC=TJ
450 REM
460 REM      OPENING OUTPUT FILE
470 REM
480      OPEN "O",#1,"A:CASE6.DAT"
490 REM
500 REM      CONSERVATION OF MASS ANALYSIS
510 REM
515      FOR P0J=0 TO 50 STEP 10
516          P0J=P0J/(1+(GAMJ-1)/2*MJ**2) * (GAMJ/(GAMJ-1))
517          RHOJ=144*P0J/R/TJ
518          NTM1=RHOJ*UJ*H/12
519          RUOLD=0
520          X=.1
530 REM

```

```

540 REM      FREESTREAM MODEL
550 REM
560 IF Y = D+S1*X THEN 740
565 IF Y = S2*X THEN 720
568 IF X = -H/S2 THEN 660
570 IF X = H/2/(S4-S2) THEN 600
580 TW1=TC/(TC/TW+(1-TC/TW)*((S2-S2)*X/(H/2+S3*X-S4*X)))
590 GOTO 610
600 TW1=TC/(TC/TW+(1-TC/TW)*((H+S2*X)/(H/2+S4*X)))
610 REM
620 YPOS=(Y-S2*X)/(D+S1*X-S2*X)
630 PROF=TE/TW1*YPOS*(1/7)+(1-TE/TW1)*YPOS*(8/7)
640 RUBL=RH01*S1*D/(D+S1*X-S2*X)*PROF
650 GOTO 750
660 REM
670 YPOS=(Y+H)/(D+H+S1*X)
680 PROF=TE/TW*YPOS*(1/7)+(1-TE/TW)*YPOS*(8/7)
690 RUBL=RH01*U1*D/(D+H+S1*X)*PROF
700 GOTO 750
710 RUBL=0
720 GOTO 750
740 RUBL=RH01*U1
750 REM
760 REM      JETSTREAM MODEL
770 REM
775 IF Y = S1*X THEN 915
778 IF Y = S4*X-H/2 THEN 890
780 IF X = -H/S2 THEN 810
790 TW2=TE/(TE/TW+(1-TE/TW)*((S2-S2)*X/(D+S1*X-S2*X)))
800 GOTO 820
810 TW2=TE/(TE/TW+(1-TE/TW)*((S2*X+H)/(D+H+S1*X)))
820 REM
830 REM      TOP PART OF JET
840 REM
845 YPOS=(S2*X-Y)/(H/2+S1*X-S4*X)
850 PROF=TC/TW2*YPOS*(1/7)+(1-TC/TW2)*YPOS*(8/7)
860 RUJET=RH0J*UJ*H/2/(H/2+S2*X-S4*X)*PROF
870 GOTO 920
880 REM
890 REM      BOTTOM PART OF JET
900 REM
905 YPOS=(Y+H)/(H/2+S4*X)
910 PROF=TC/TW*YPOS*(1/7)+(1-TC/TW)*YPOS*(8/7)
915 RUJET=RH0J*UJ*H/2/(H/2+S4*X)*PROF
920 GOTO 920
915 RUJET=0
920 REM
930 REM      SUPERPOSITION OF TWO STREAMS
940 REM
950 RU=RUBL+RUJET
960 IF RUOLD RU THEN 1000
970 RUOLD=RU
980 X=X+.01
990 GOTO 830
1000 REM
1010 REM      FOUND OPTIMUM LSHR FOR CURRENT POJ
1020 REM
1030 CMIR=MTMI/NCAP
1040 WRITE #1, X, CMIR
1045 PRINT POJ, X, CMIR
1050 NEXT POJ
1060 END

```


Appendix F

Schlieren Photographs

Schlieren photos were taken for most of the test runs and, occasionally, for several different injection pressure settings during the same run. The schlieren photos for Runs 26, 27, and two for 32 appear in the main text as Figures 37, 38, 45, and 46, respectively. Also note that the photos for Runs 56-61 are inserted after the runs they were repeated for just as the data in the remaining appendices are. In all cases, the freestream and TMI flows are from right to left.



Figure 61. Schlieren Photo of Initial TMI Jet Checkout at $p_{o1} = 0$ psia, $p_{oj} = 38$ psia

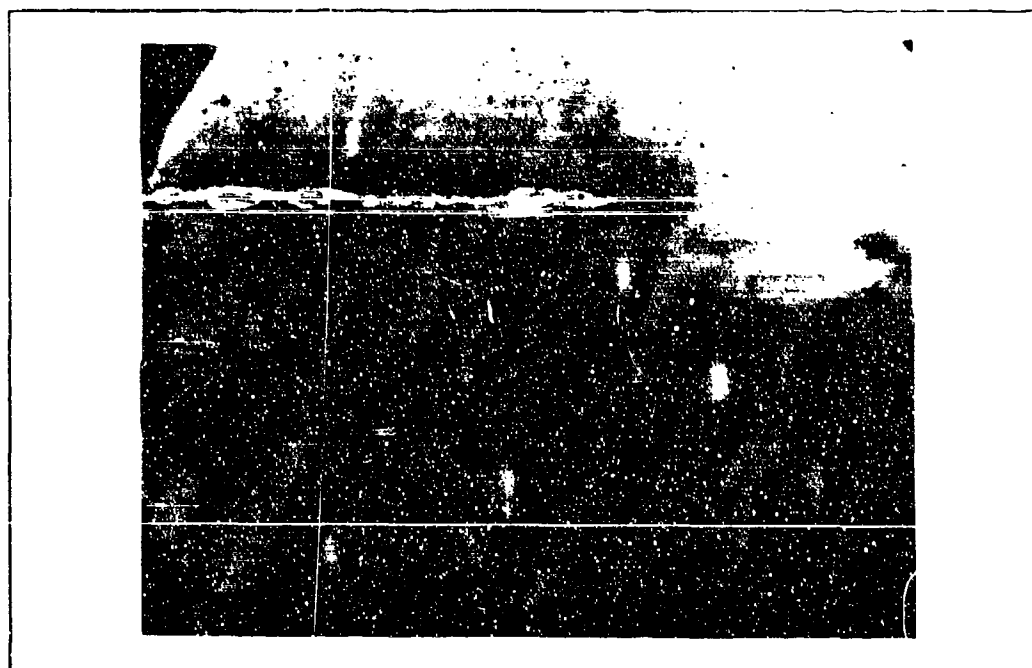


Figure 62. Schlieren Photo of TMI Jet Checkout at $p_{o1} = 0$ psia, $p_{oj} = 50$ psia After TMI Corners Welded & TMI Supply Line Enlarged

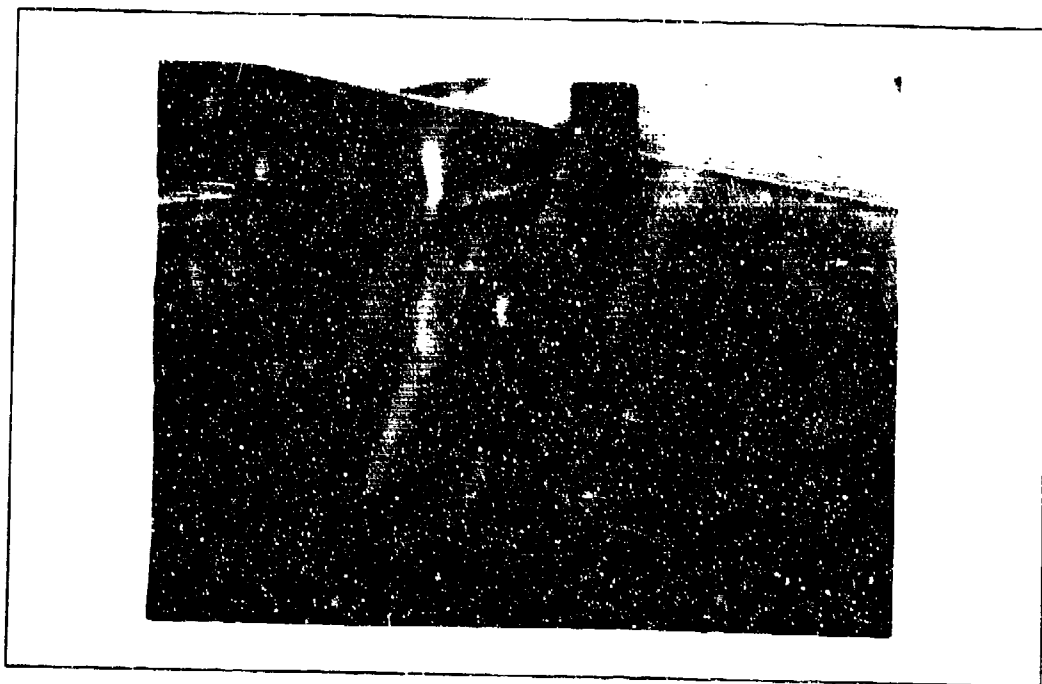


Figure 63. Run 1 Schlieren Photo with $p_{oj} = 0$ psia



Figure 64. Run 2 Schlieren Photo with $p_{oj} = 0$ psia



Figure 65. Run 5 Schlieren Photo with $p_{oj} = 18$ psia

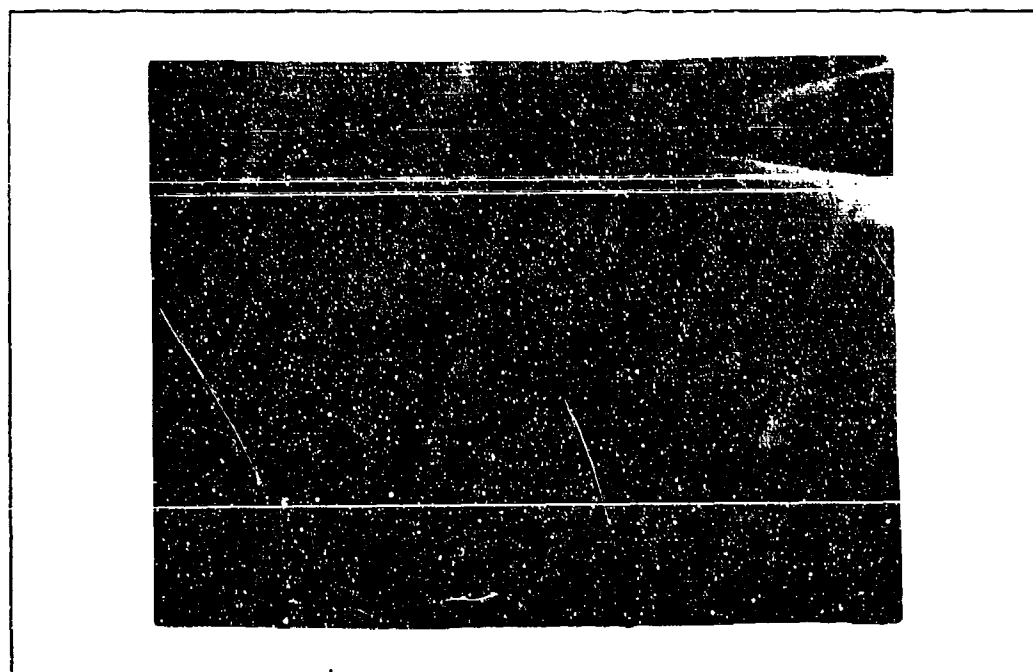


Figure 66. Run 6 Schlieren Photo with $p_{oj} = 46$ psia

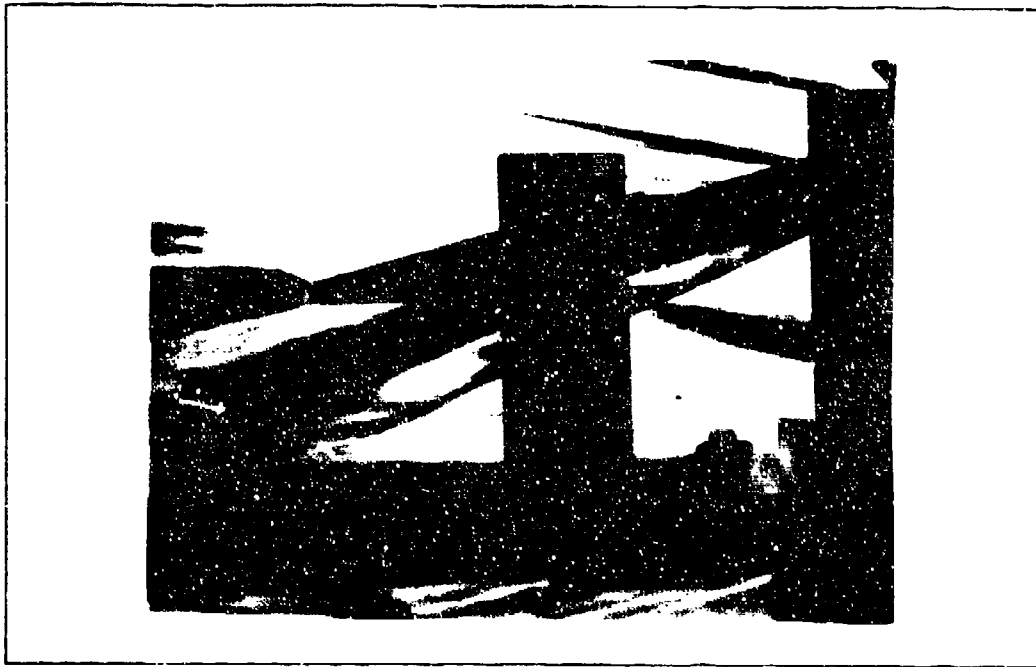


Figure 67. Run 9 Schlieren Photo with $p_{oj} = 0$ psia

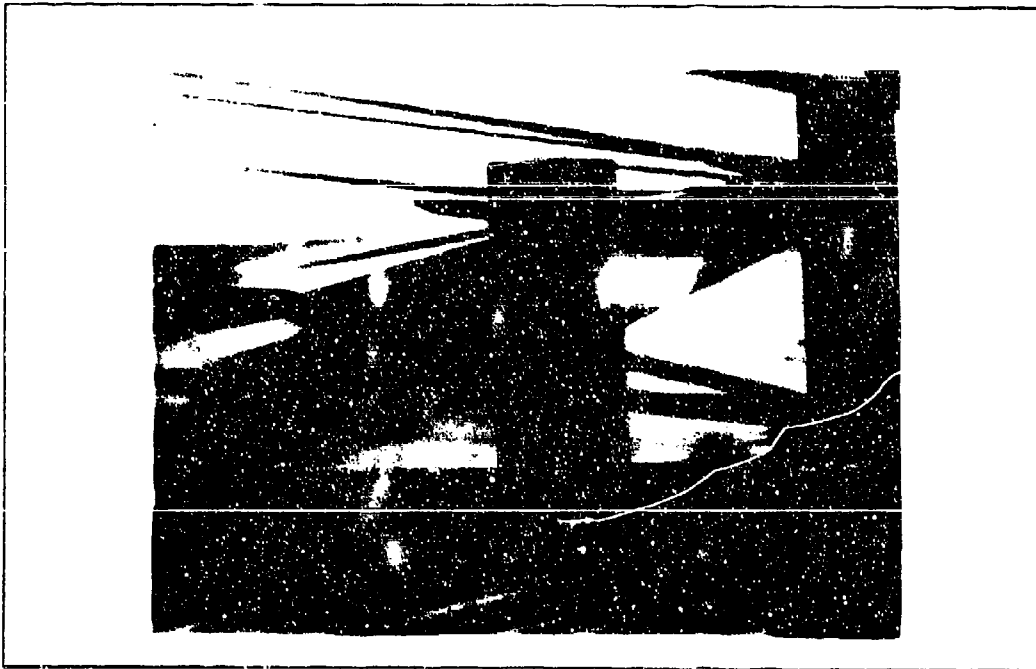


Figure 68. Run 10 Schlieren Photo with $p_{oj} = 0$ psia

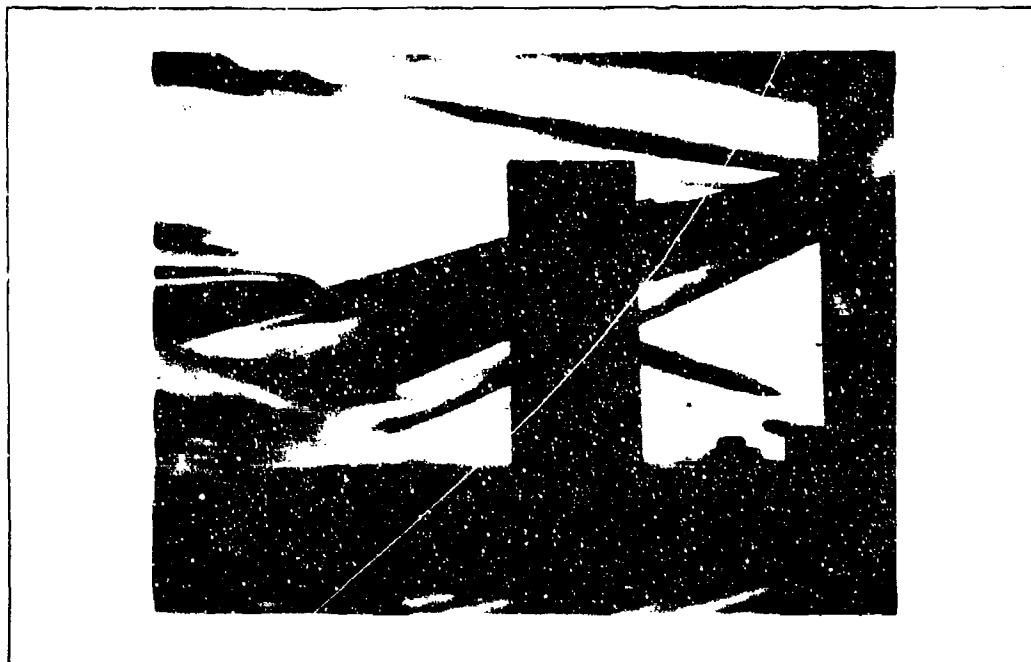


Figure 69. Run 11 Schlieren Photo with $p_{oj} = 7$ psia

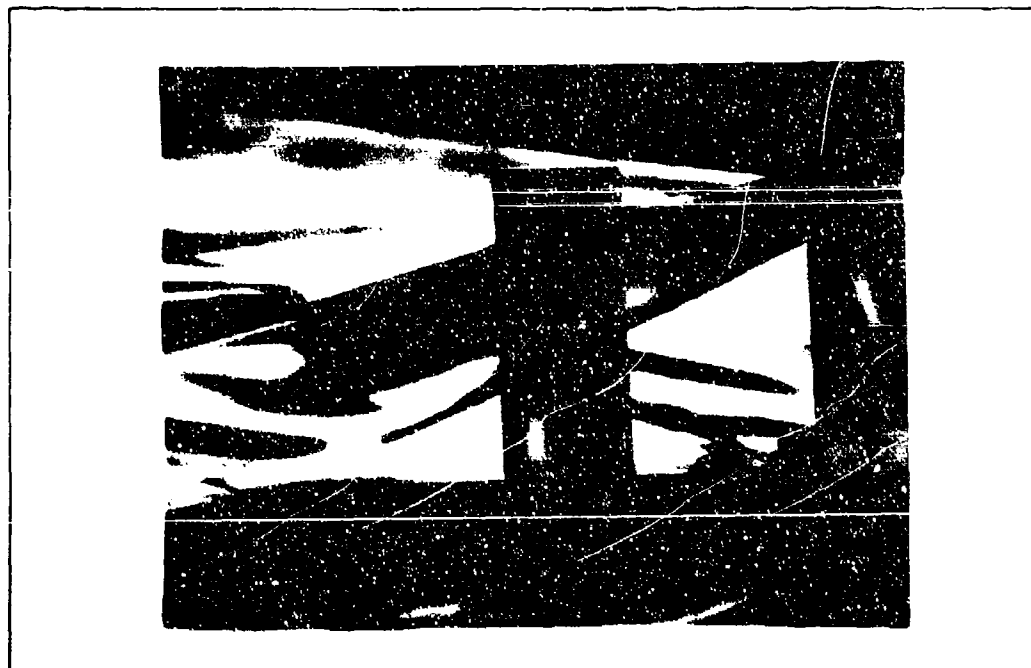


Figure 70. Run 12 Schlieren Photo with $p_{oj} = 15$ psia



Figure 71. Run 13 Schlieren Photo with $p_{0j} = 25$ psia

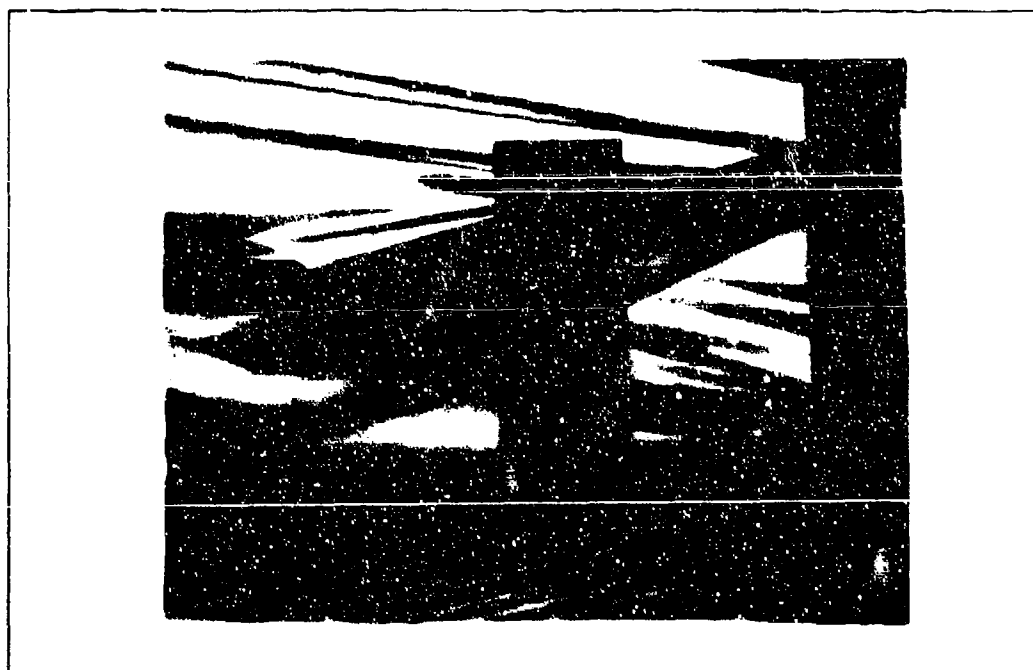


Figure 72. Run 14 Schlieren Photo with $p_{0j} = 45$ psia

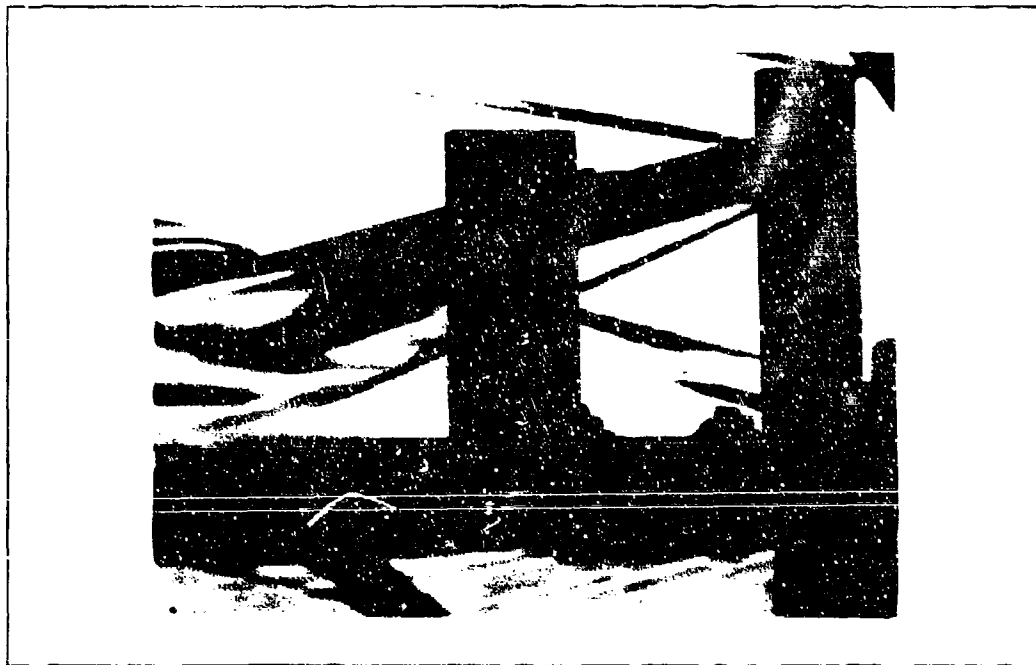


Figure 73. Run 15 Schlieren Photo with $p_{o_i} = 10$ psia

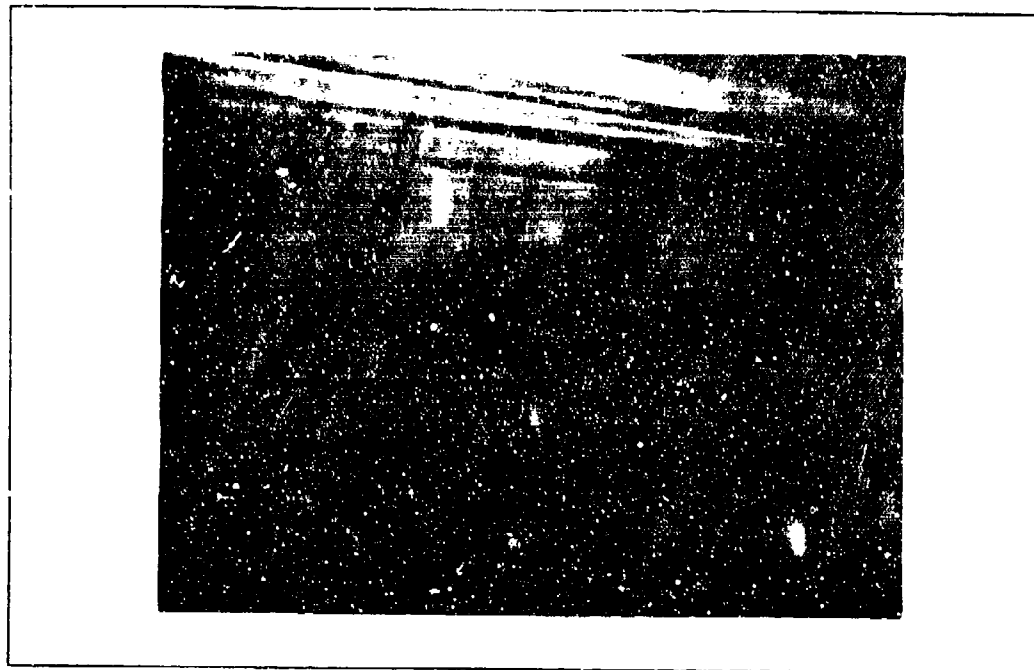


Figure 74. Run 17 Schlieren Photo with $p_{oj} = 18$ psia

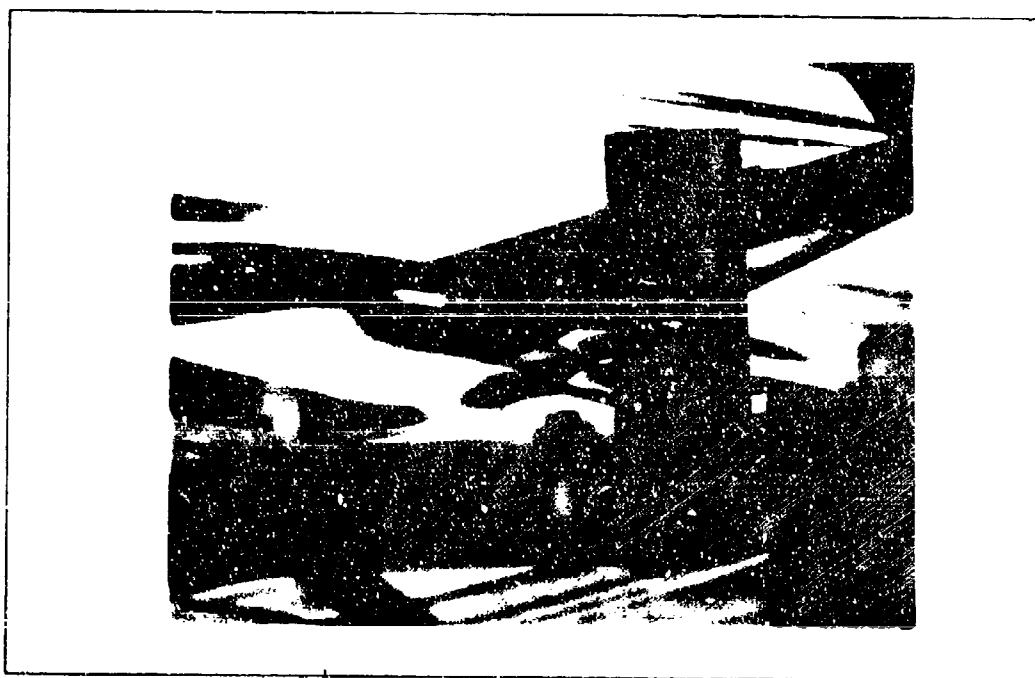


Figure 75. Run 17 Schlieren Photo with $p_{oj} = 26$ psia



Figure 76. Run 18 Schlieren Photo with $p_{oj} = 14$ psia

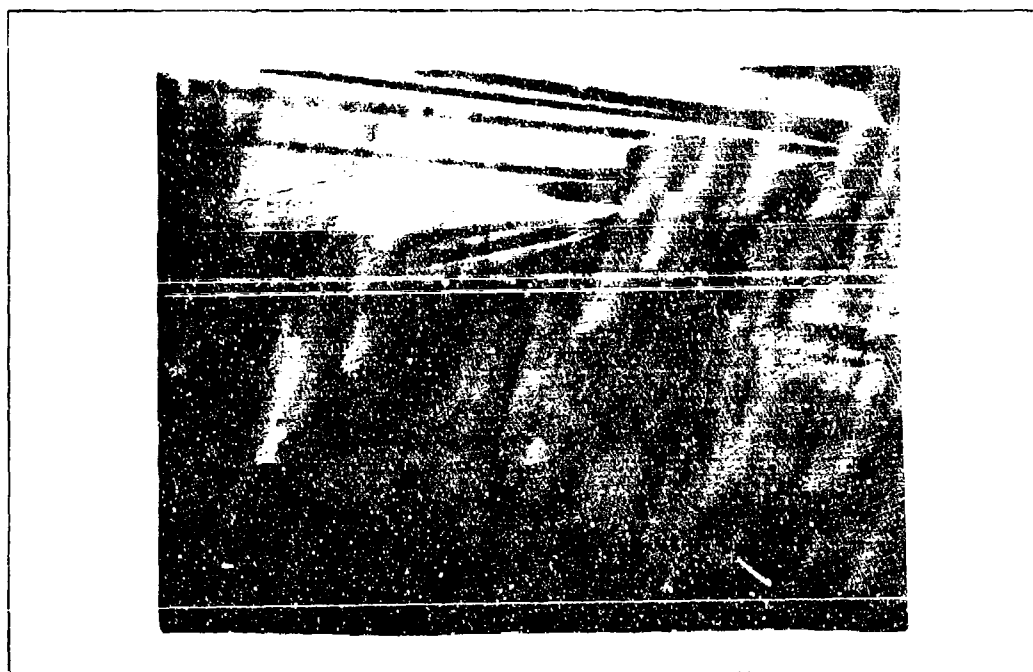


Figure 77. Run 19 Schlieren Photo with $p_{oj} = 30$ psia

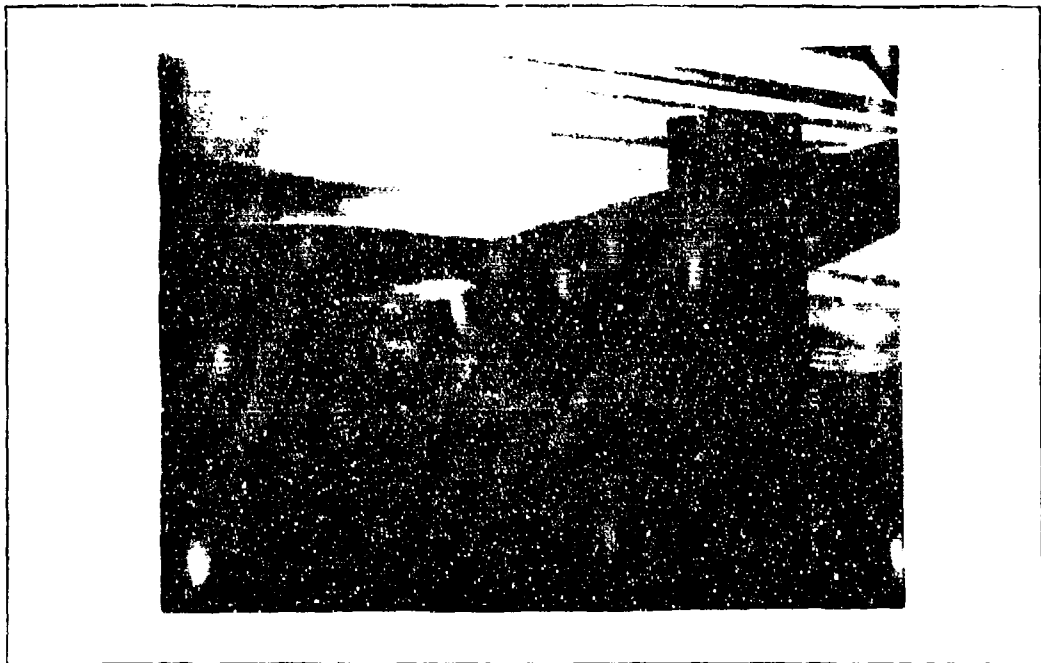


Figure 78. Run 20 Schlieren Photo with $p_{0j} = 10$ psia

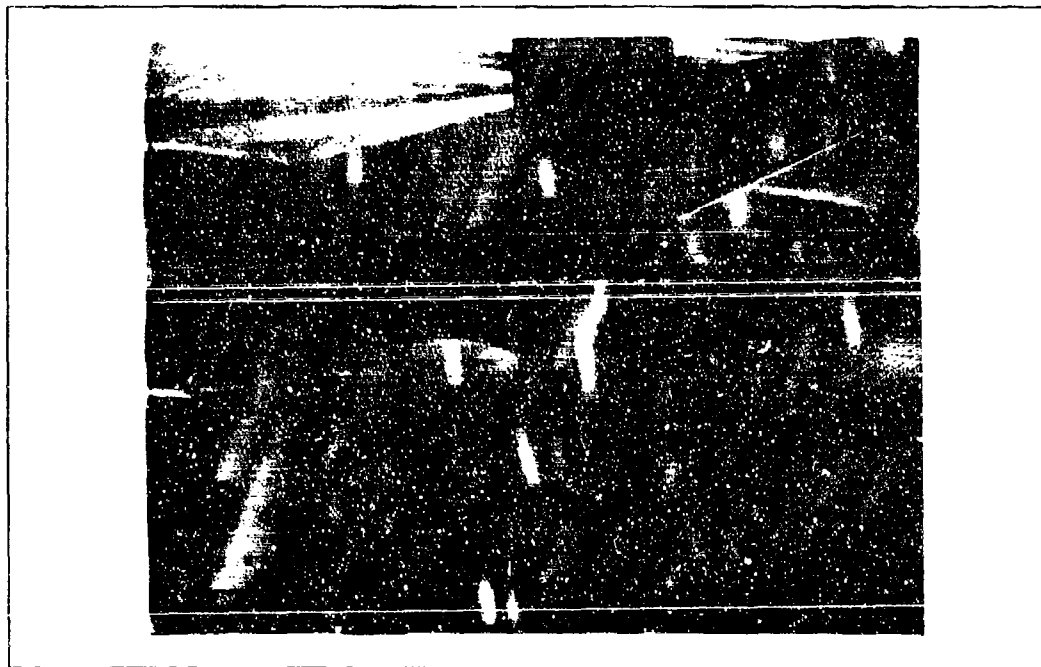


Figure 79. Run 56 Schlieren Photo with $p_{0j} = 32$ psia

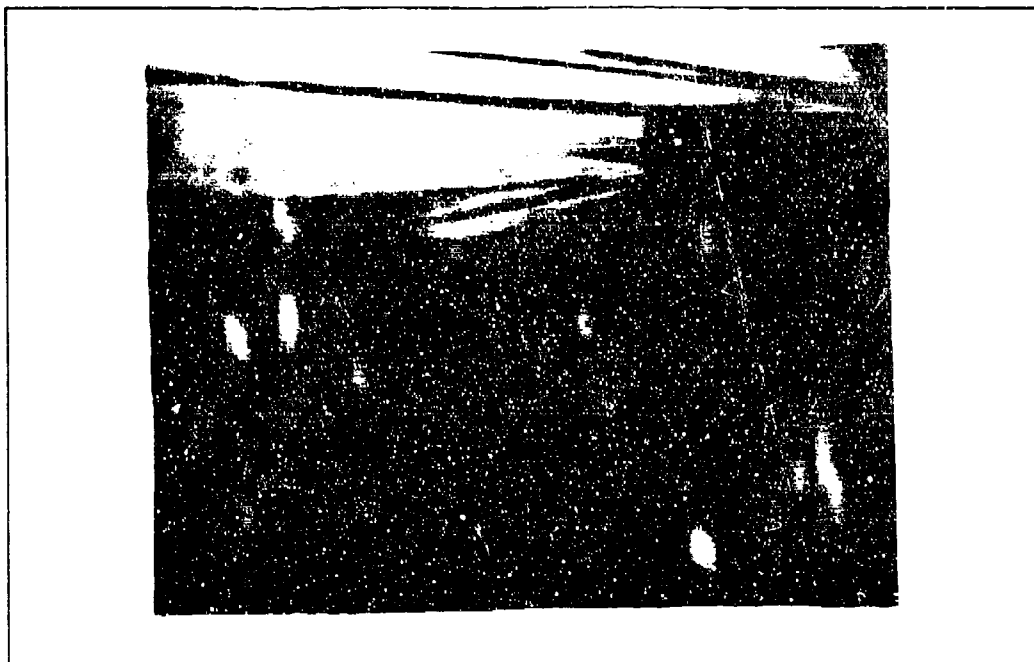


Figure 80. Run 21 Schlieren Photo with $p_{oj} = 11$ psia

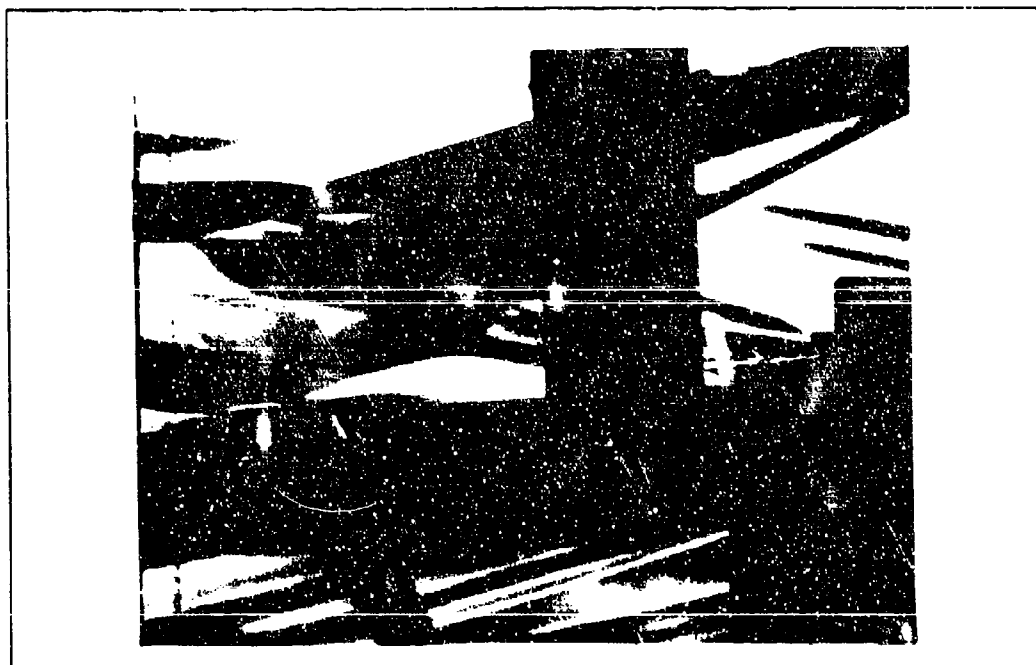


Figure 81. Run 57 Schlieren Photo with $p_{oj} = 46$ psia



Figure 82. Run 22 Schlieren Photo with $p_{0j} = 0$ psia



Figure 83. Run 22 Schlieren Photo with $p_{0j} = 10$ psia

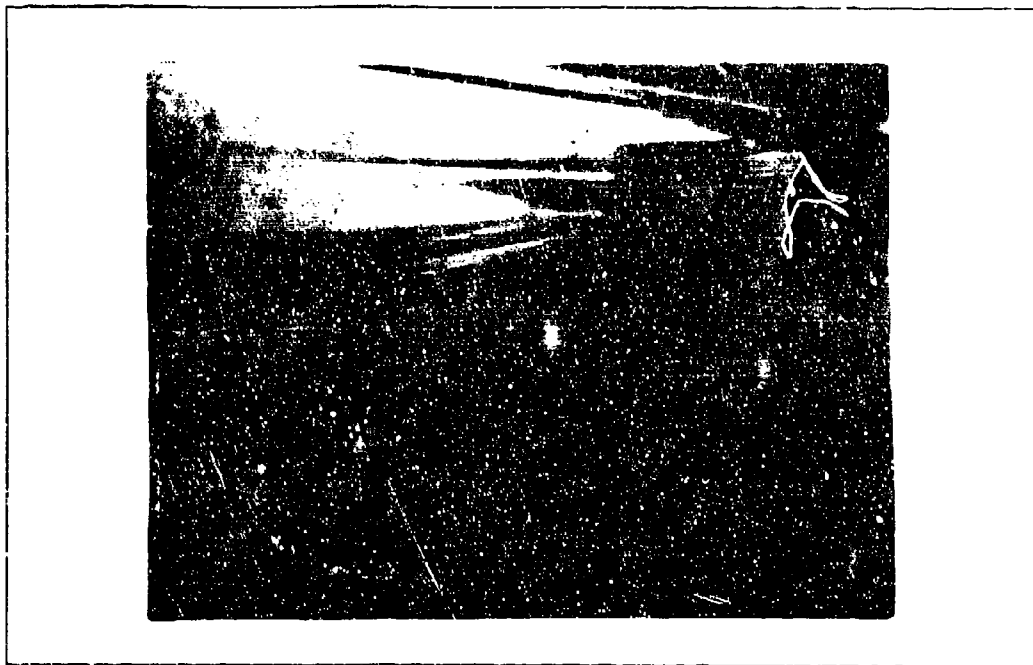


Figure 84. Run 23 Schlieren Photo with $p_{0j} = 0$ psia

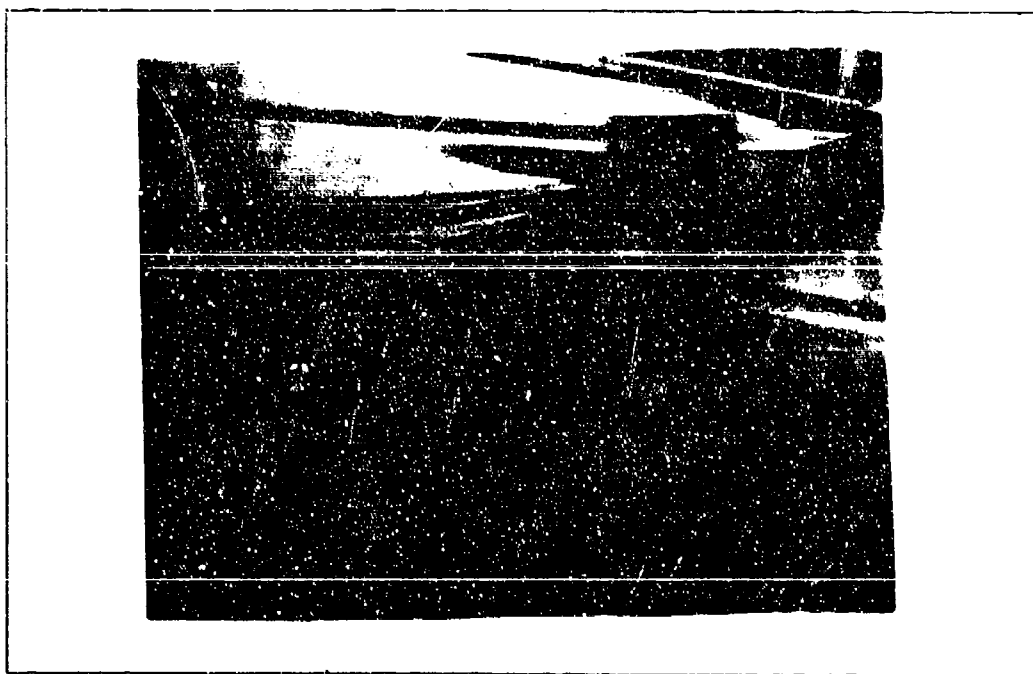


Figure 85. Run 23 Schlieren Photo with $p_{0j} = 35$ psia

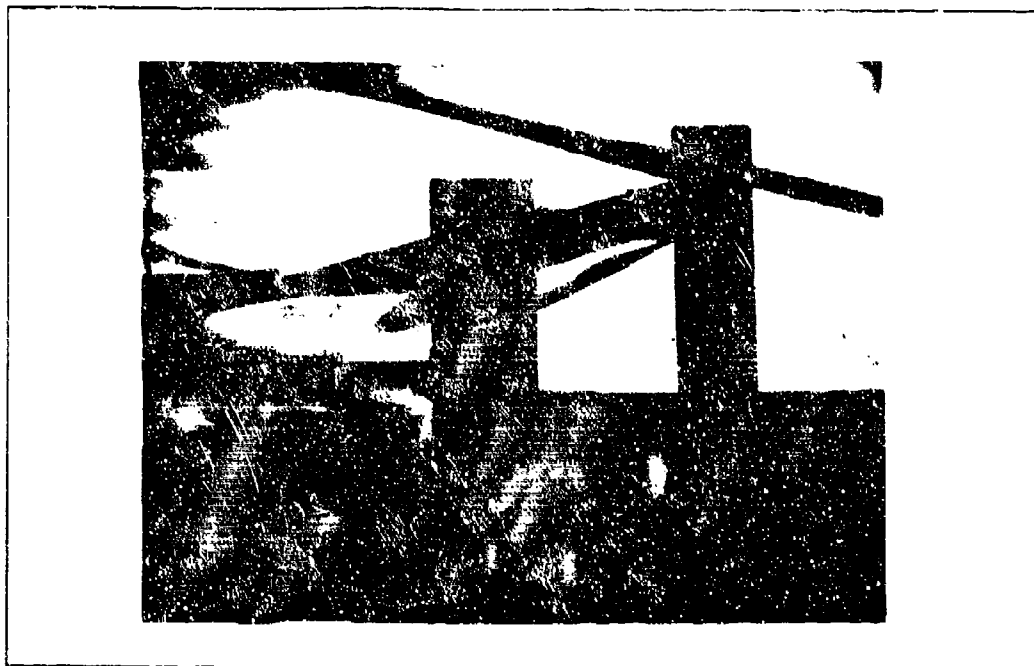


Figure 86. Run 25 Schlieren Photo with $p_{oj} = 0$ psia



Figure 87. Run 25 Schlieren Photo with $p_{oj} = 18$ psia

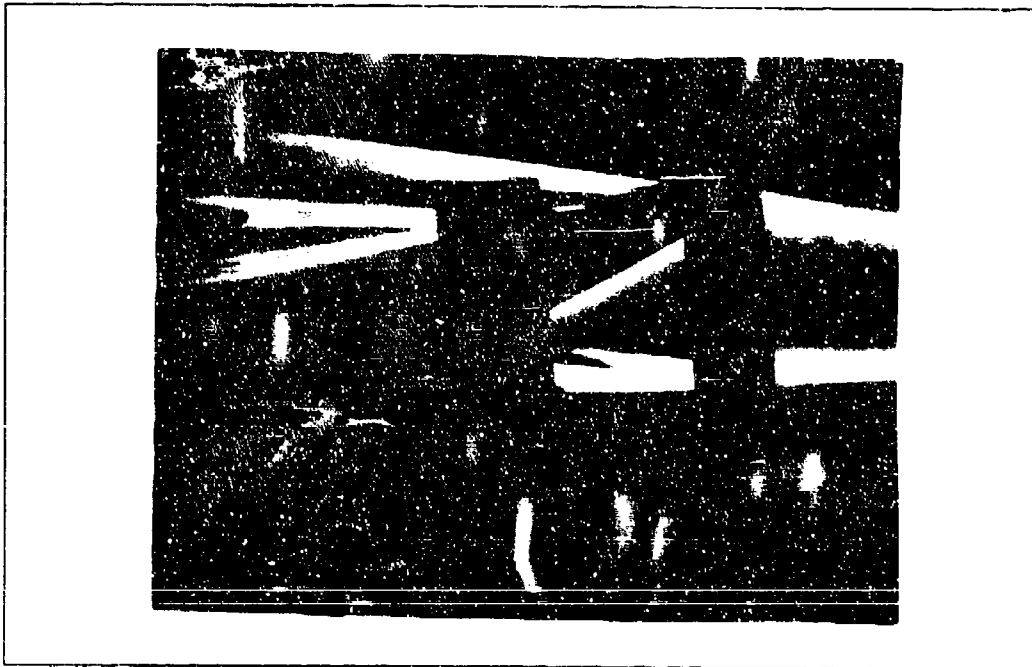


Figure 88. Run 28 Schlieren Photo with $p_{o_j} = 18$ psia

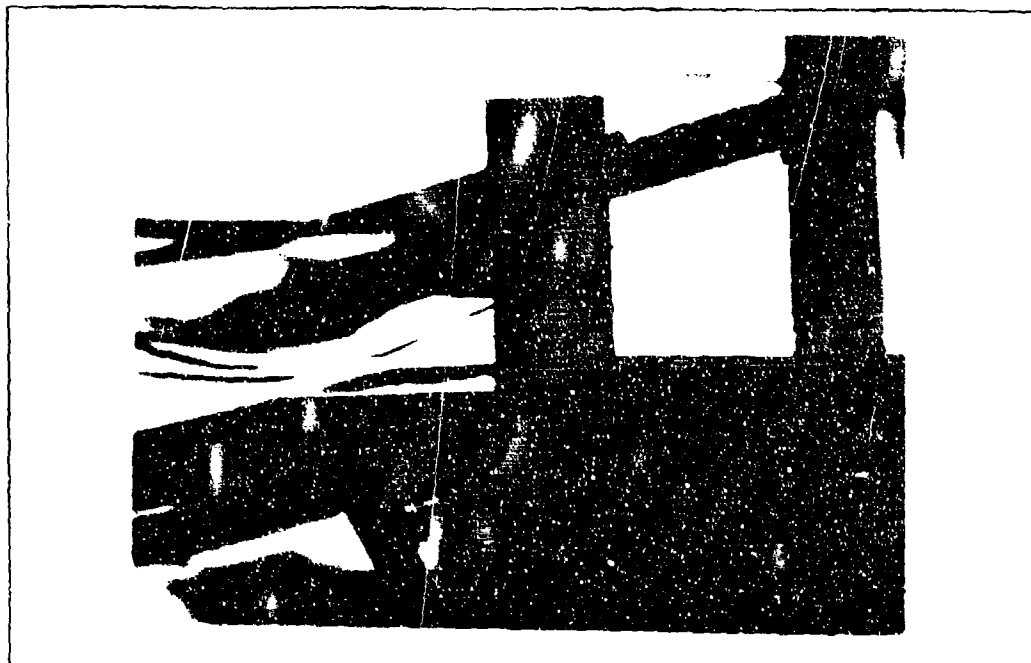


Figure 89. Run 58 Schlieren Photo with $p_{oj} = 7.7$ psia

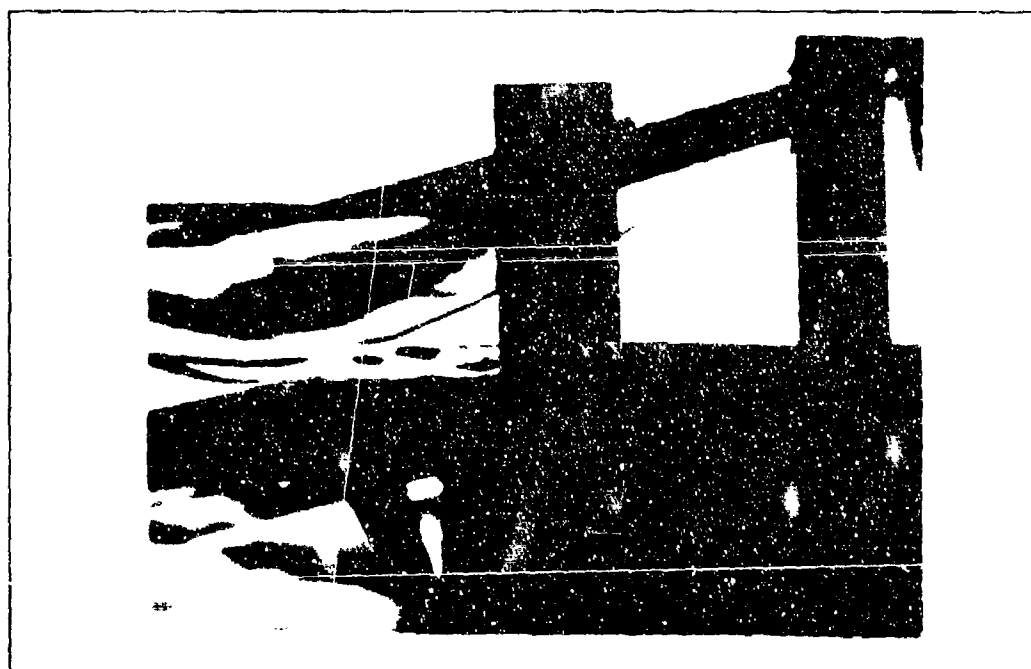


Figure 90. Run 58 Schlieren Photo with $p_{oj} = 12$ psia

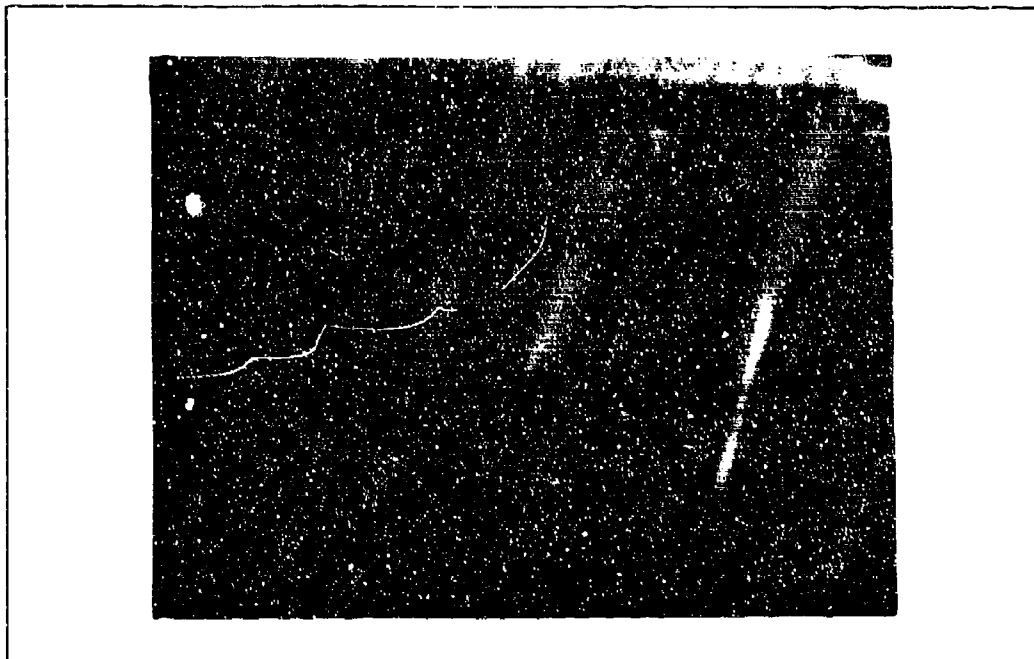


Figure 91. Run 30 Schlieren Photo with $p_{oj} = 0$ psia

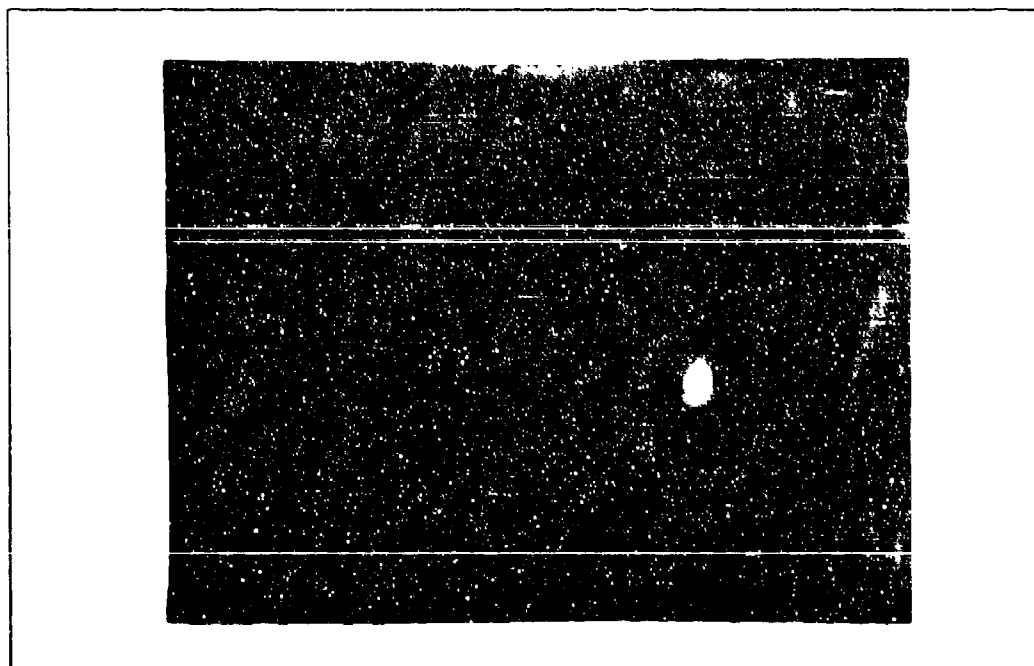


Figure 92. Run 30 Schlieren Photo with $p_{oj} = 12$ psia

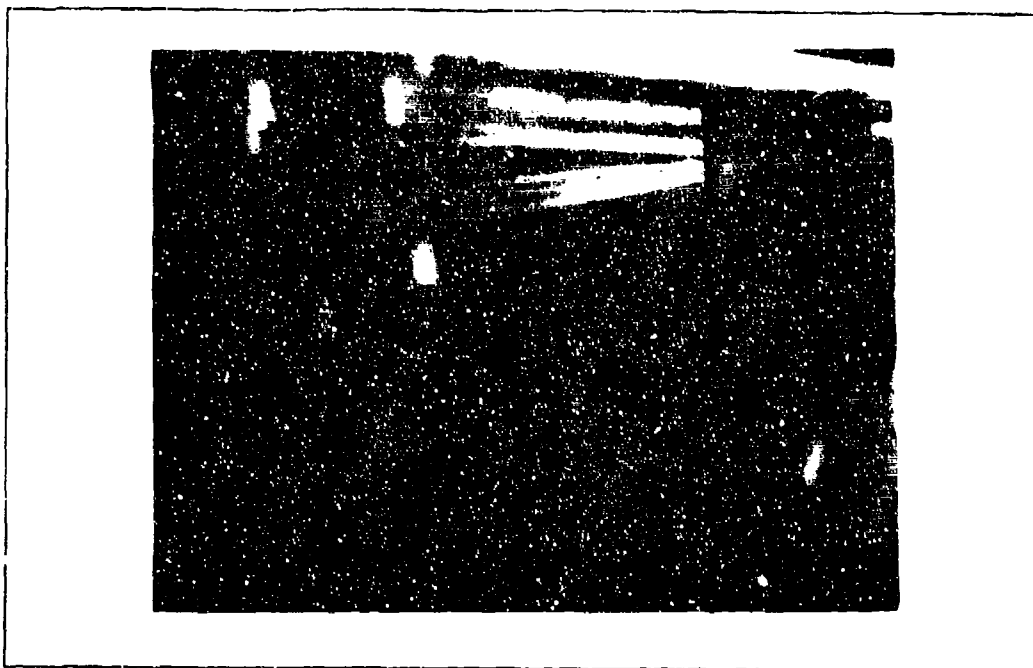


Figure 93. Run 30 Schlieren Photo with $p_{o_j} = 24$ psia

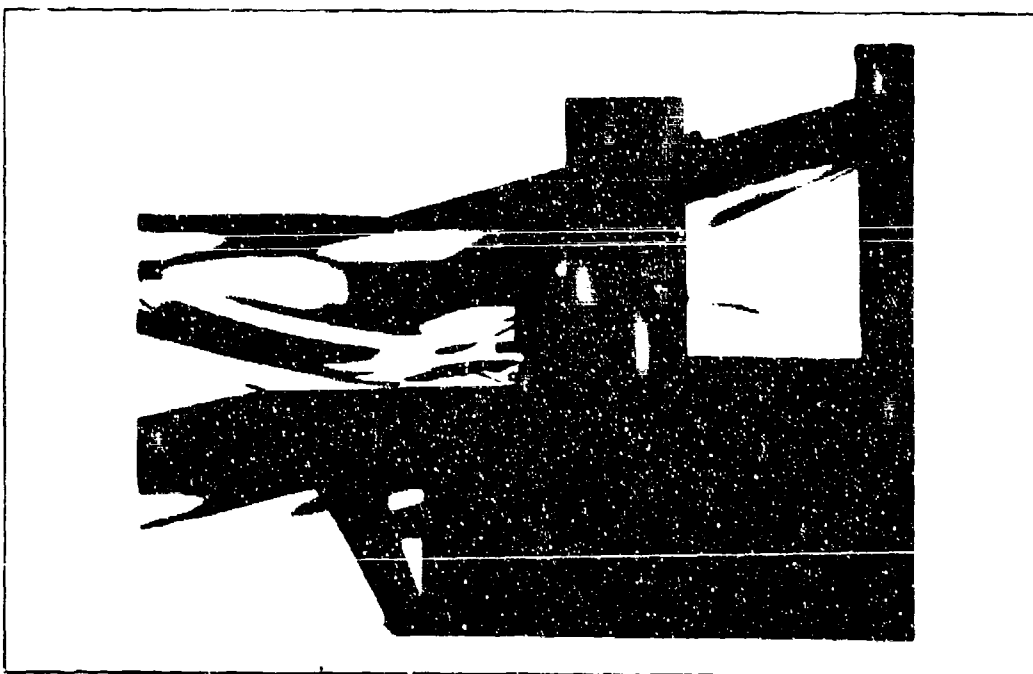


Figure 94. Run 59 Schlieren Photo with $p_{o_j} = 8.6$ psia



Figure 95. Run 33 Schlieren Photo with $p_o = 17$ psia

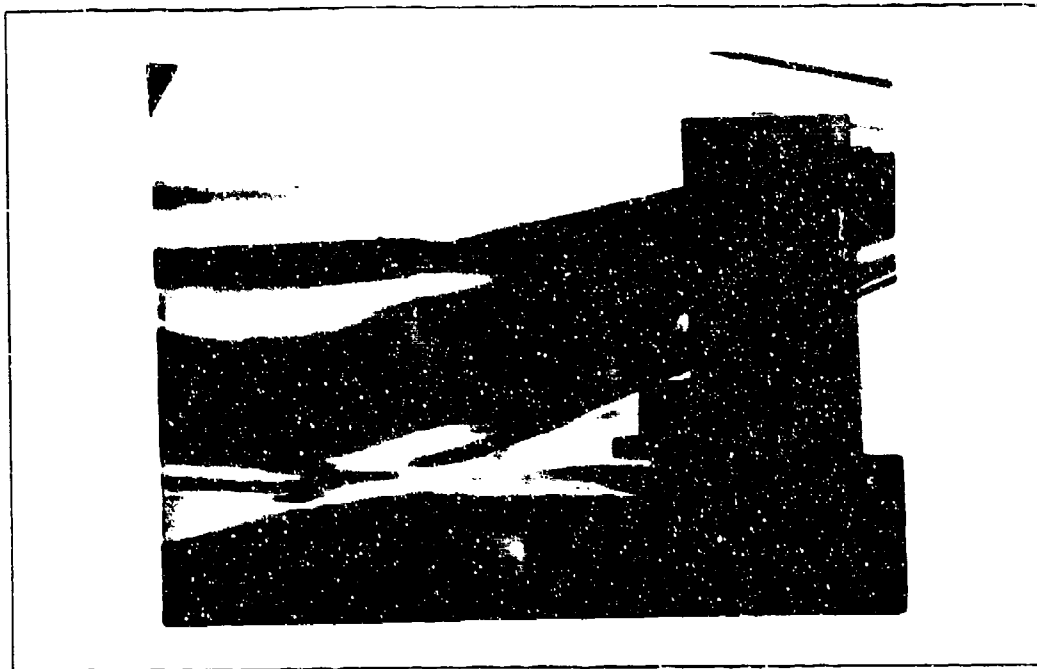


Figure 96. Run 34 Schlieren Photo with $p_{o_1} = 6$ psia

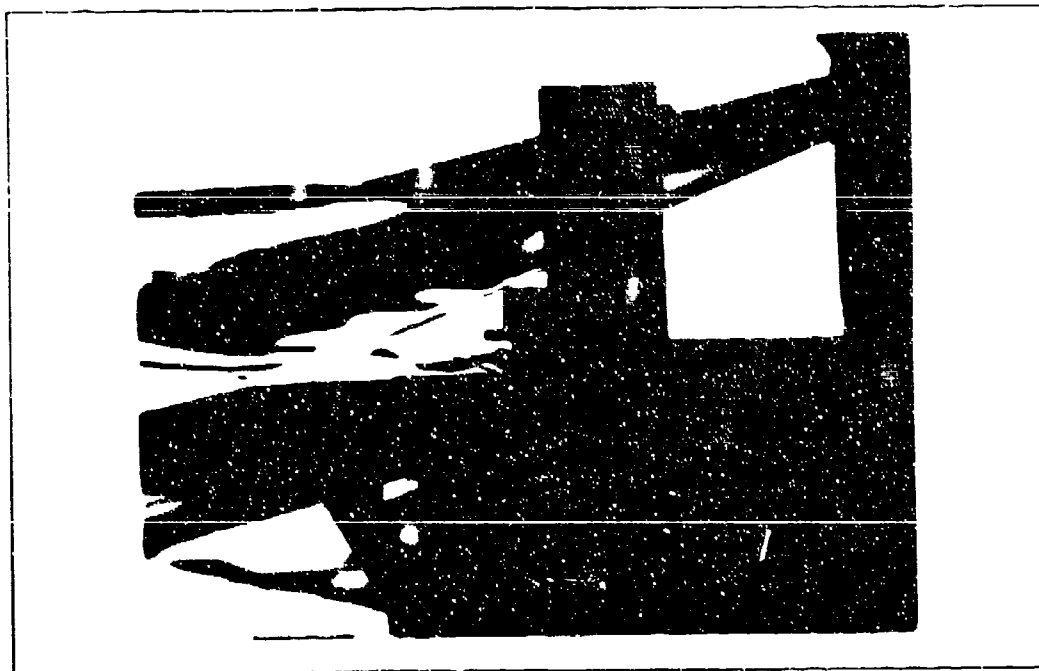


Figure 97. Run 61 Schlieren Photo with $p_{o_1} = 10.4$ psia



Figure 98. Run 35 Schlieren Photo with $p_{oj} = 15$ psia

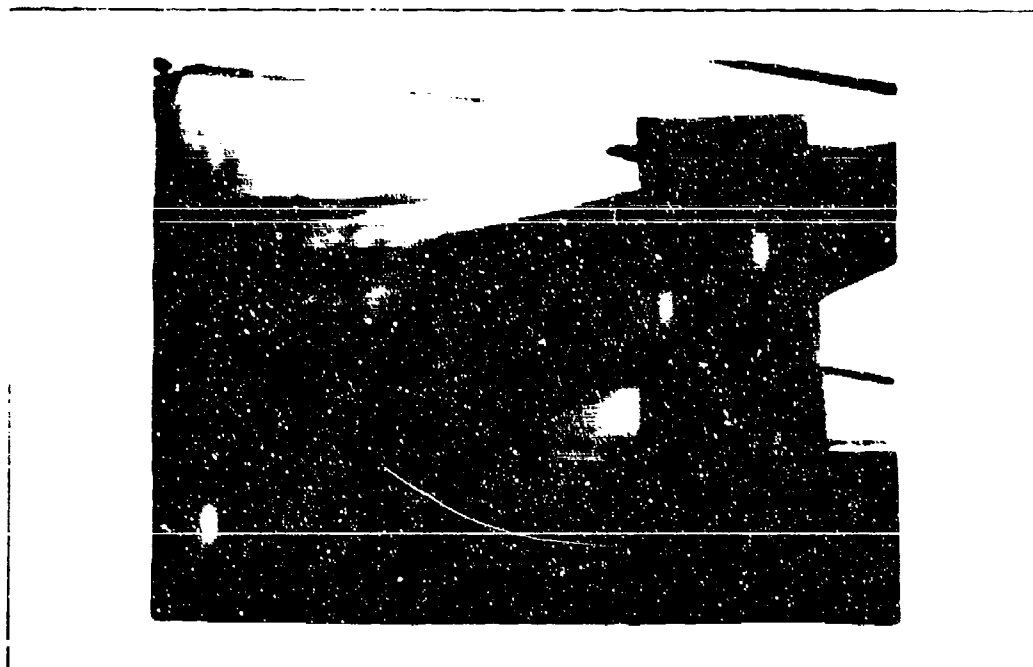


Figure 99. Run 37 Schlieren Photo with $p_{oj} = 23$ psia

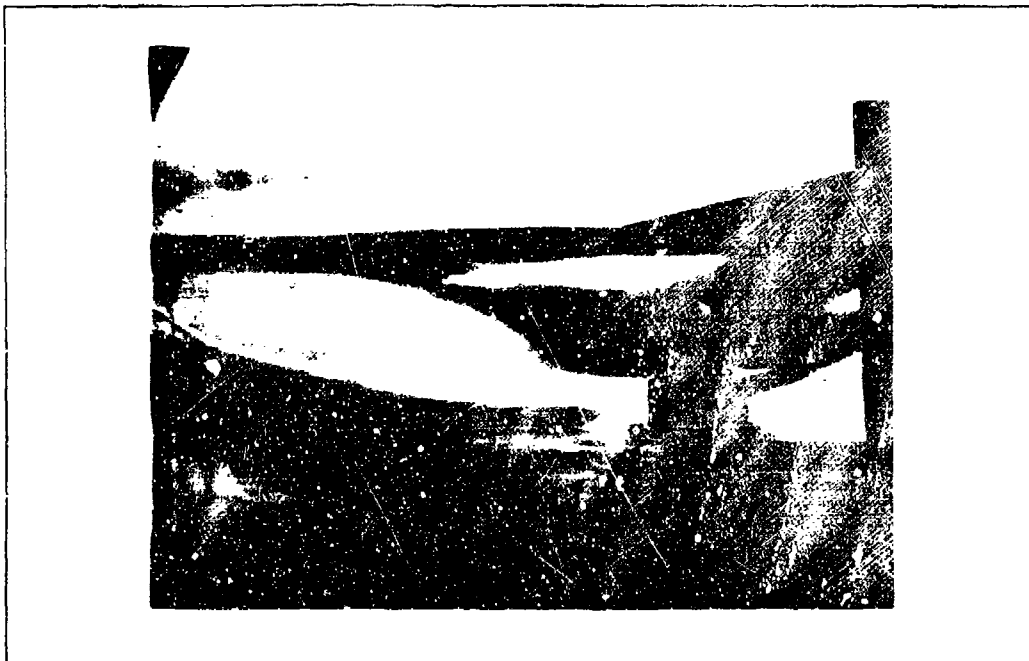


Figure 100. Run 38 Schlieren Photo with $p_{o,j} = 23$ psia

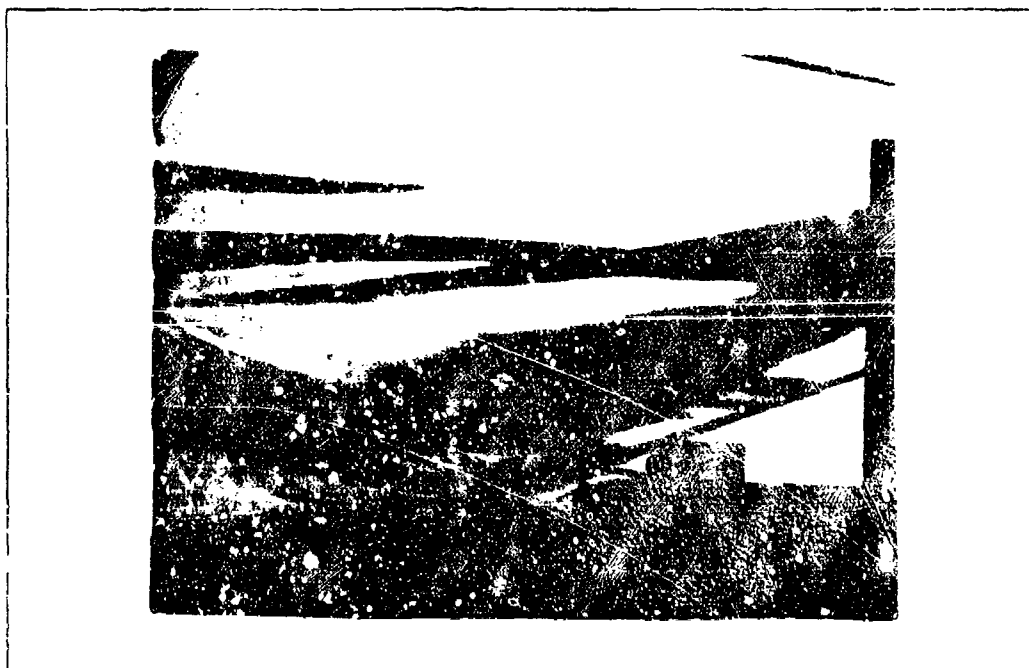


Figure 101. Run 39 Schlieren Photo with $p_{o,j} = 23$ psia

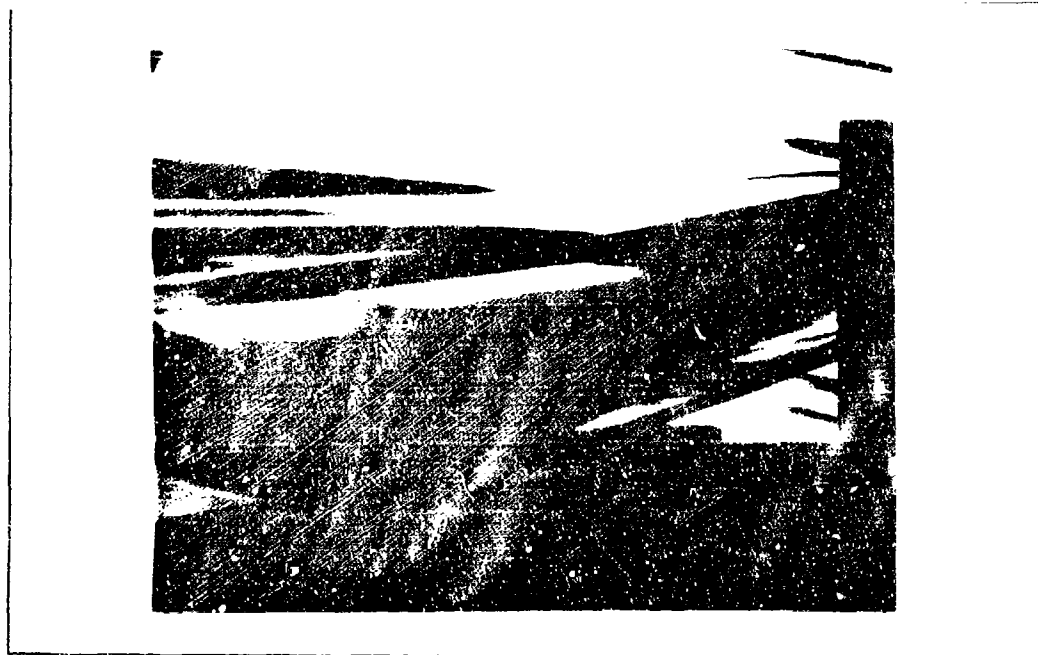


Figure 102. Run 40 Schlieren Photo with $p_{c_1} = 46$ psia

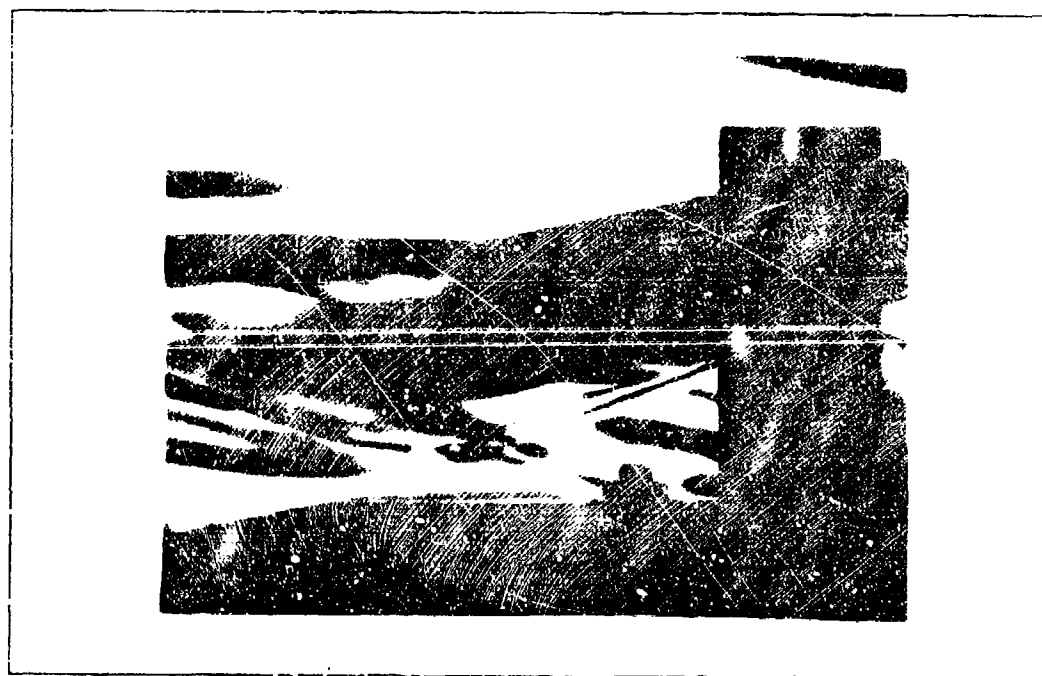


Figure 103. Run 41 Schlieren Photo with $p_{o_1} = 26$ psia



Figure 104. Run 42 Schlieren Photo with $p_{oj} = 40$ psia

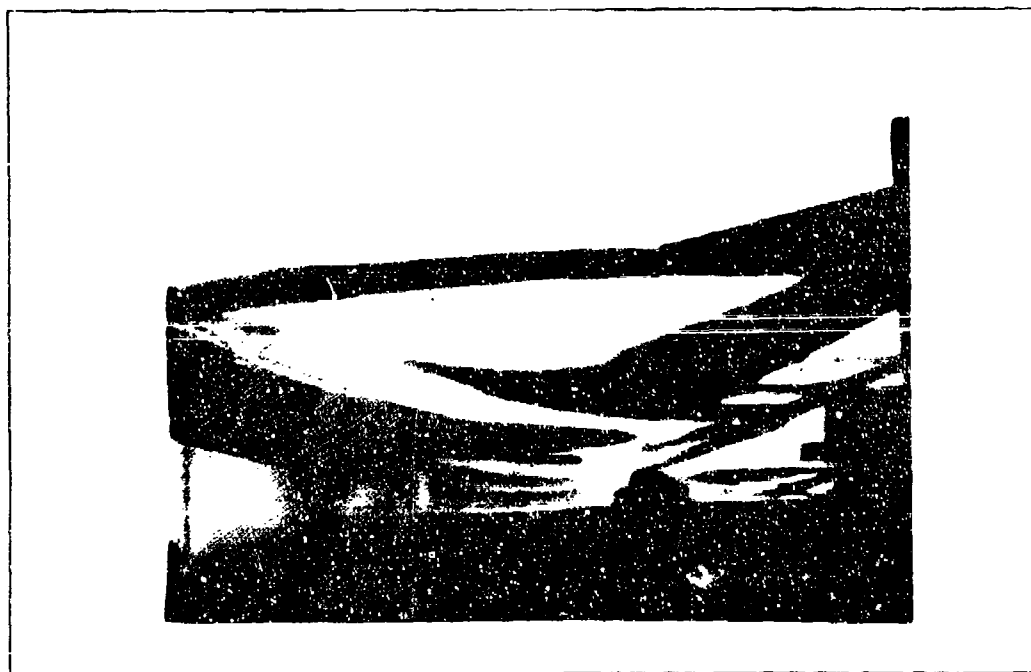


Figure 105. Run 43 Schlieren Photo with $p_{oj} = 8$ psia



Figure 106. Run 44 Schlieren Photo with $p_{oj} = 24$ psia

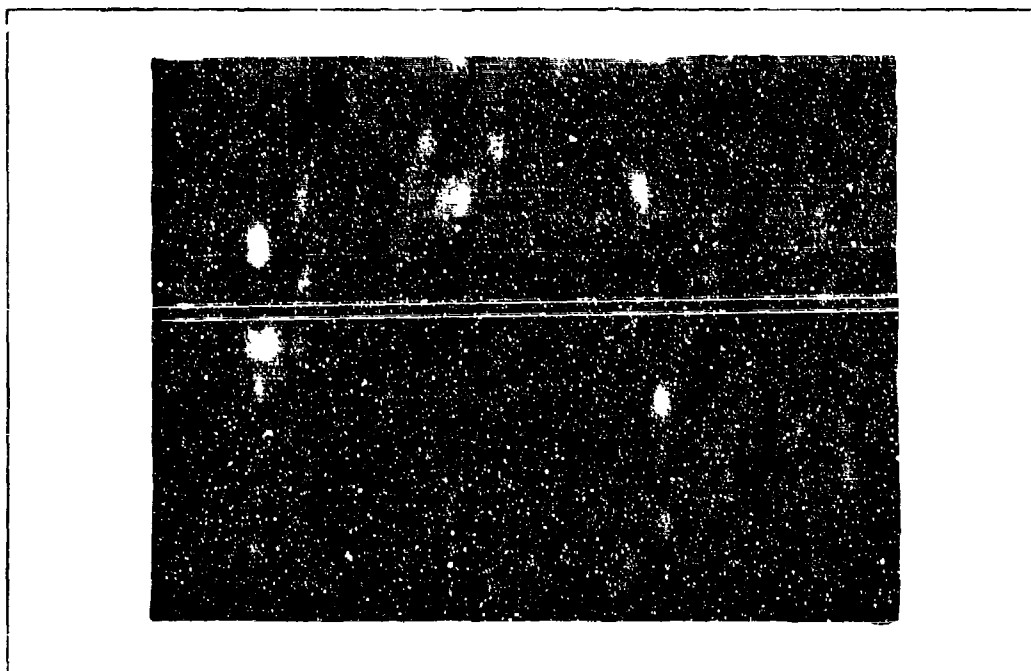


Figure 107. Run 45 Schlieren Photo with $p_{oj} = 20$ psia

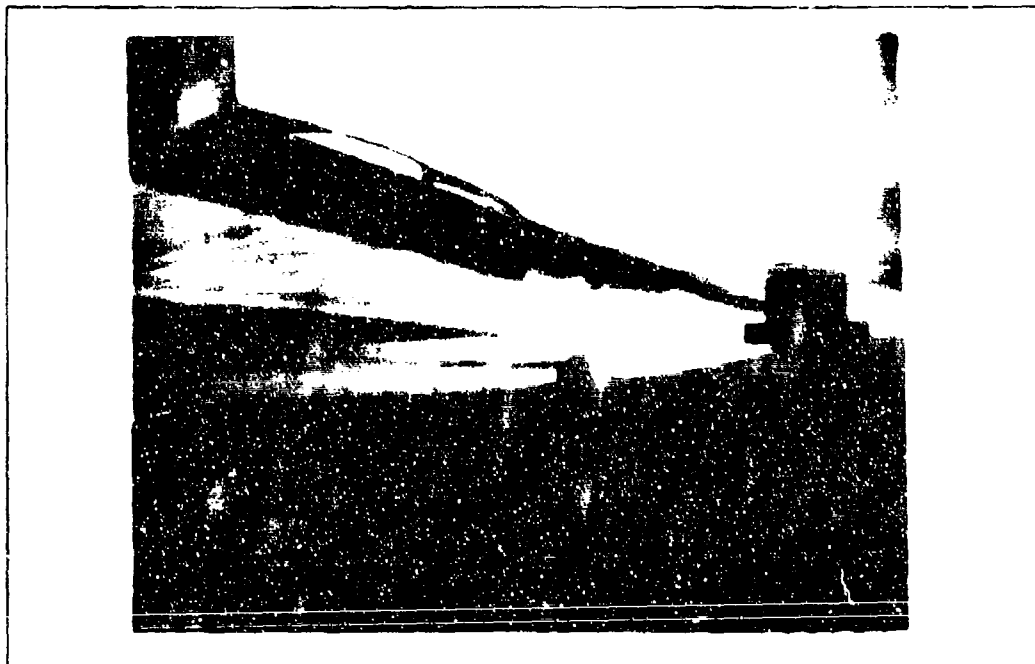


Figure 108. Run 51 Schlieren Photo with $p_{oj} = 0$ psia

Appendix G

C/L Static Pressure Distribution Plots

These plots show the wall static pressure along the centerline of the model from the slot exit ($x=12$ in) to about 1.5 in aft of the shoulder. This length varied depending on the number of inserts in the model. The position of the shoulder is designated by SHR. Two plots were generated for a particular run when more than five TMI pressure curves were desired. One should note that PTMI is equivalent to p_{0j} . Also note that single curve plots of C/L static pressure for Runs 3, 5, 8, 10, and 14 appeared in Figures 27, 28, 29, 30, and 31; while multiple curve plots for Runs 19, 35, and 32 were shown in Figures 42, 43, and 44.

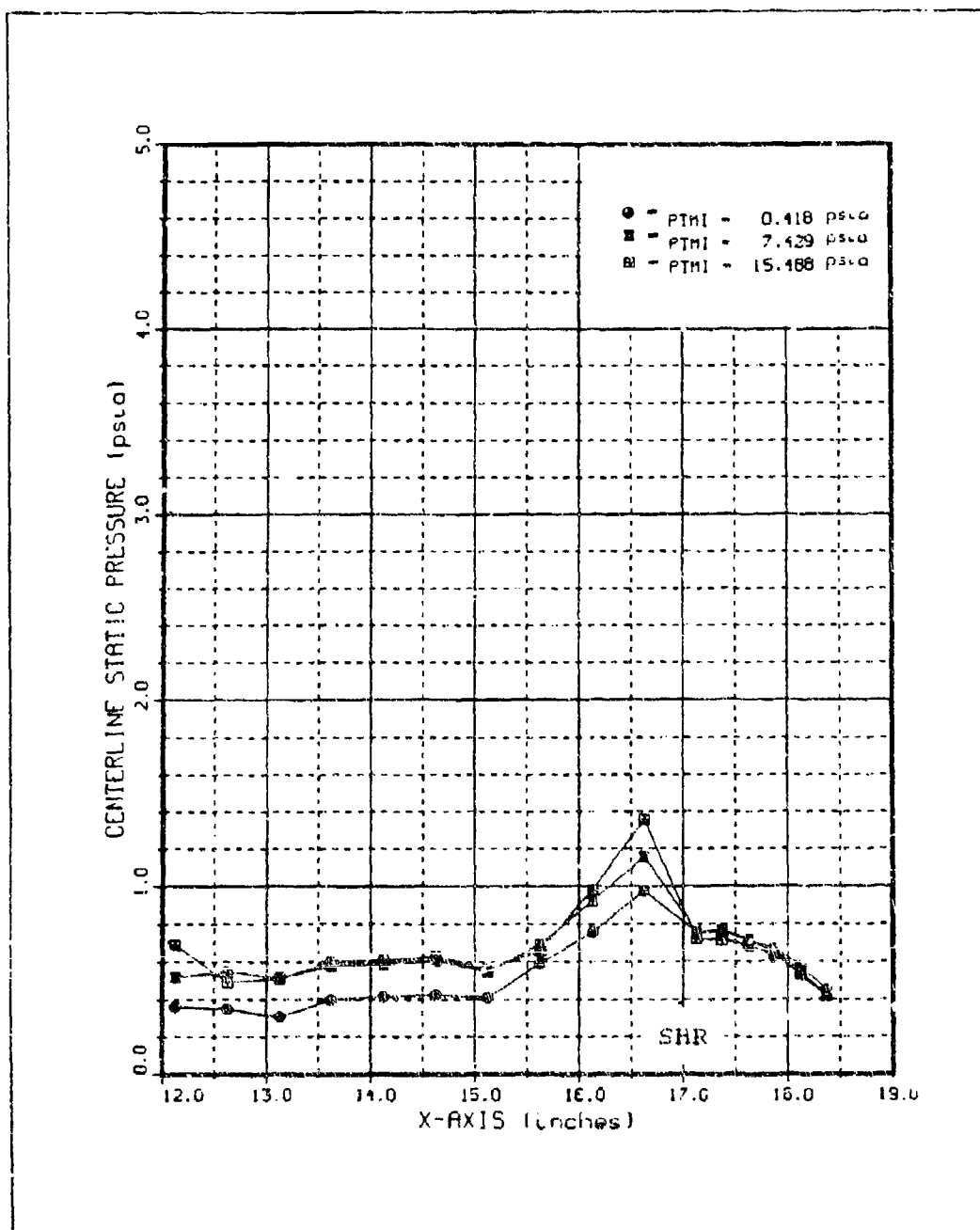


Figure 109. Runs 9,11,12 C/L Static Pressure Distributions

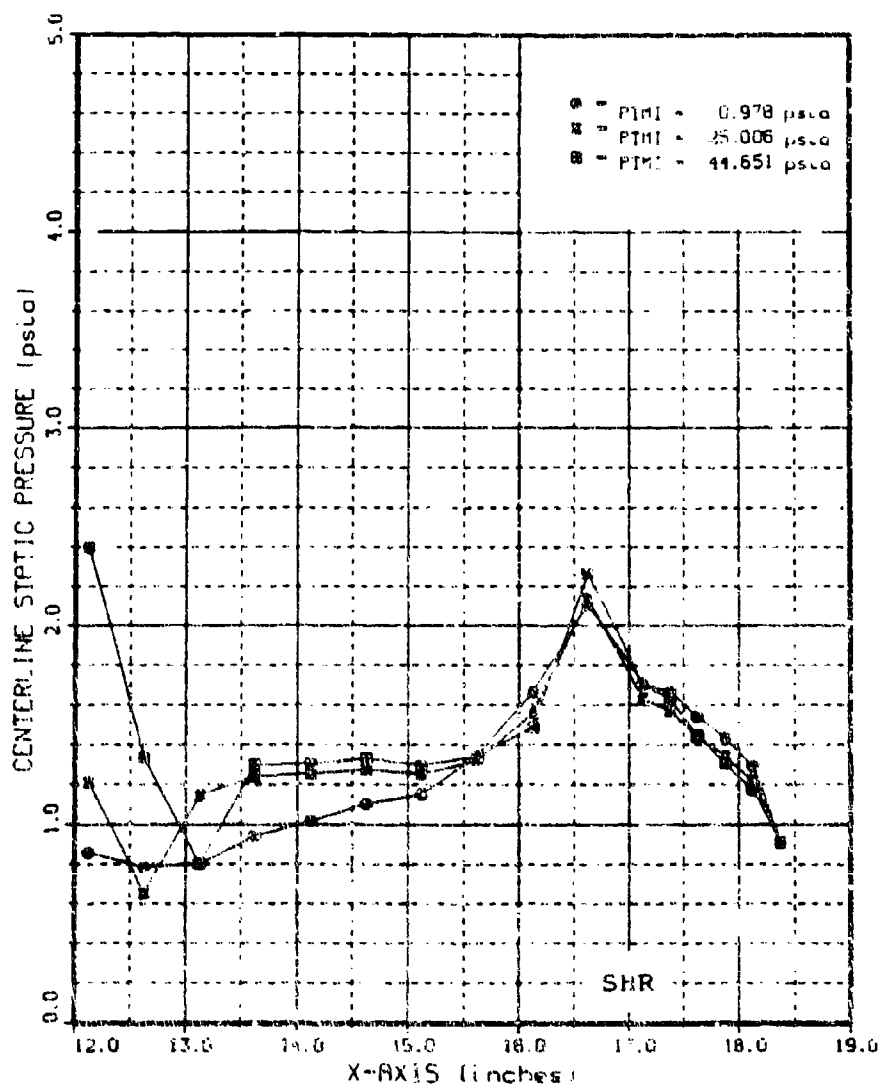


Figure 110. Runs 10,13,14 C/L Static Pressure Distributions

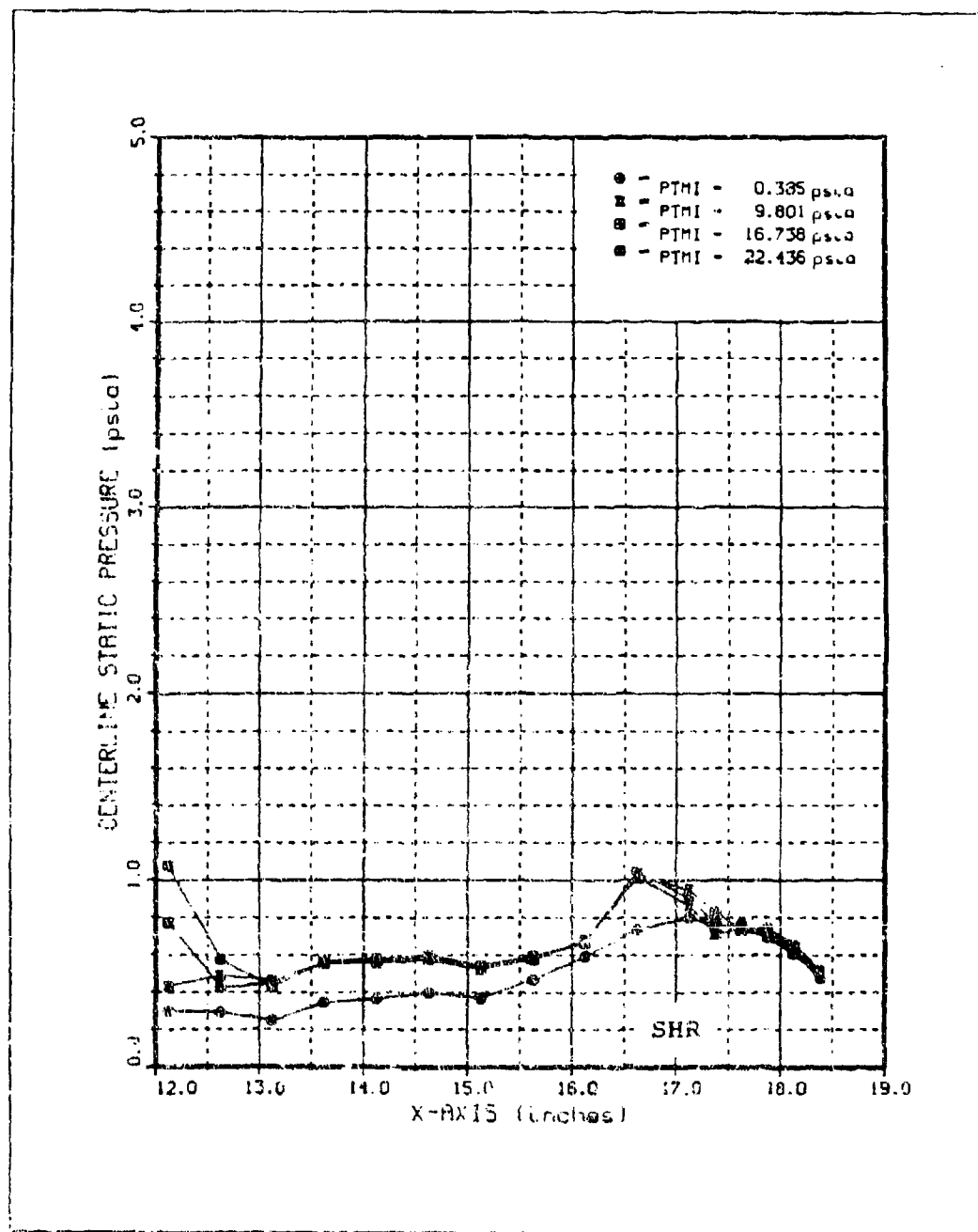


Figure 111. Run 15 C/L Static Pressure Distributions

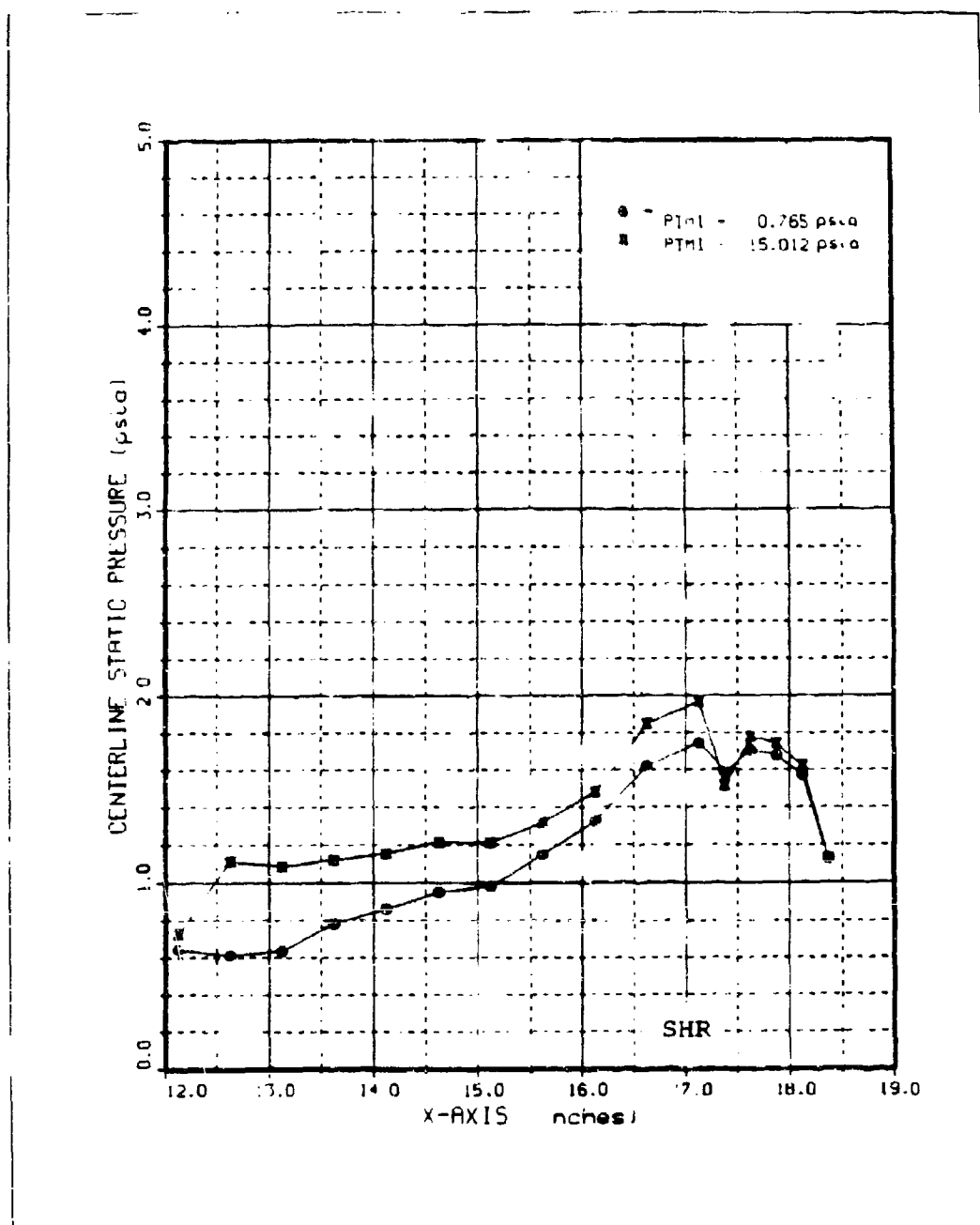


Figure 112. Run 16 C/L Static Pressure Distributions

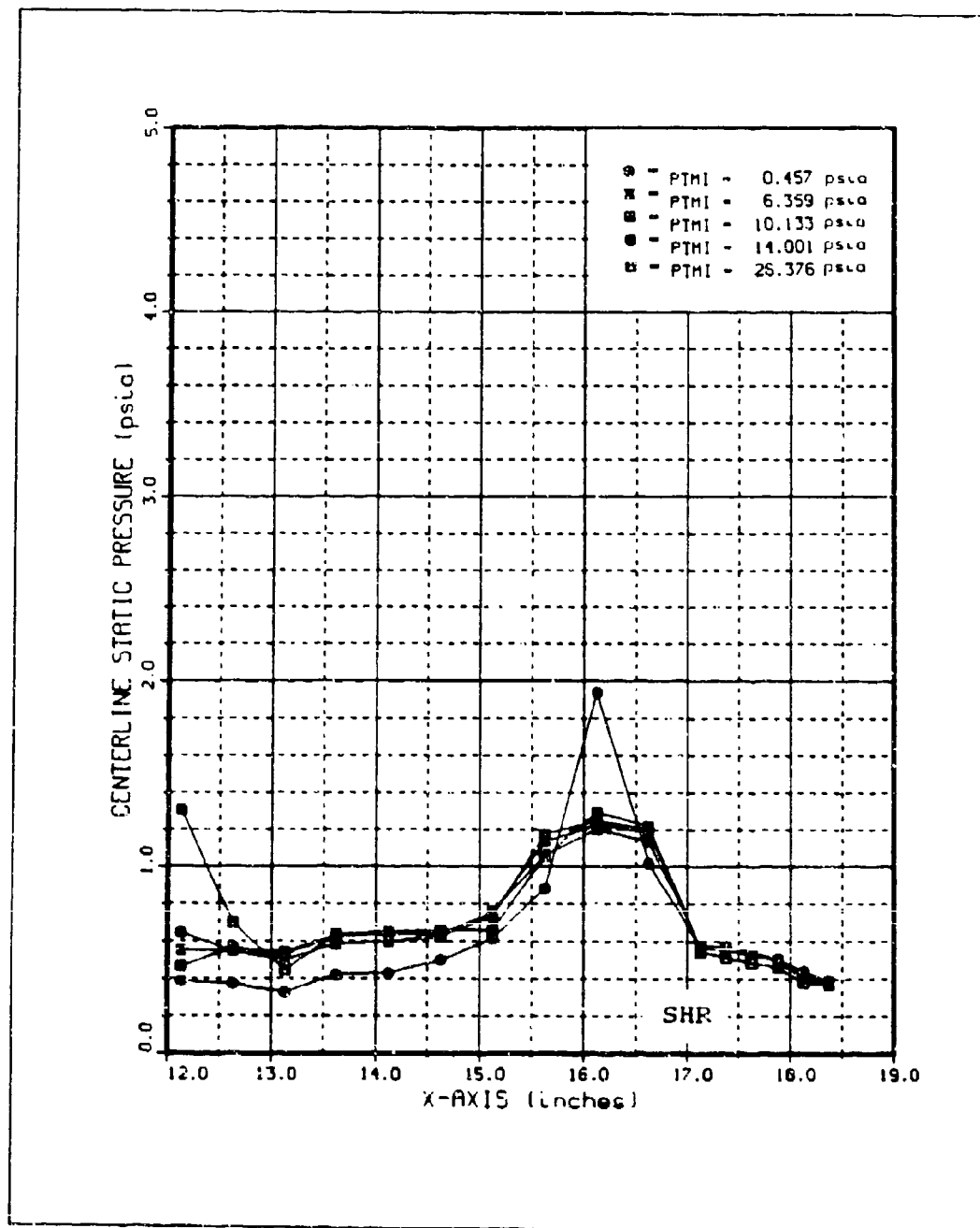


Figure 113. Run 17 C/L Static Pressure Distributions

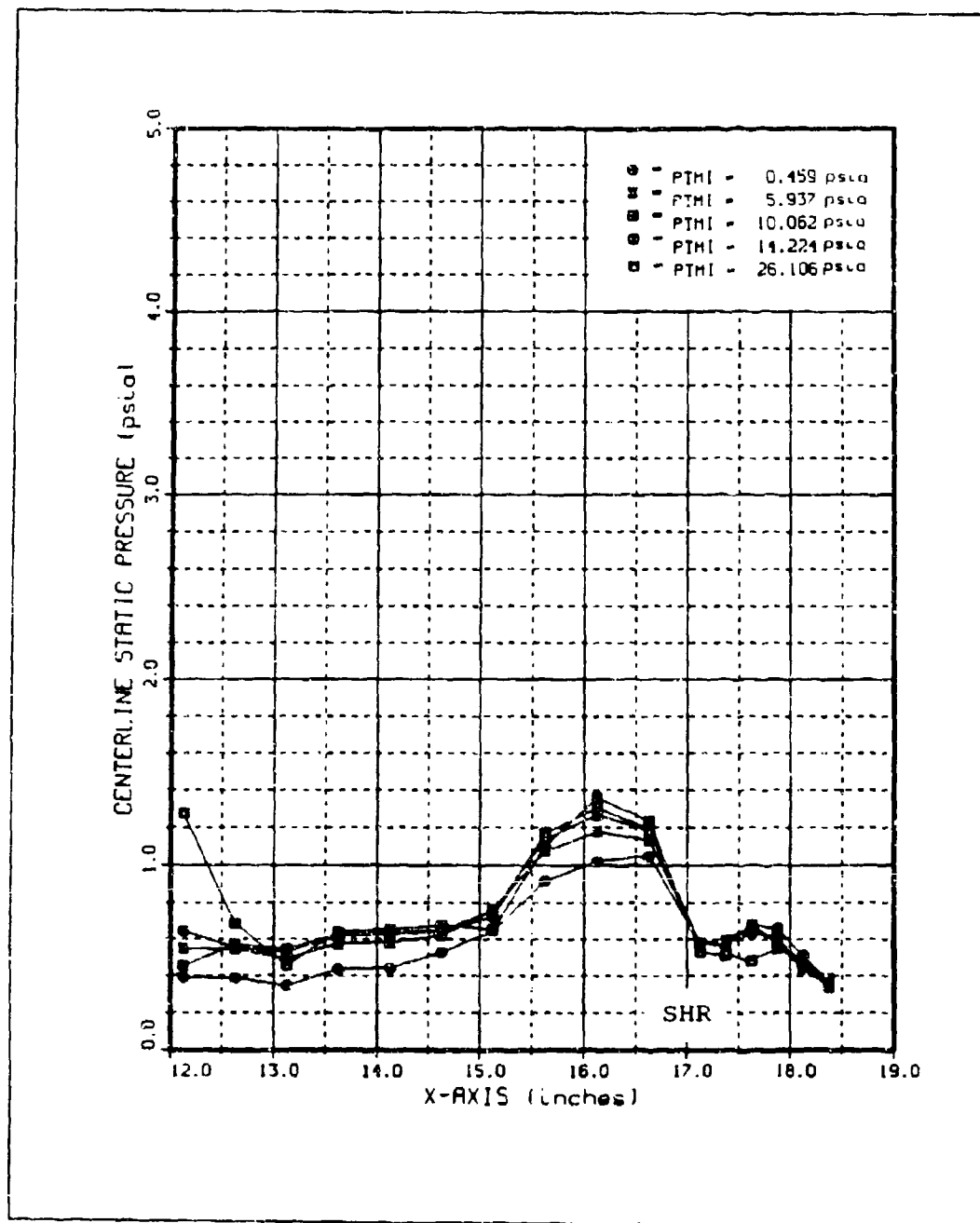


Figure 114. Run 18 C/L Static Pressure Distributions

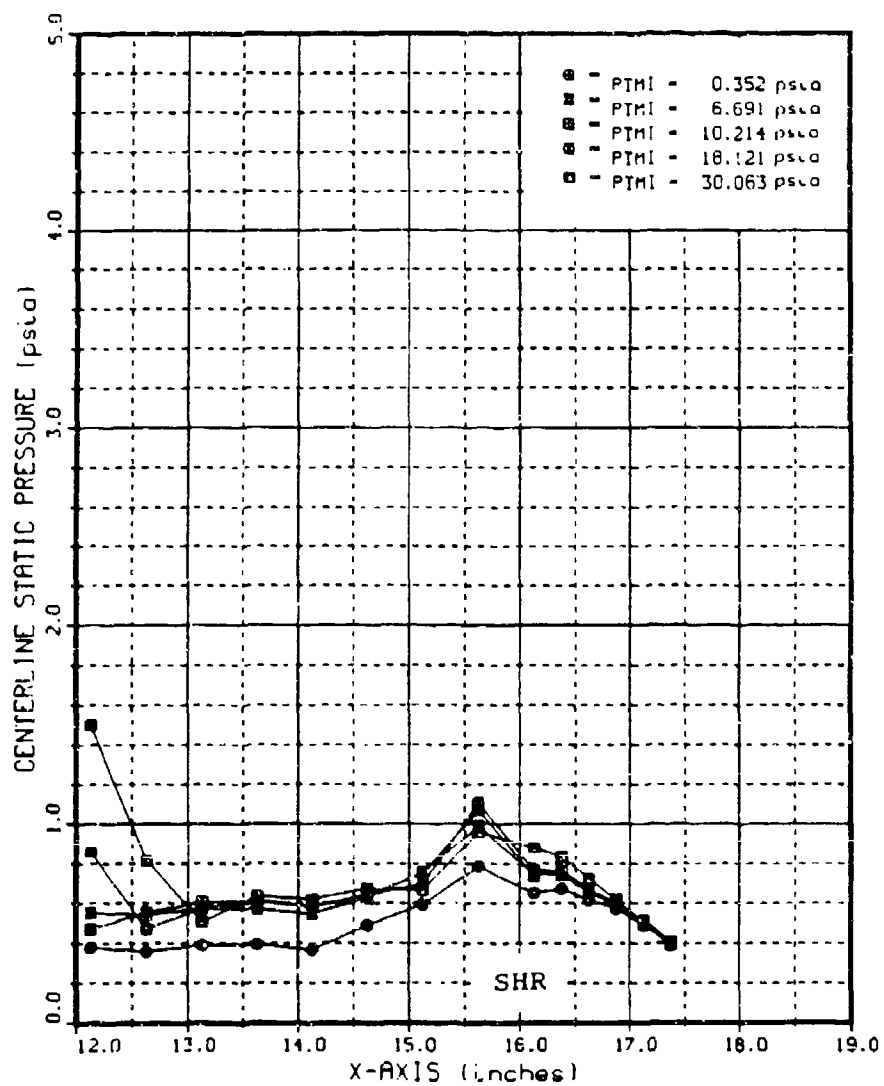


Figure 115. Run 20 C/L Static Pressure Distributions

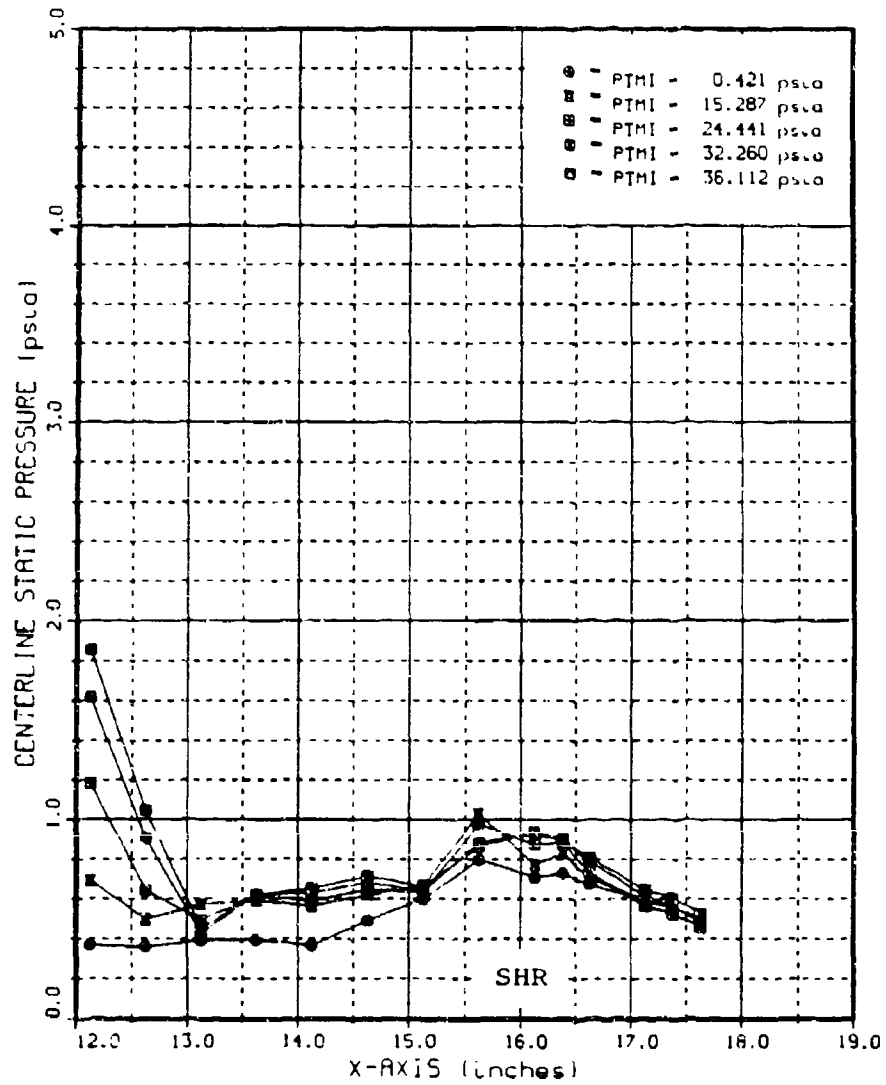


Figure 116. Run 56 C/L Static Pressure Distributions

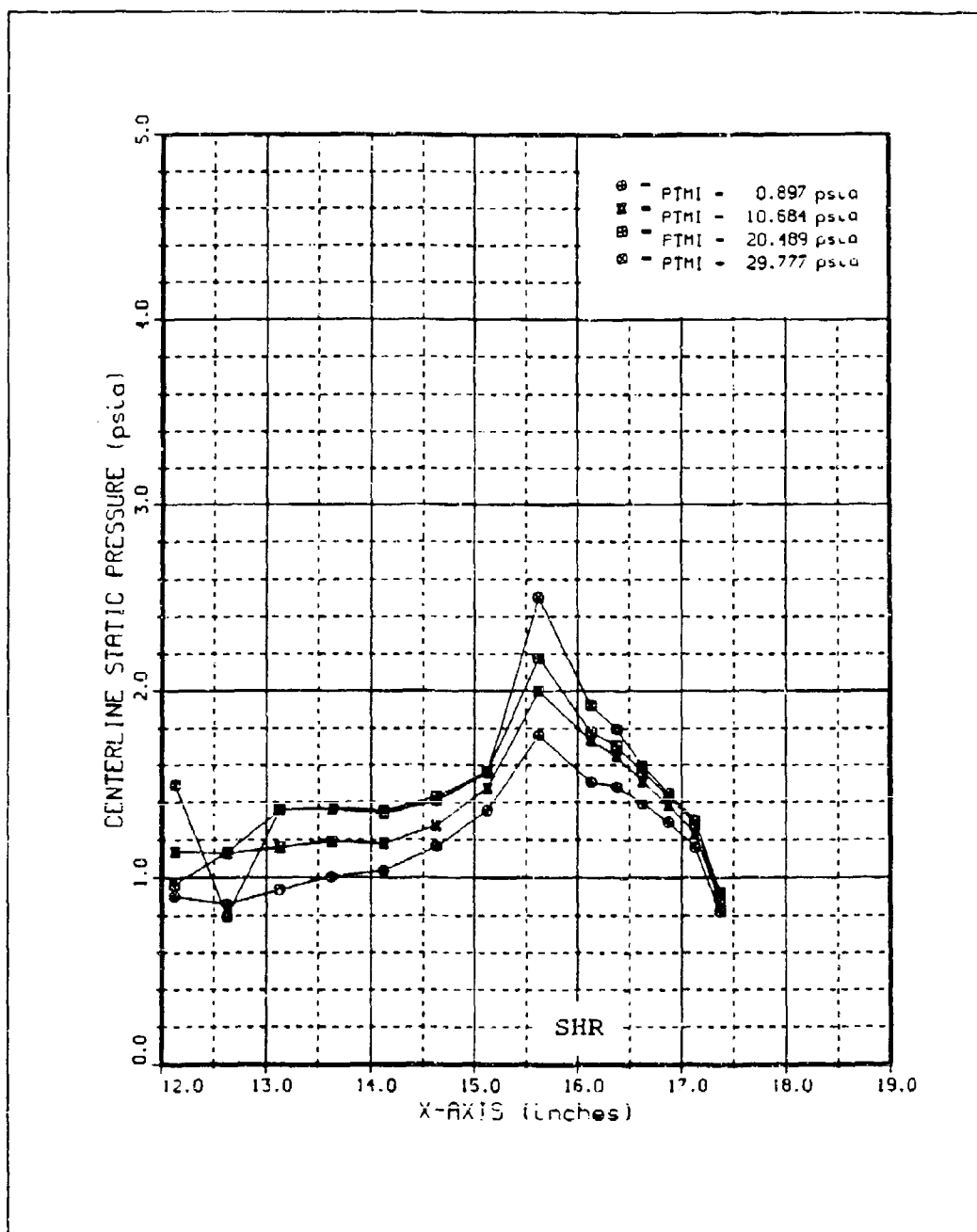


Figure 117. Run 21 C/L Static Pressure Distributions

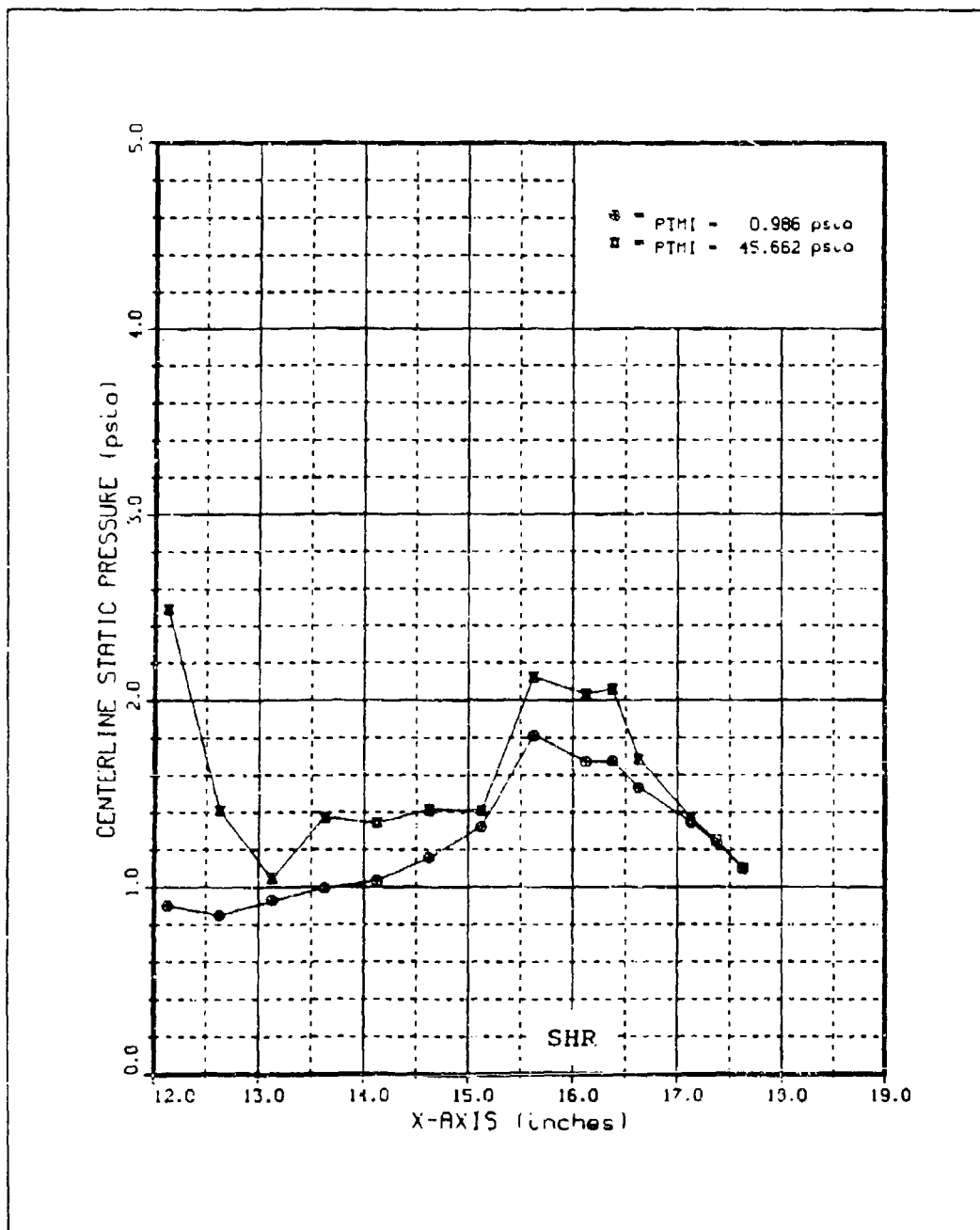


Figure 118. Run 57 C/L Static Pressure Distributions

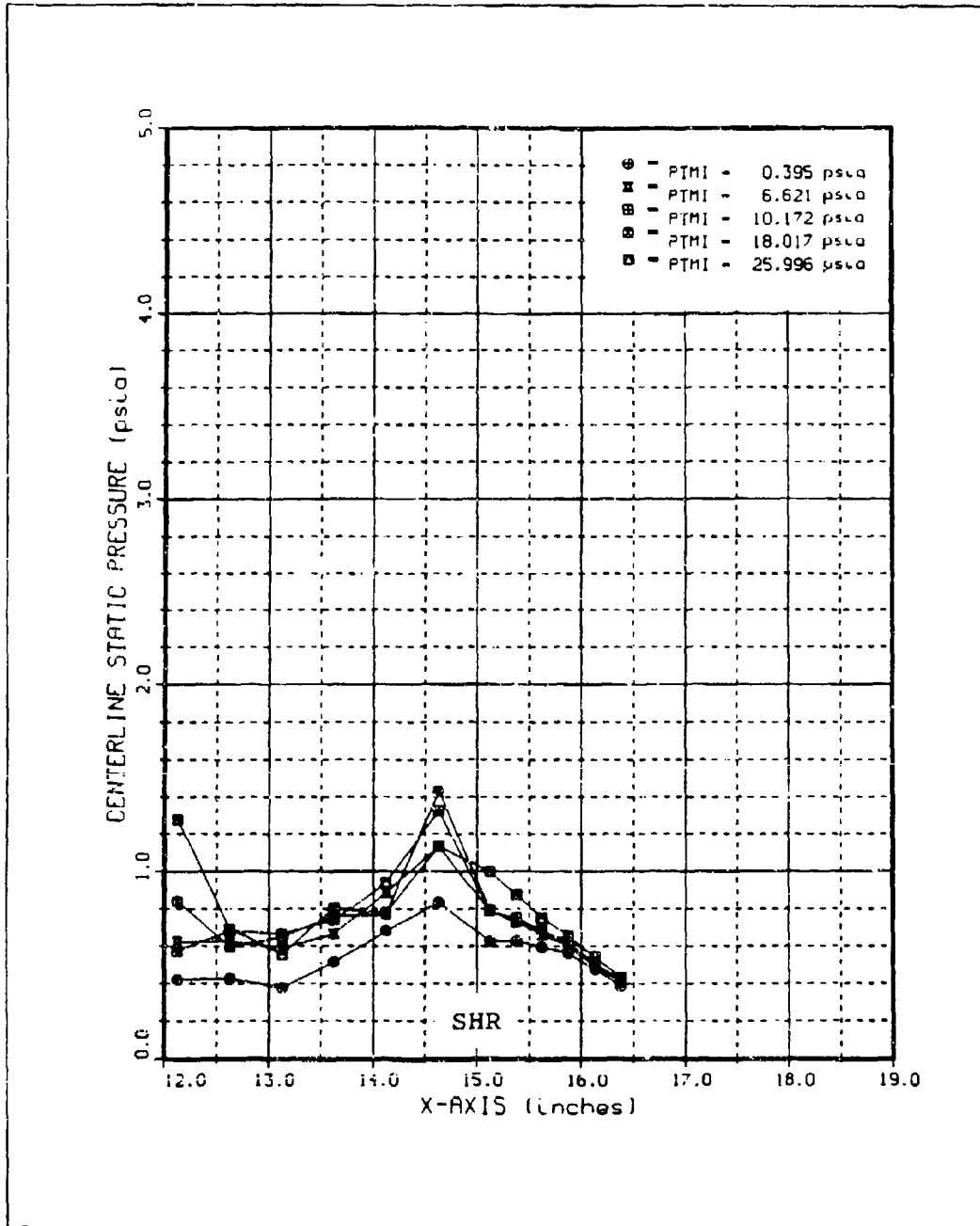


Figure 119. Run 22 C/L Static Pressure Distributions

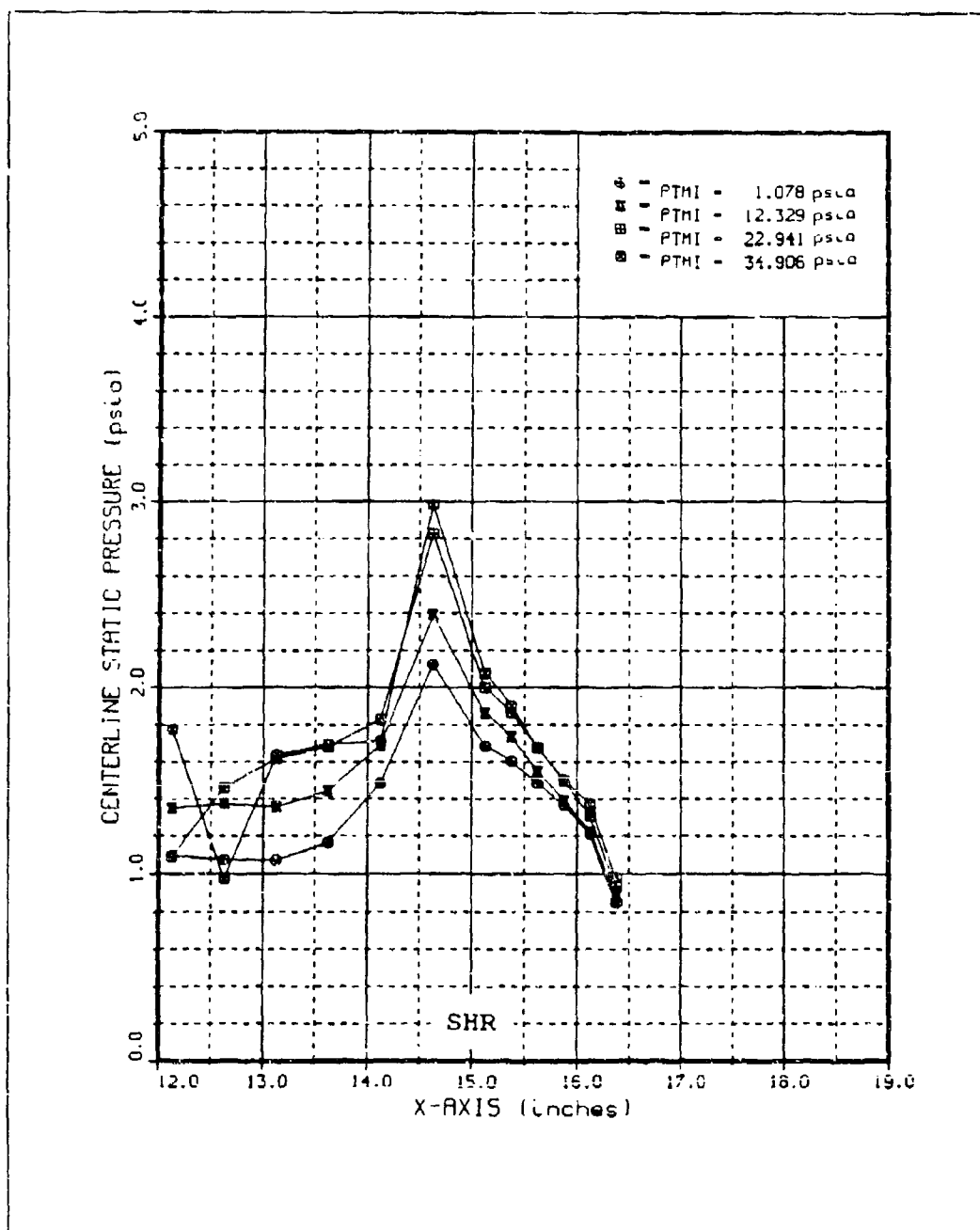


Figure 120. Run 23 C/L Static Pressure Distributions

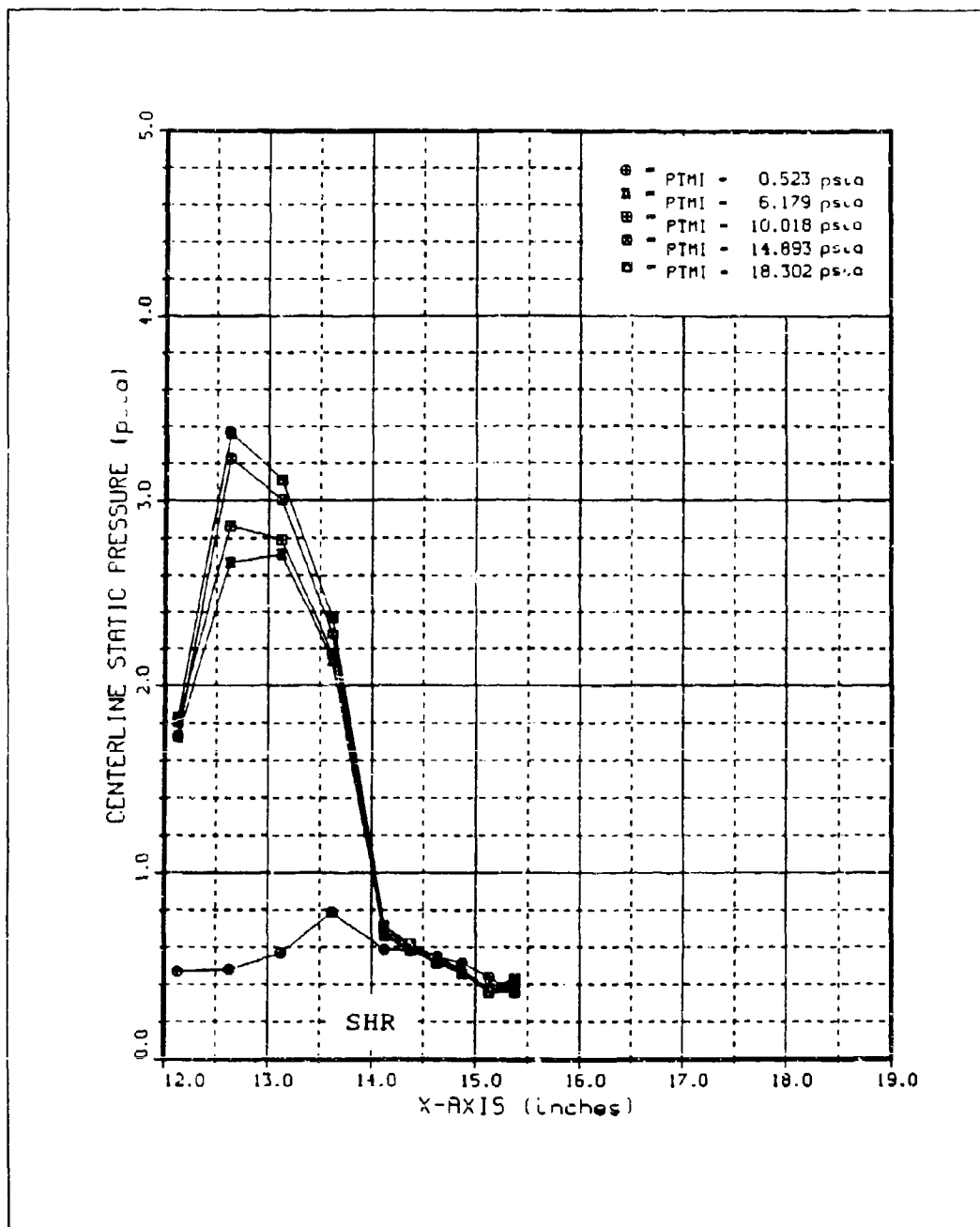


Figure 121. Run 24 C/L Static Pressure Distributions

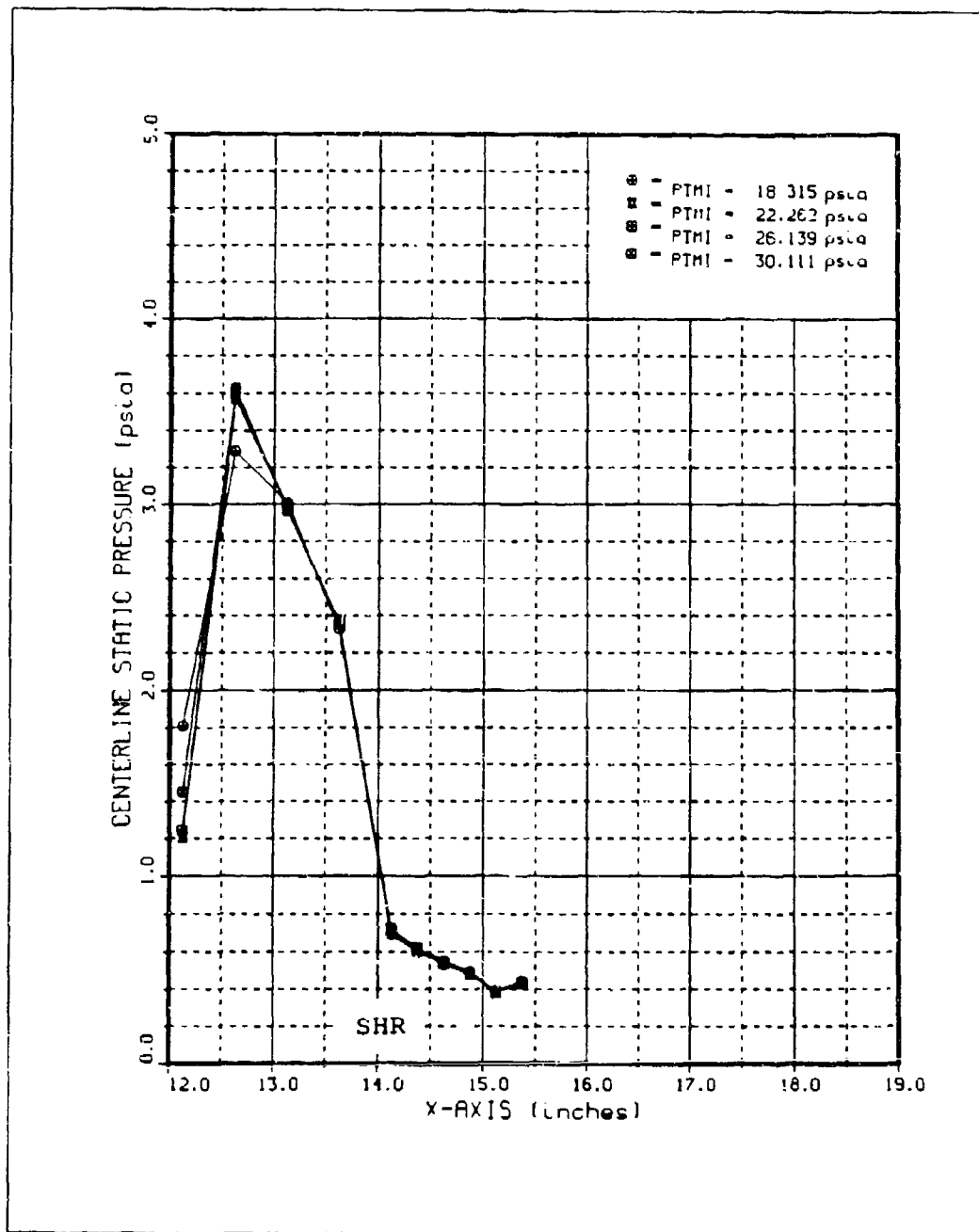


Figure 122. Run 25 C/L Static Pressure Distributions

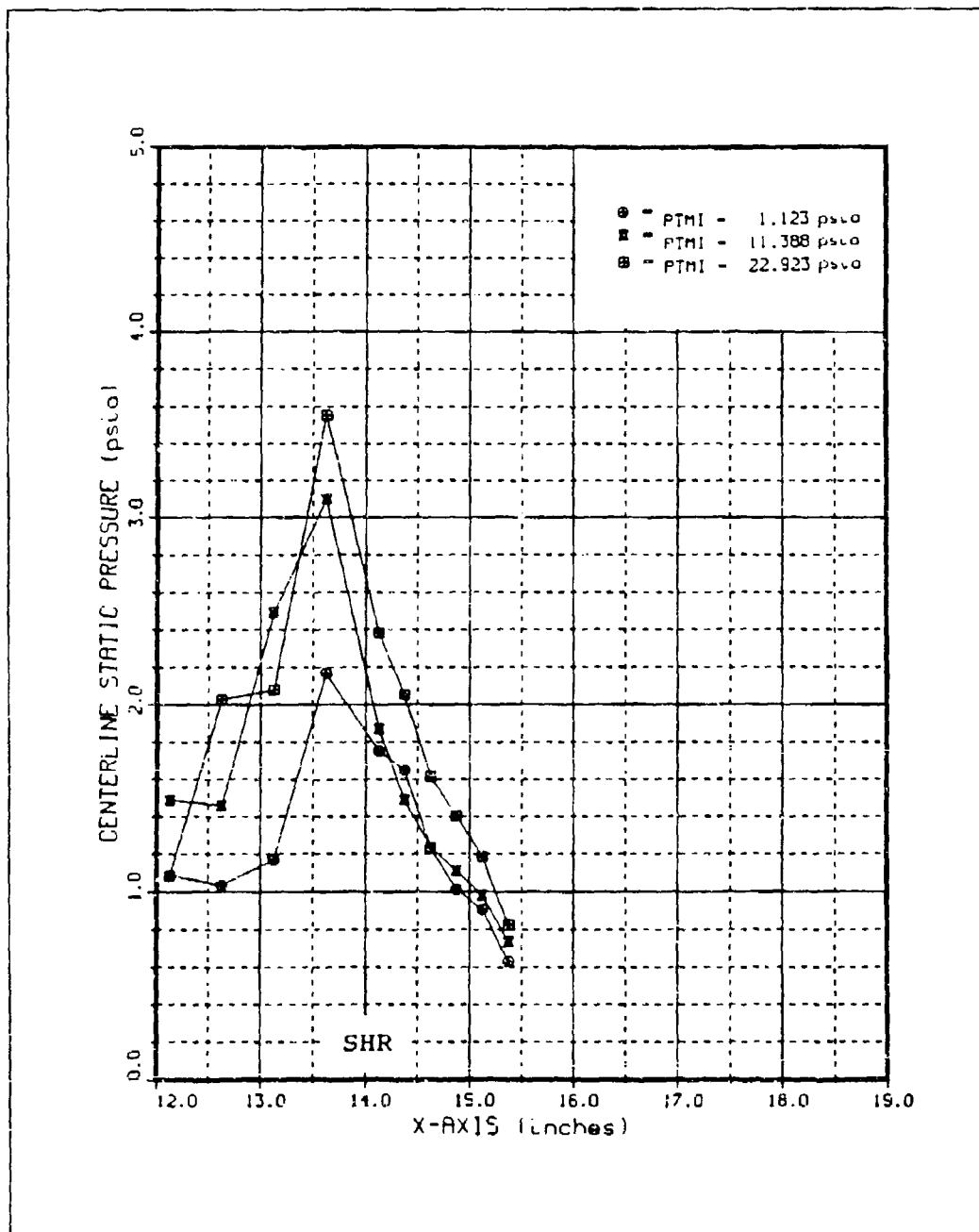


Figure 123. Run 27 C/L Static Pressure Distributions

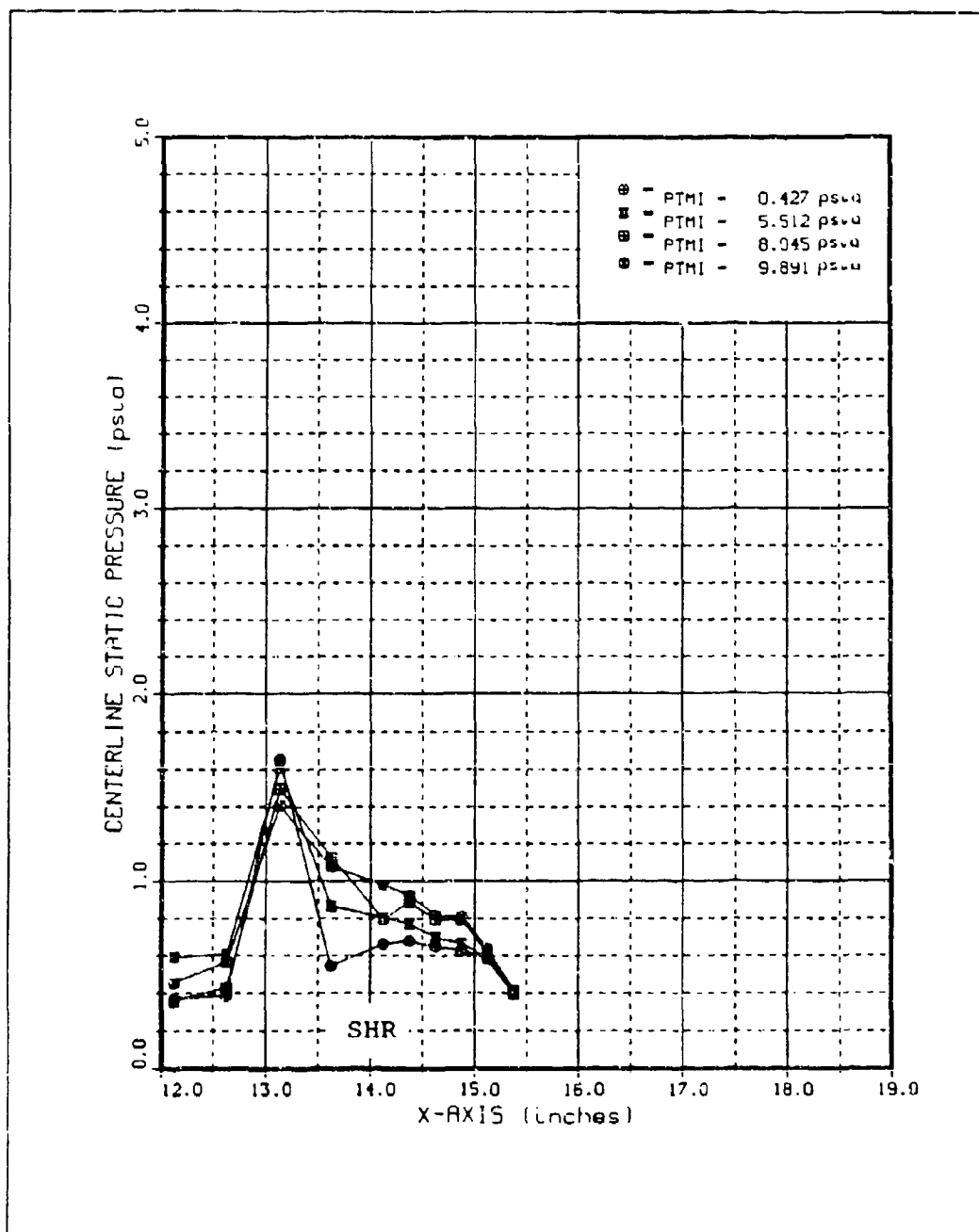


Figure 124. Run 28 C/L Static Pressure Distributions for $p_{oj}=0-10$ psia

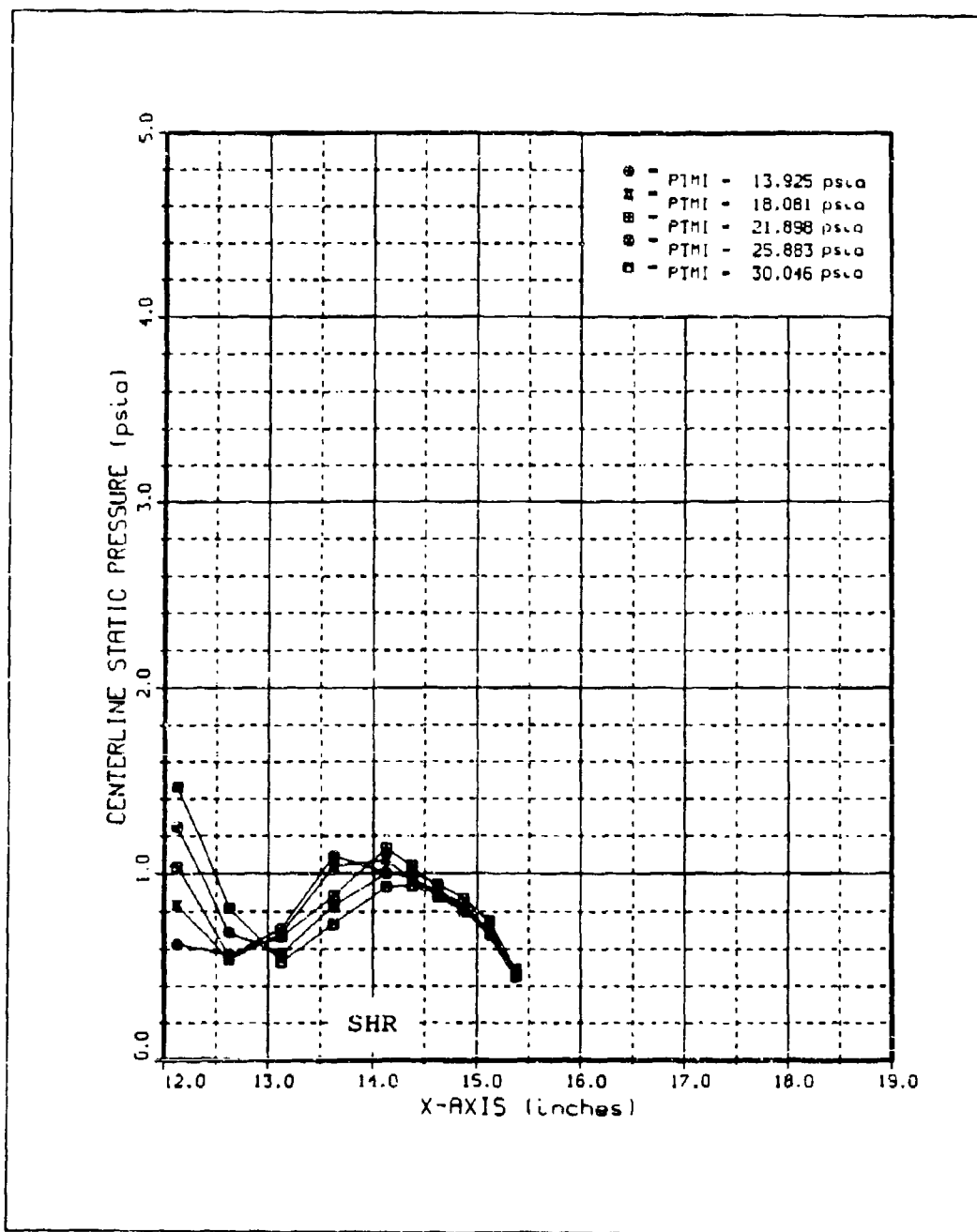


Figure 125. Run 28 C/L Static Pressure Distributions. for $p_{oj}=14-30$ psia

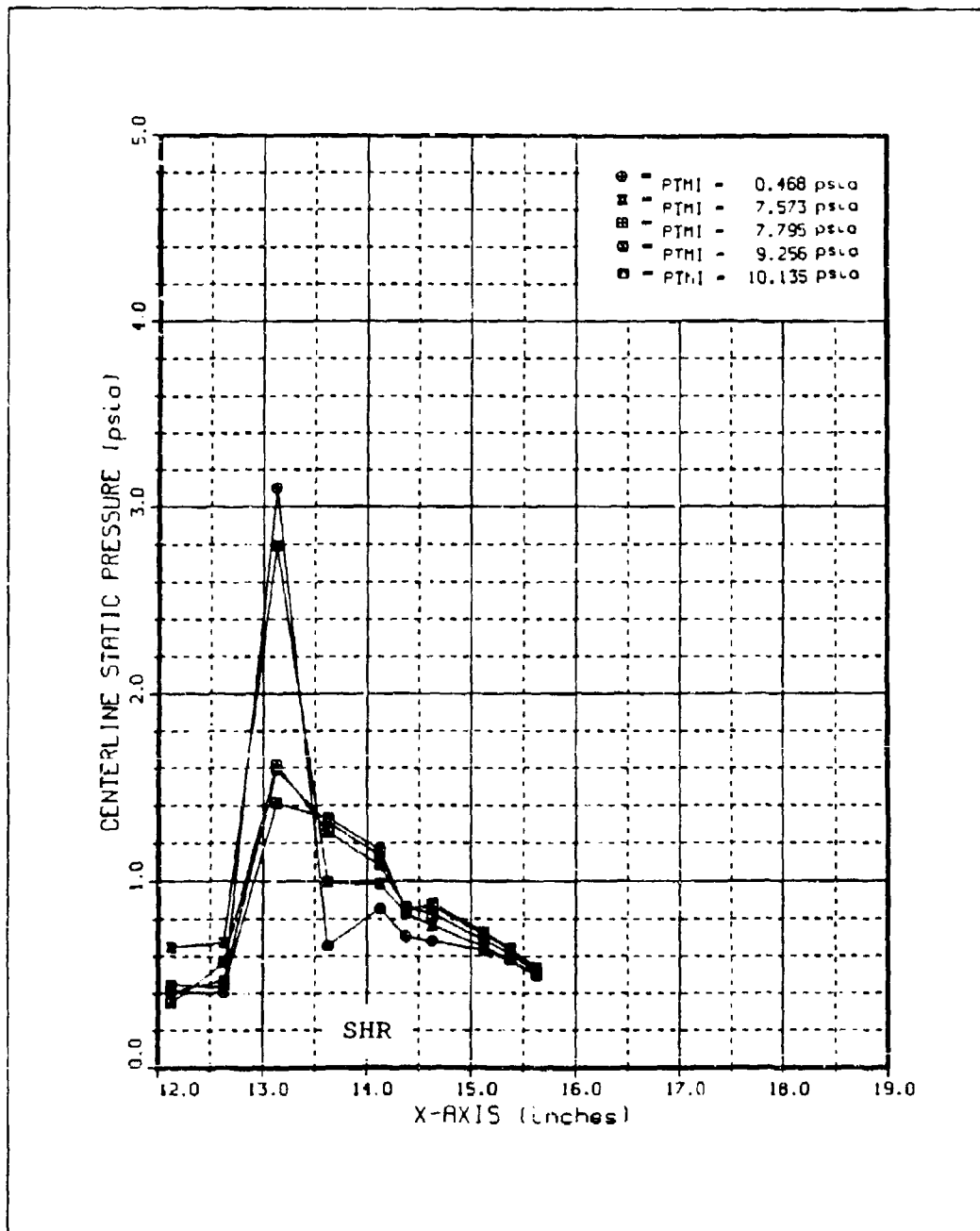


Figure 126. Run 58 C/L Static Pressure Distributions for $p_{0j}=0-10$ psia

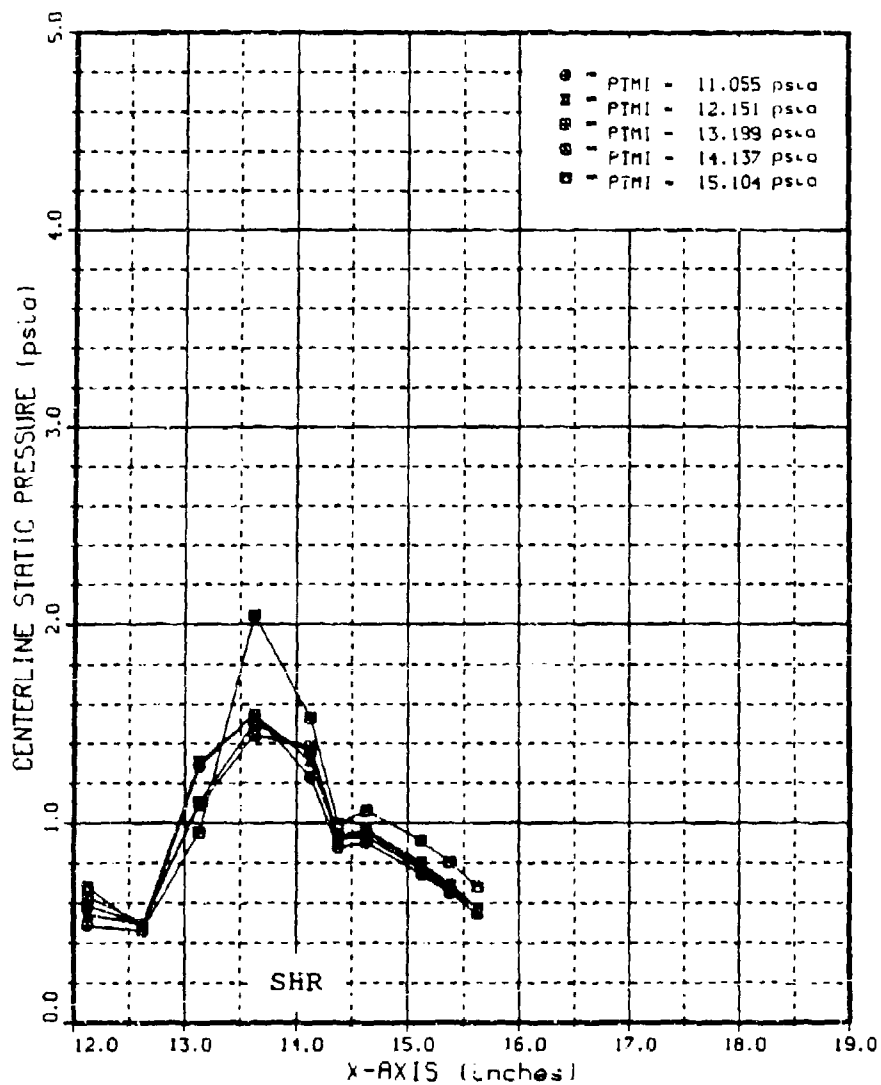


Figure 127. Run 58 C/L Static Pressure Distributions. for $p_{o_j}=11-15$ psia

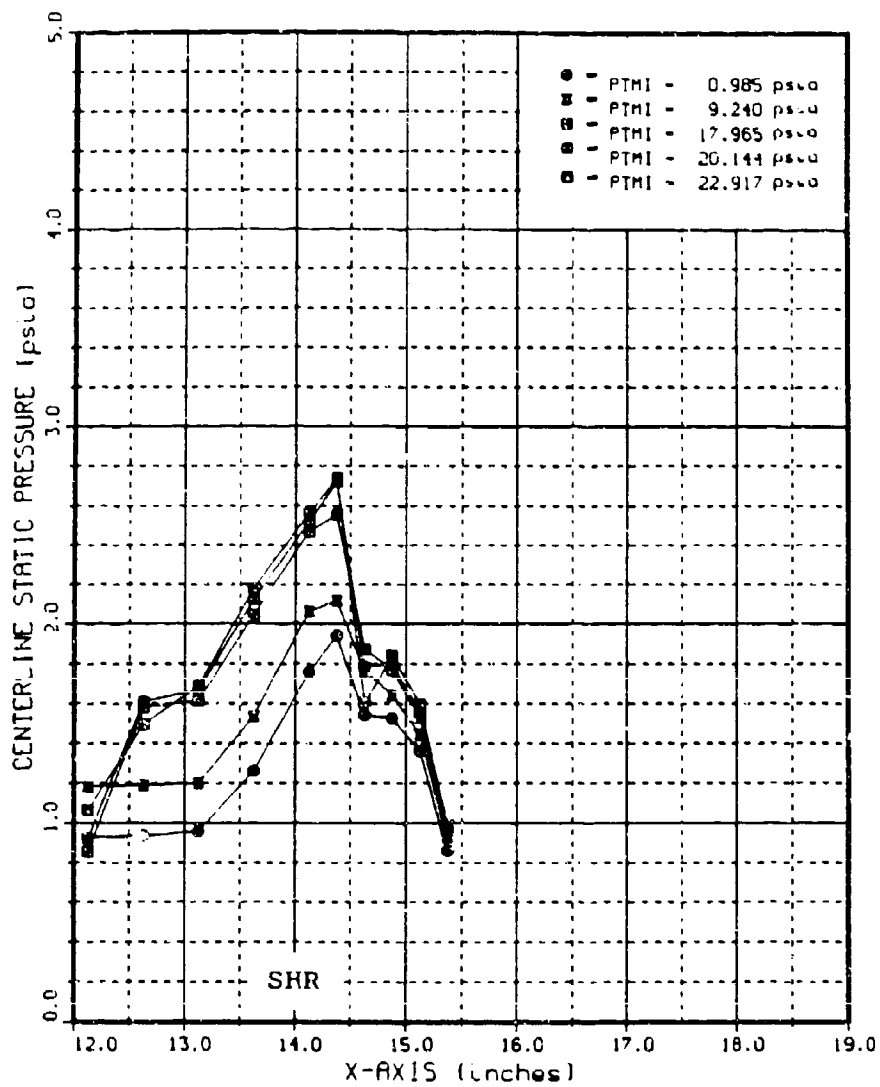


Figure 128. Run 29 C/L Static Pressure Distributions

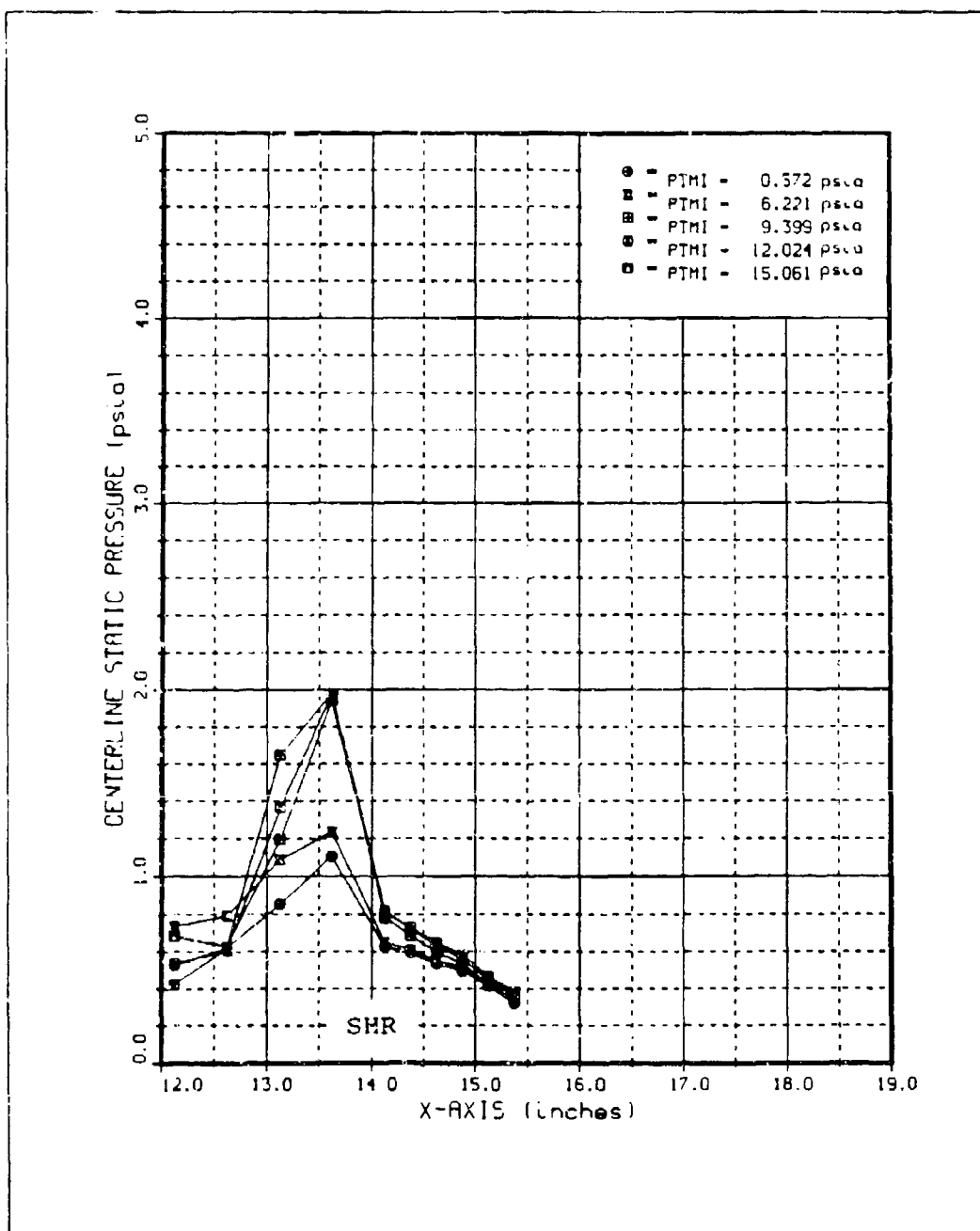


Figure 129. Run 30 C/L Static Pressure Distributions for $p_{0j}=0-15$ psia

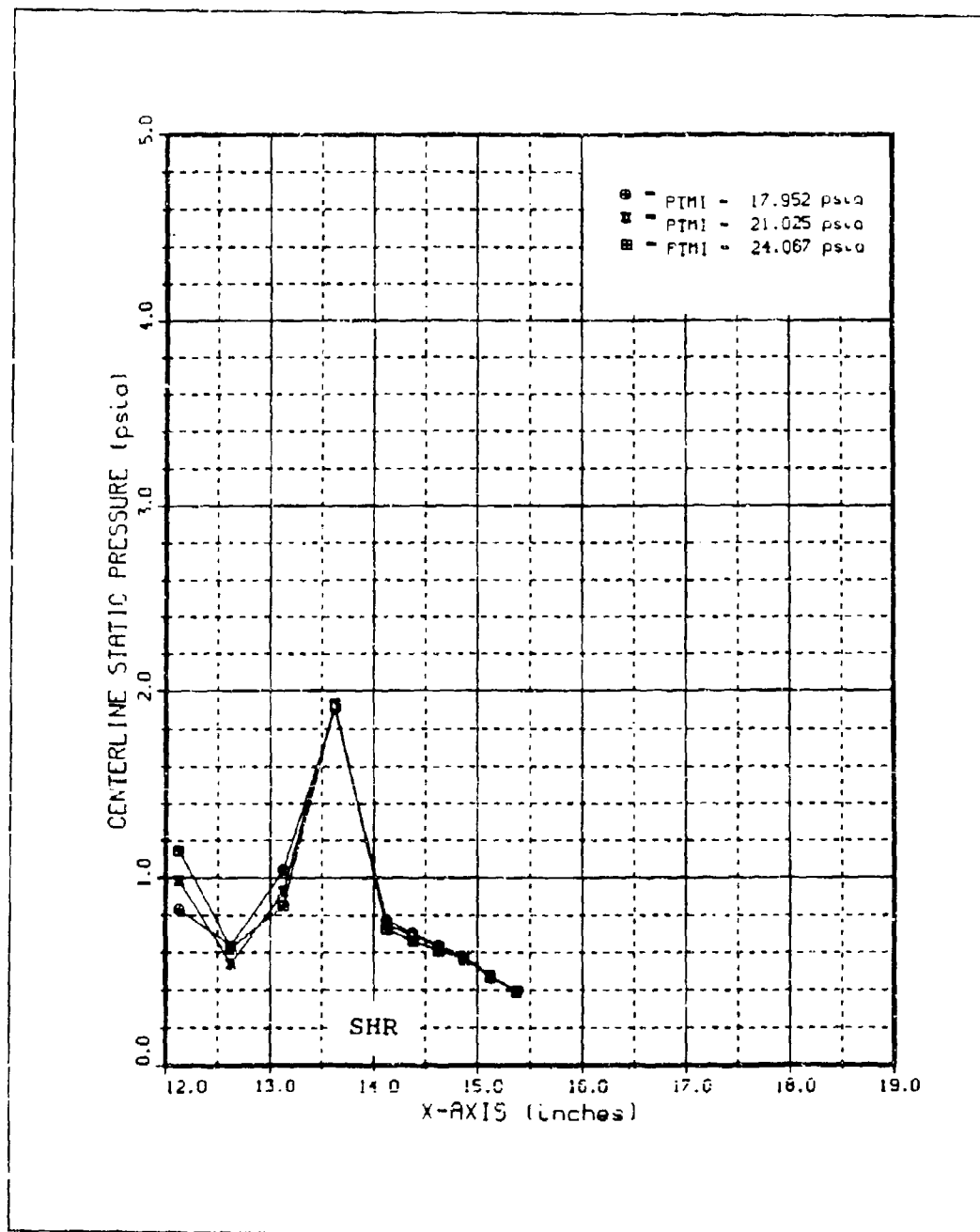


Figure 130. Run 30 C/L Static Pressure Distributions. for $p_{o_j}=18-24$ psia

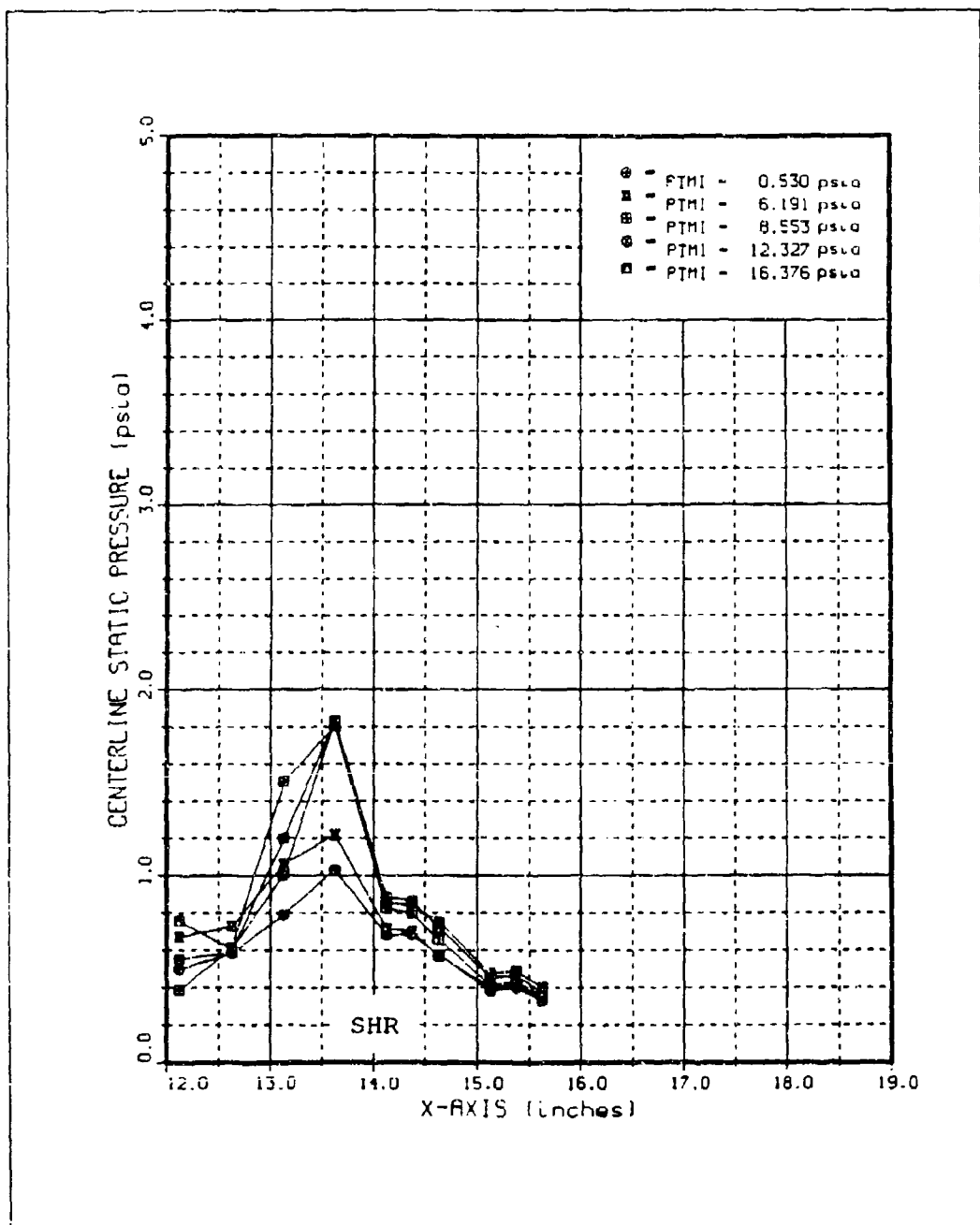


Figure 131. Run 59 C/L Static Pressure Distributions

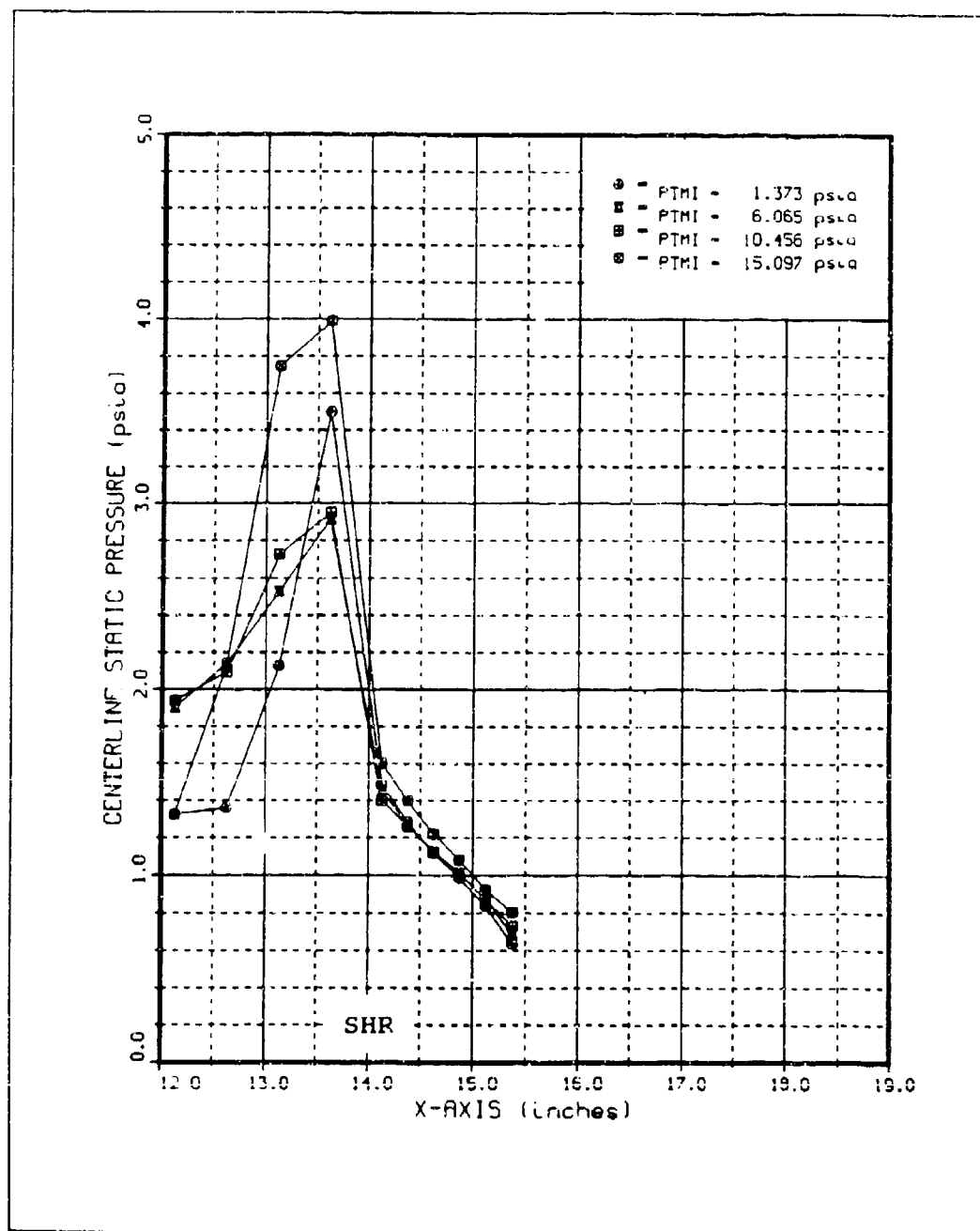


Figure 132. Run 31 C/L Static Pressure Distributions

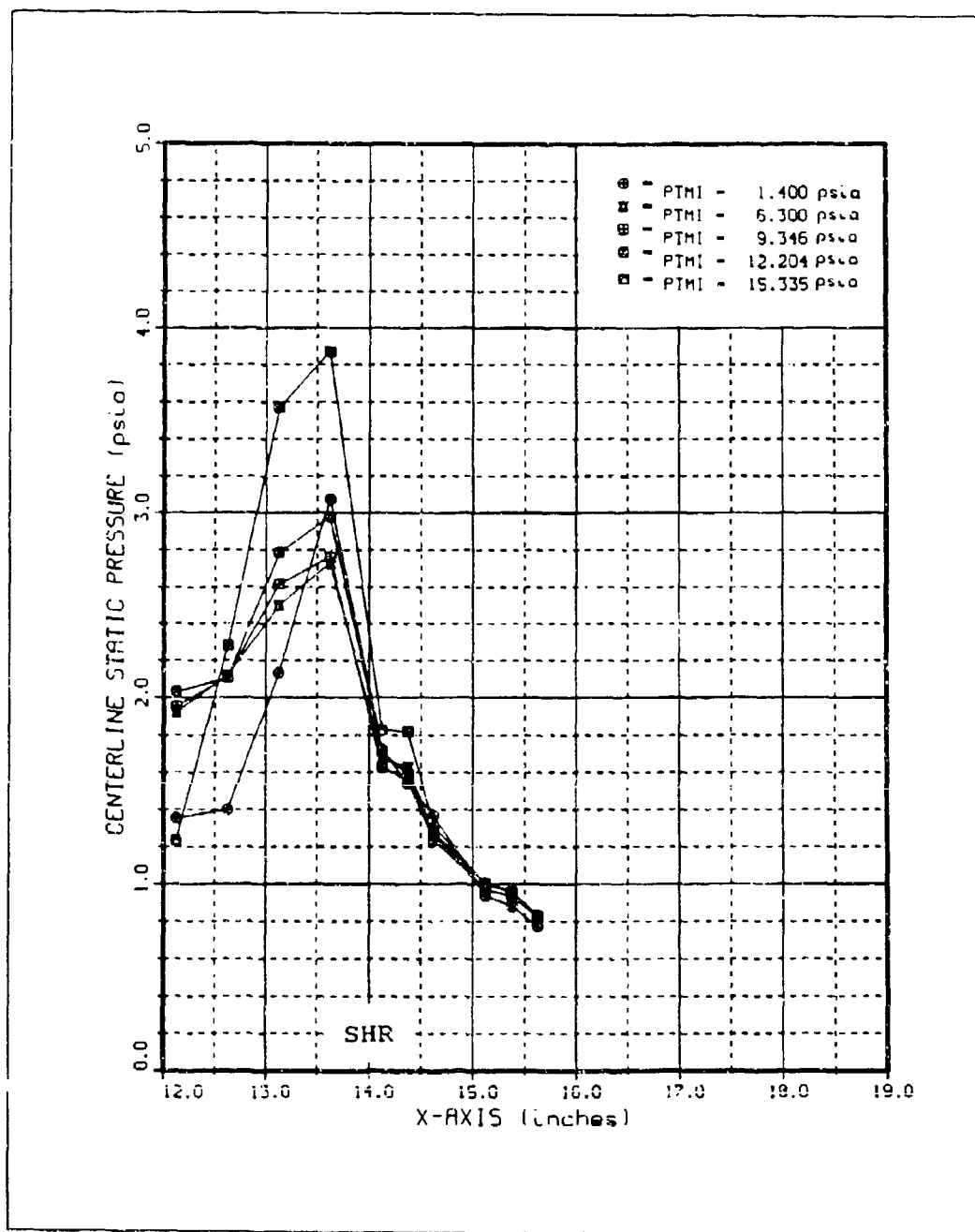


Figure 133. Run 60 C/L Static Pressure Distributions

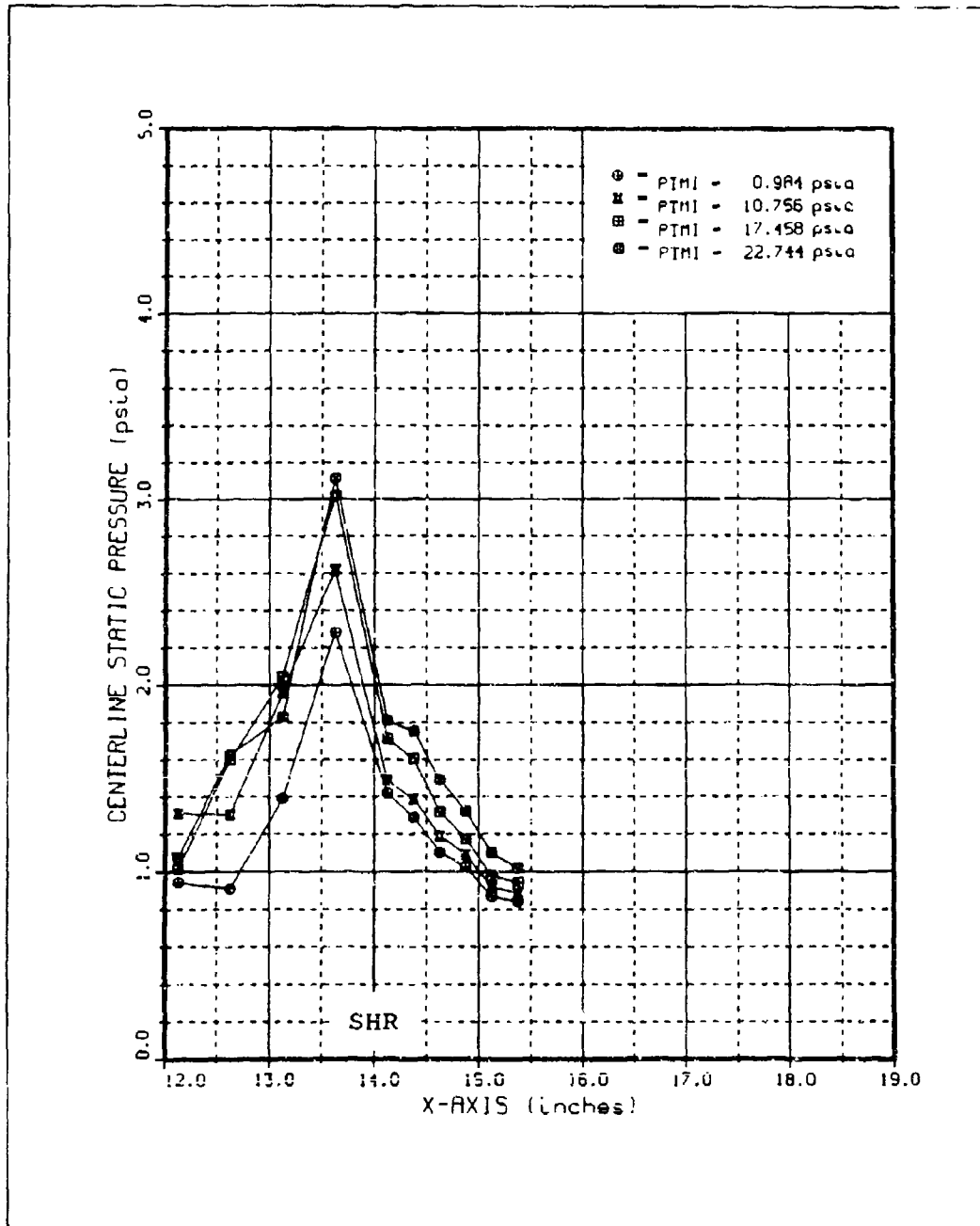


Figure 134. Run 33 C/L Static Pressure Distributions

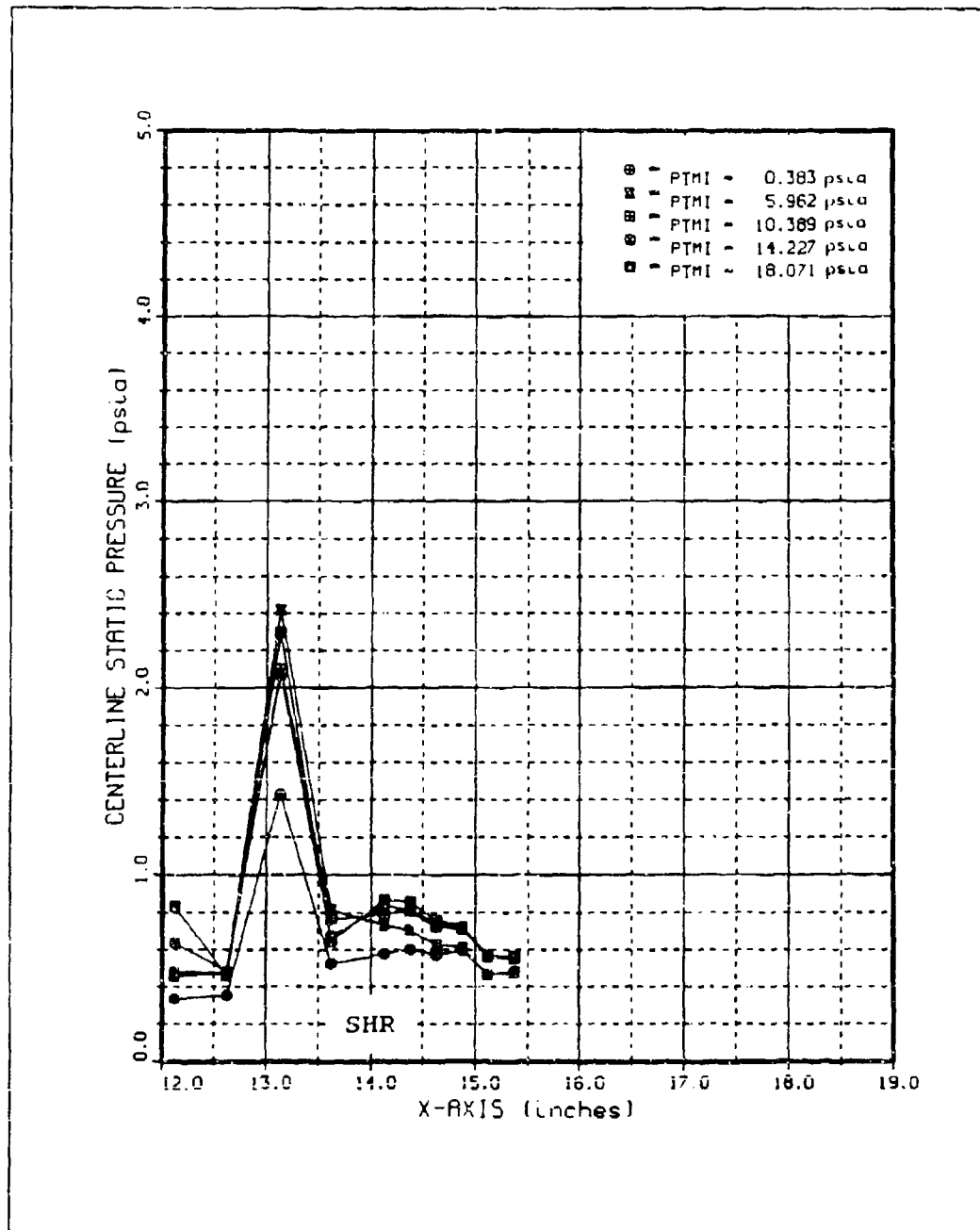


Figure 135. Run 34 C/L Static Pressure Distributions

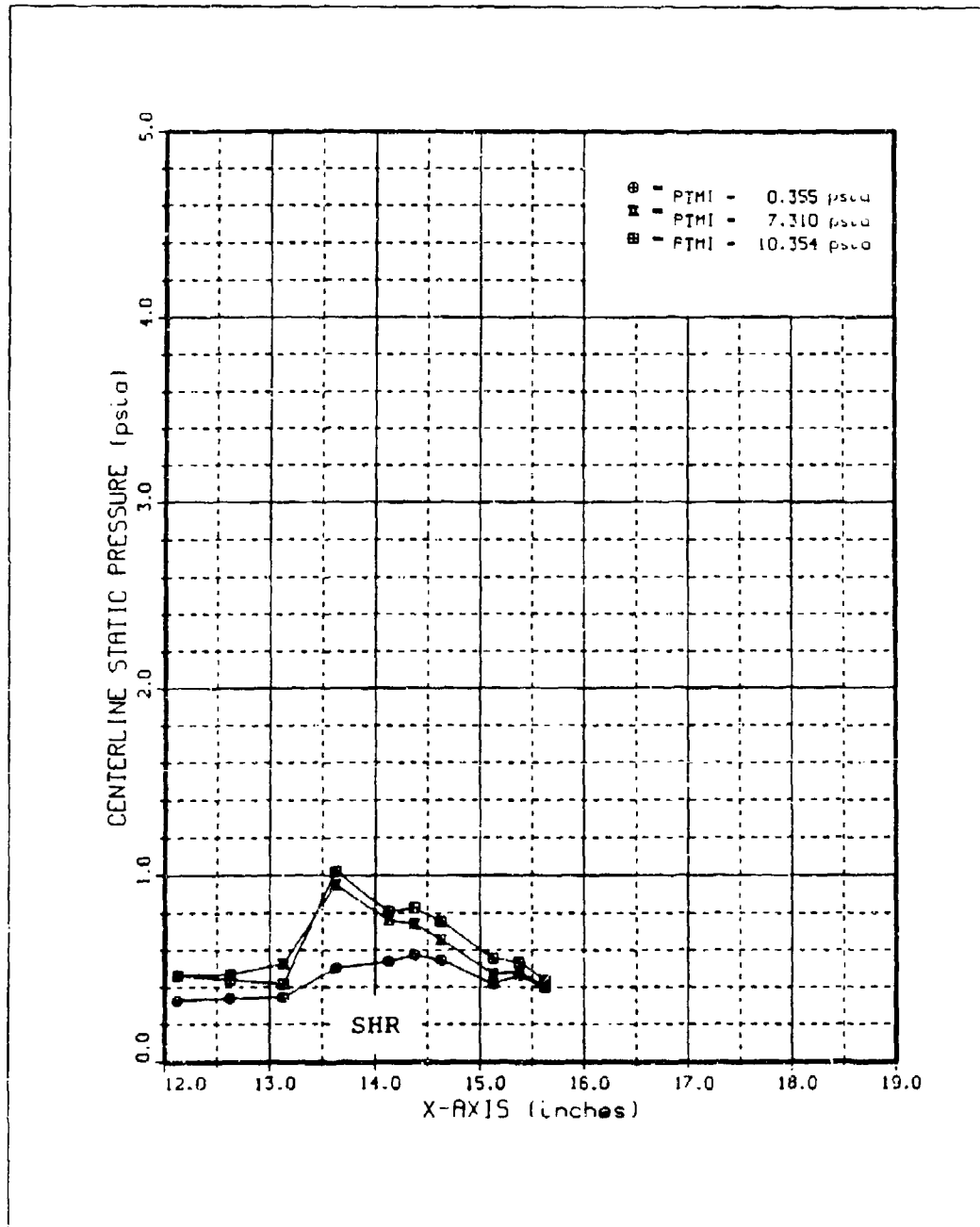


Figure 136. Run 61 C/L Static Pressure Distributions for $p_{0j}=0-10$ psia

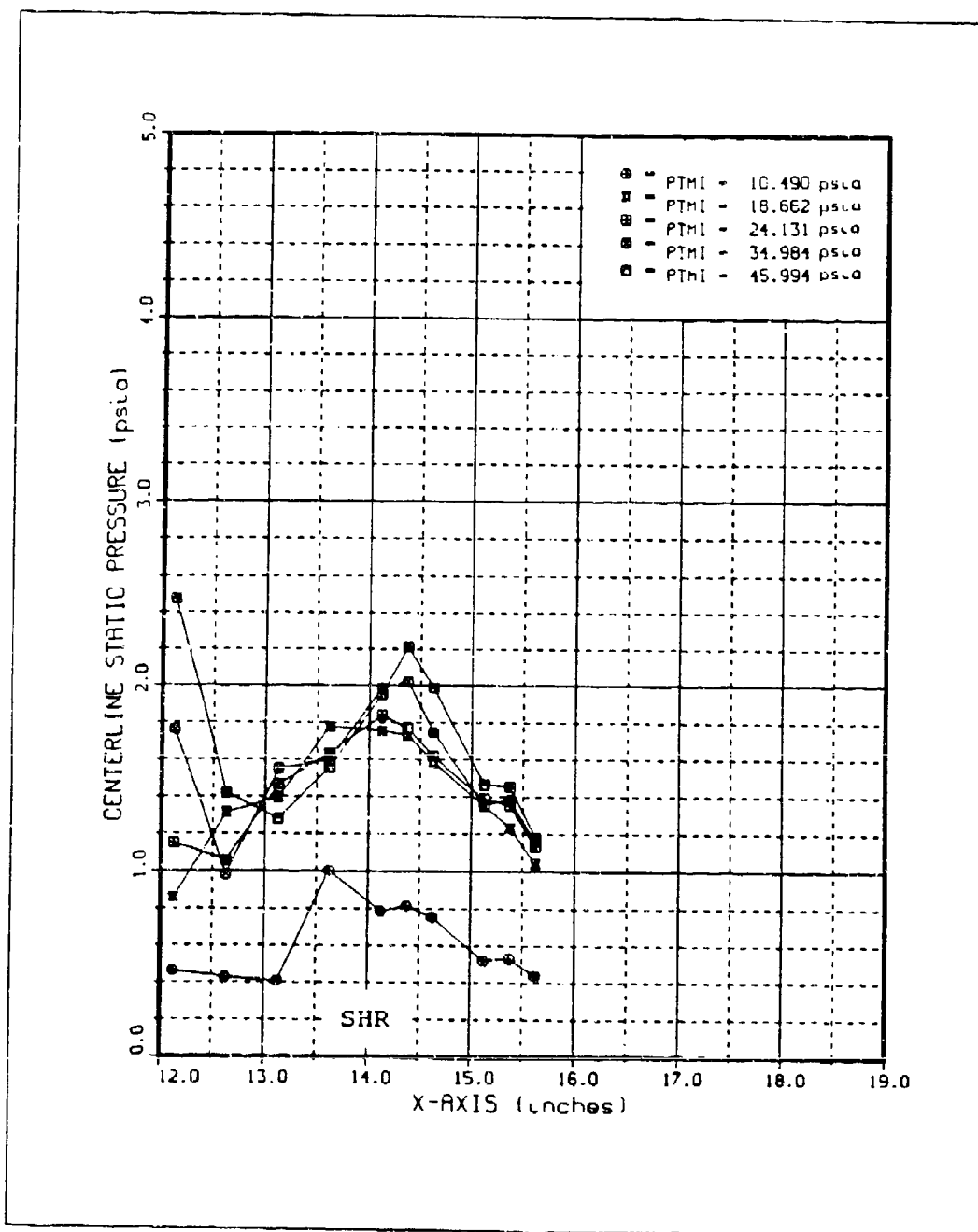


Figure 137. Run 61 C/L Static Pressure Distributions for $p_{0j}=10-46$ psia

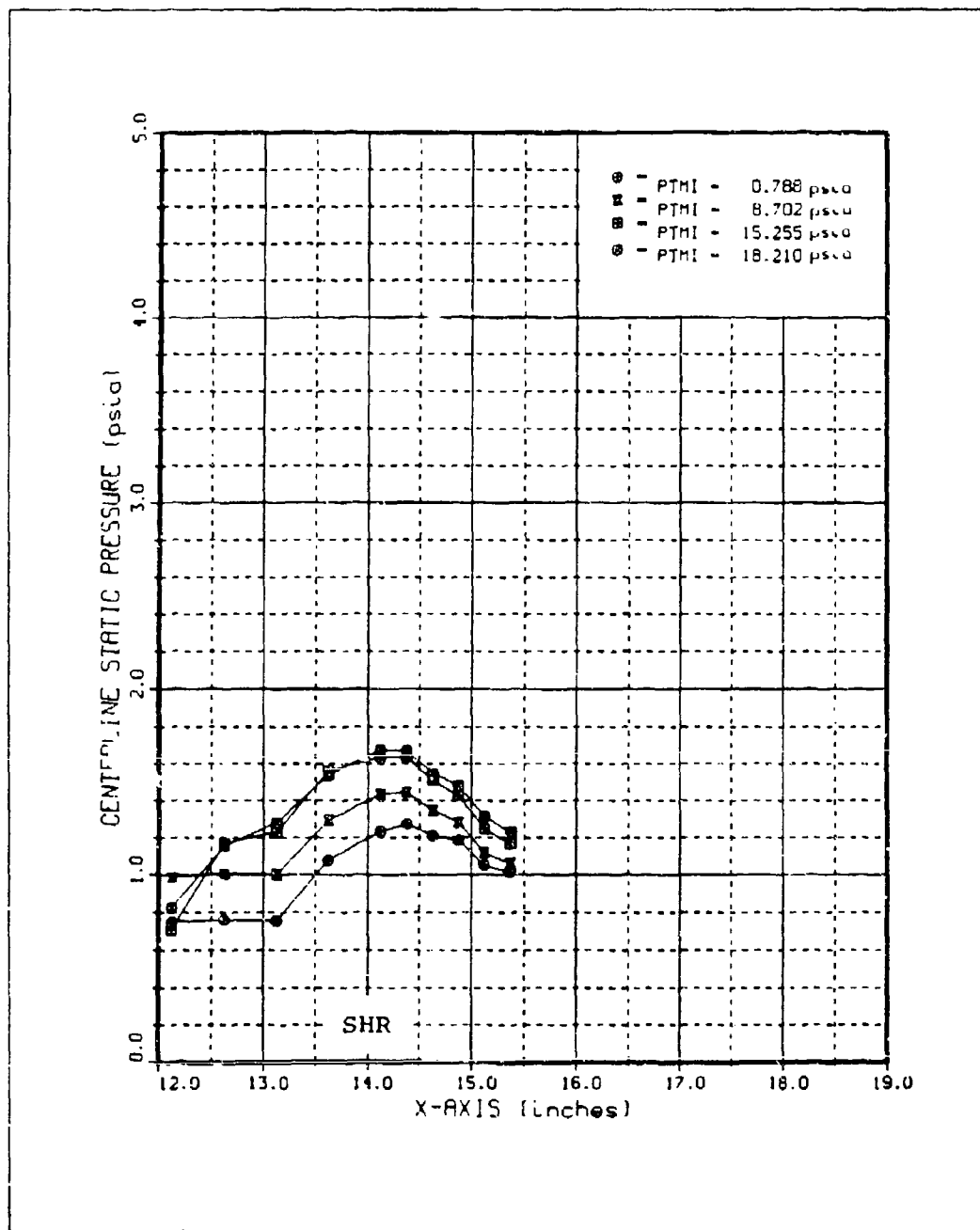


Figure 138. Run 35 C/L Static Pressure Distributions. for $p_{0j}=0-18$ psia

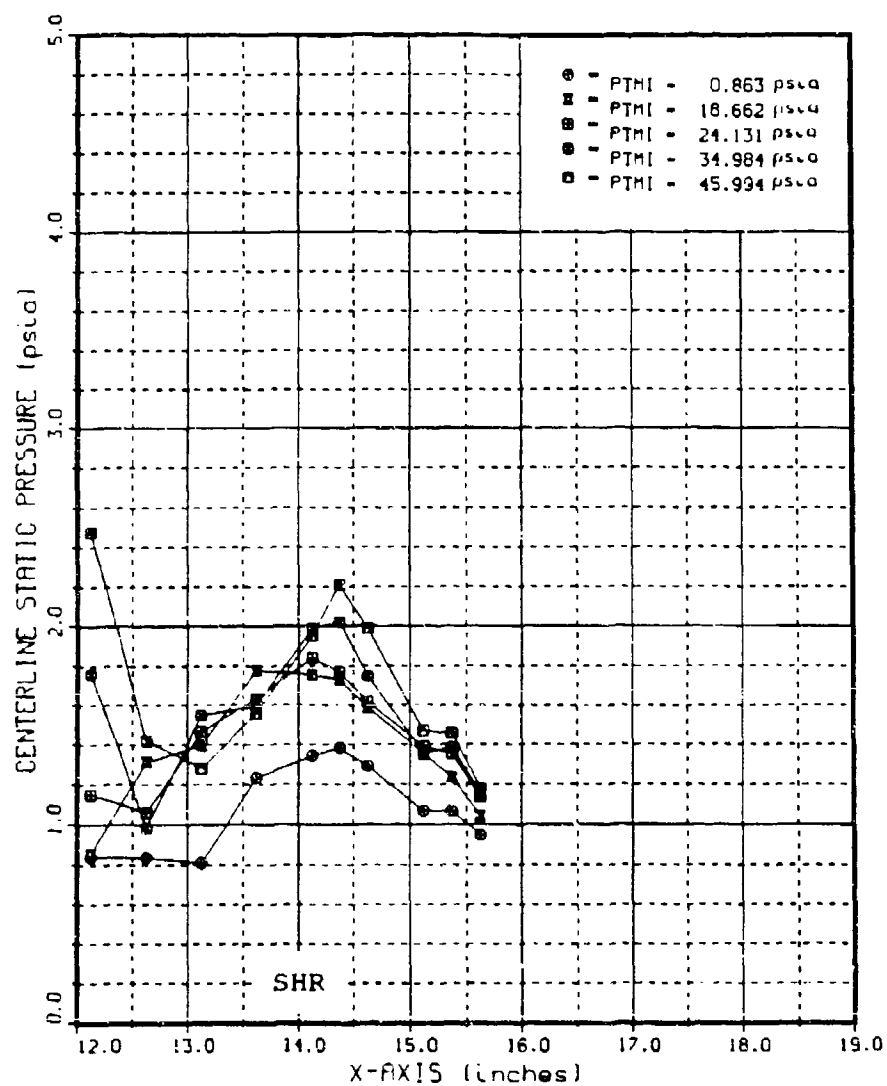


Figure 139. Run 62 C/L Static Pressure Distributions

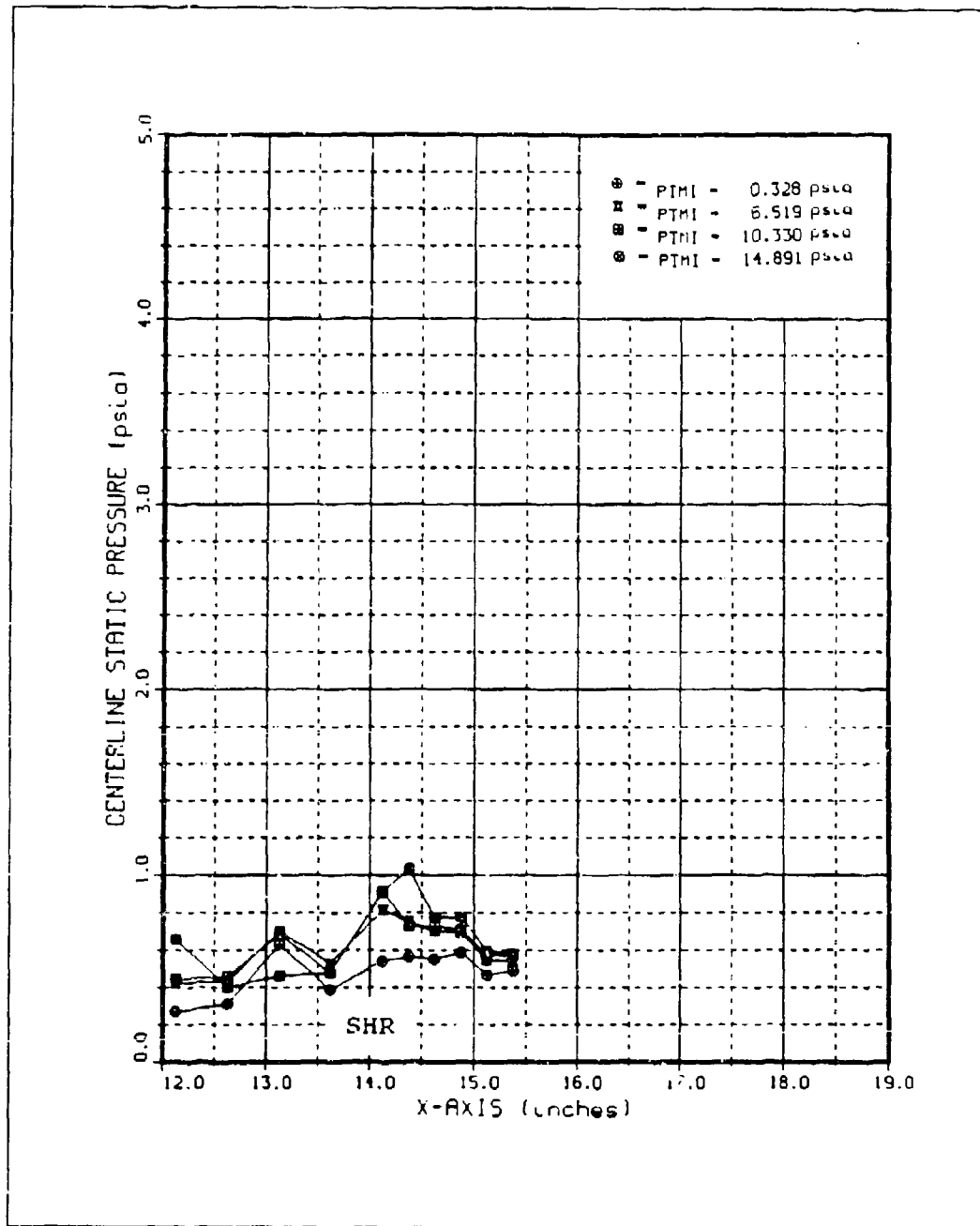


Figure 140. Run 36 C/L Static Pressure Distributions

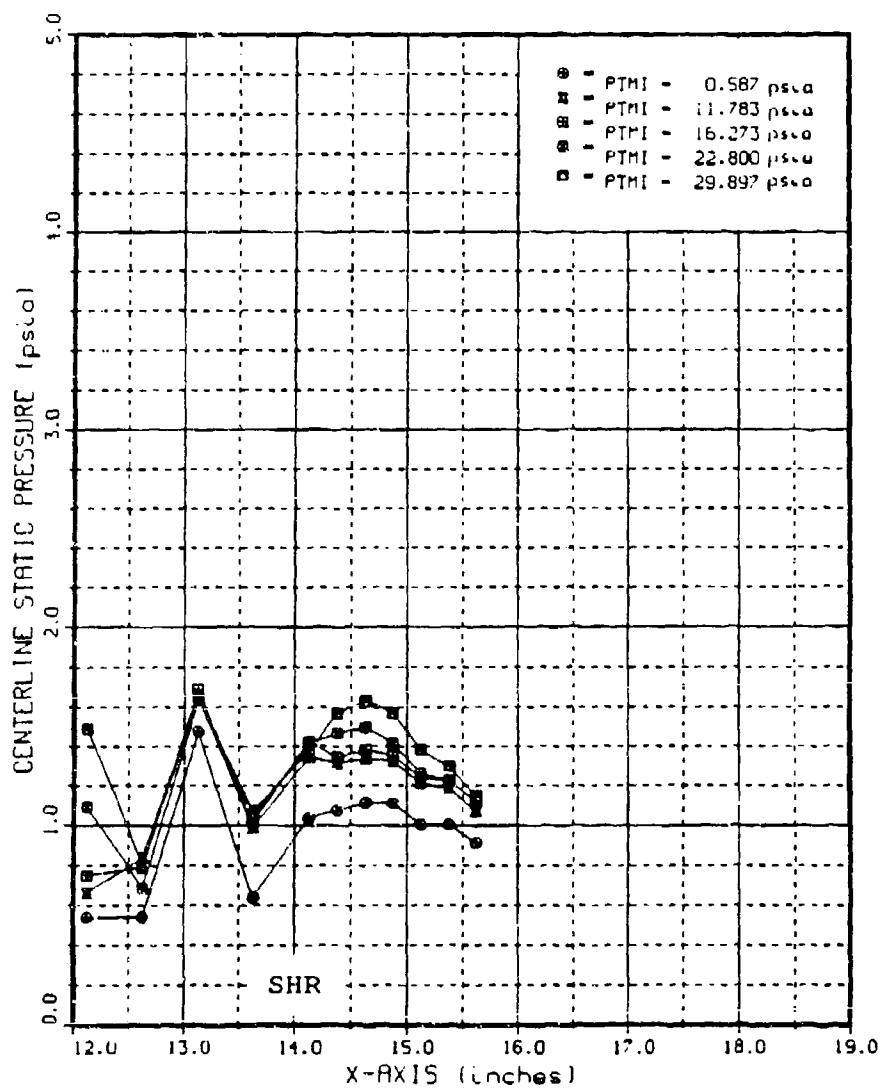


Figure 141. Run 37 C/L Static Pressure Distributions

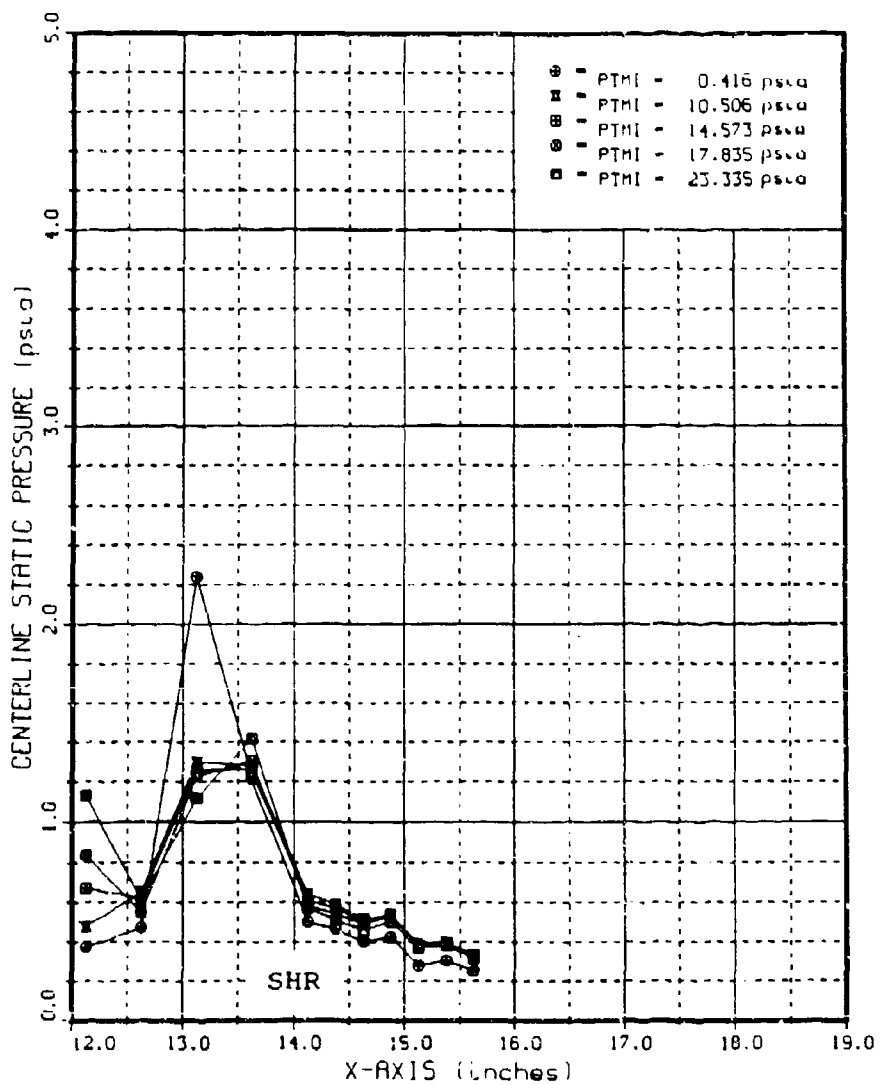


Figure 142. Run 38 C/L Static Pressure Distributions

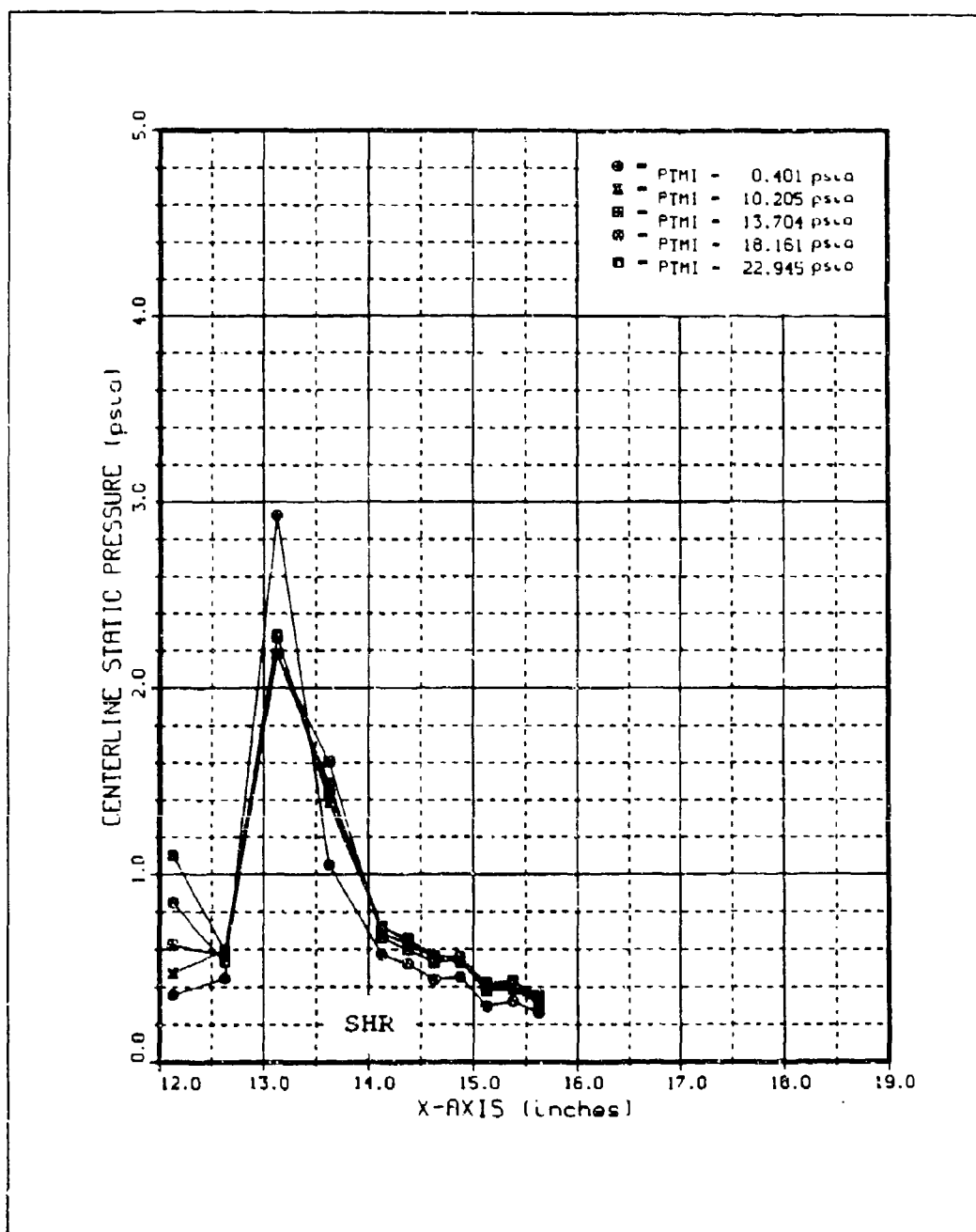


Figure 143. Run 39 C/L Static Pressure Distributions

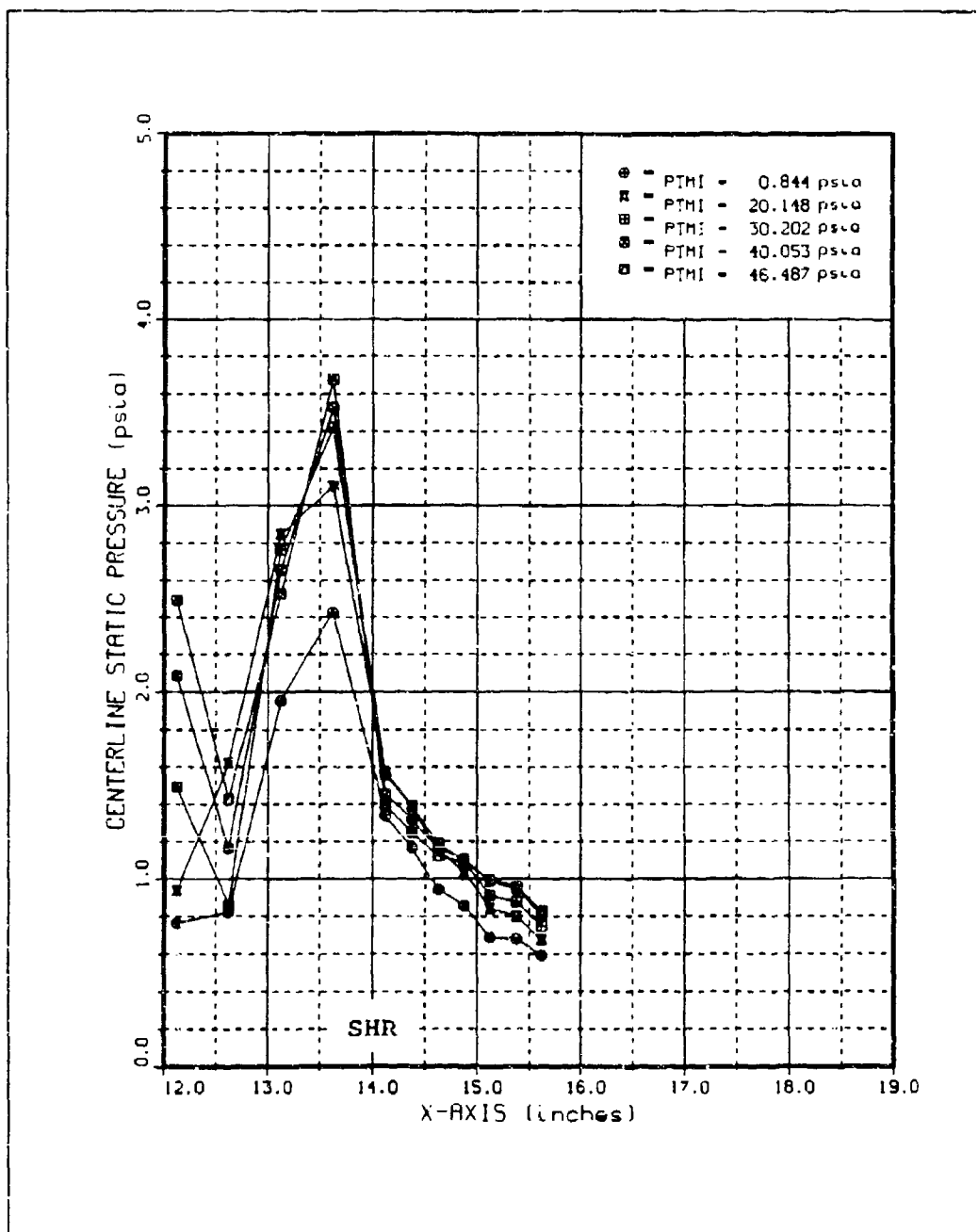


Figure 144. Run 40 C/L Static Pressure Distributions

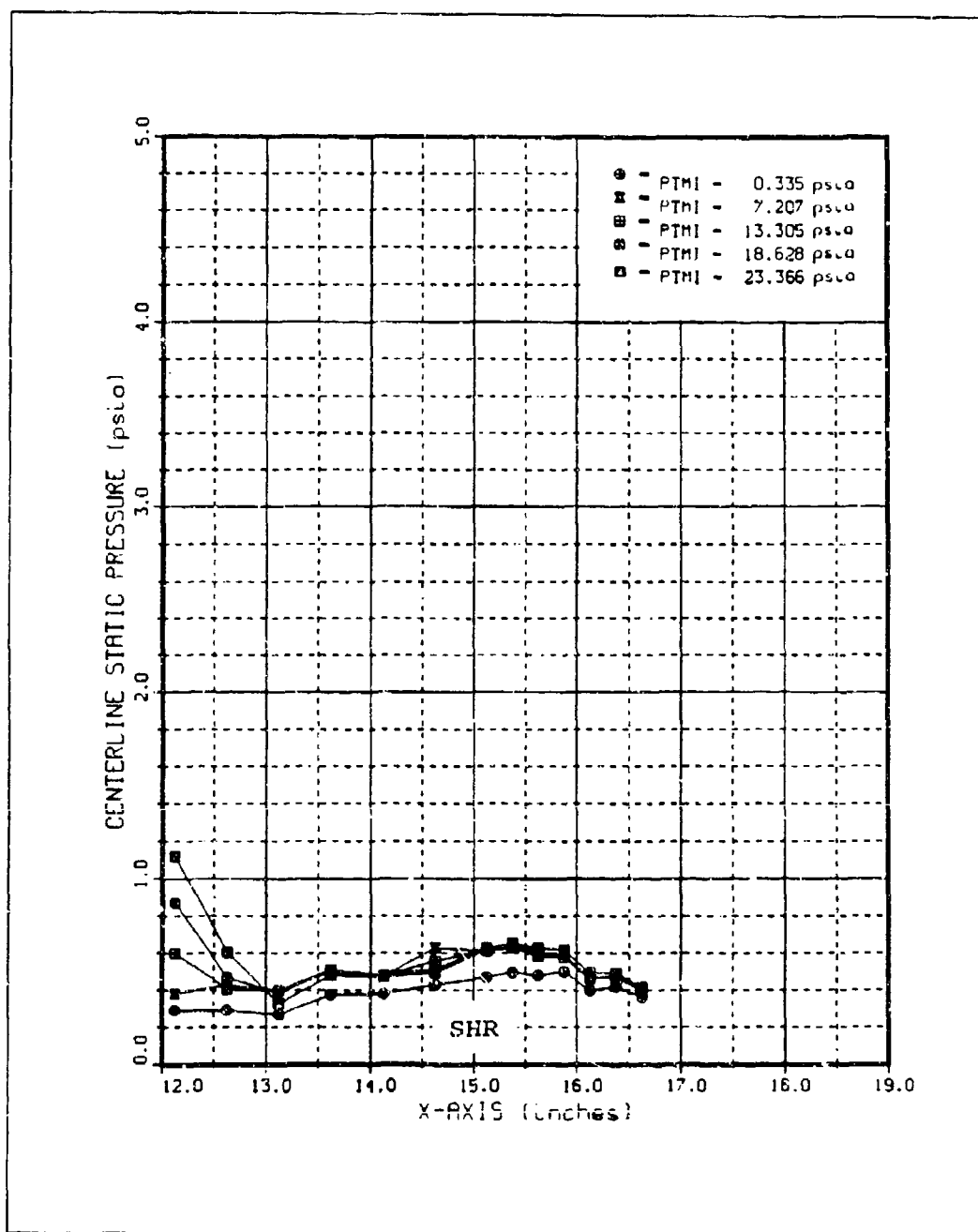


Figure 145. Run 41 C/L Static Pressure Distributions for $p_{oj}=0-23$ psia

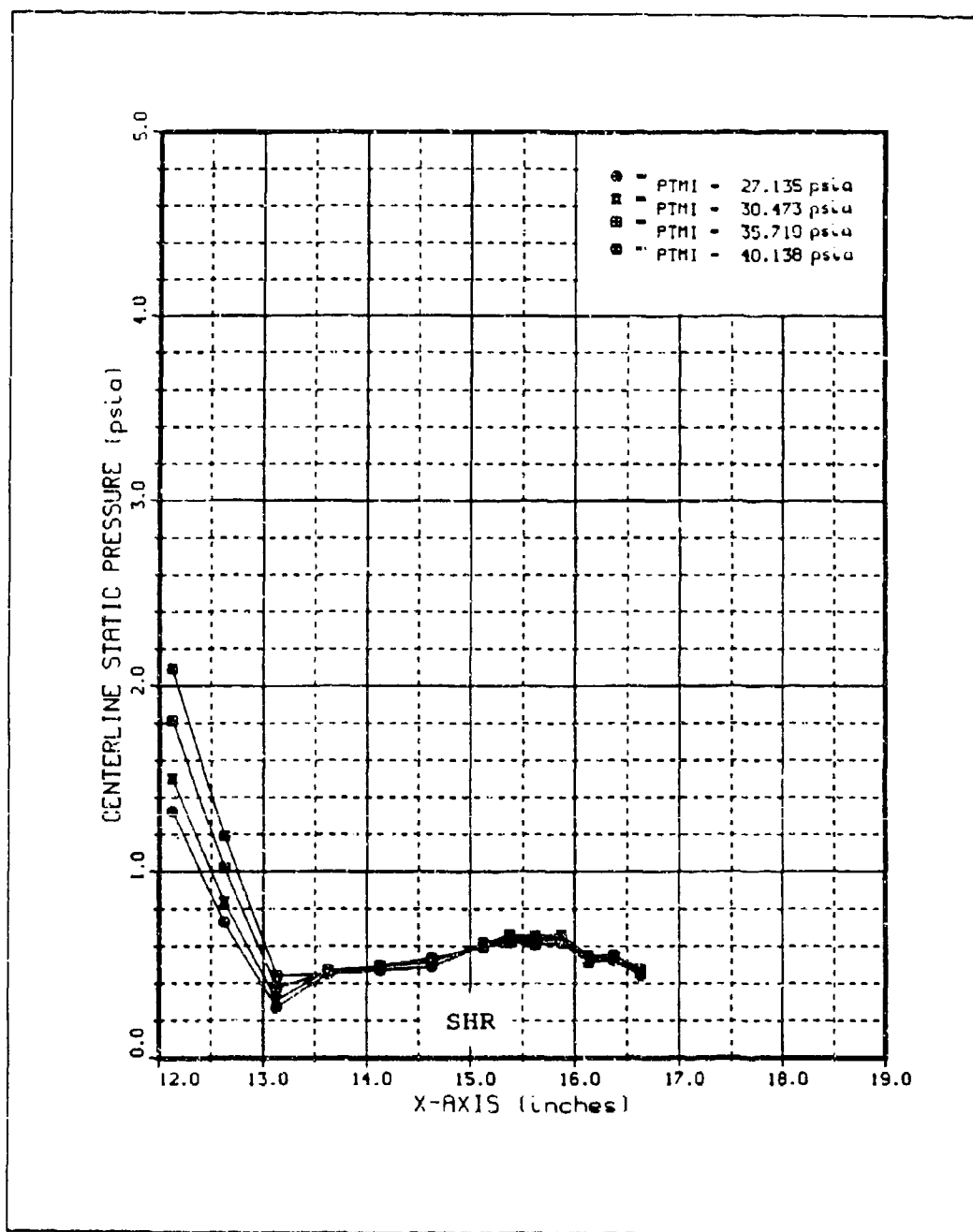


Figure 146. Run 41 C/L Static Pressure Distributions for p_{0j} = 27-40 psia

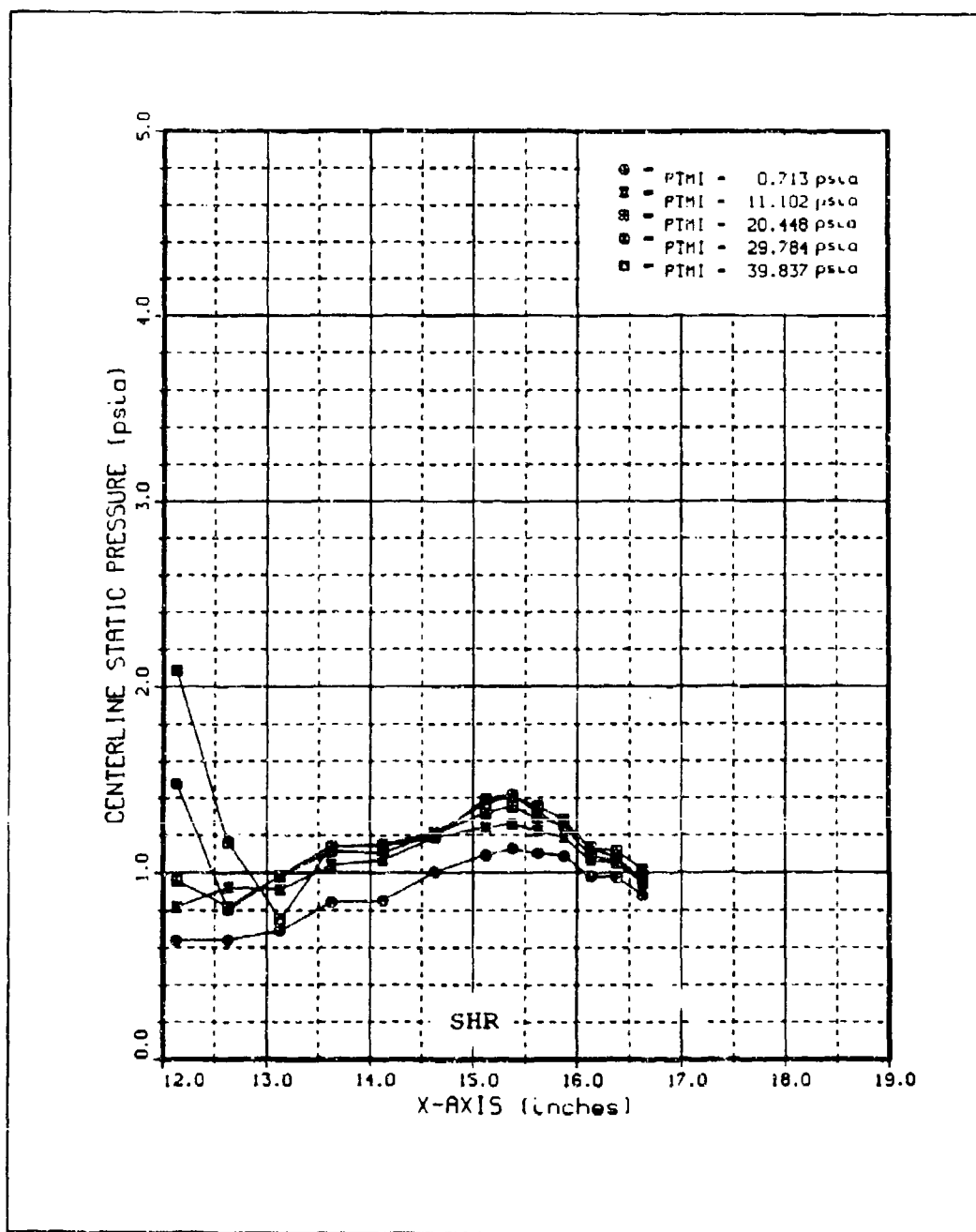


Figure 147. Run 42 C/L Static Pressure Distributions

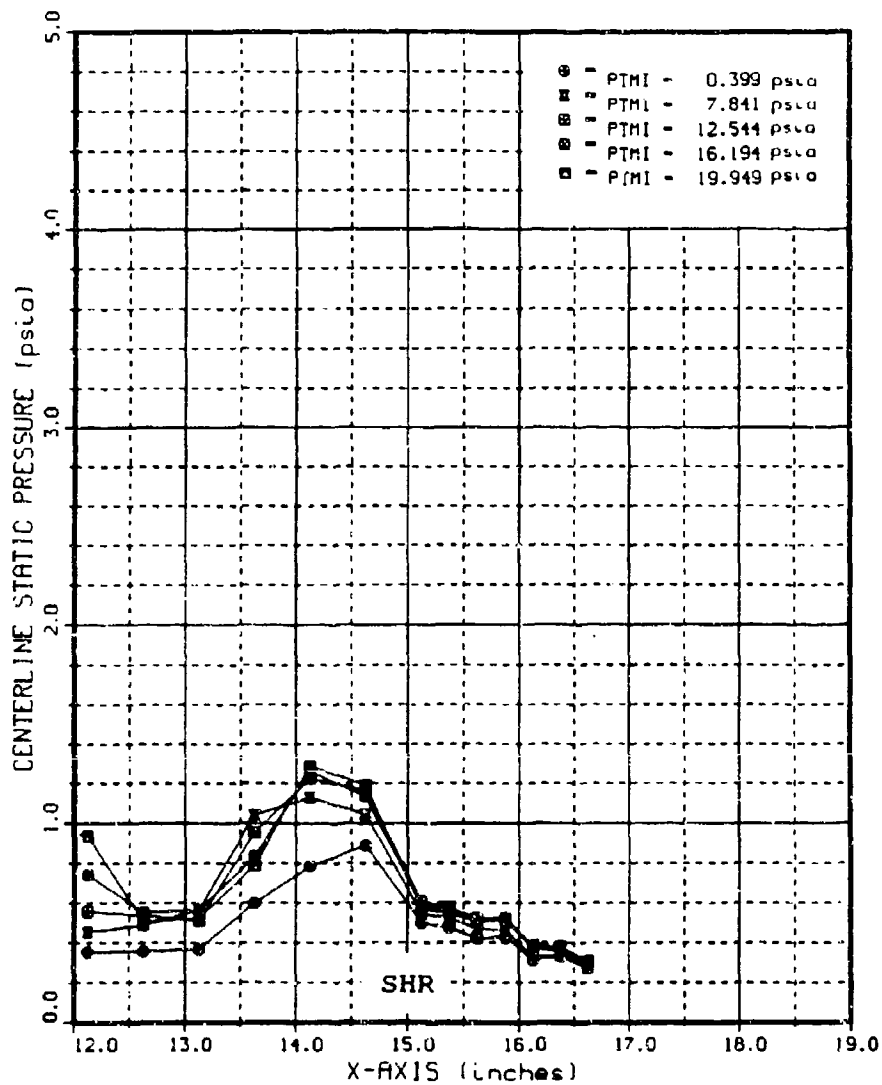


Figure 148. Run 43 C/L Static Pressure Distributions

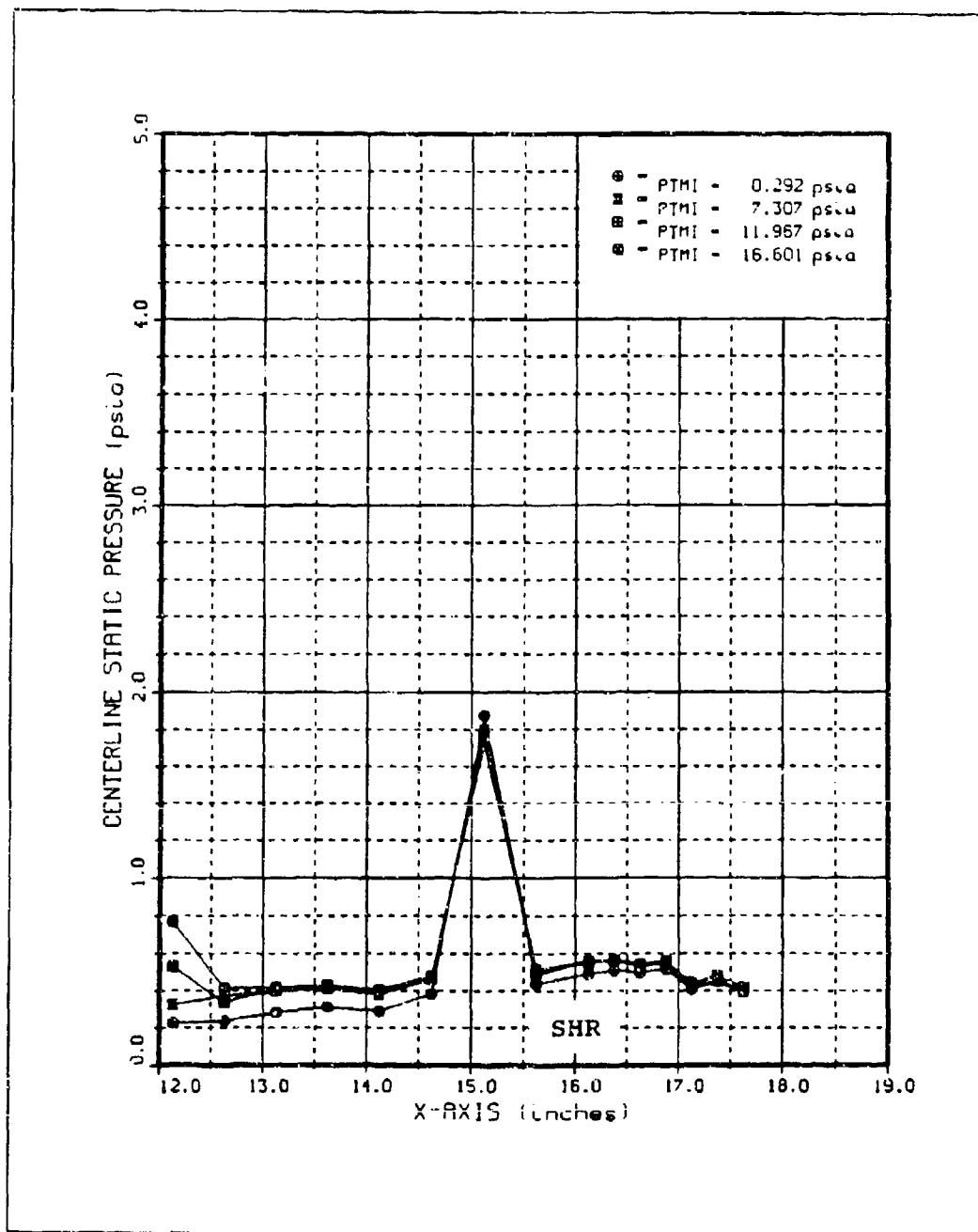


Figure 149. Run 44 C/L Static Pressure Distributions for $p_{0j}=0-17$ psia

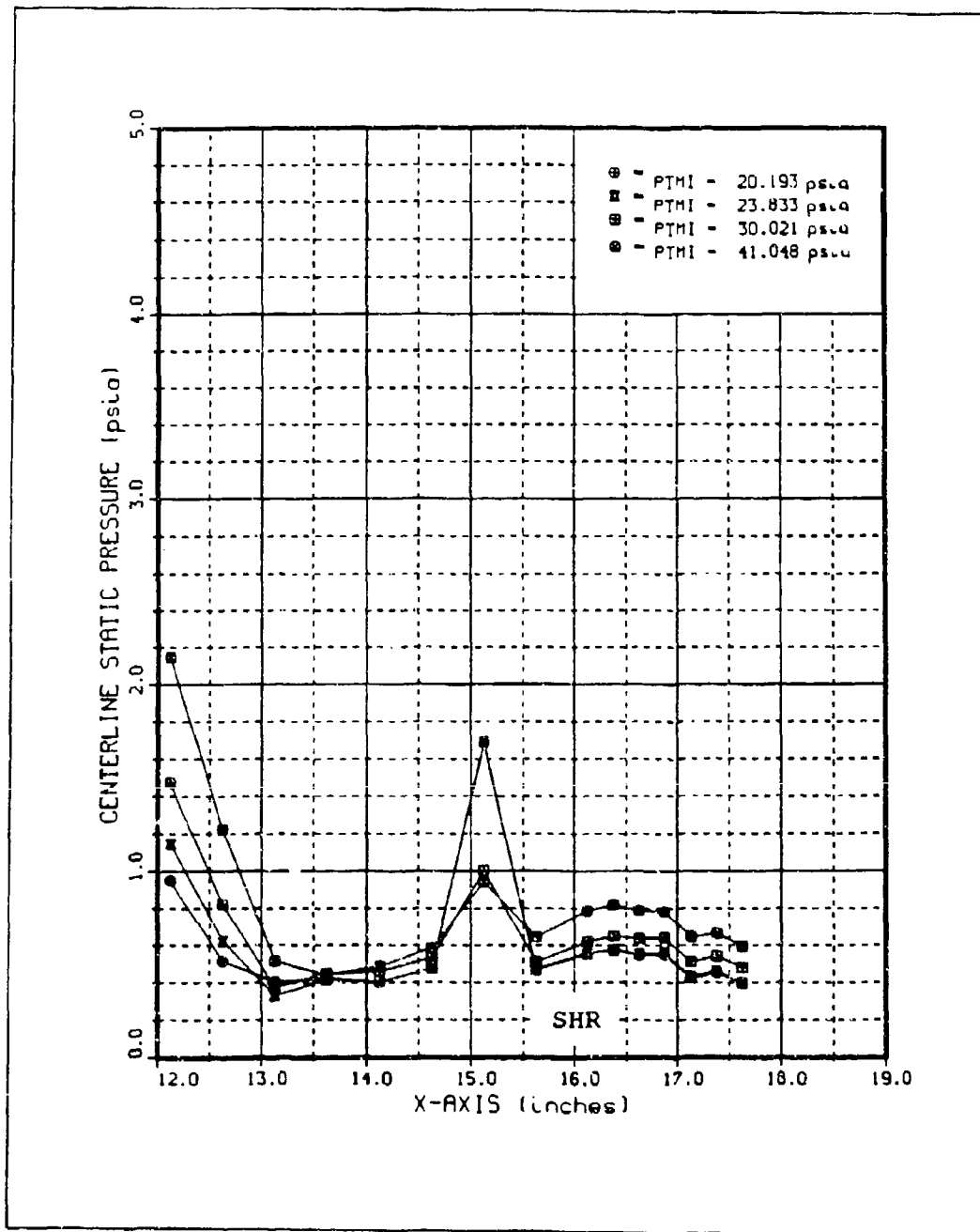


Figure 150. Run 44 C/L Static Pressure Distributions. for $p_{oj}=20-41$ psia

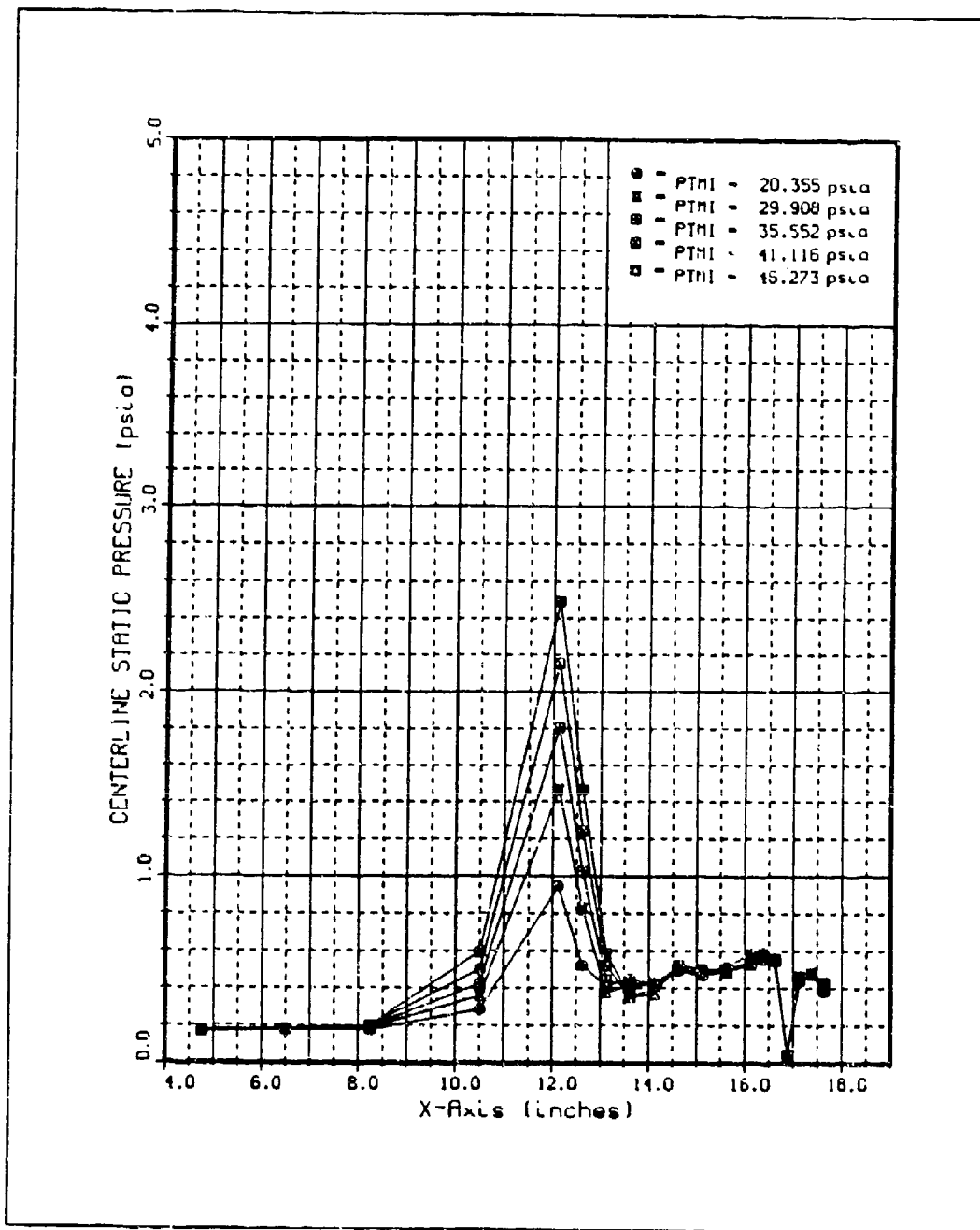


Figure 151. Run 54 C/L Static Pressure Distributions

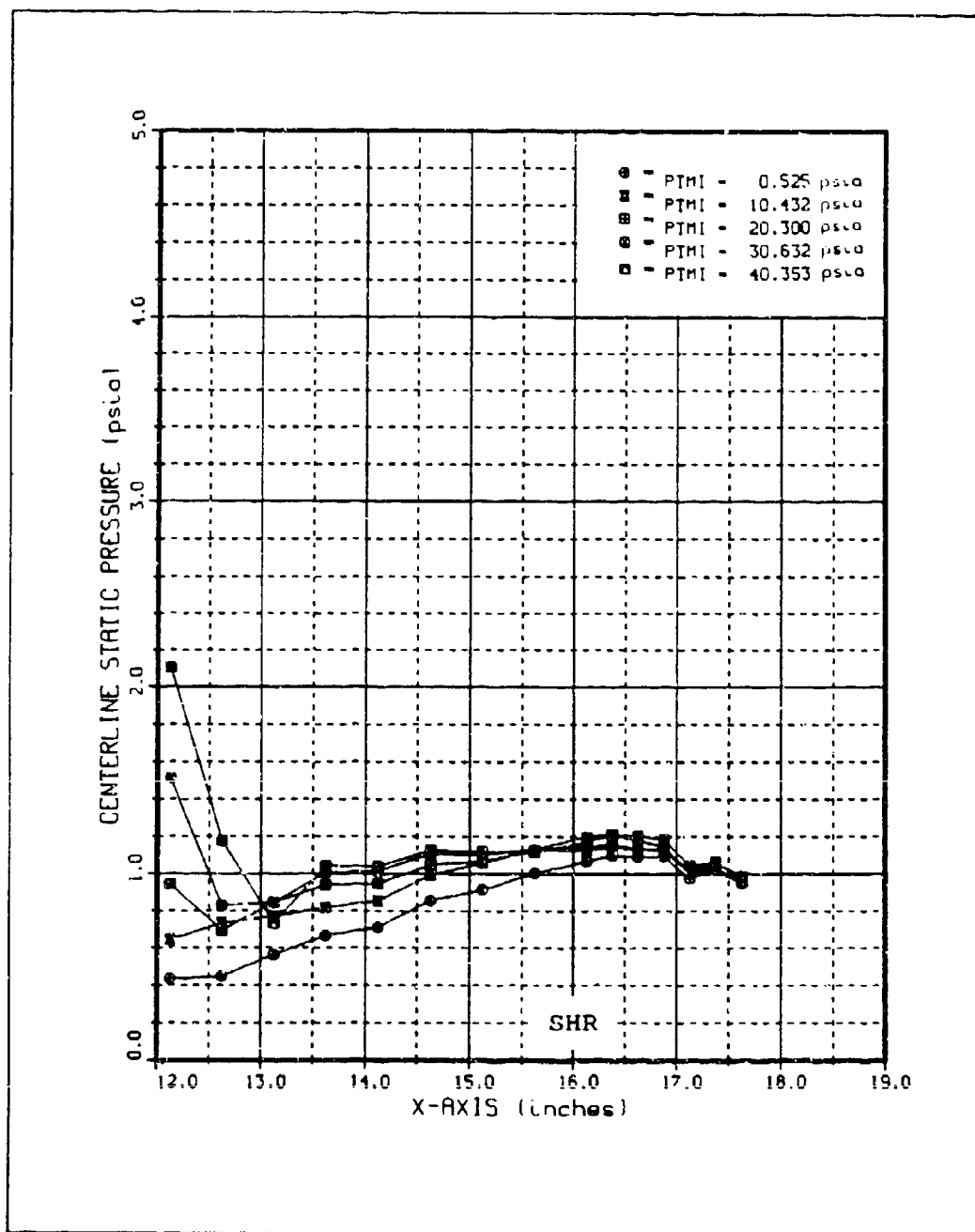


Figure 152. Run 45 C/L Static Pressure Distributions

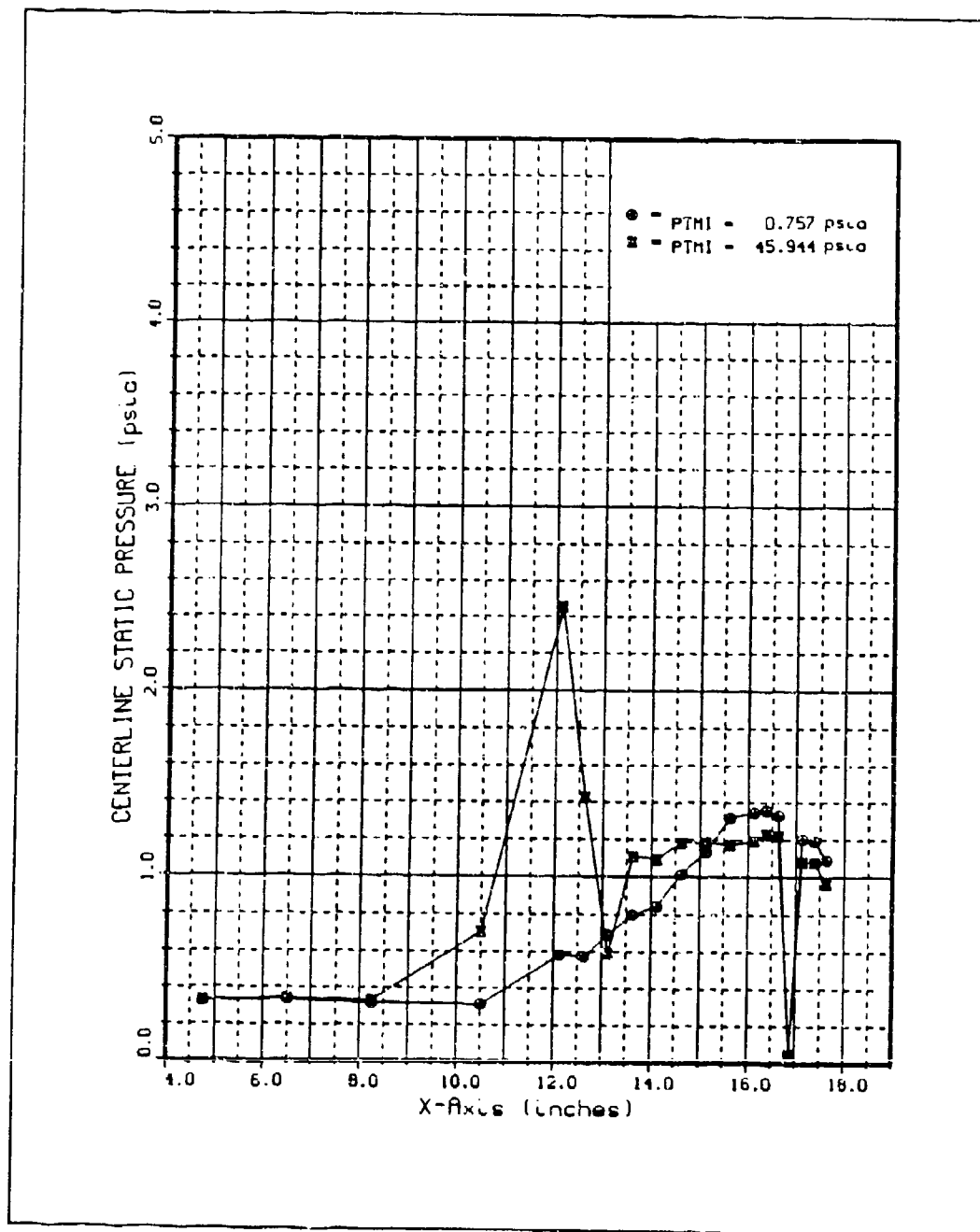


Figure 153. Run 55 C/L Static Pressure Distributions

Appendix H

Pitot Pressure Profile Plots

These plots were generated from vertical surveys at the model centerline ($Y=0$ in) with a traversing probe sensing pitot pressure. Pitot pressure is defined as the total pressure behind a normal shock generated by the probe tip (assuming the measured flow is supersonic). Pitot pressure profiles for Runs 3 ($p_{o_j} = 9$ psia), 4, and 3 ($X=11.8$ in) appeared in the main text as Figures 22, 23, and 24, respectively. Also up front are plots for Runs 9, 11, and 12 in Figure 33; Runs 10, 13, and 14 in Figure 34; and Runs 51 and 52 in Figure 35.

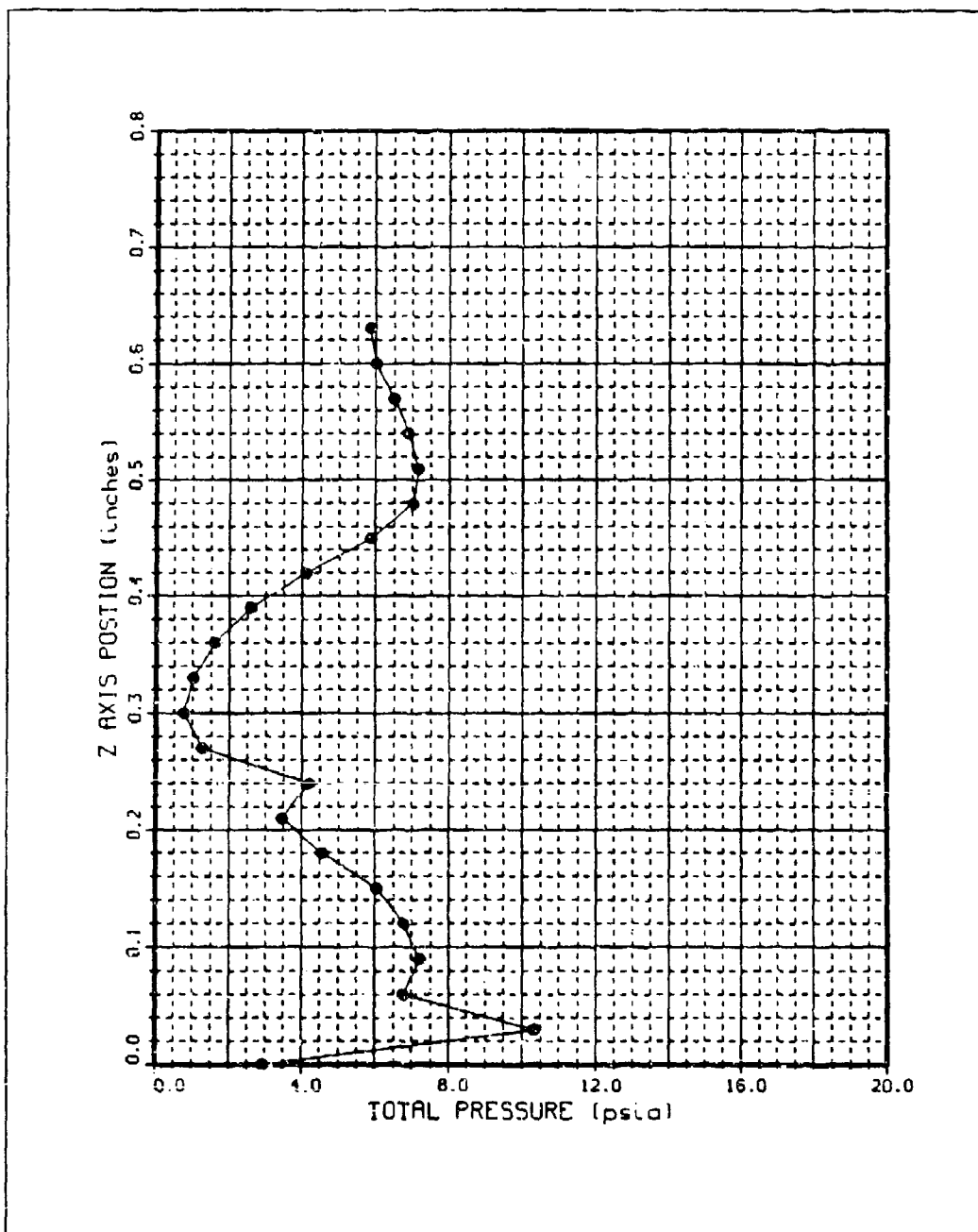


Figure 154. Run 5 Pitot Pressure Profile at $X = 12.1$ in,
 $p_{0j} = 18$ psia

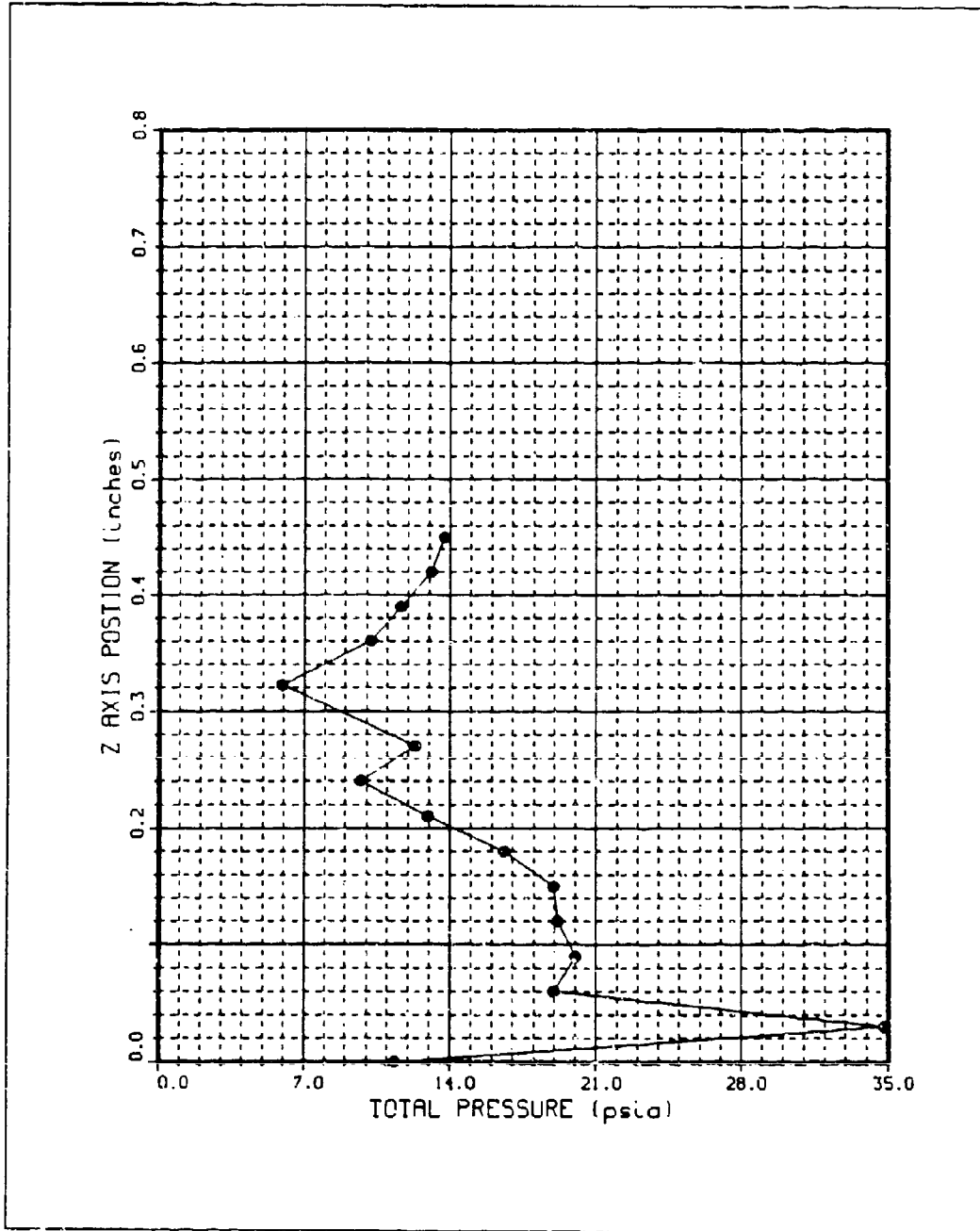


Figure 155. Run 8 Pitot Pressure Profile at $X = 12.1$ in,
 $p_{0j} = 46$ psia

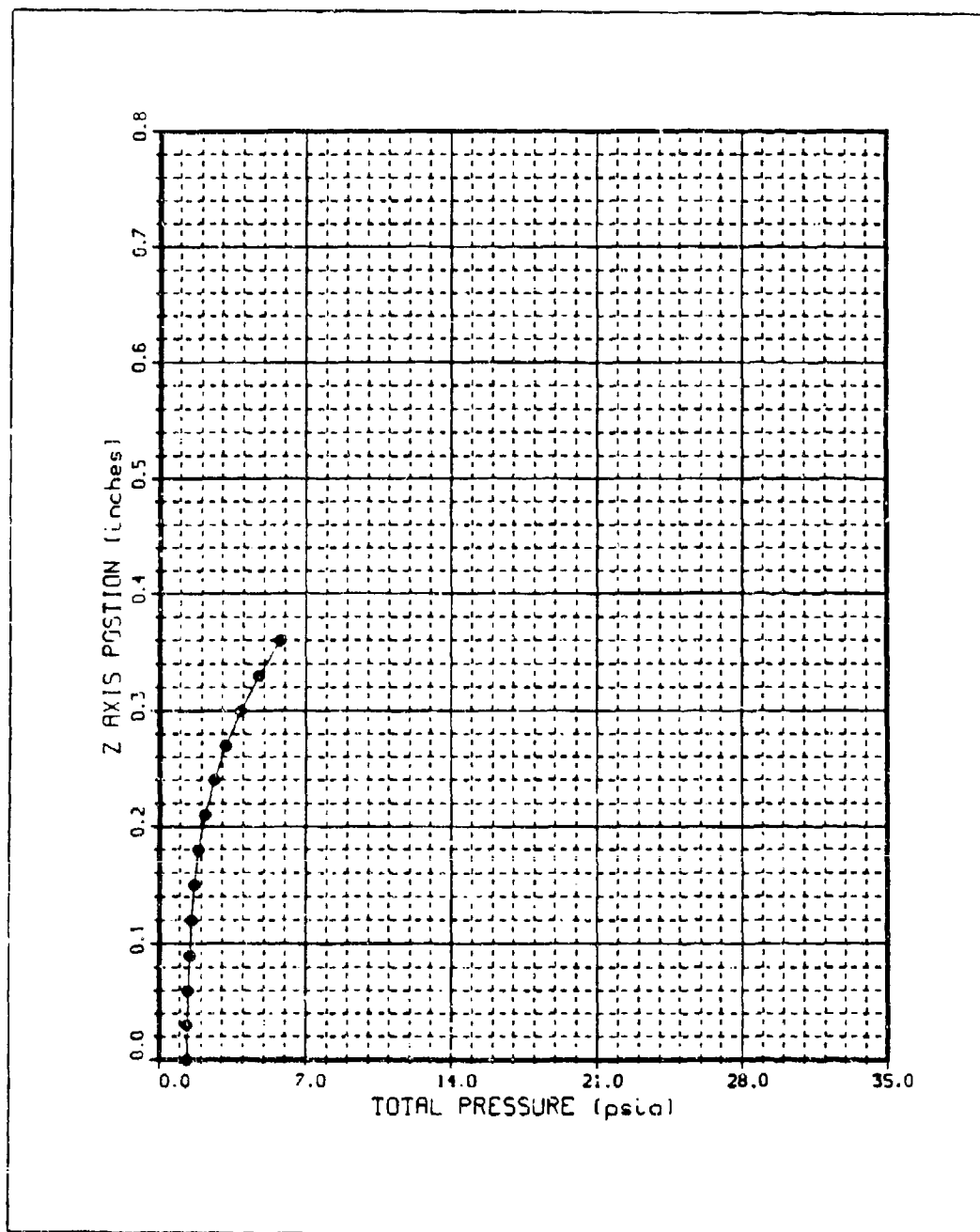


Figure 156. Run 15 Pitot Pressure Profile at $X = 17.3$ in,
 $p_{0j} = 0$ psia

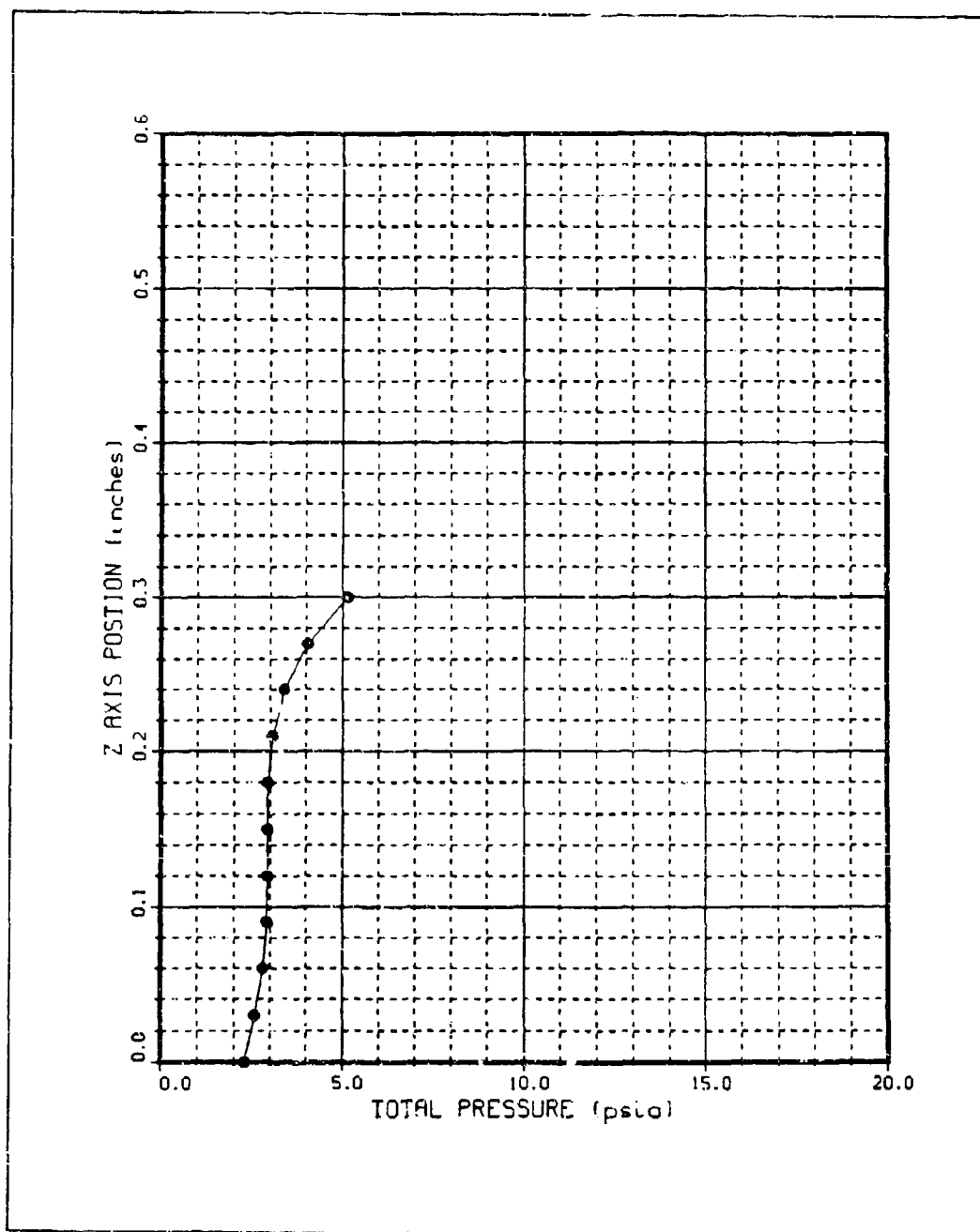


Figure 157. Run 16 Pitot Pressure Profile at X = 17.3 in,
 $p_{o,j} = 0$ psia

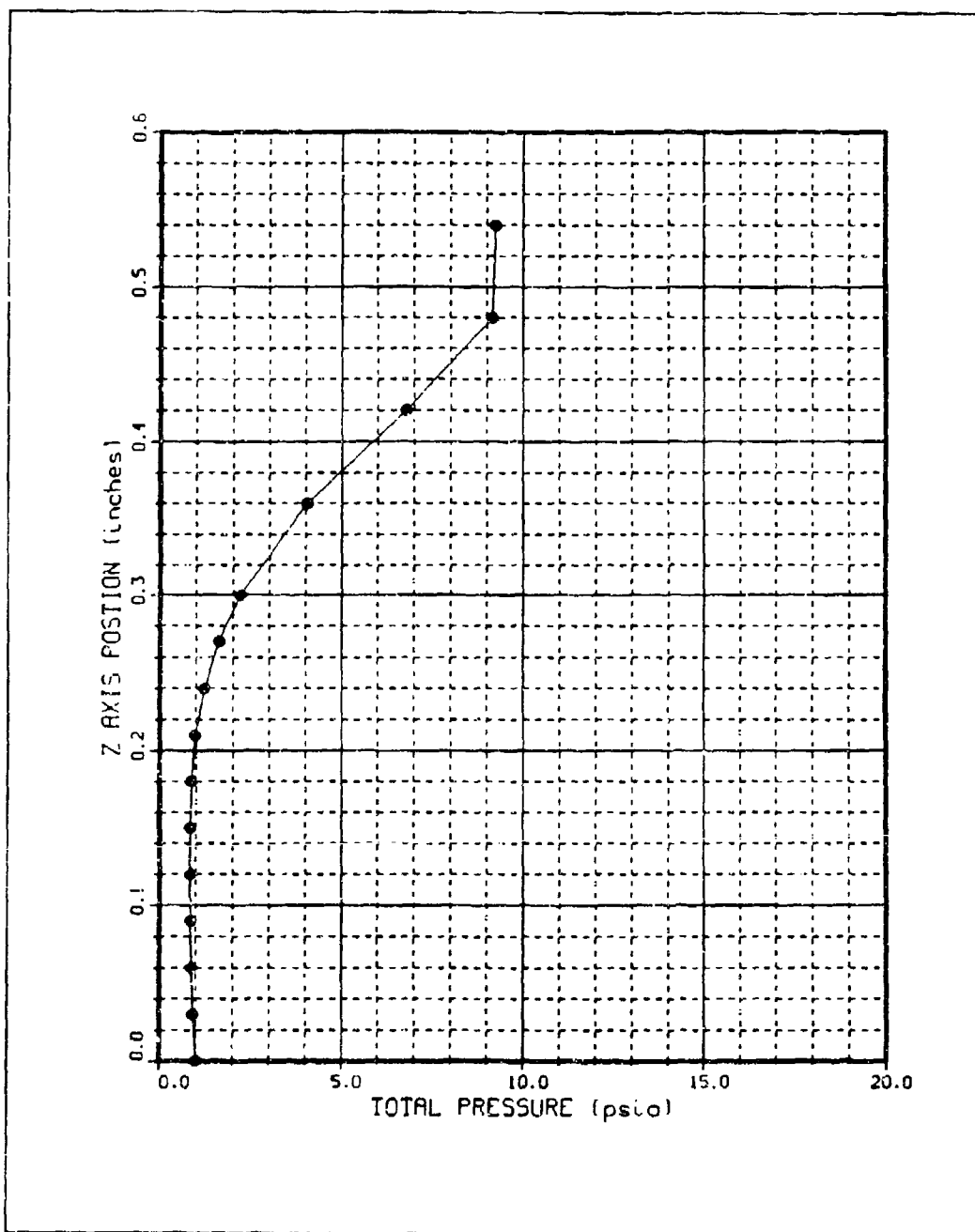


Figure 158. Run 17 Pitot Pressure Profile at $X = 15.5$ in,
 $p_{o_j} = 0$ psia

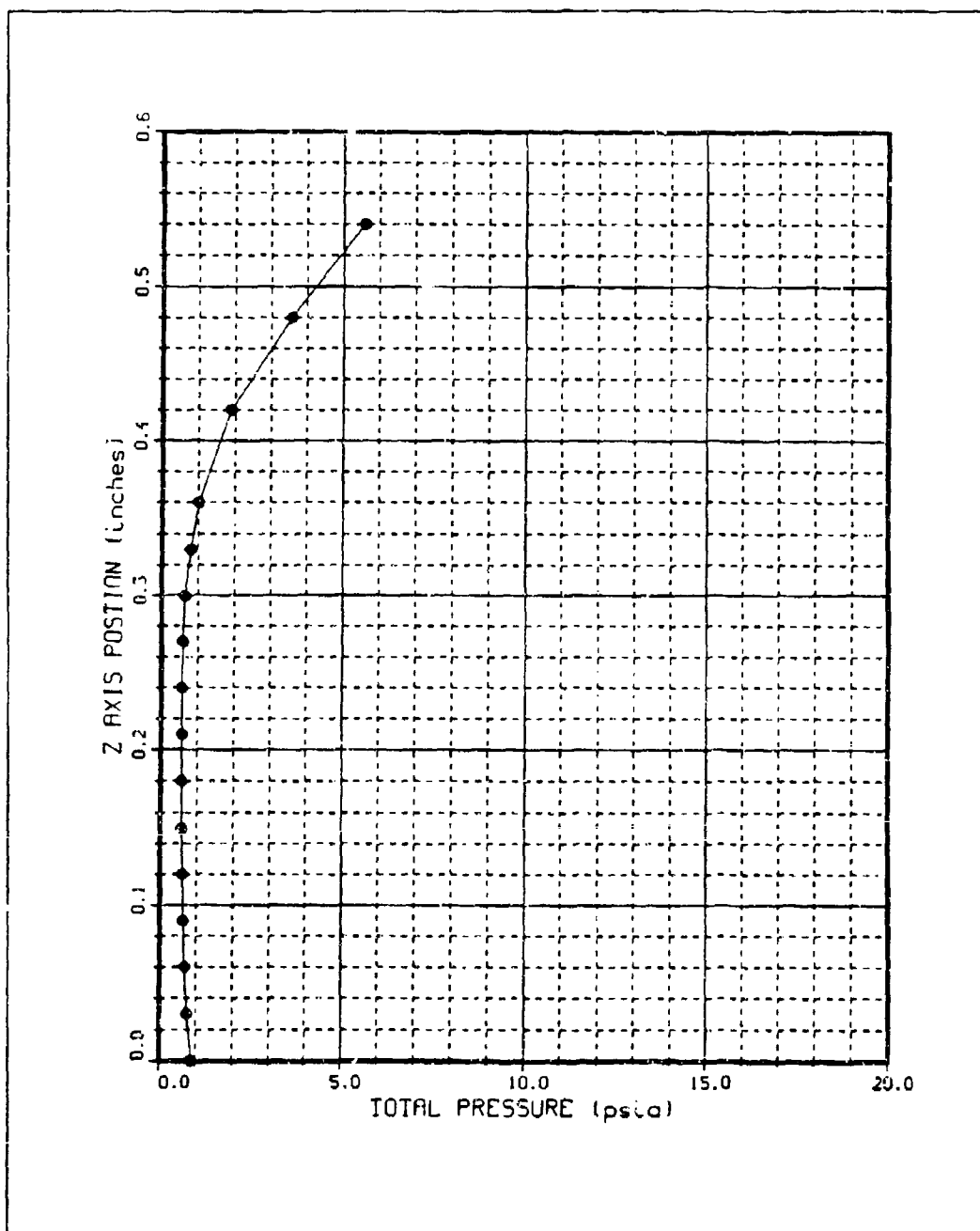


Figure 159. Run 18 Pitot Pressure Profile at X = 15 in,
 $p_{o,j} = 0$ psia

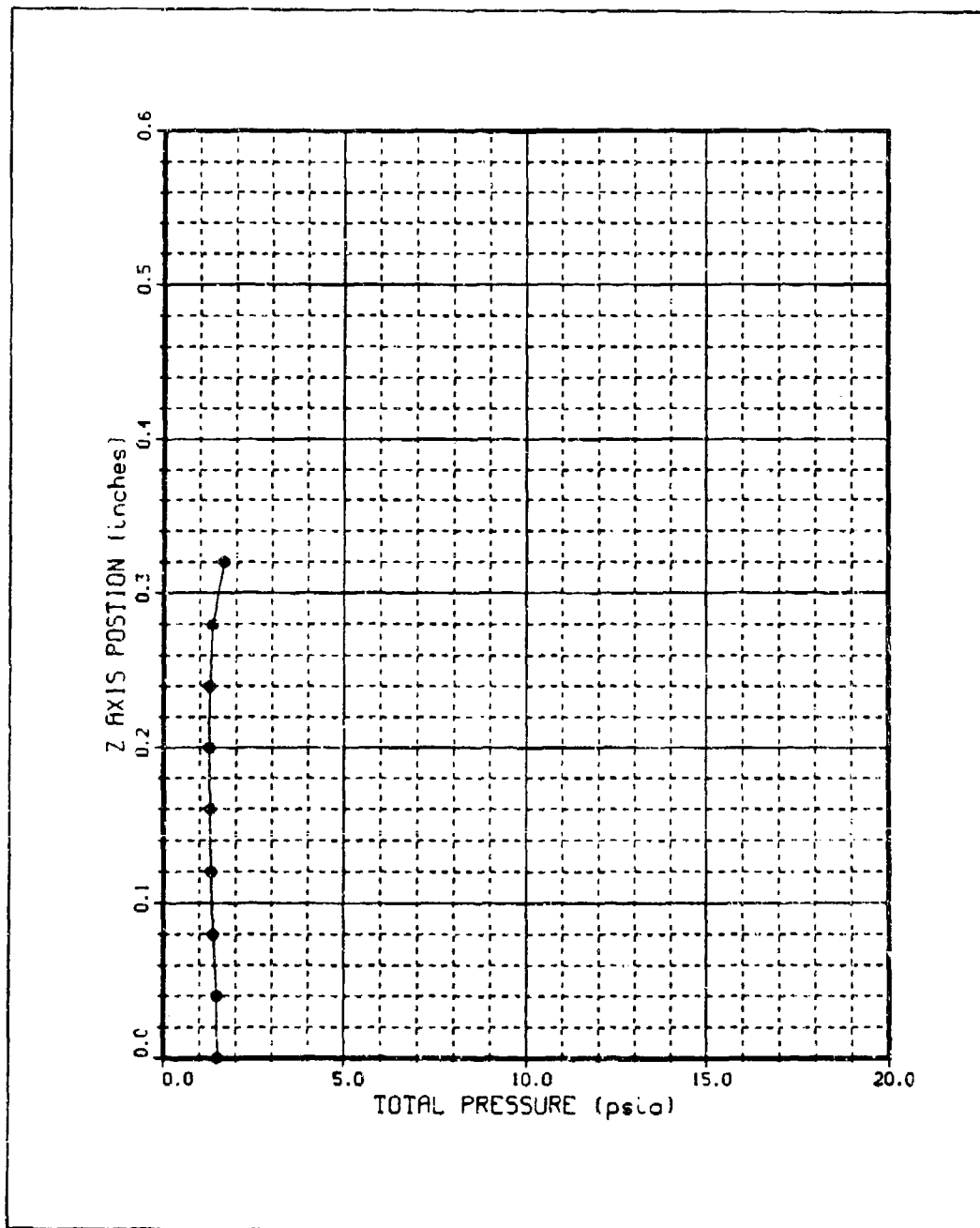


Figure 160. Run 19 Pitot Pressure Profile at X = 15 in,
 $P_{0j} = 0$ psia

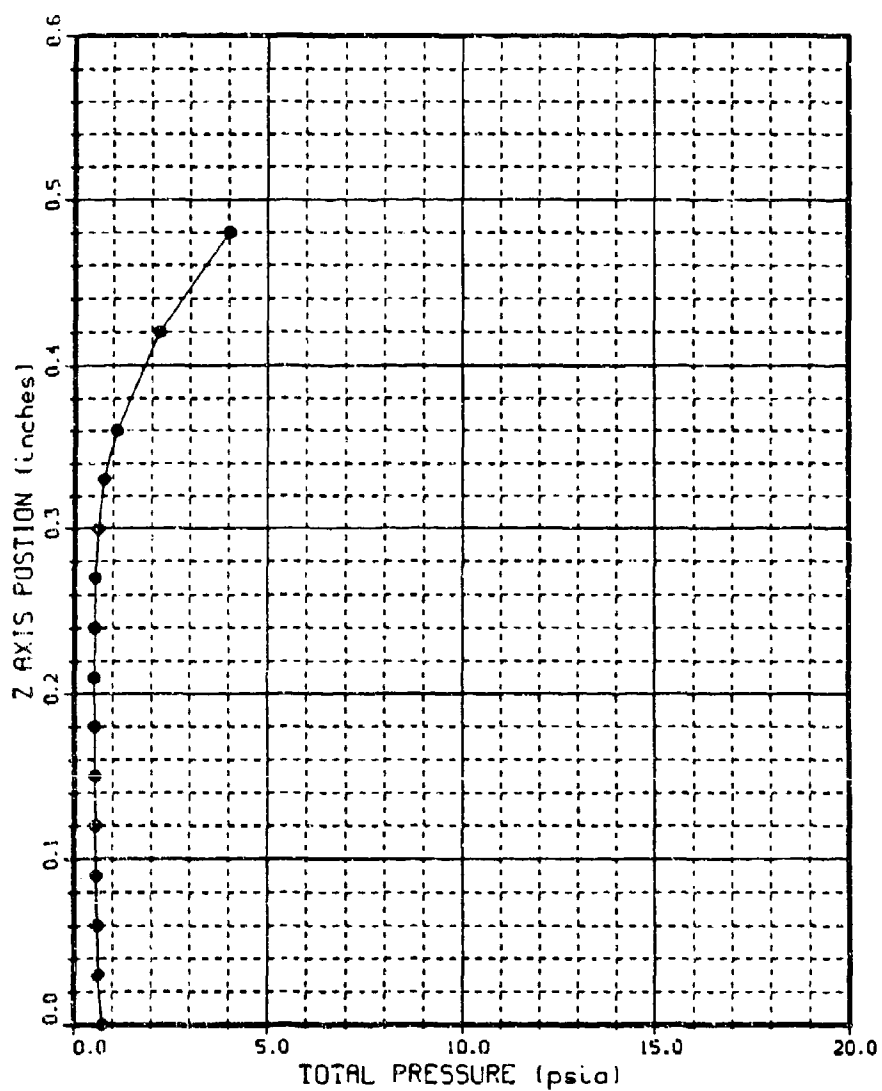


Figure 161. Run 20 Pitot Pressure Profile at X = 15 in,
 $P_{0j} = 0$ psia

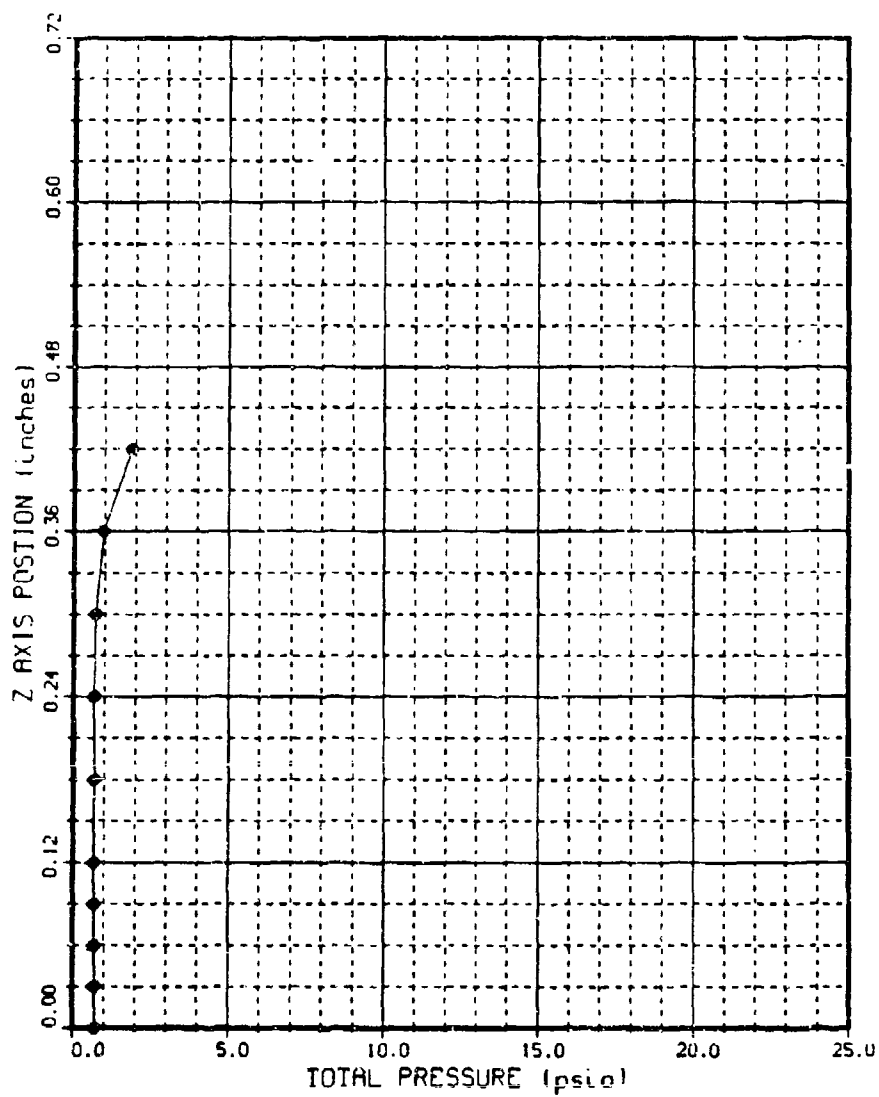


Figure 162. Run 56 Pitot Pressure Profile at X = 15 in,
 $p_{0j} = 36$ psia

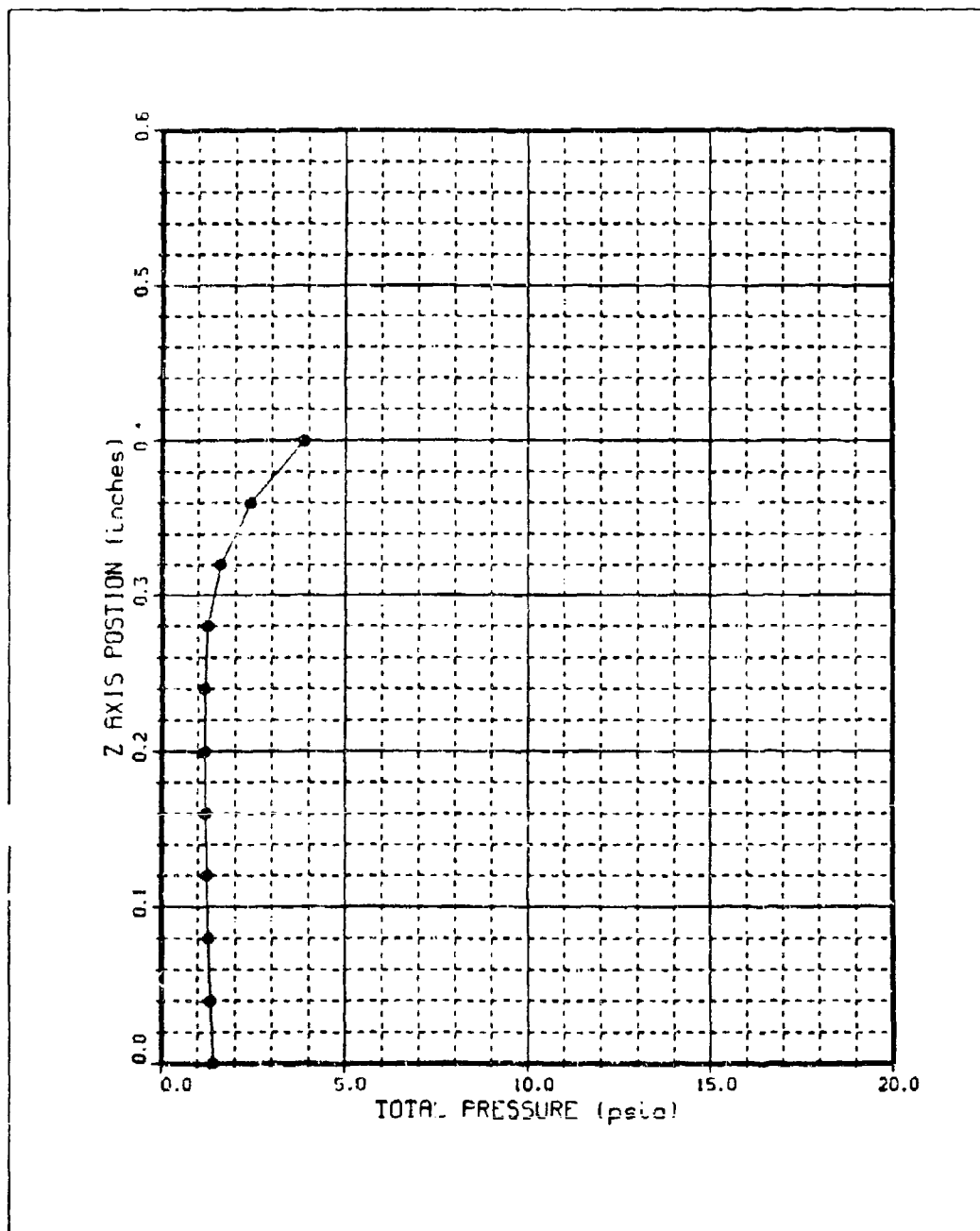


Figure 163. Run 21 Pitot Pressure Profile at X = 15 in,
 $p_{o,j} = 0$ psia

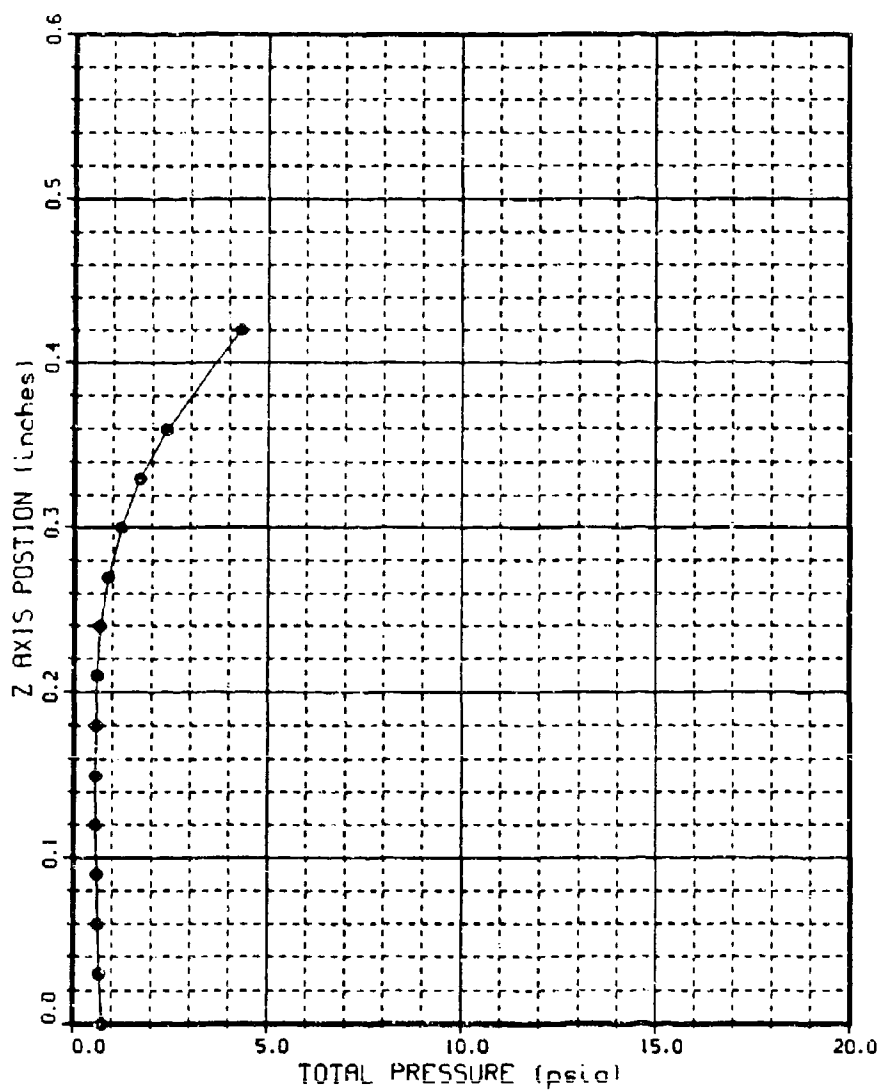


Figure 164. Run 22 Pitot Pressure Profile at X = 14 in,
 $P_{0j} = 0$ psia

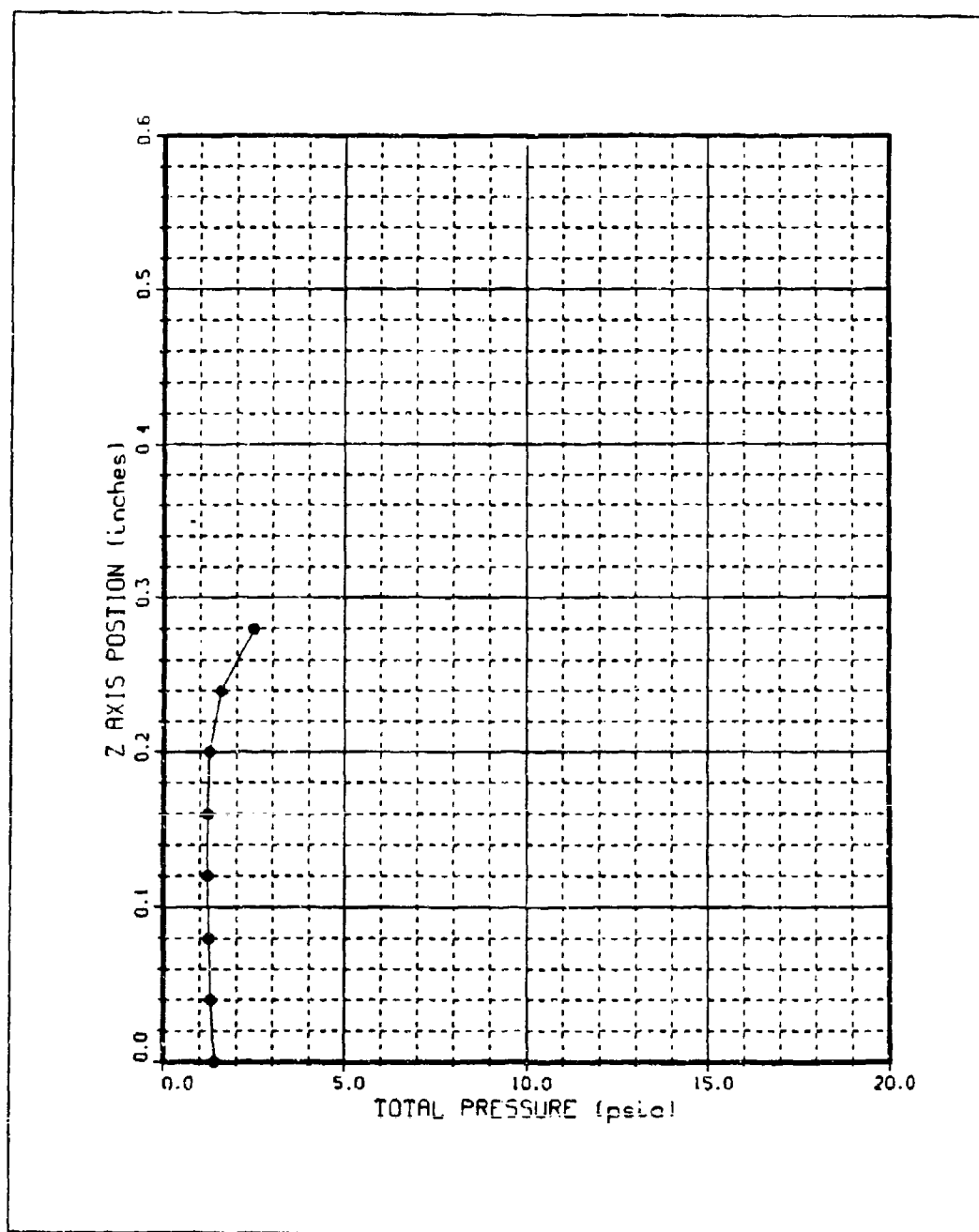


Figure 165. Run 23 Pitot Pressure Profile at X = 14 in,
 $p_{0j} = 0$ psia

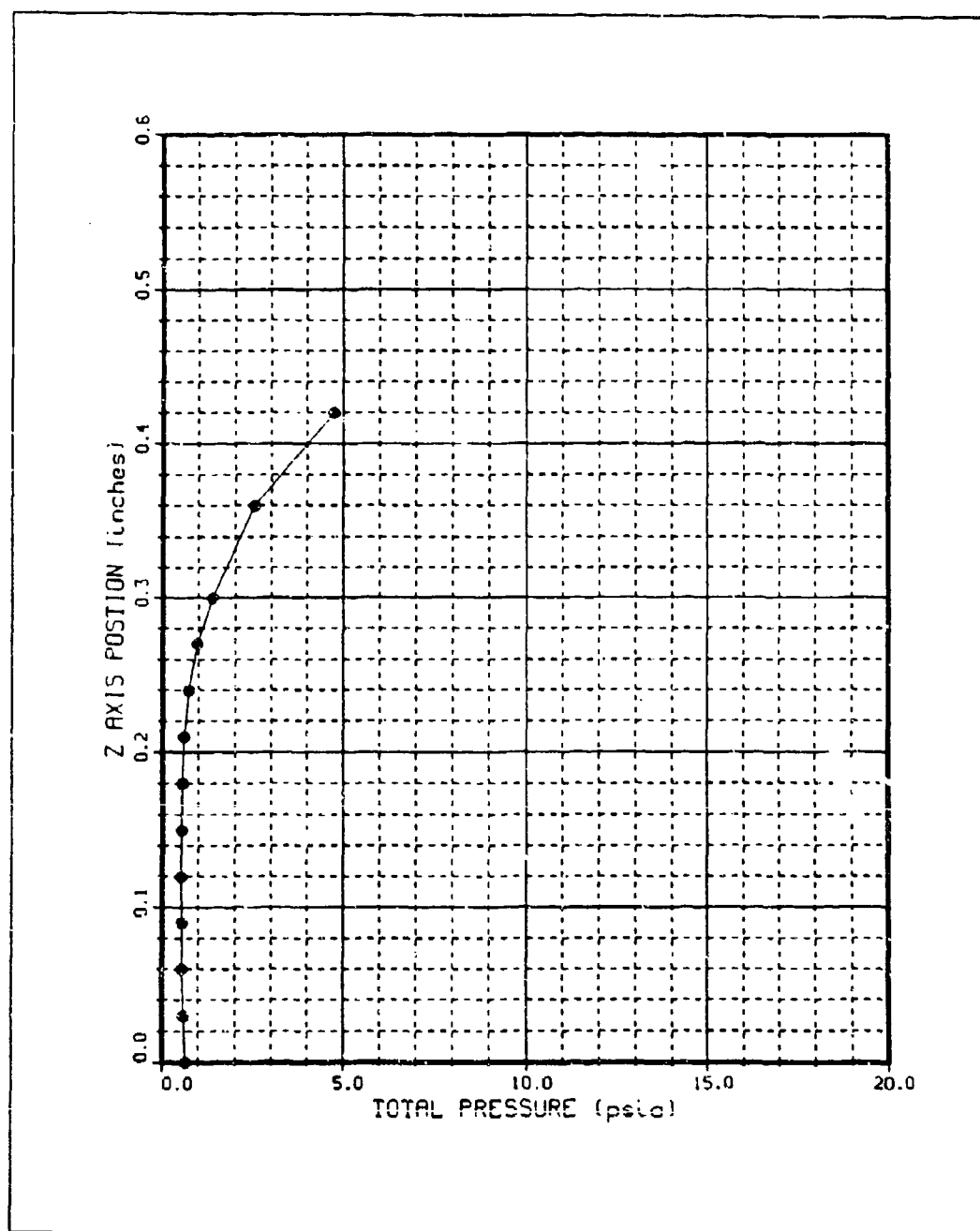


Figure 166. Run 24 Pitot Pressure Profile at X = 13 in,
 $p_{oj} = 0$ psia

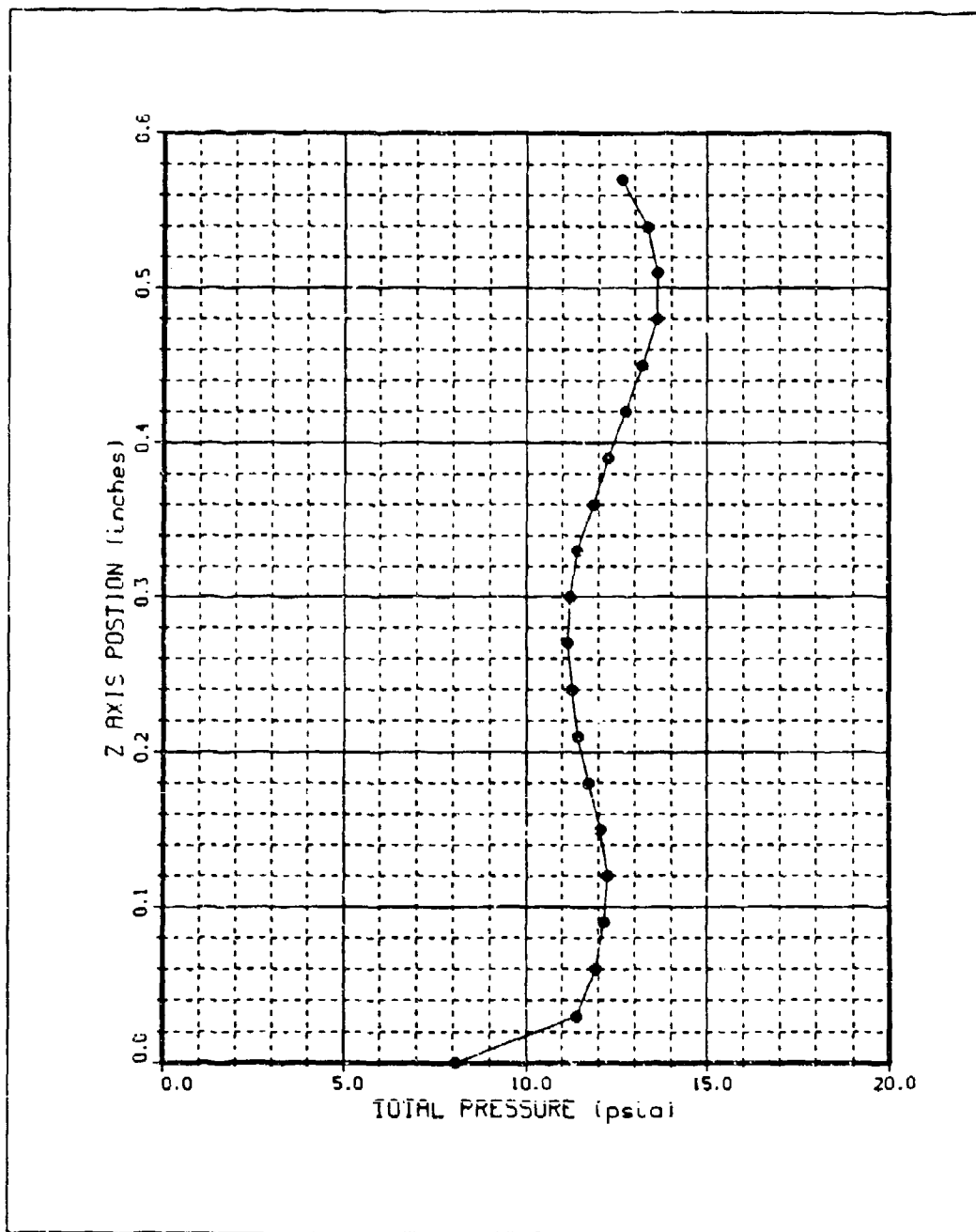


Figure 167. Run 25 Pitot Pressure Profile at X = 13 in,
 $p_{o,i} = 18$ psia

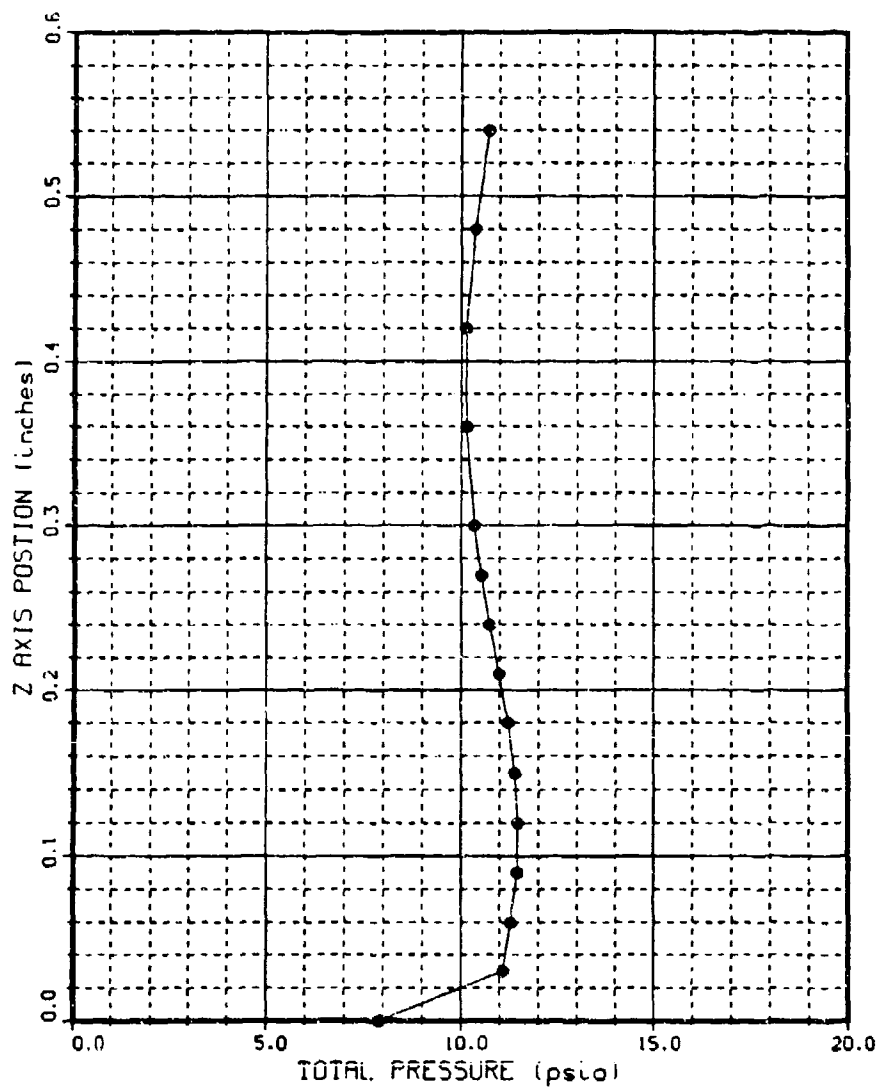


Figure 168. Run 25 Pitot Pressure Profile at $X = 13.5$ in, $p_{0j} = 18$ psia

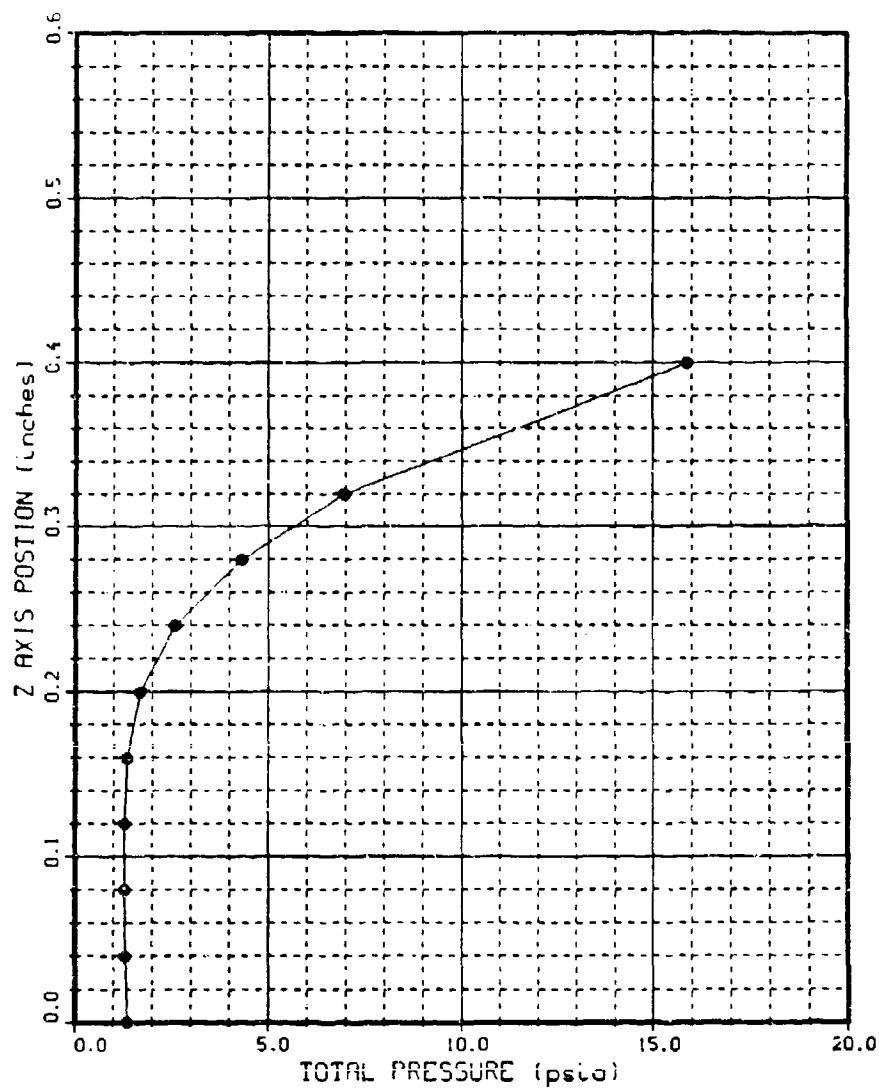


Figure 169. Run 26 Pitot Pressure Profile at X = 13 in,
 $p_{o,j} = 0$ psia

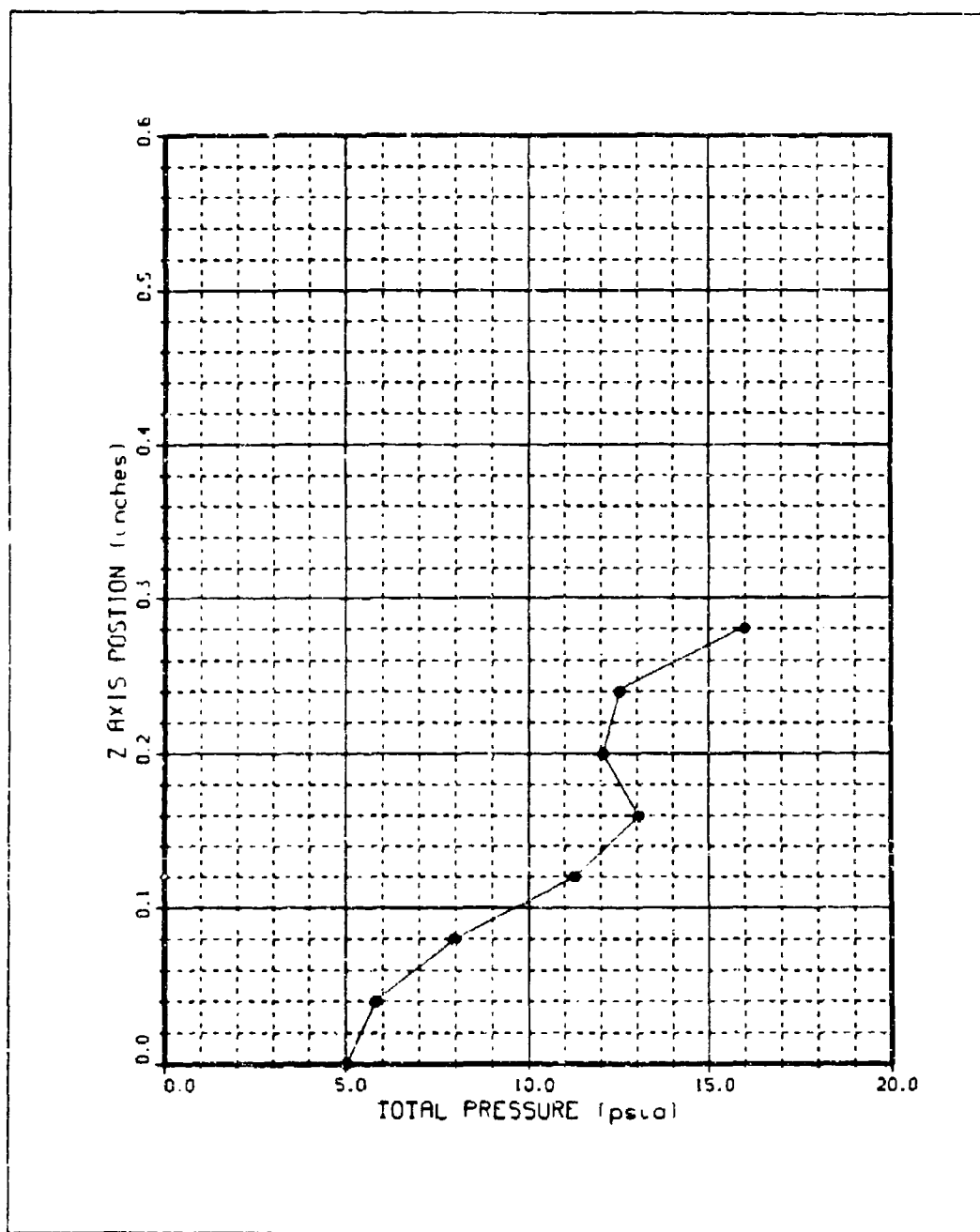


Figure 170. Run 27 Pitot Pressure Profile at $X = 13.5$ in,
 $p_{0i} = 23$ psia

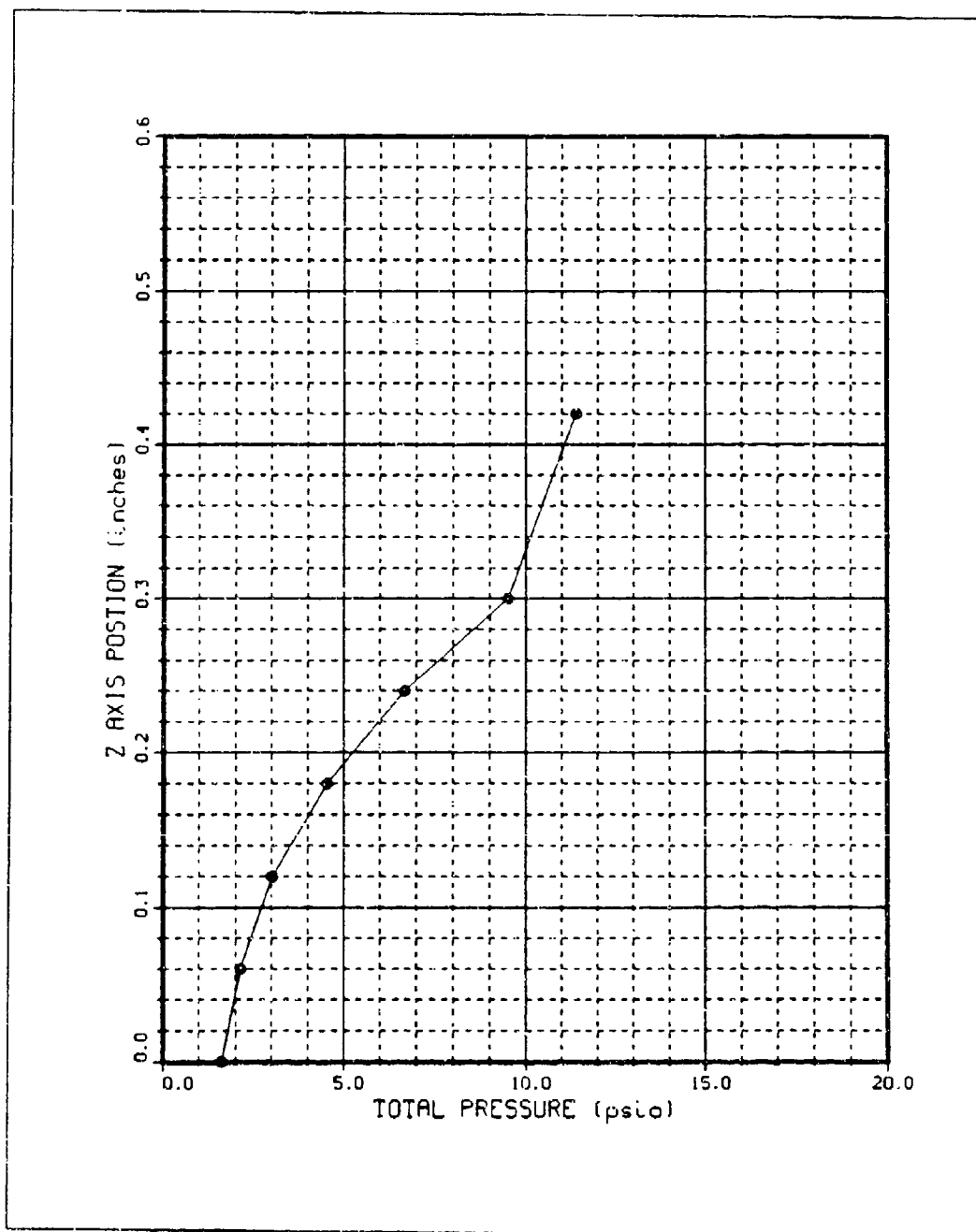


Figure 171. Run 28 Pitot Pressure Profile at $X = 14.4$ in,
 $p_{0j} = 0$ psia

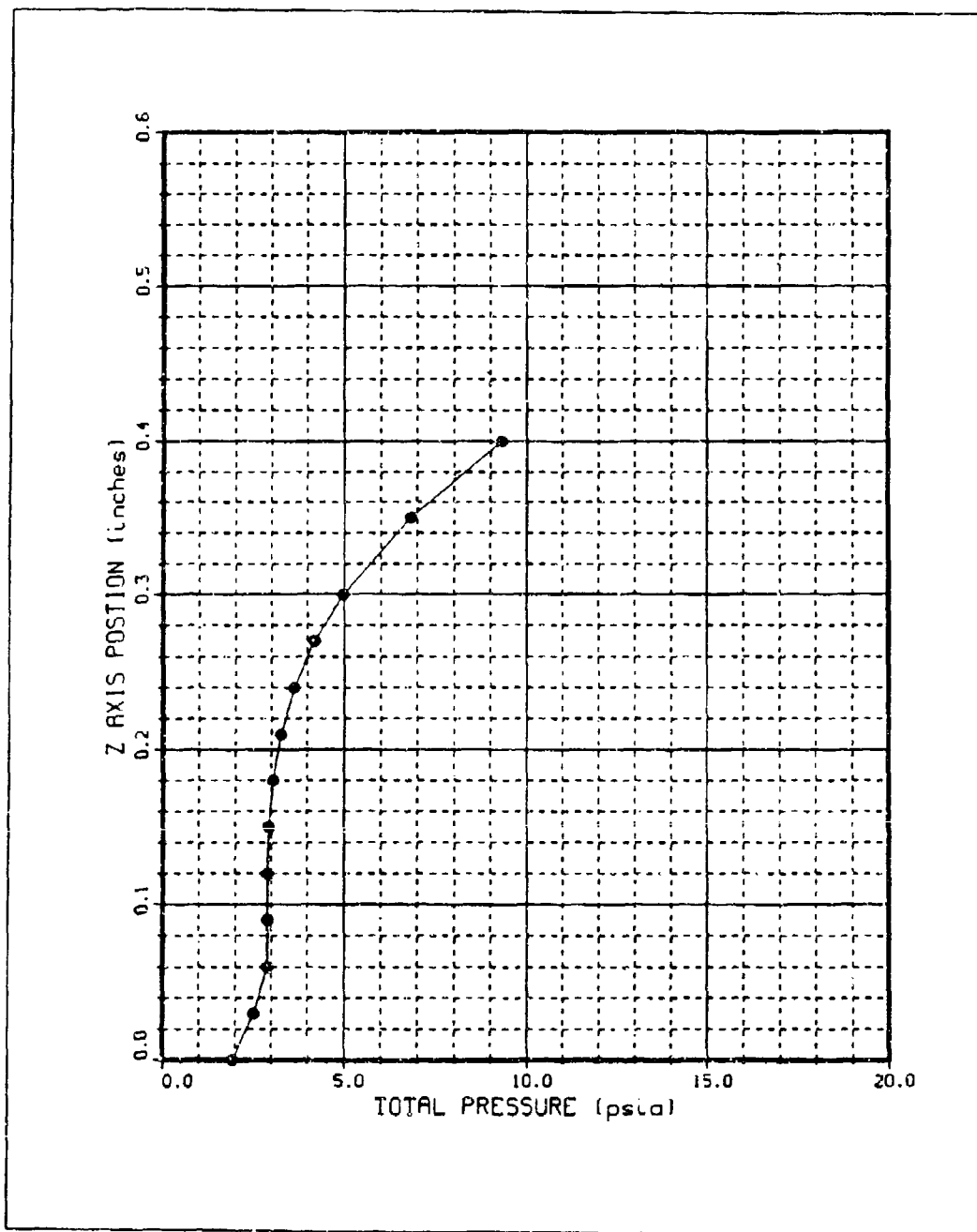


Figure 172. Run 28 Pitot Pressure Profile at X = 14.4 in,
 $p_{o,i} = 10$ psia

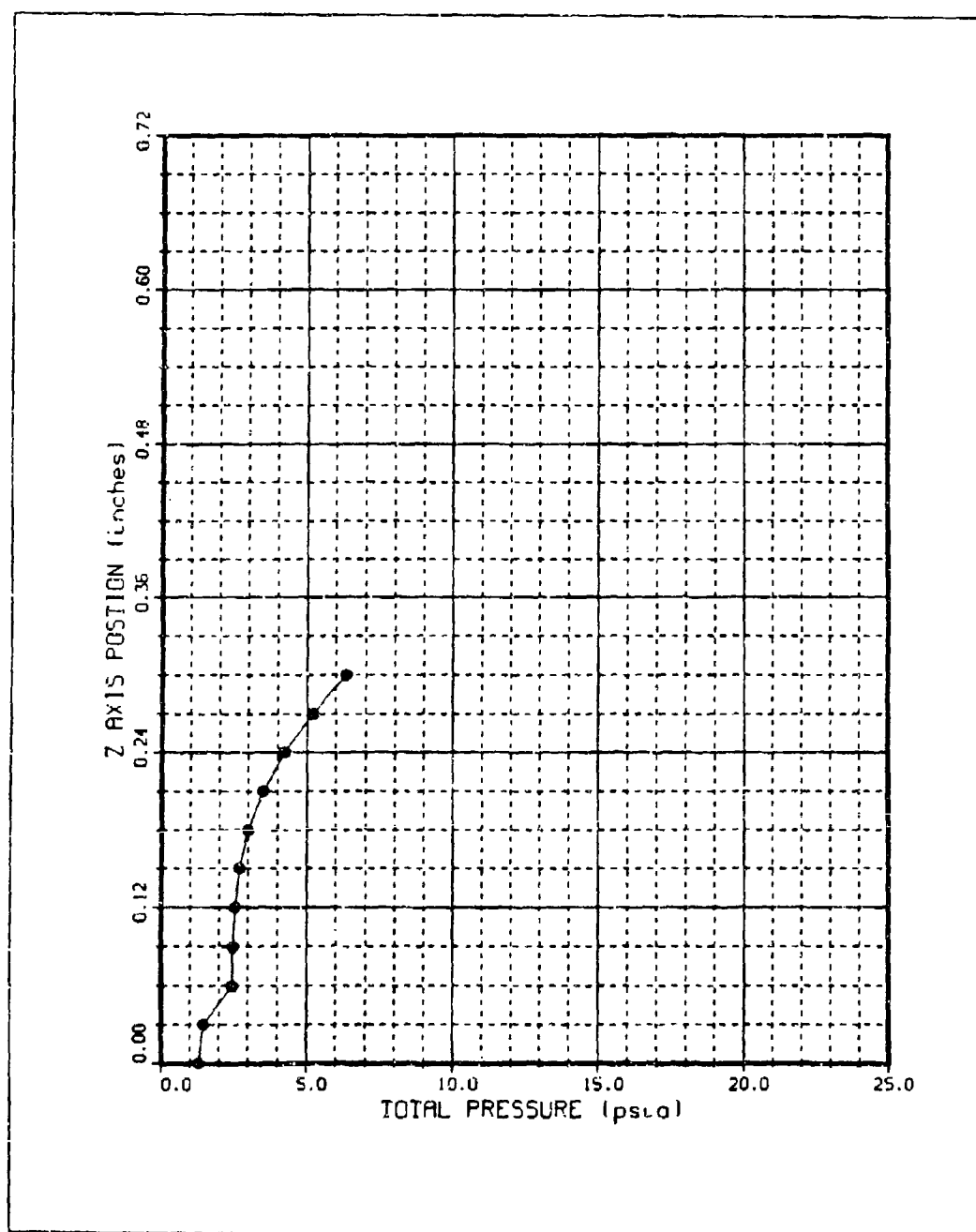


Figure 173. Run 58 Pitot Pressure Profile at $X = 14.2$ in,
 $p_{o1} = 7.6$ psia

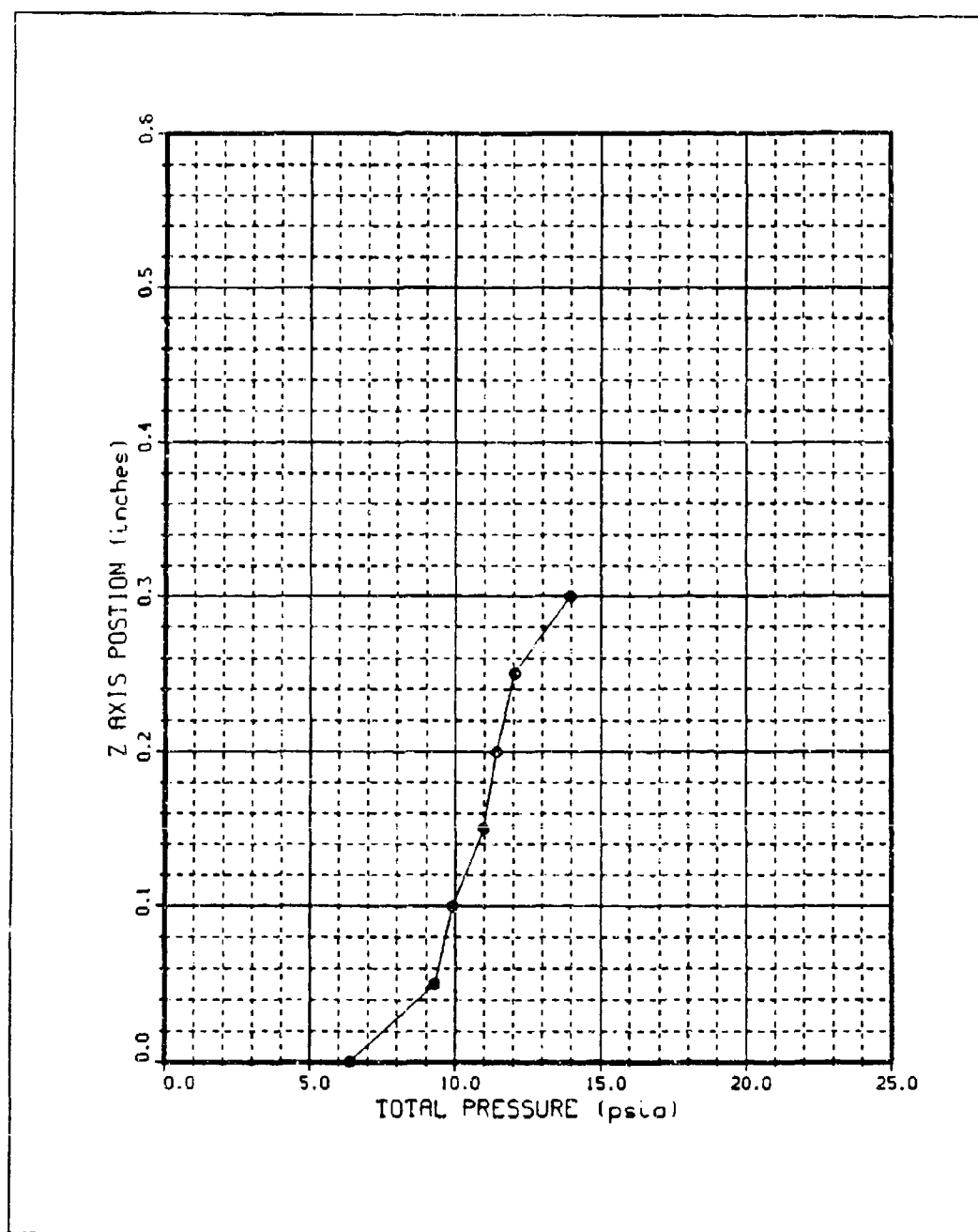


Figure 174. Run 29 Pitot Pressure Profile at $X = 14.4$ in,
 $p_{0j} = 26$ psia

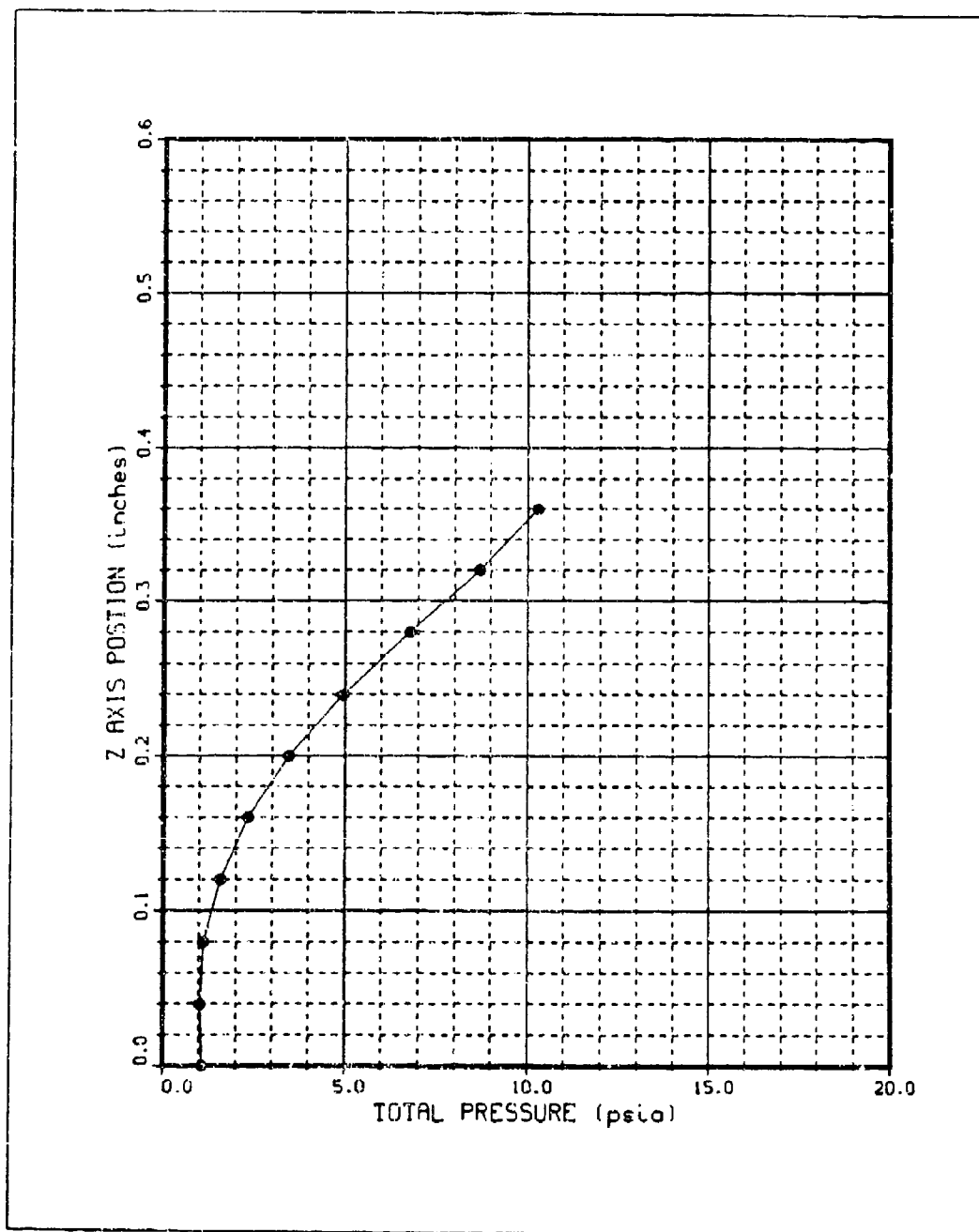


Figure 175. Run 30 Pitot Pressure Profile at X = 13 in,
 $p_{oj} = 0$ psia

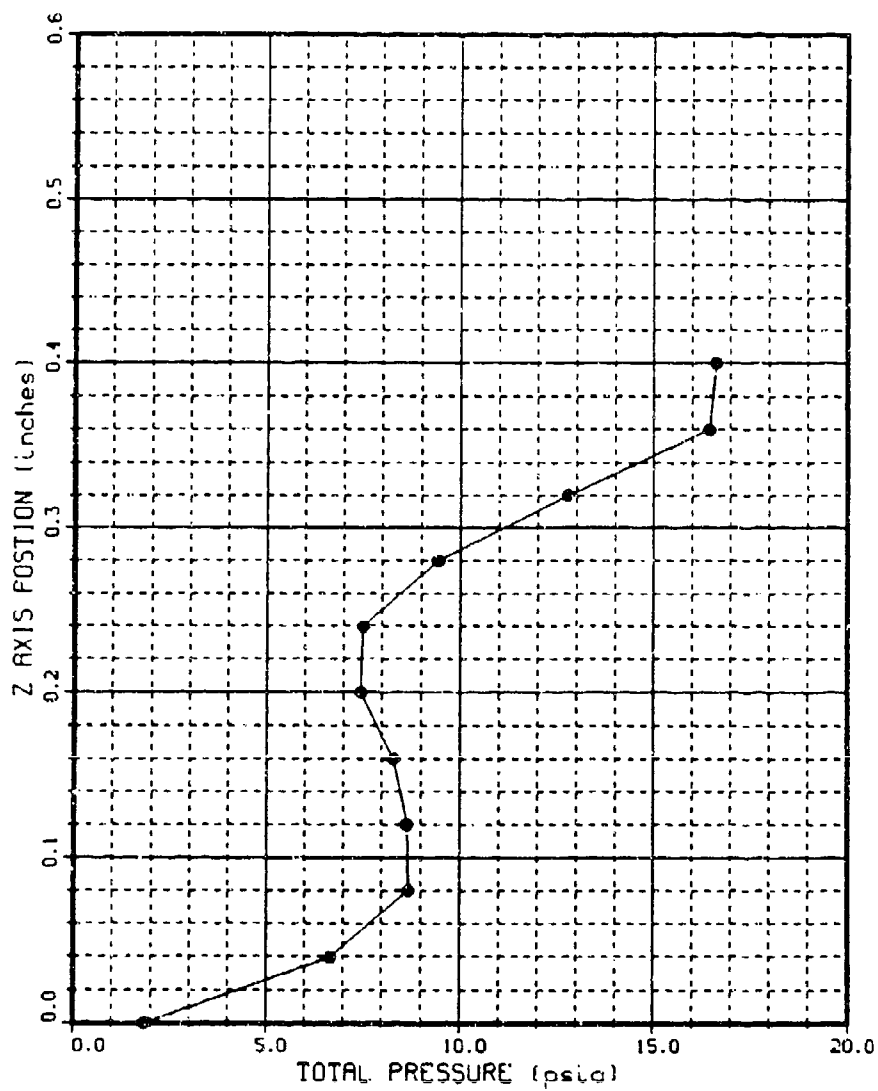


Figure 176. Run 30 Pitot Pressure Profile at X = 13 in,
 $P_{0j} = 18$ psia

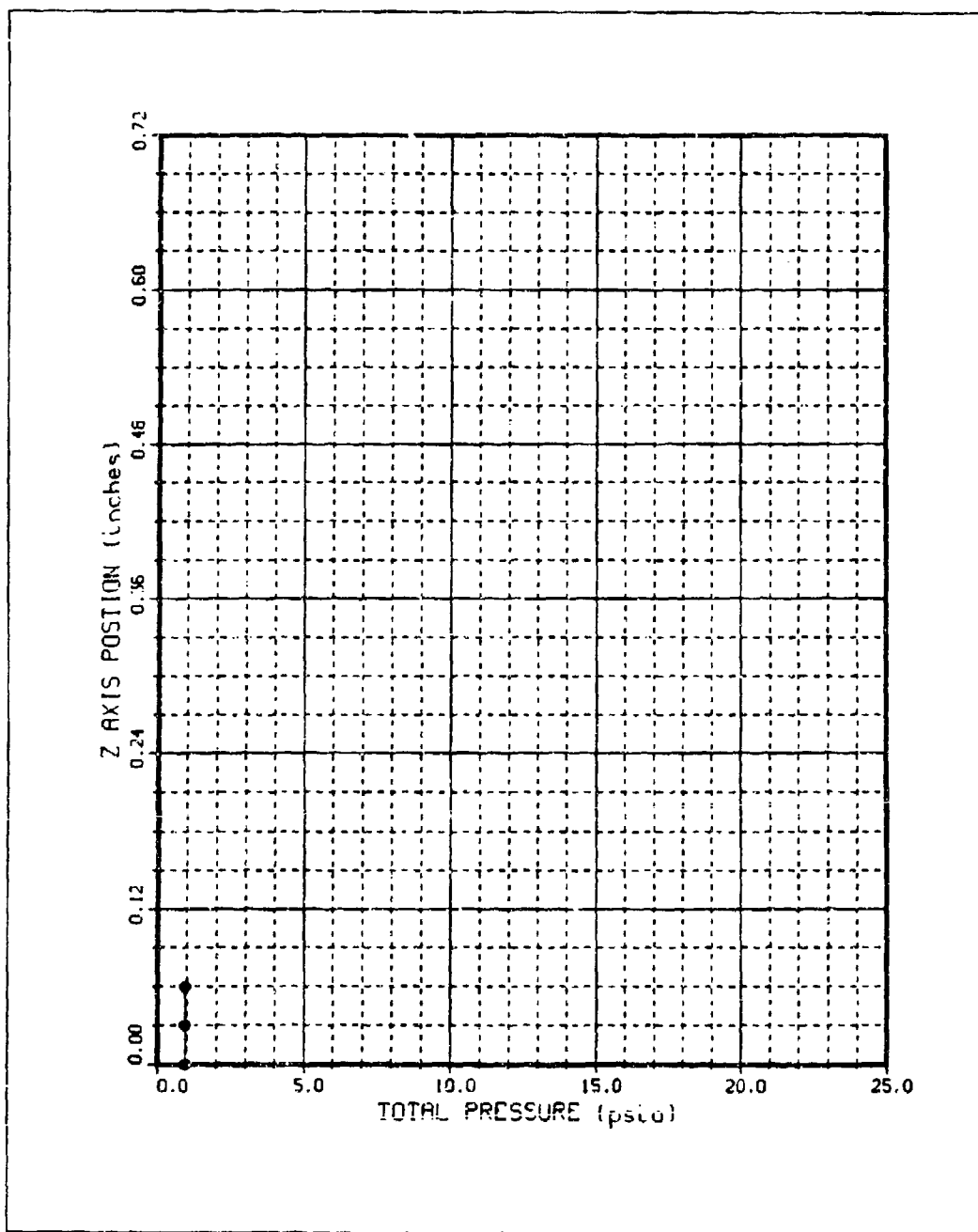


Figure 177. Run 59 Pitot Pressure Profile at X = 12.9 in,
 $P_{0j} = 6.3$ psia

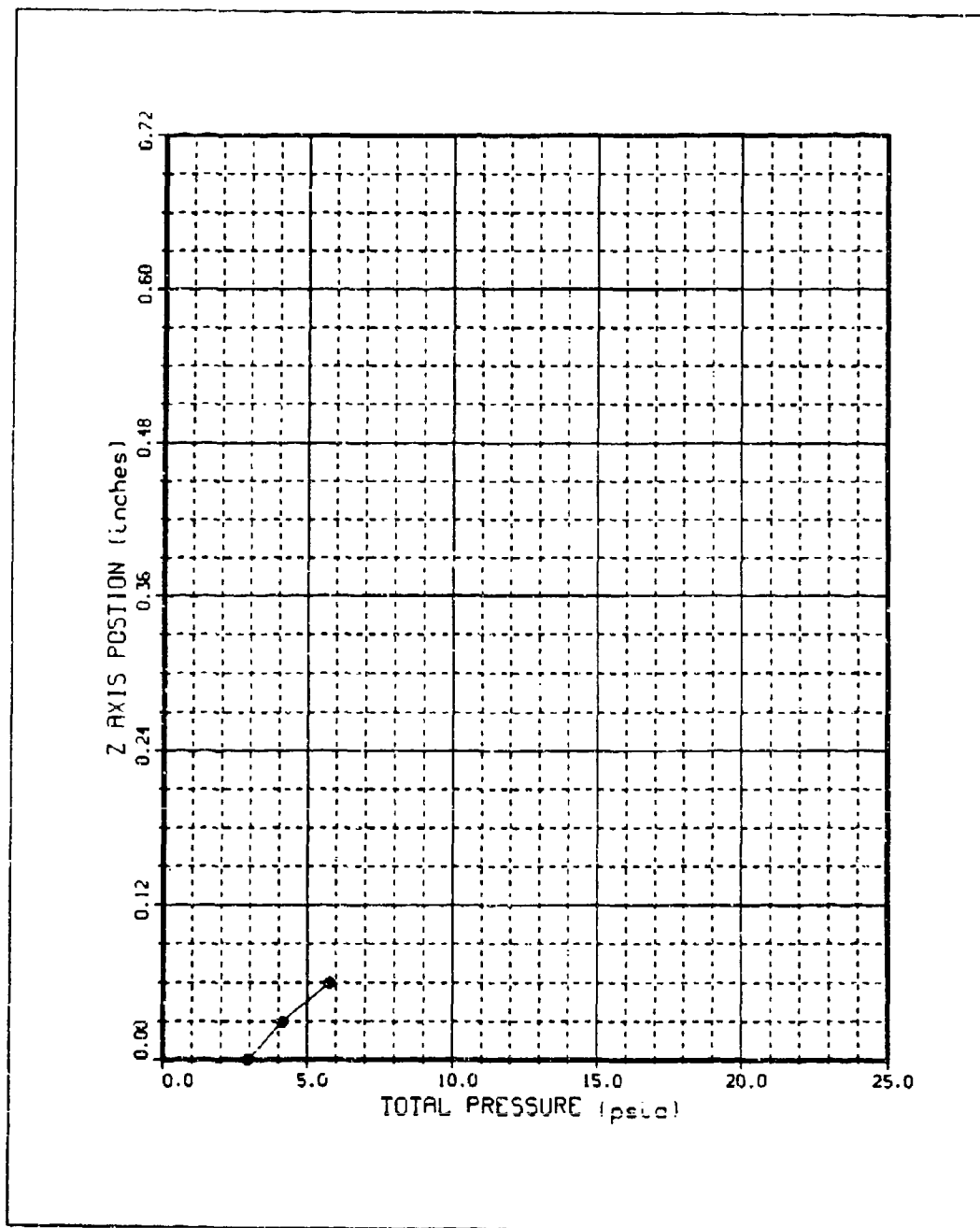


Figure 178. Run 59 Pitot Pressure Profile at $X = 12.9$ in,
 $p_{0j} = 8.6$ psia

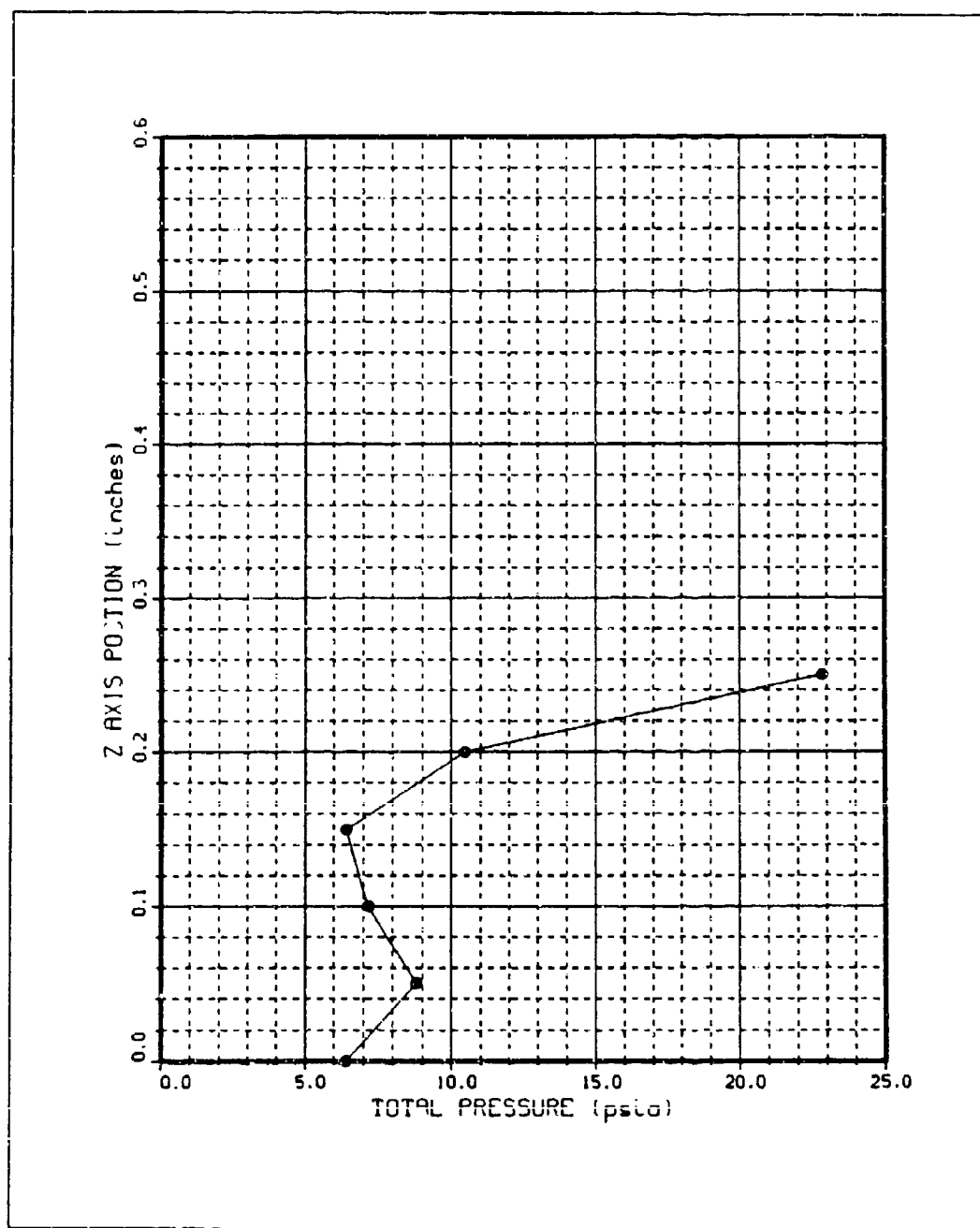


Figure 179. Run 31 Pitot Pressure Profile at $X = 13$ in,
 $P_{0j} = 15$ psia

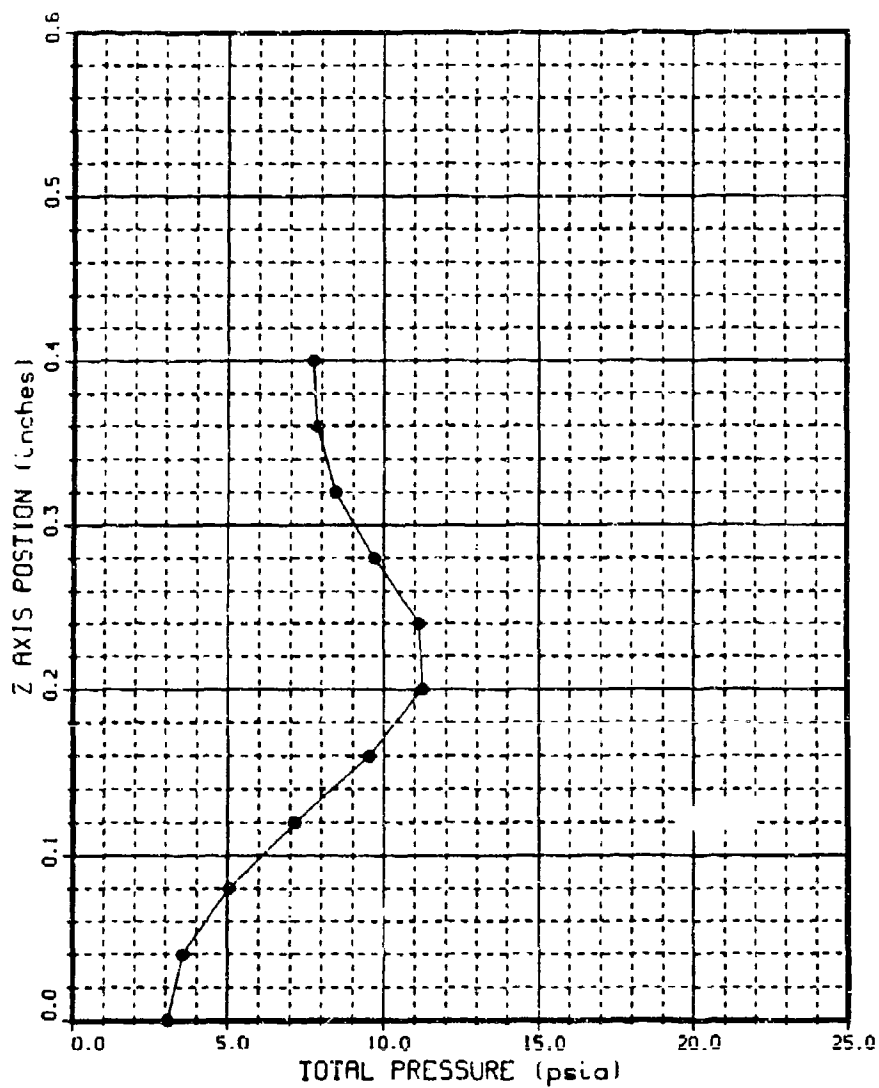


Figure 180. Run 32 Pitot Pressure Profile at $X = 13.5$ in,
 $p_{o,i} = 0$ psia

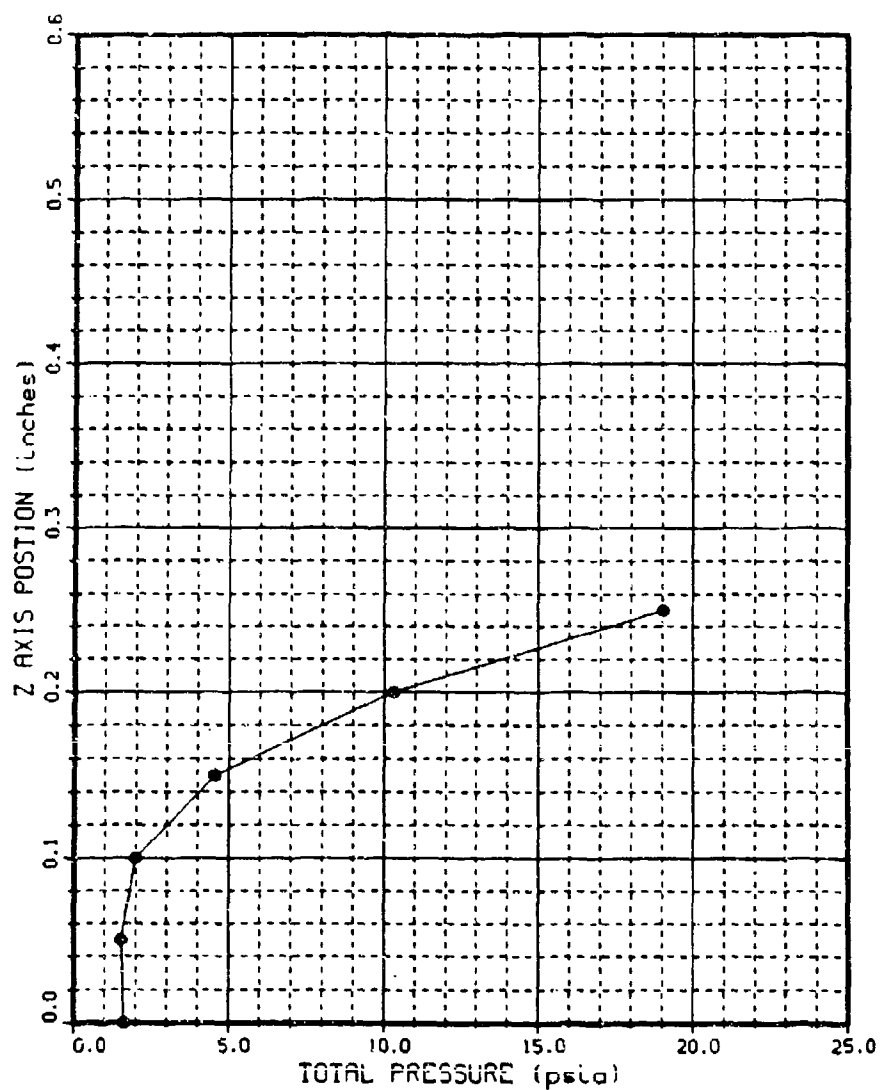


Figure 181. Run 33 Pitot Pressure Profile at X = 13 in,
 $P_{0j} = 0$ psia

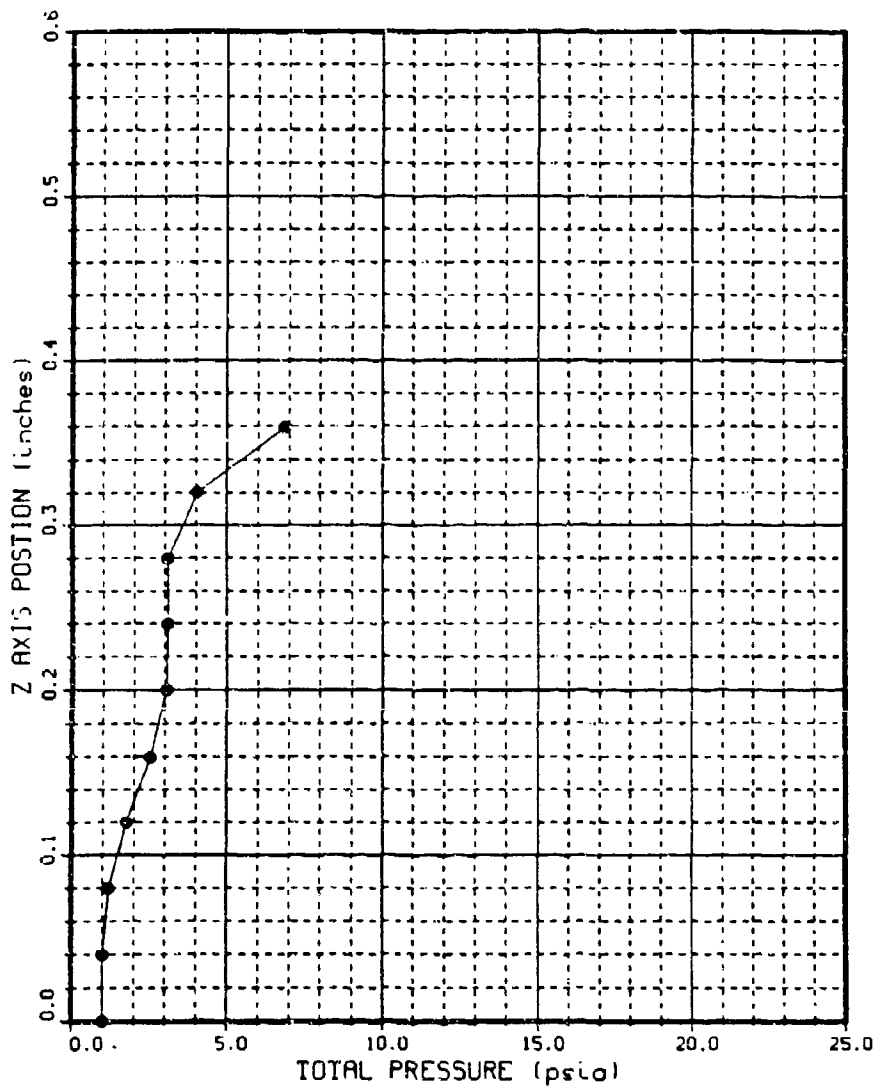


Figure 182. Run 34 Pitot Pressure Profile at $X = 13.5$ in,
 $p_{0j} = 7.6$ psia

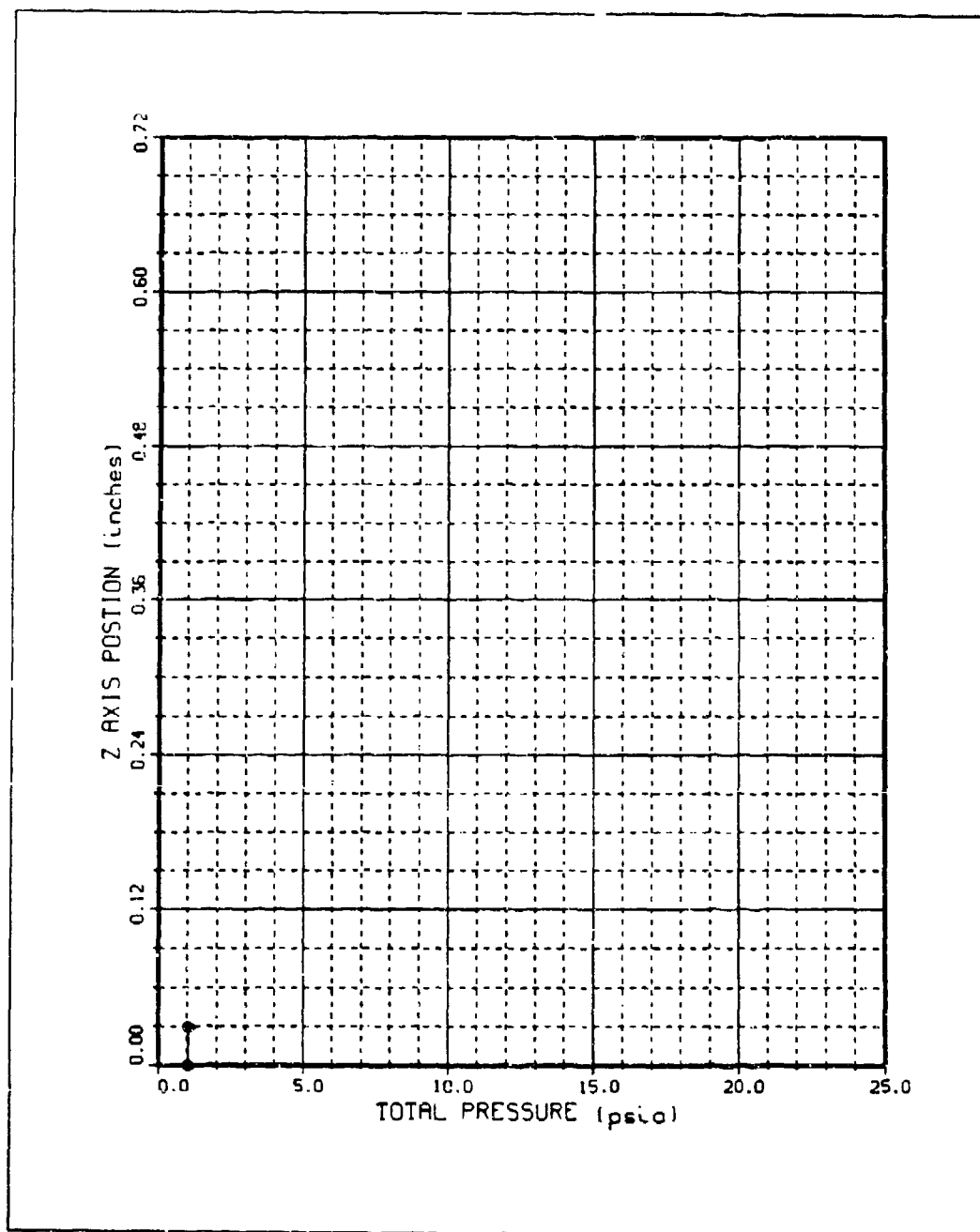


Figure 183. Run 61 Pitot Pressure Profile at X = 13.5 in,
 $P_{0j} = 7.4$ psia

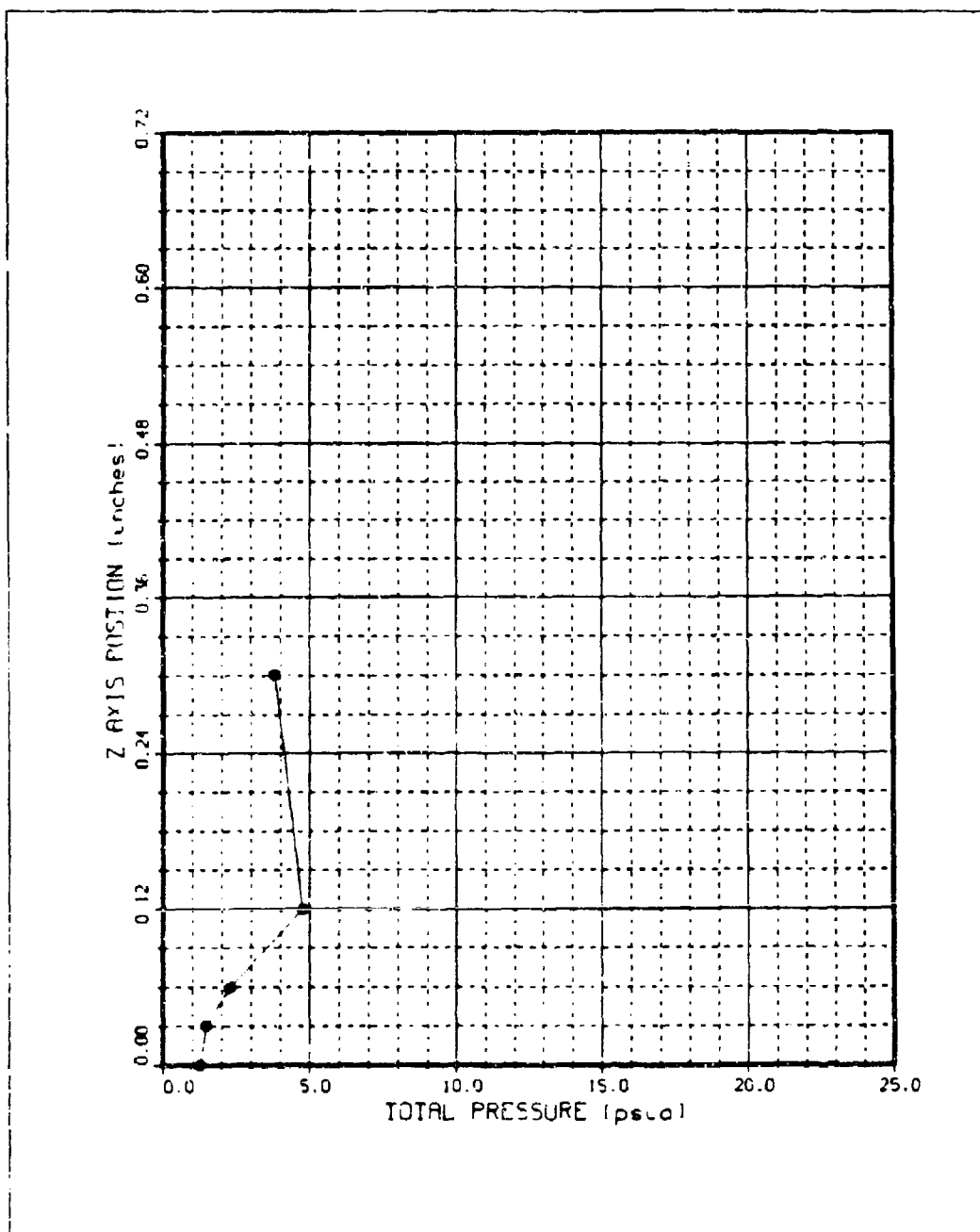


Figure 184. Run 61 Pitot Pressure Profile at X = 13.5 in,
 $p_{01} = 10$ psia

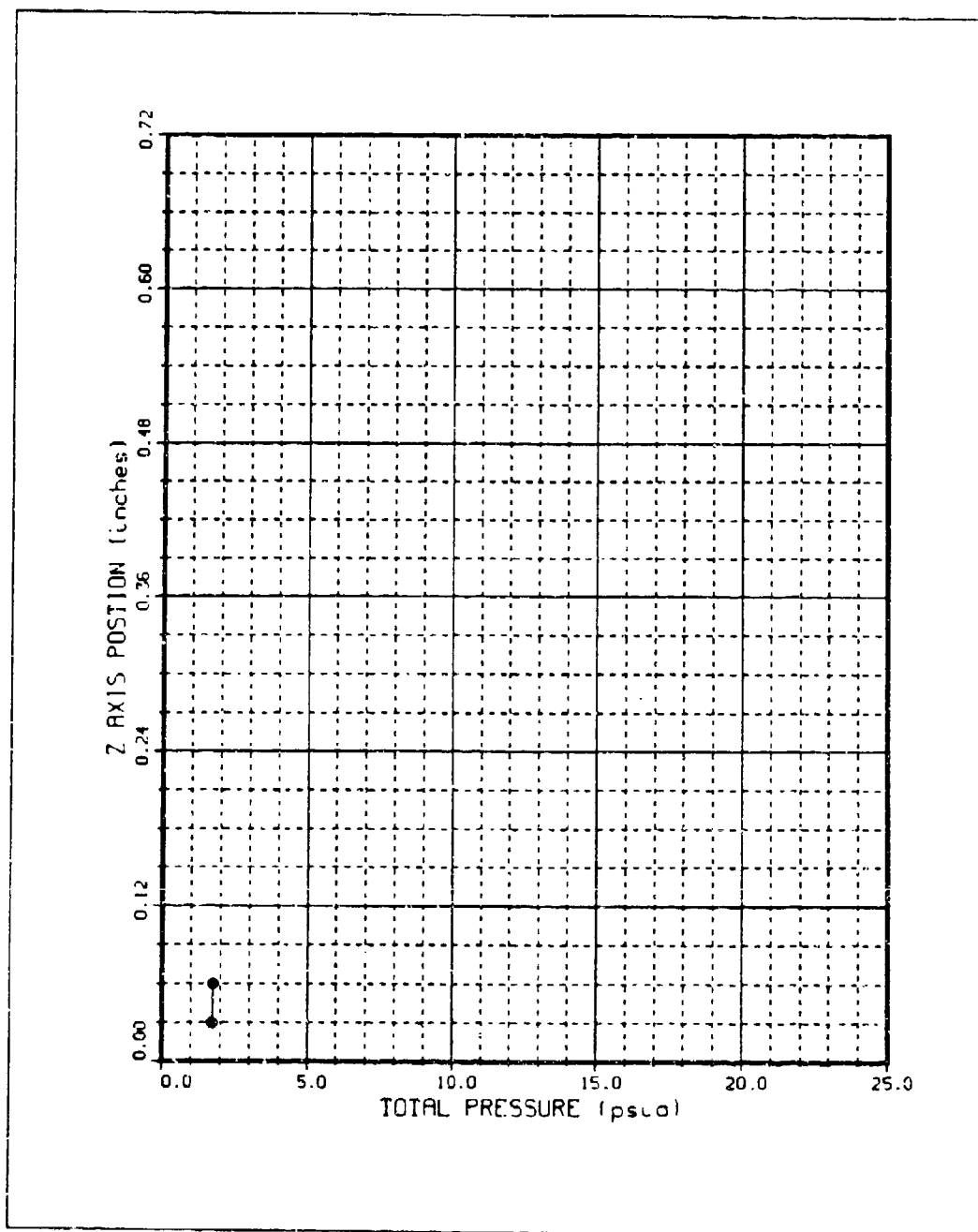


Figure 185. Run 62 Pitot Pressure Profile at $X = 13.5$ in,
 $p_{0j} = 19$ psia

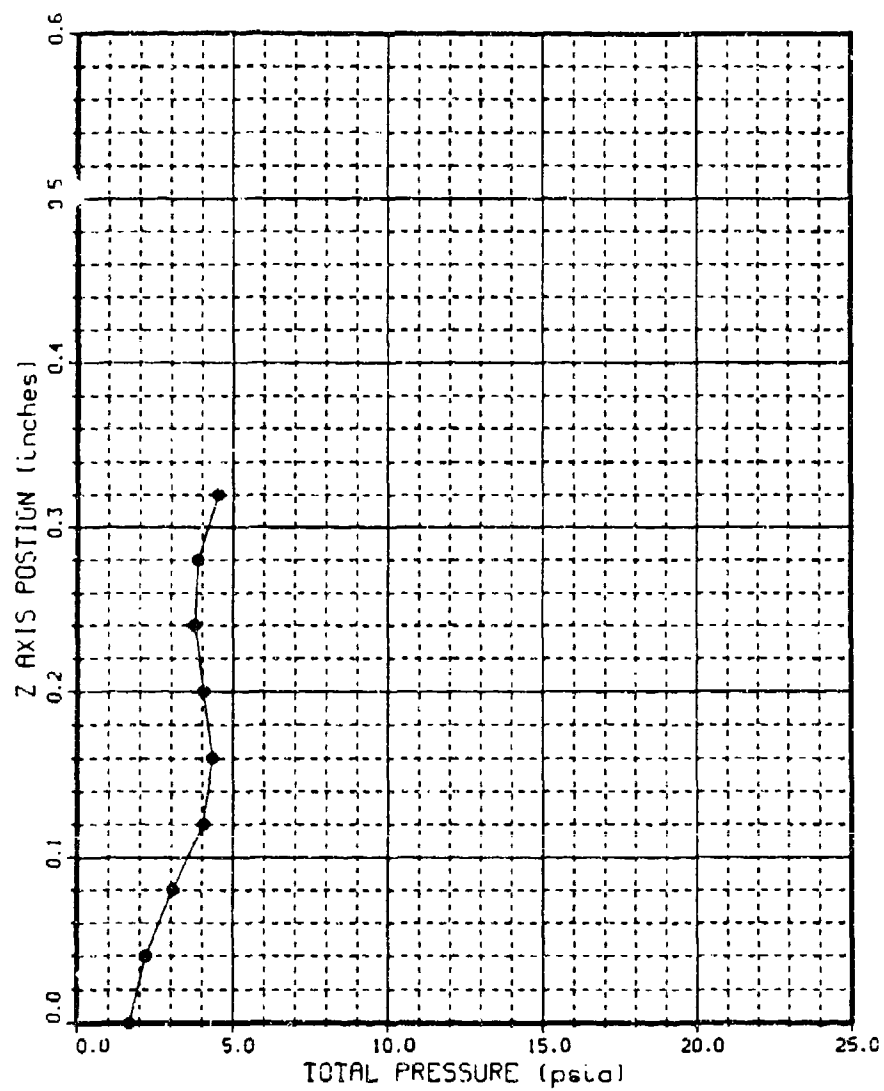


Figure 186. Run 36 Pitot Pressure Profile at X = 14.2 in,
 $p_{o,j} = 10$ psia

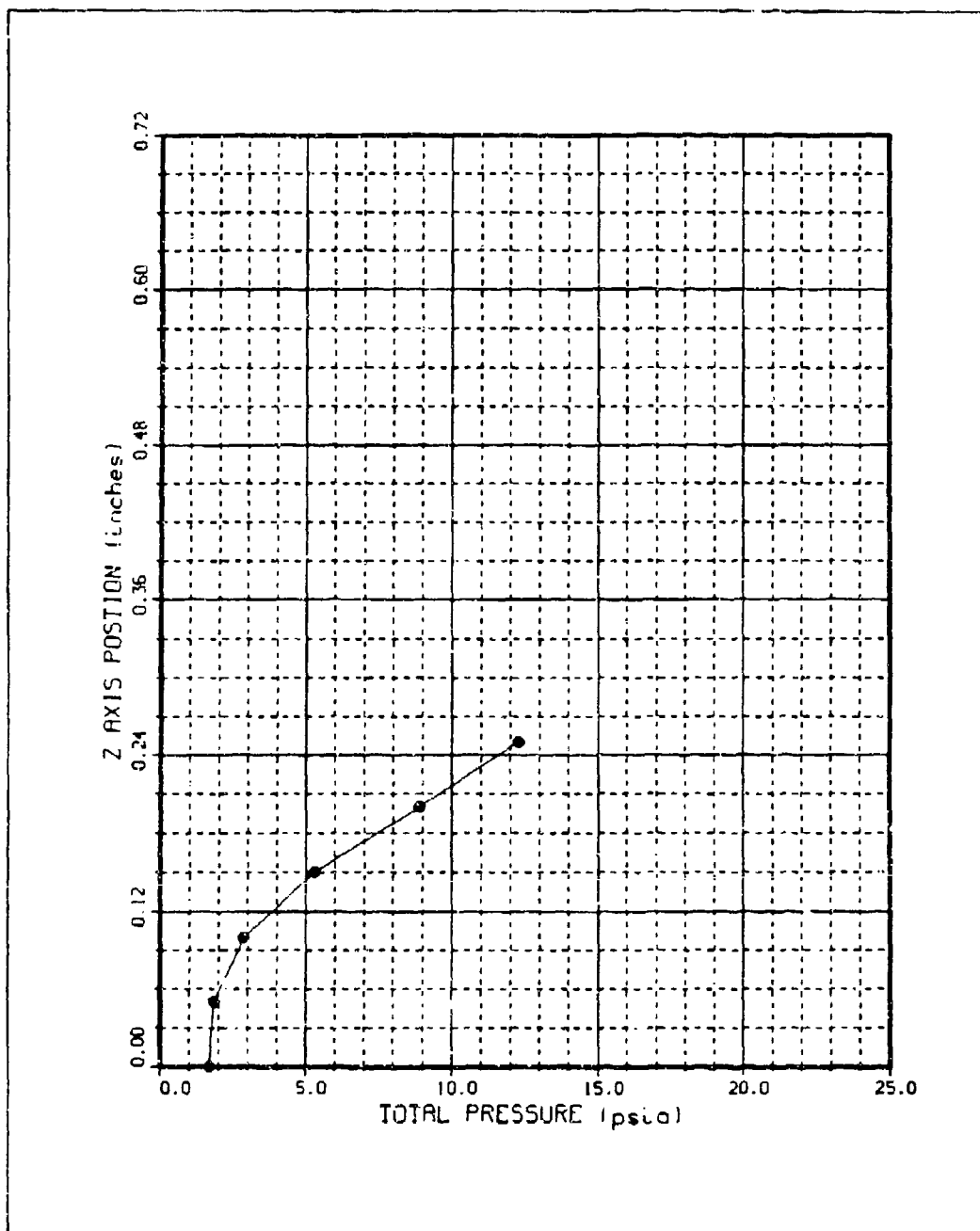


Figure 187. Run 37 Pitot Pressure Profile at $X = 14.2$ in,
 $P_{0j} = 11$ psia

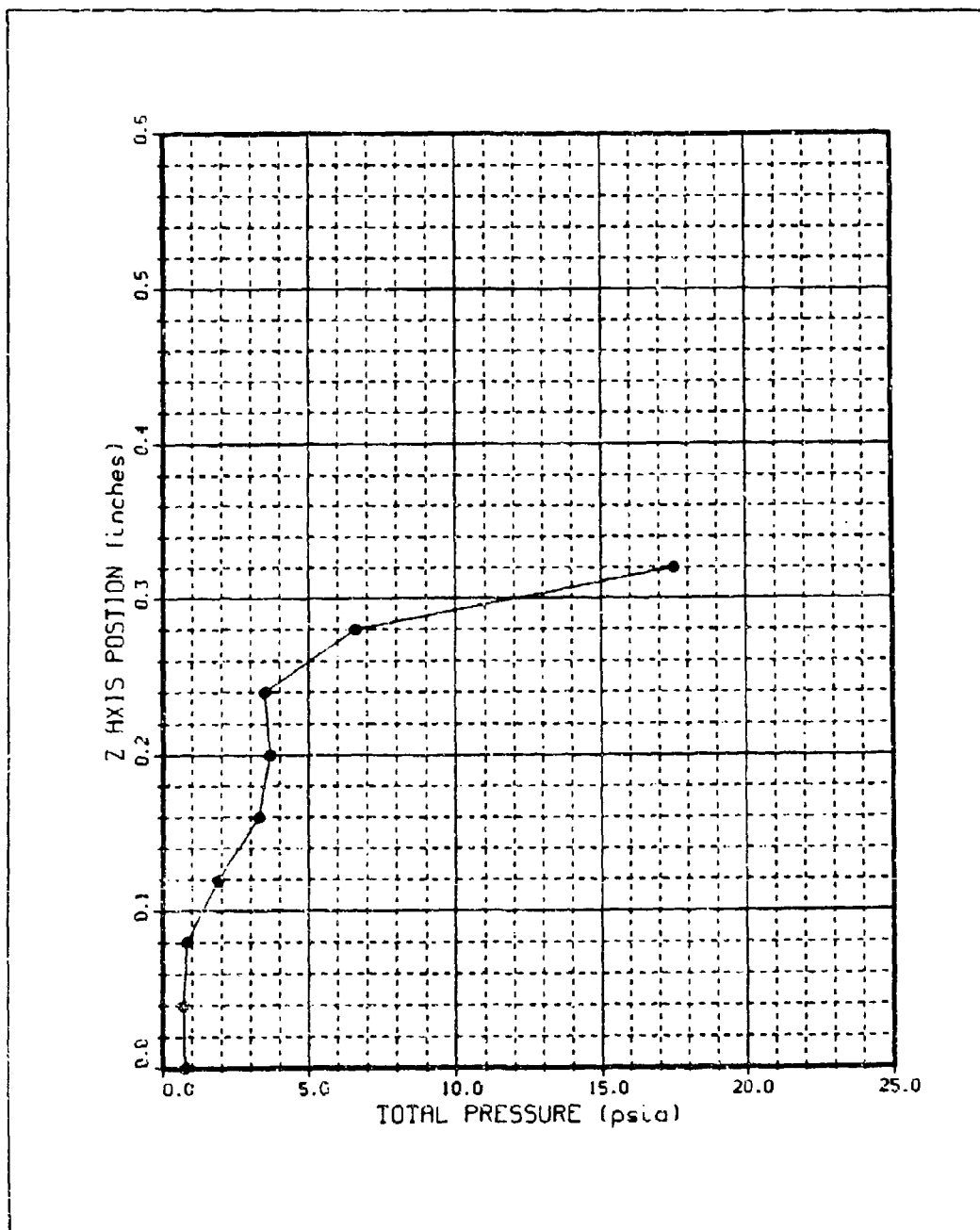


Figure 188. Run 39 Pitot Pressure Profile at X = 12.6 in,
 $p_{0j} = 6.2$ psia

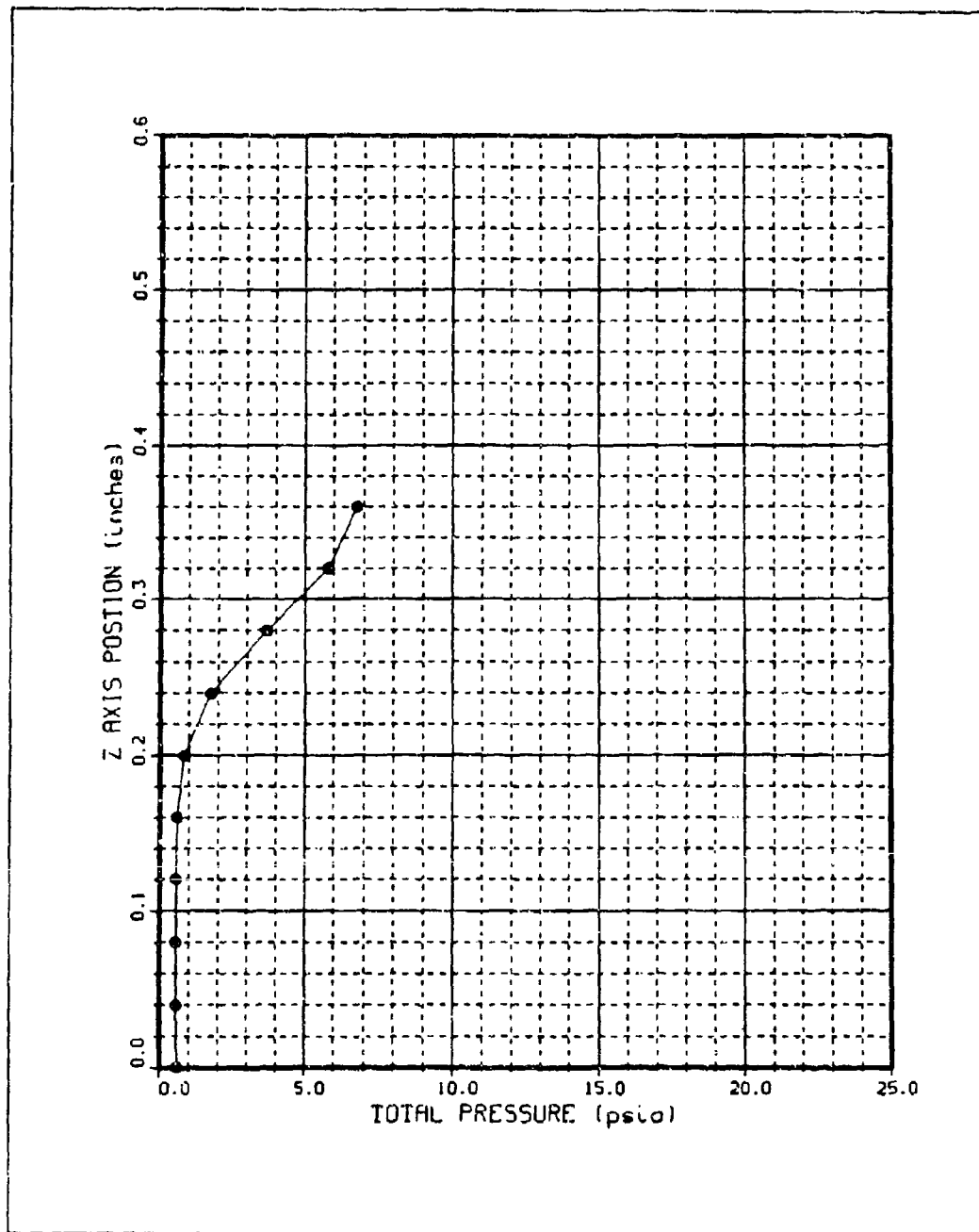


Figure 189. Run 41 Pitot Pressure Profile at X = 14.5 in,
 $p_{o_j} = 27$ psia

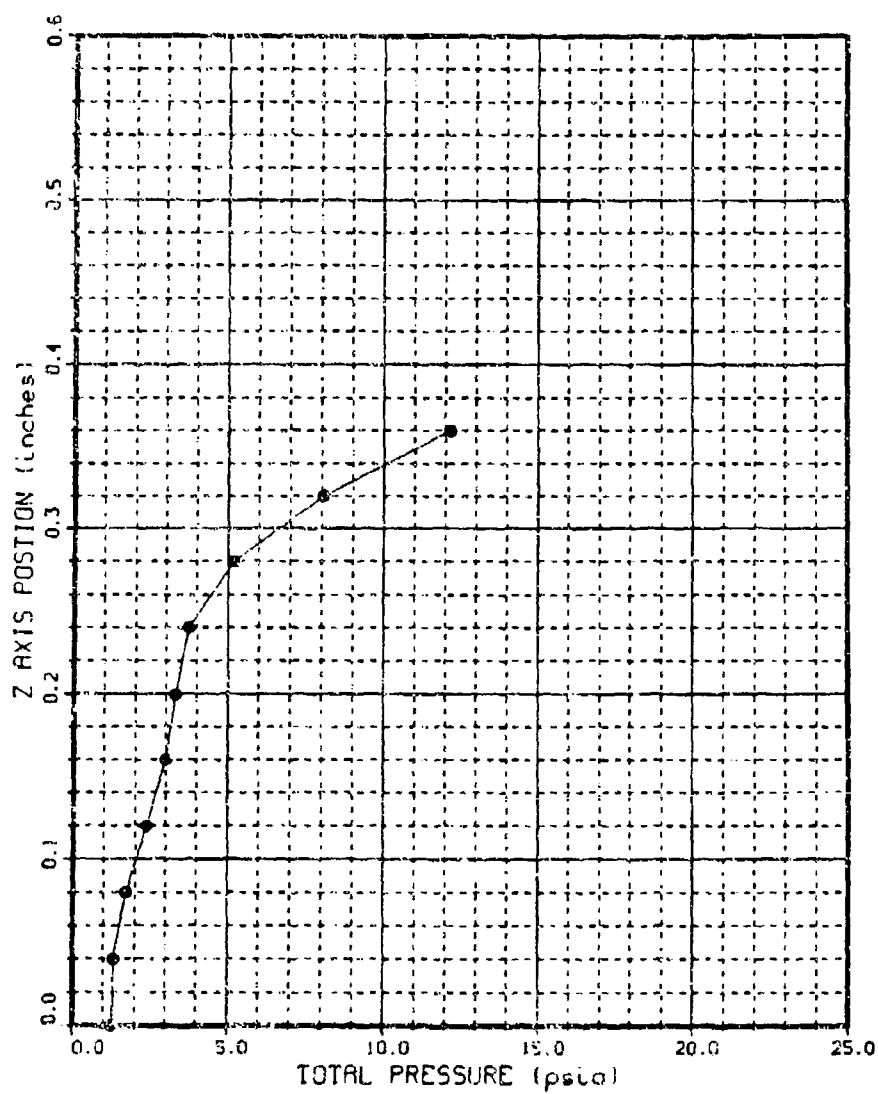


Figure 190. Run 43 Pitot Pressure Profile at $X = 13.5$ in,
 $P_{0j} = 7.9$ psia

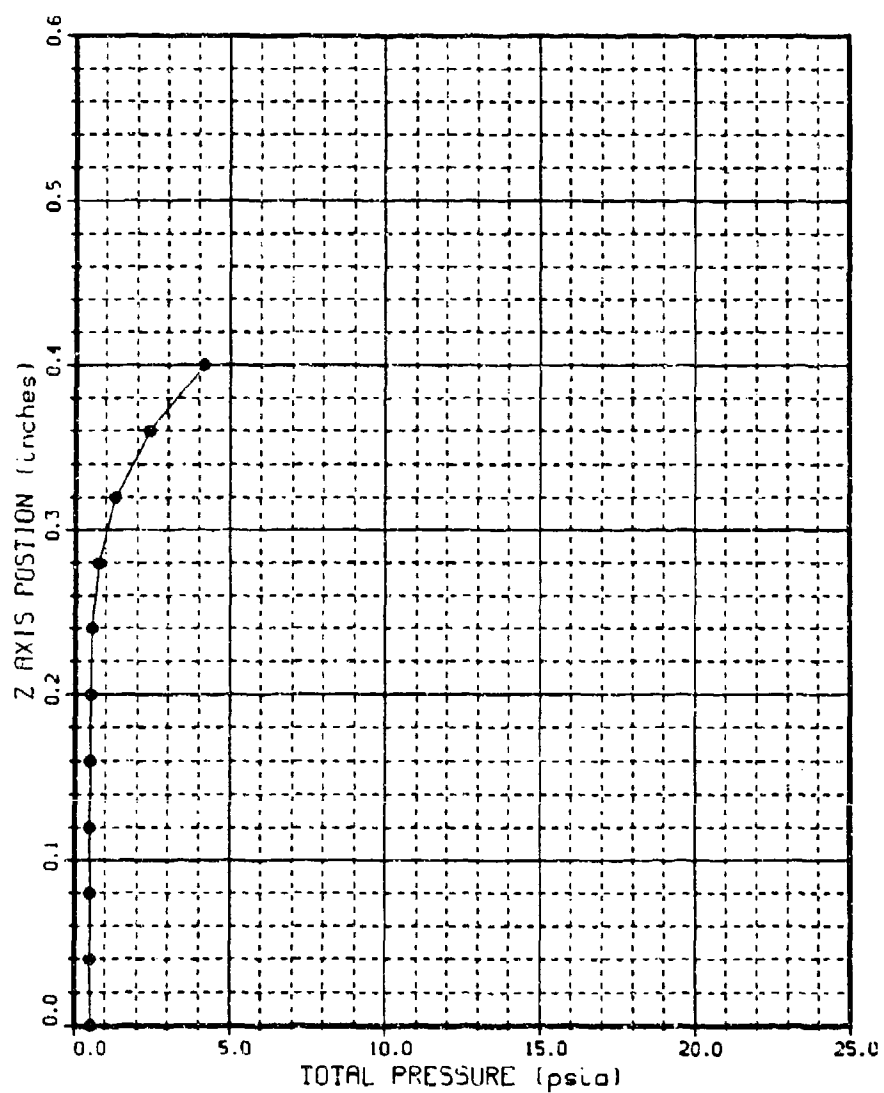


Figure 191. Run 44 Pitot Pressure Profile at $X = 15.5$ in,
 $p_{0j} = 24$ psia

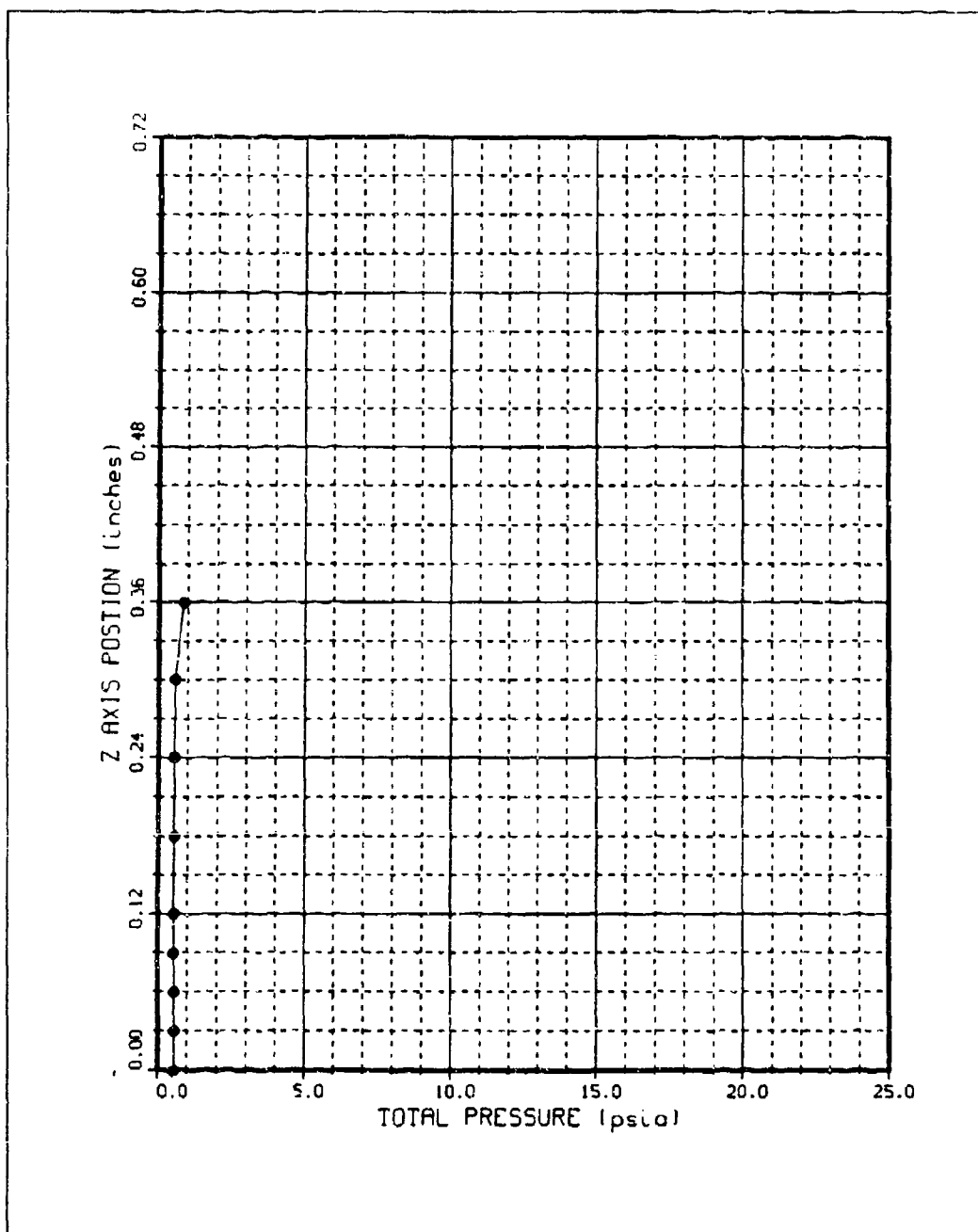


Figure 192. Run 54 Pitot Pressure Profile at $X = 15.3$ in,
 $p_{0j} = 46$ psia

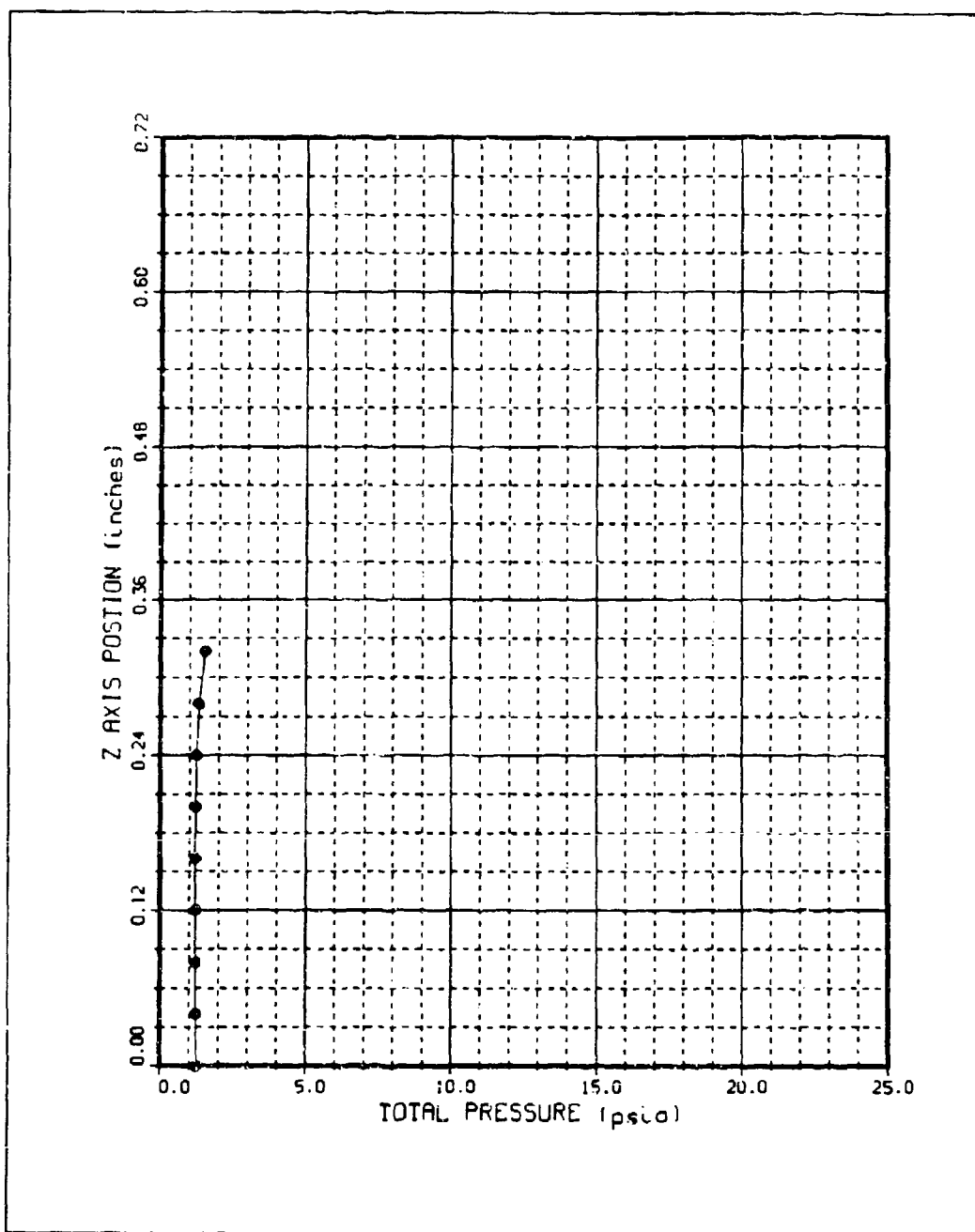


Figure 193. Run 55 Pitot Pressure Profile at X = 15.3 in,
 $p_{0j} = 46$ psia

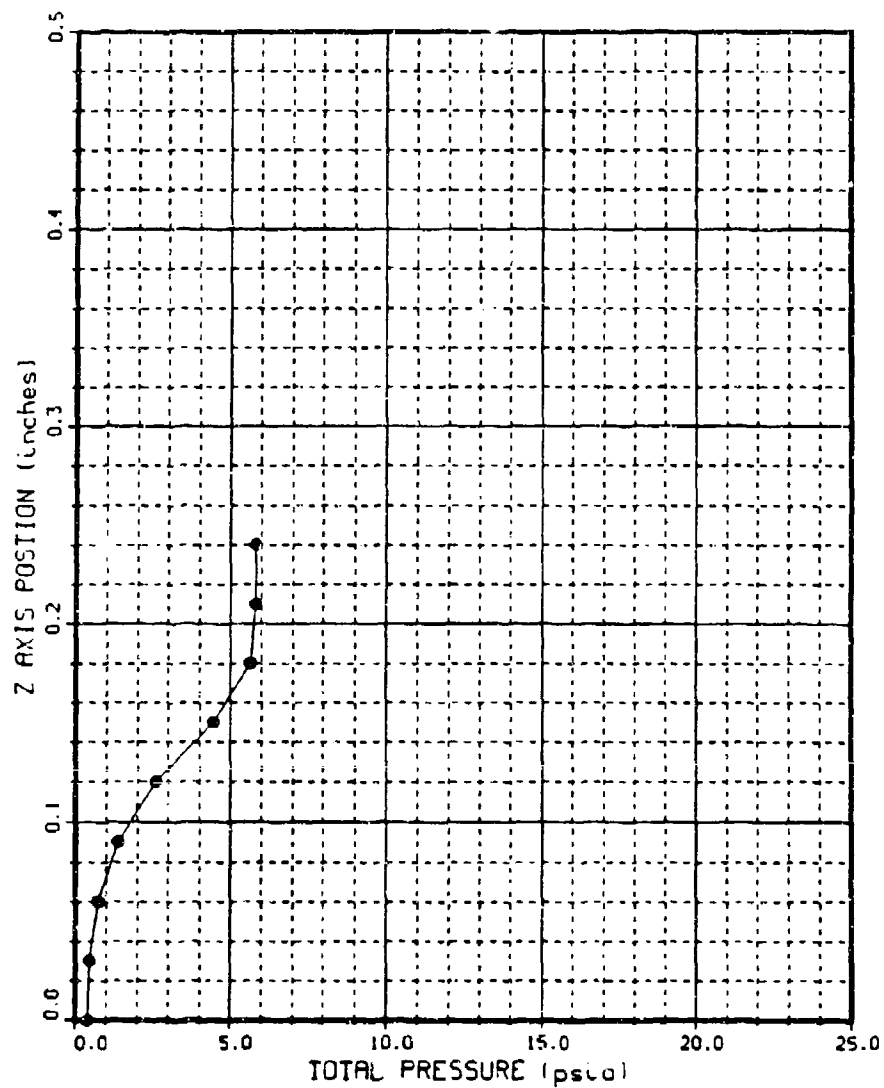


Figure 194. Run 51 Pitot Pressure Profile at $X = 10.5$ in,
 $p_{0j} = 0$ psia

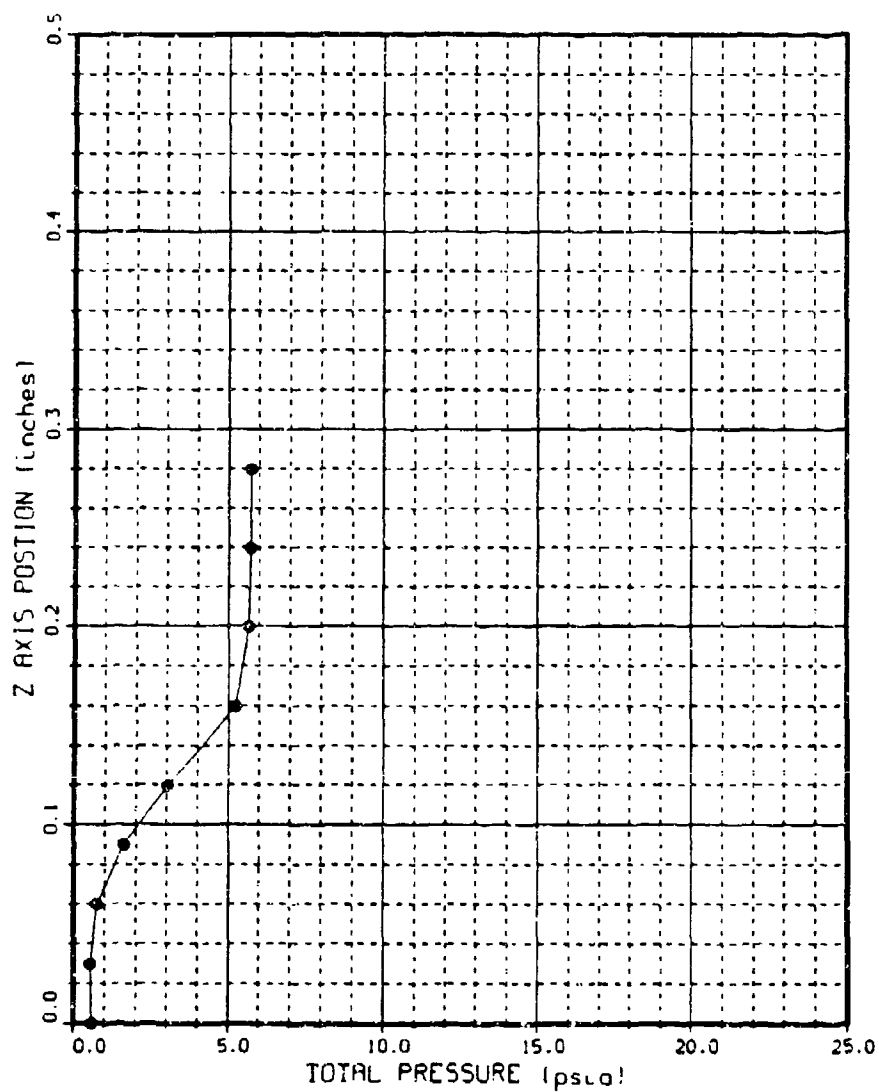


Figure 195. Run 51 Pitot Pressure Profile at $X = 11.5$ in,
 $P_{0j} = 0$ psia

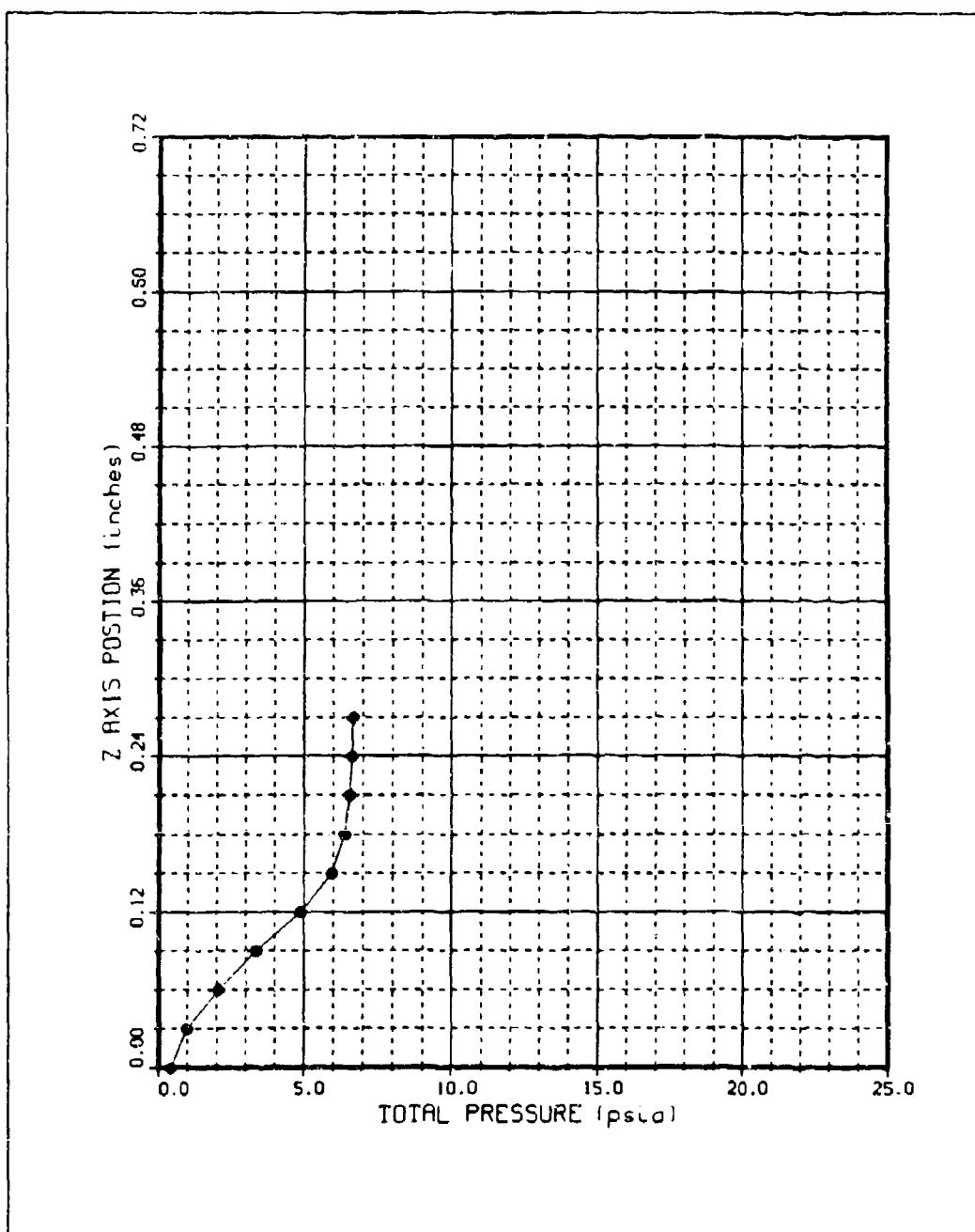


Figure 196. Run 53 Pitot Pressure Profile at $X = 11.5$ in,
 $p_{0i} = 0$ psia

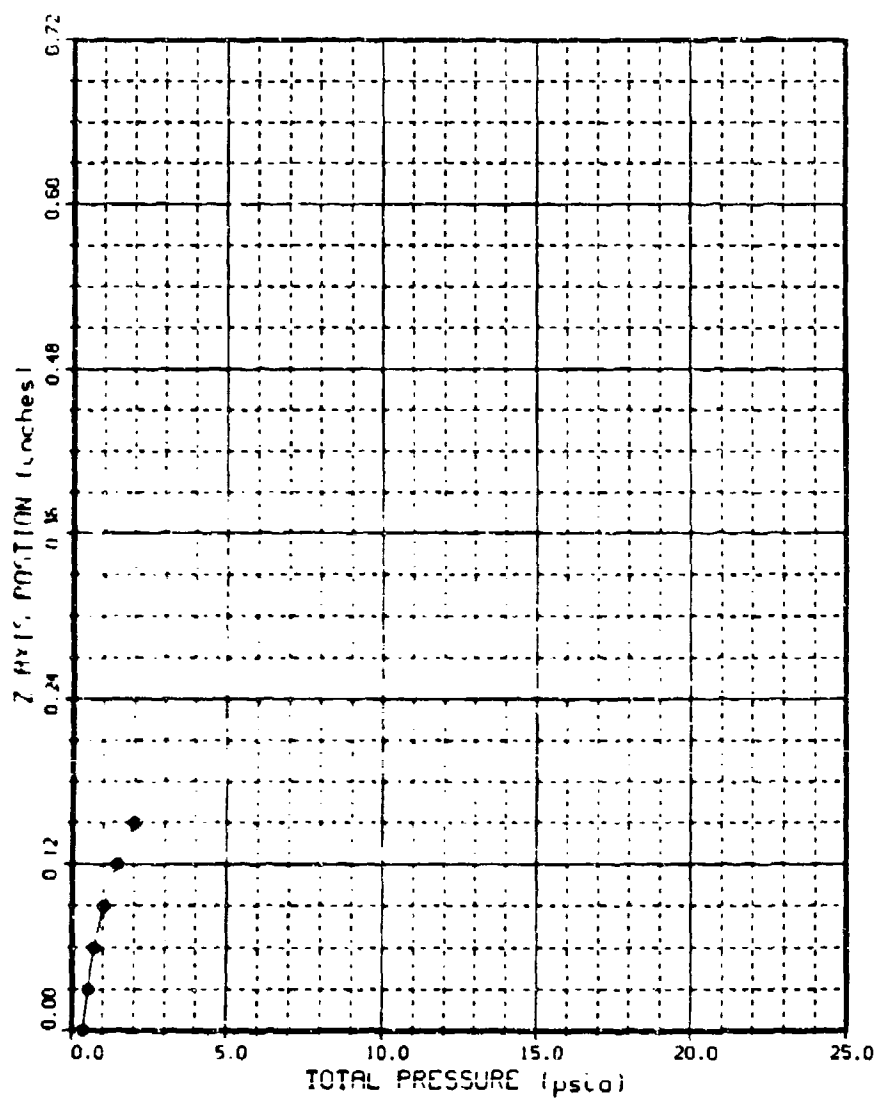


Figure 197. Run 53 Pitot Pressure Profile at $X = 14$ in,
 $P_{0j} = 0$ psia

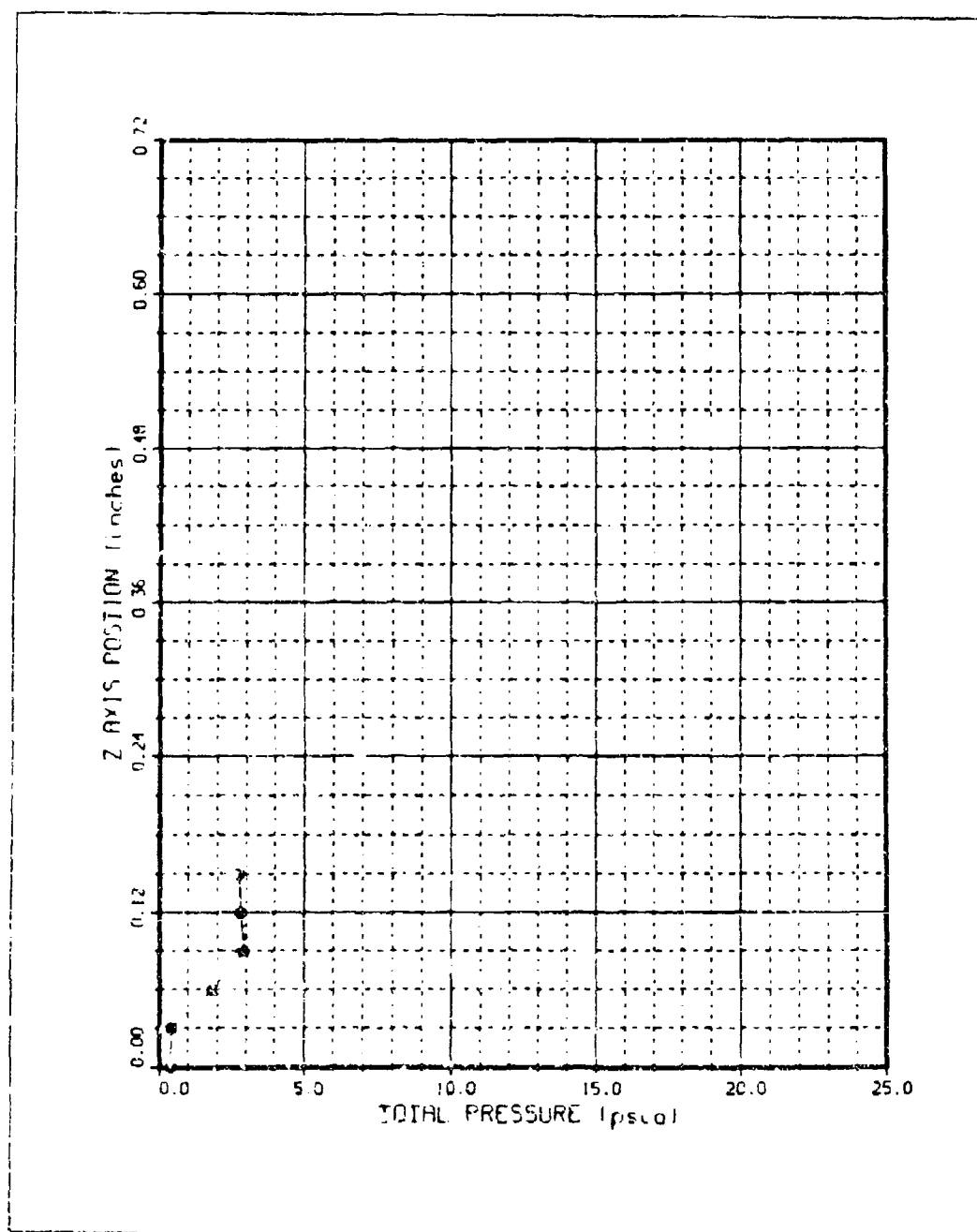


Figure 198. Run 53 Pitot Pressure Profile at X = 14 in,
 $p_{01} = 10$ psia

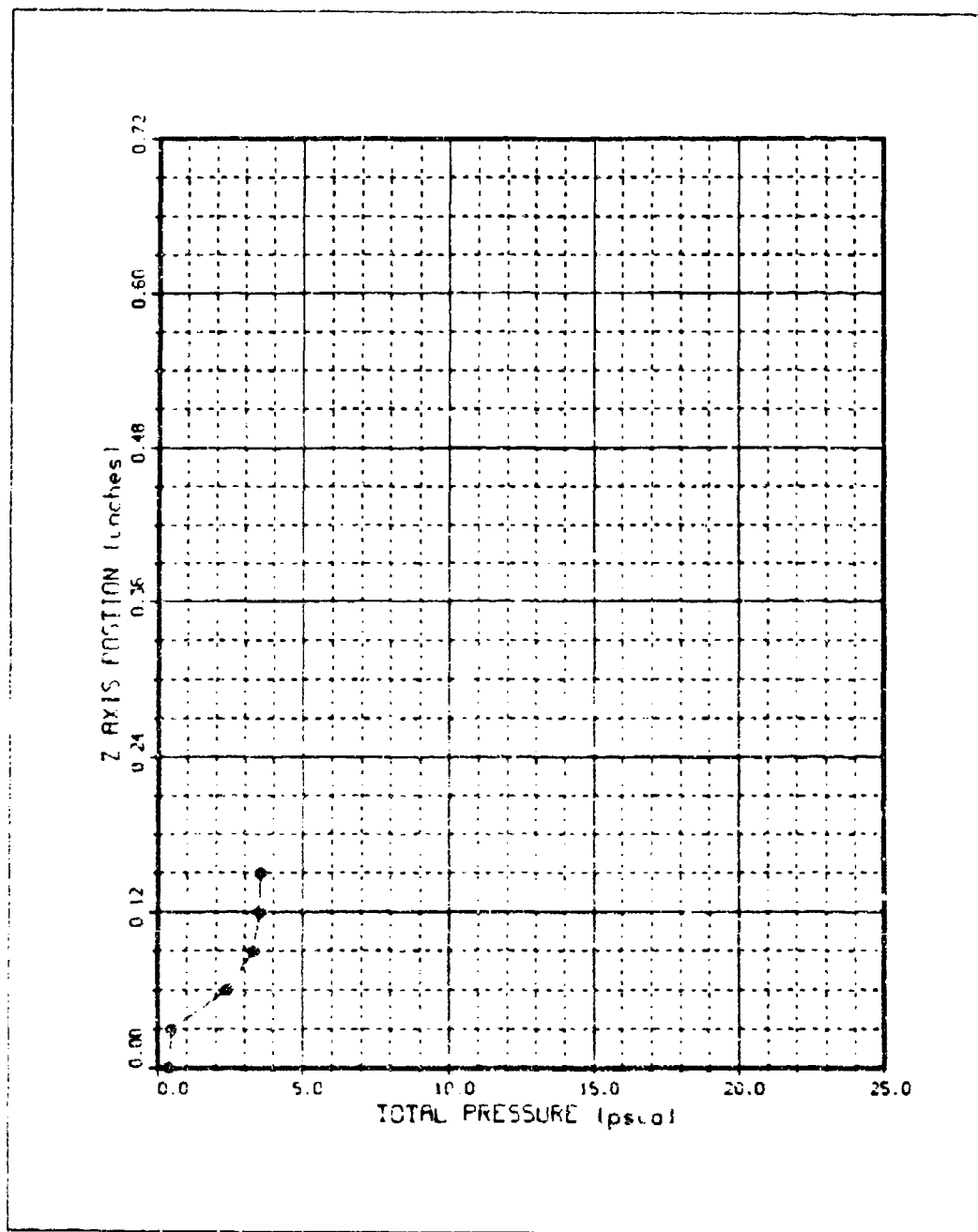


Figure 199. Run 53 Pitot Pressure Profile at X = 14 in,
 $p_{01} = 20$ psia

Appendix I

Pitot Pressure vs TMI Pressure Plots

These graphs were created by positioning the pitot pressure probe tip in the separation bubble/impingement zone just off the surface while incrementally increasing the TMI pressure. The plot for Run 58 is displayed in the main text in Figure 47.

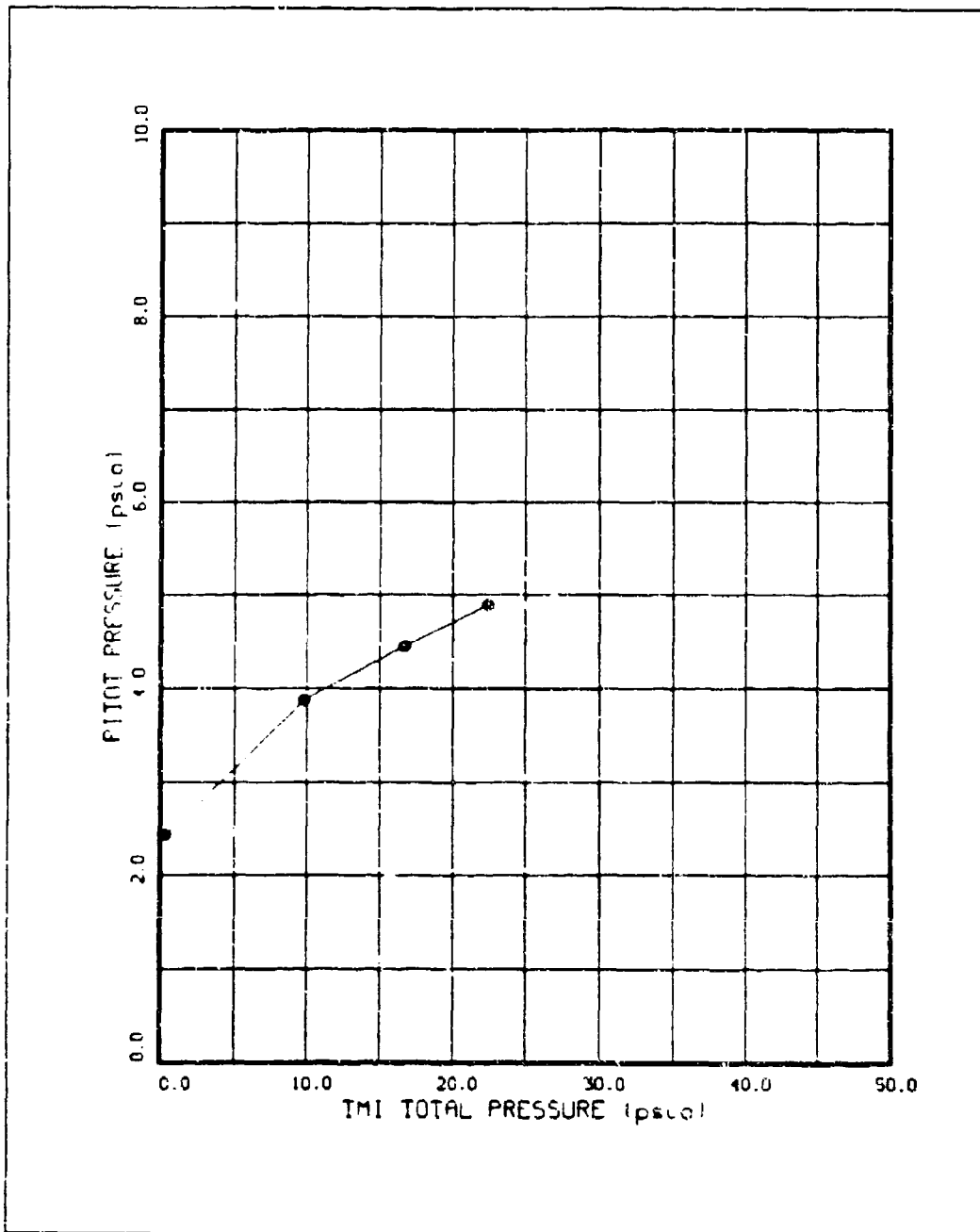


Figure 200. Run 15 Pitot Pressure vs. TMI Pressure

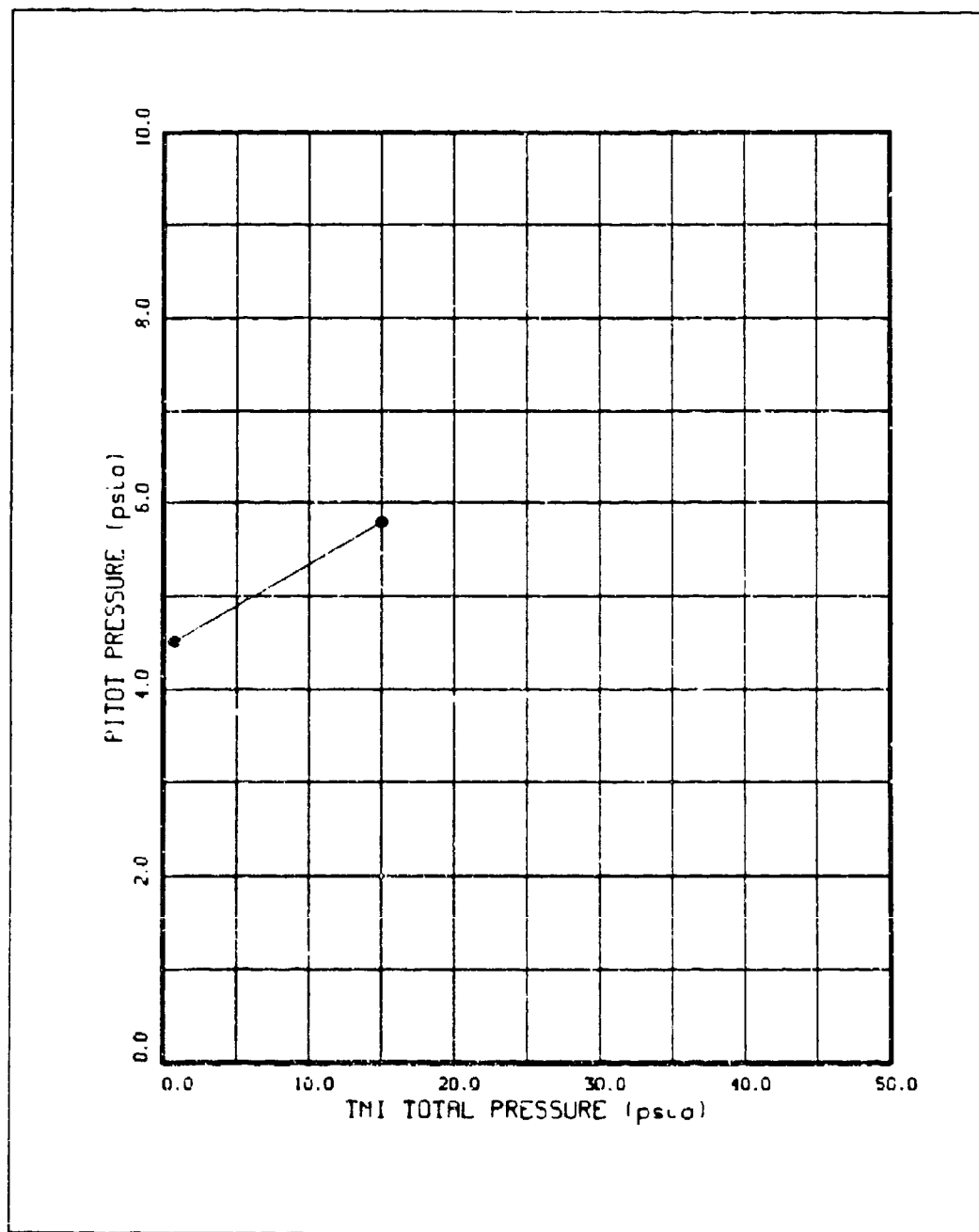


Figure 201. Run 16 Pitot Pressure vs. TMI Pressure

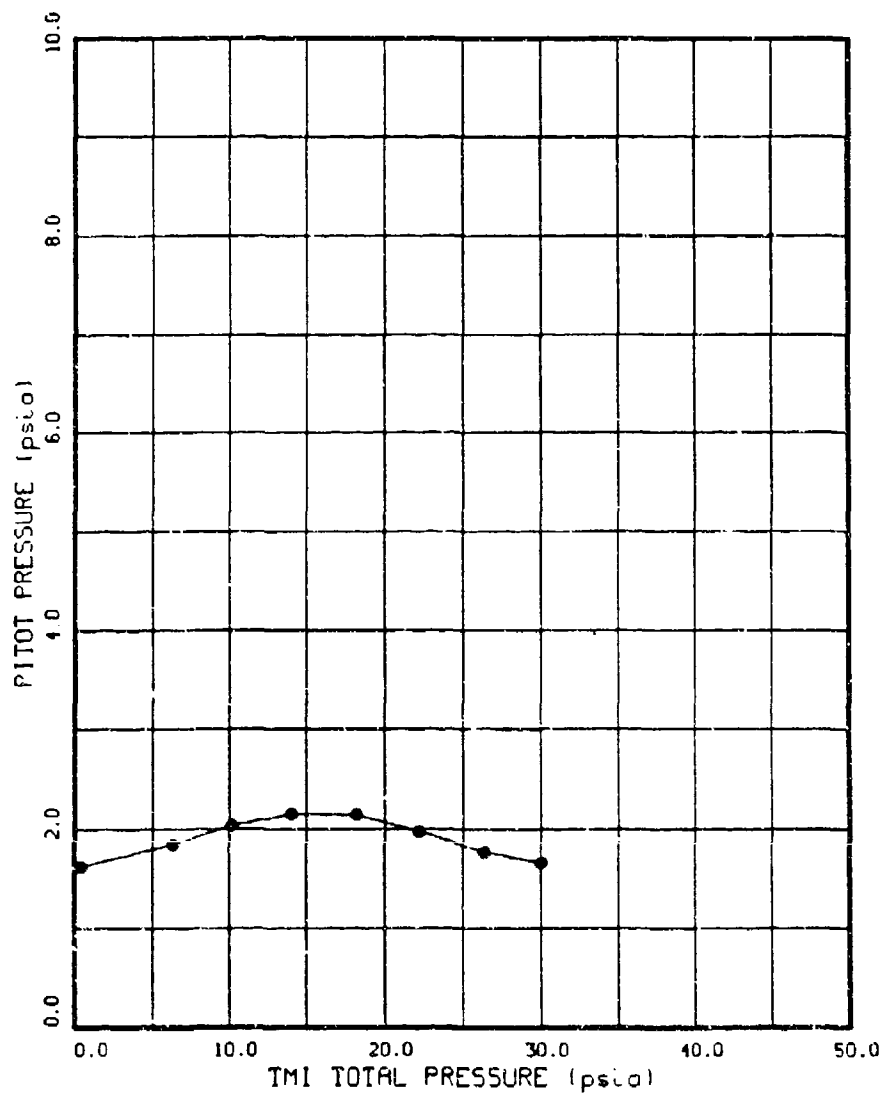


Figure 202. Run 17 Pitot Pressure vs. TMI Pressure

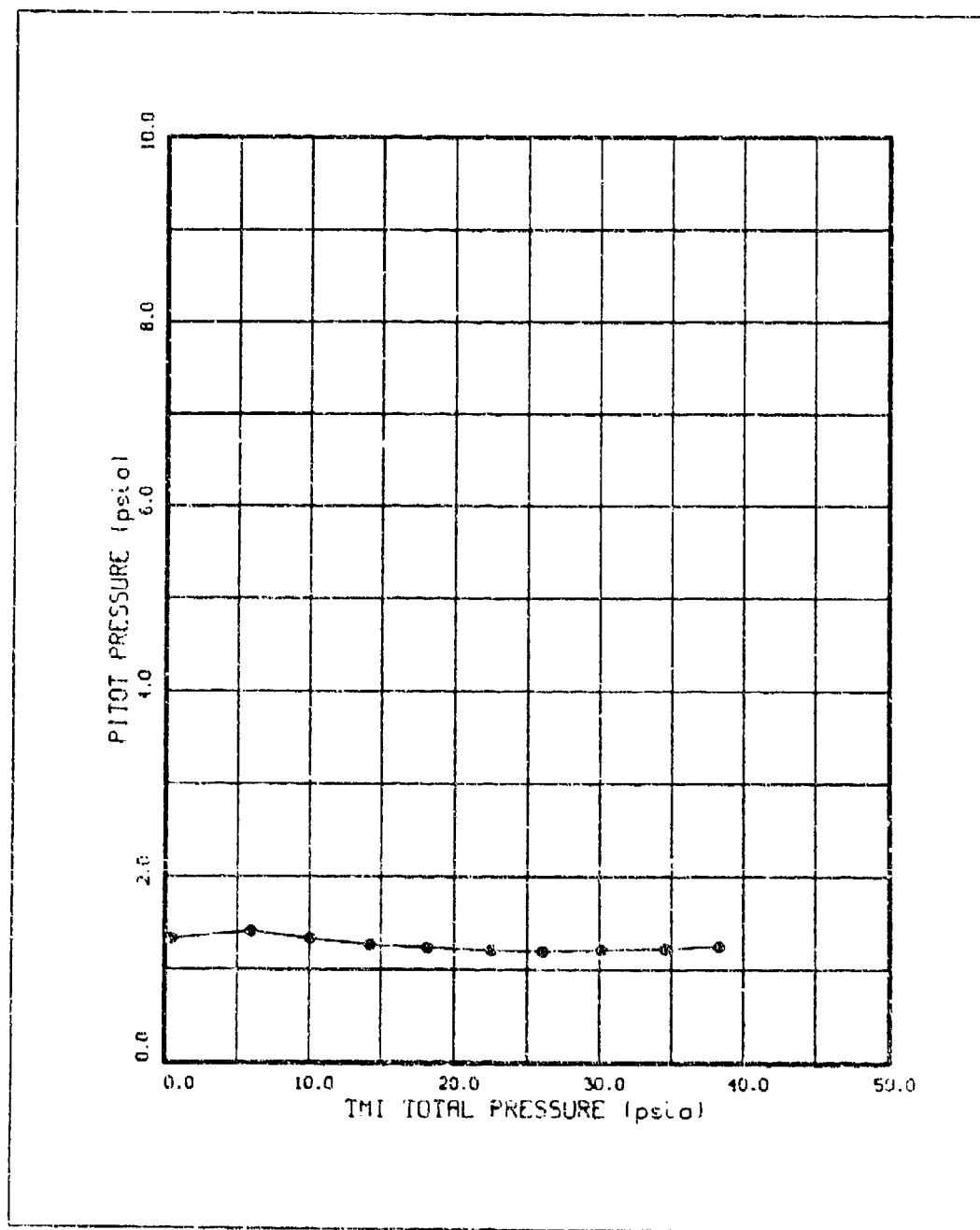


Figure 203. Run 18 Pitot Pressure vs. TMI Pressure

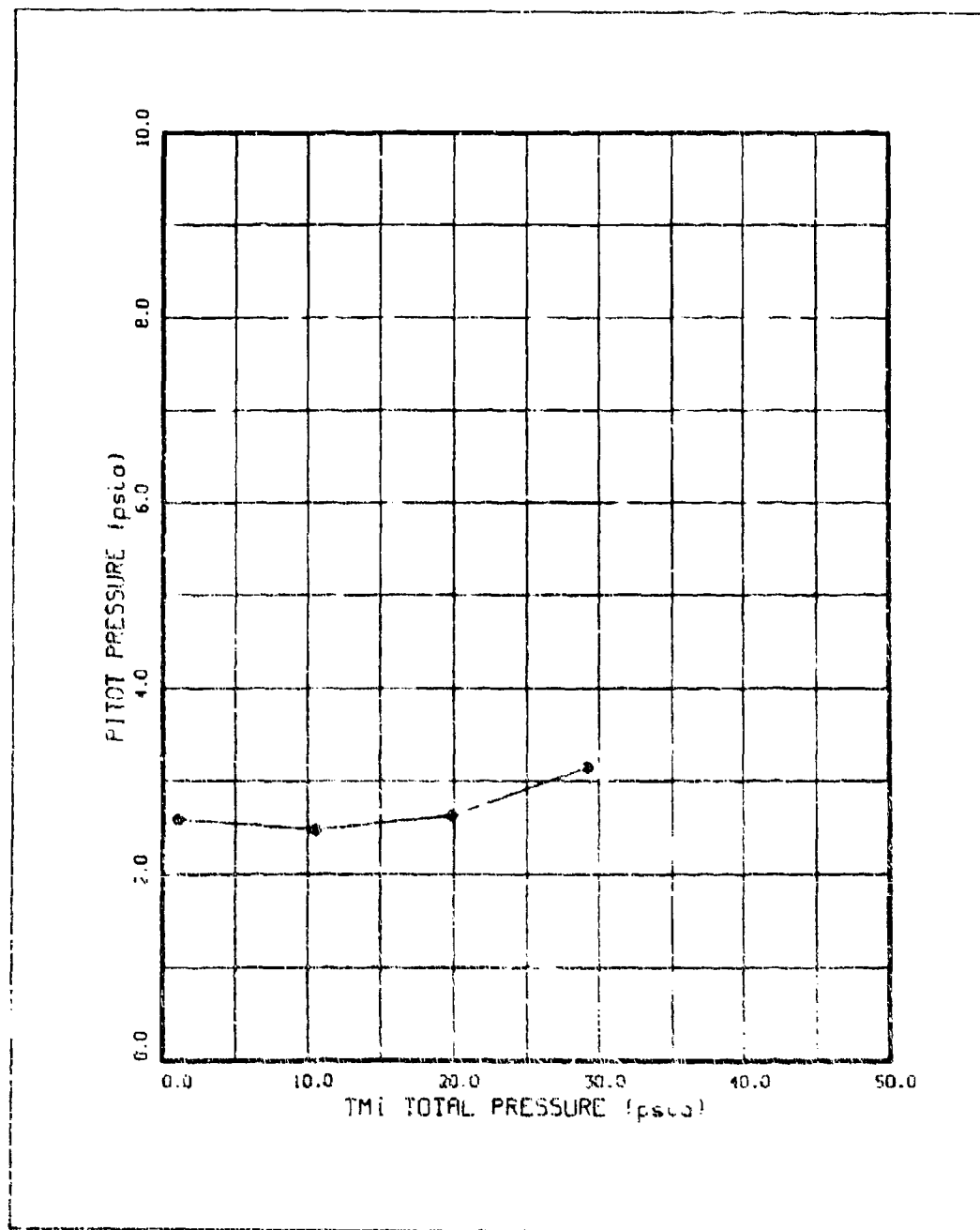


Figure 204. Run 19 Pitot Pressure vs. TMI Pressure

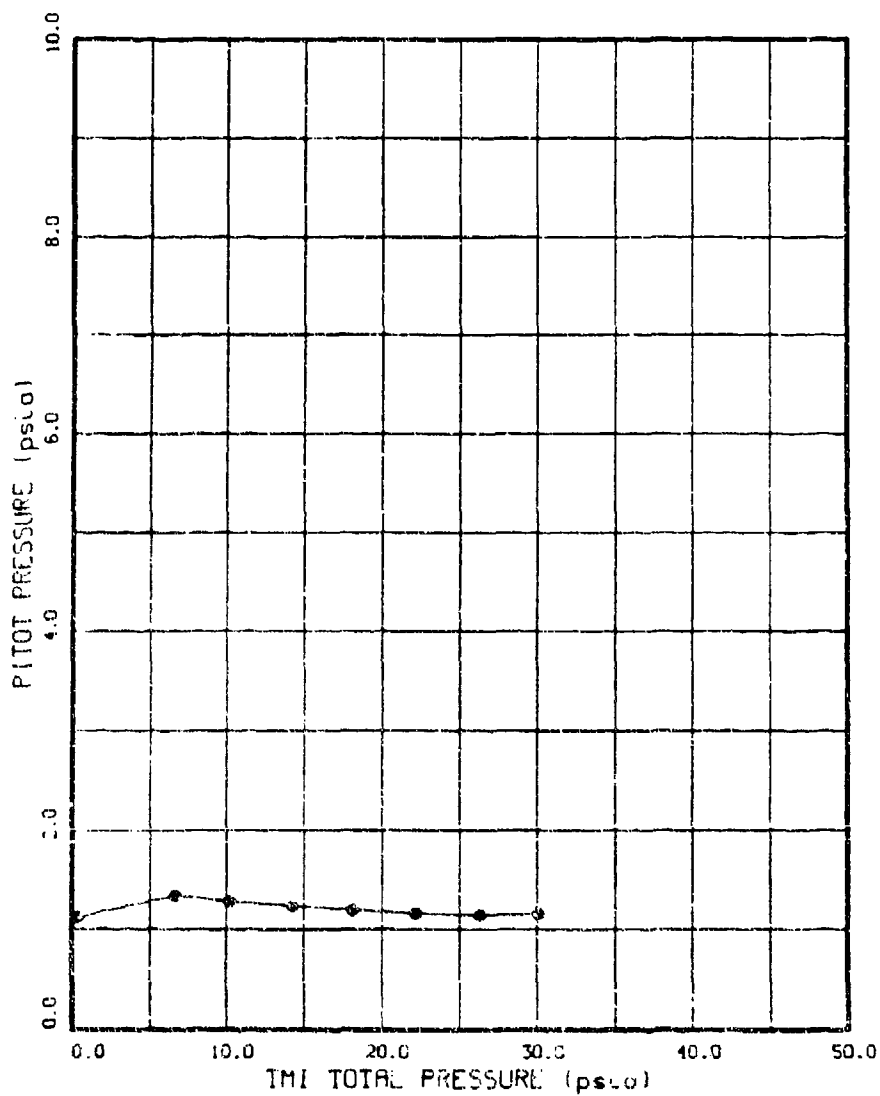


Figure 205. Run 20 Pitot Pressure vs. TMI Pressure

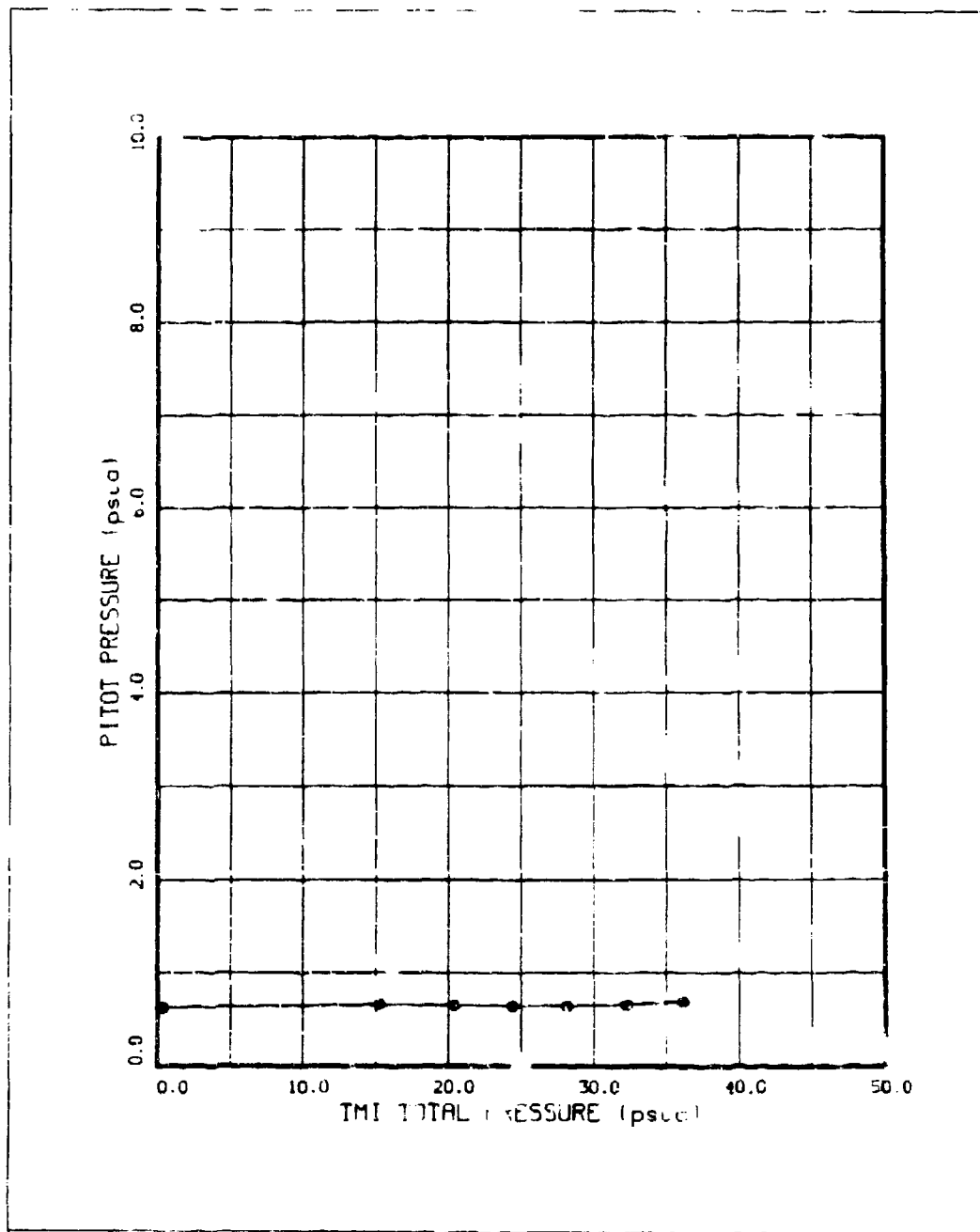


Figure 206. Run 56 Pitot Pressure vs. TMI Pressure

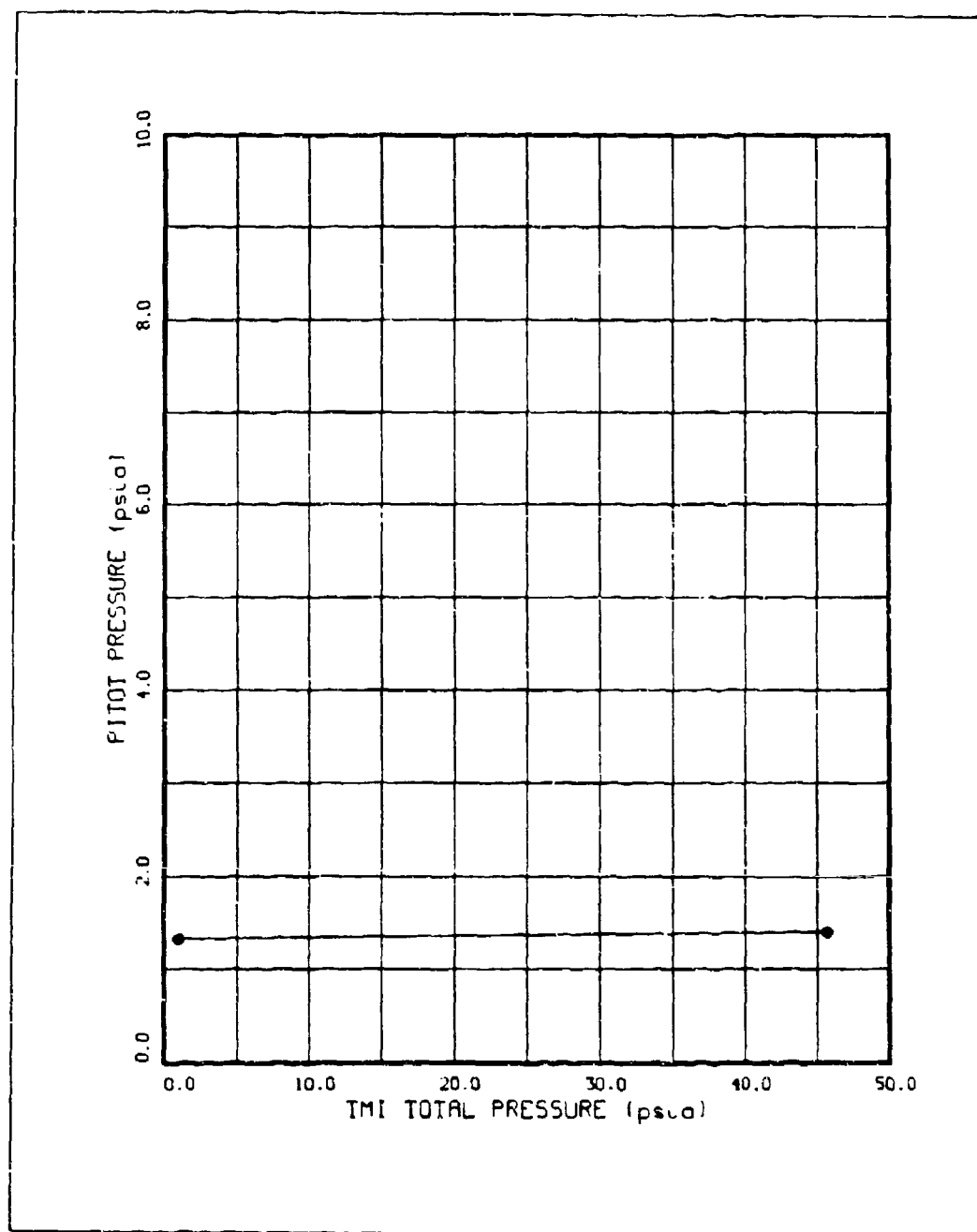


Figure 207. Run 57 Pitot Pressure vs. TMI Pressure

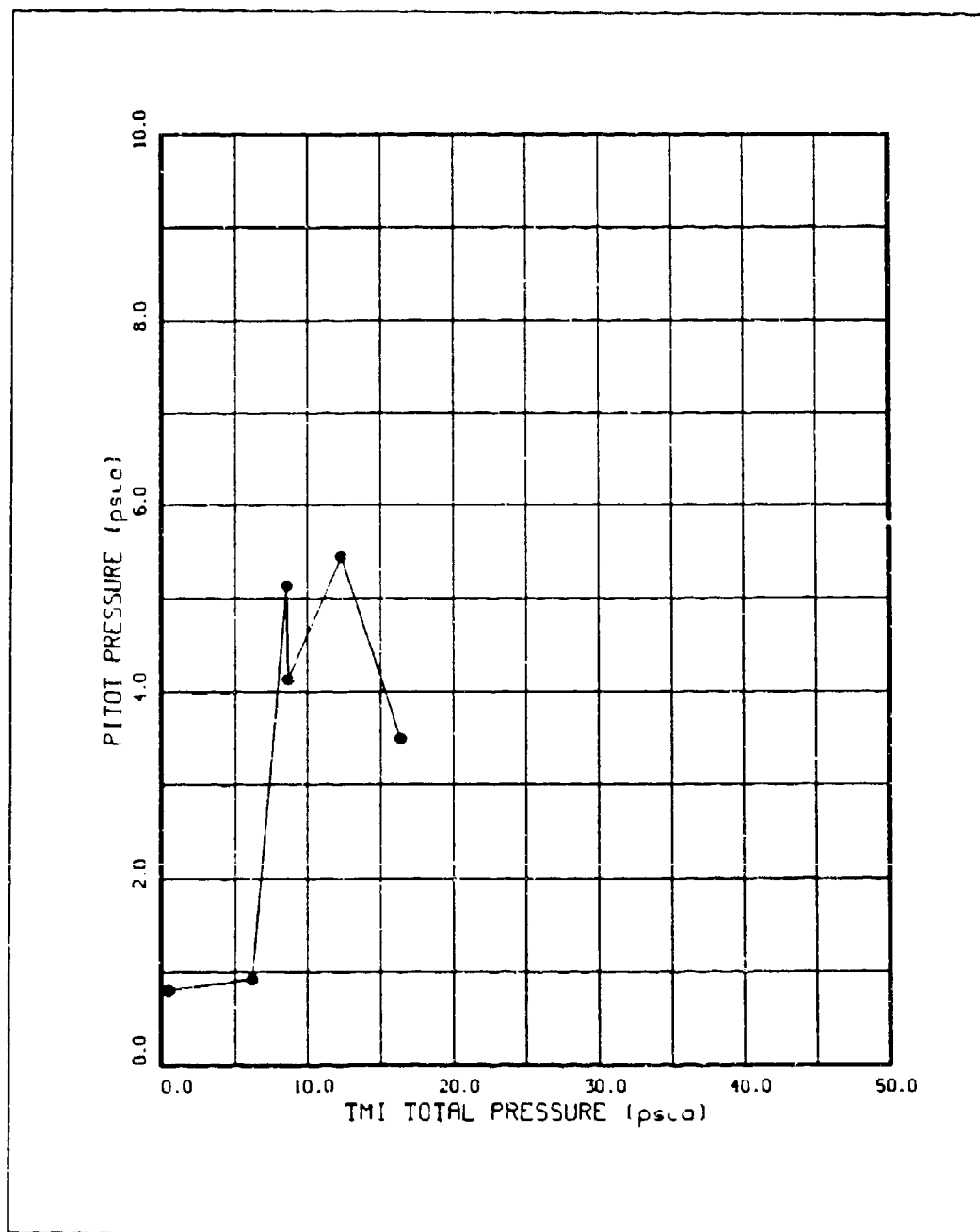


Figure 208. Run 59 Pitot Pressure vs. TMI Pressure

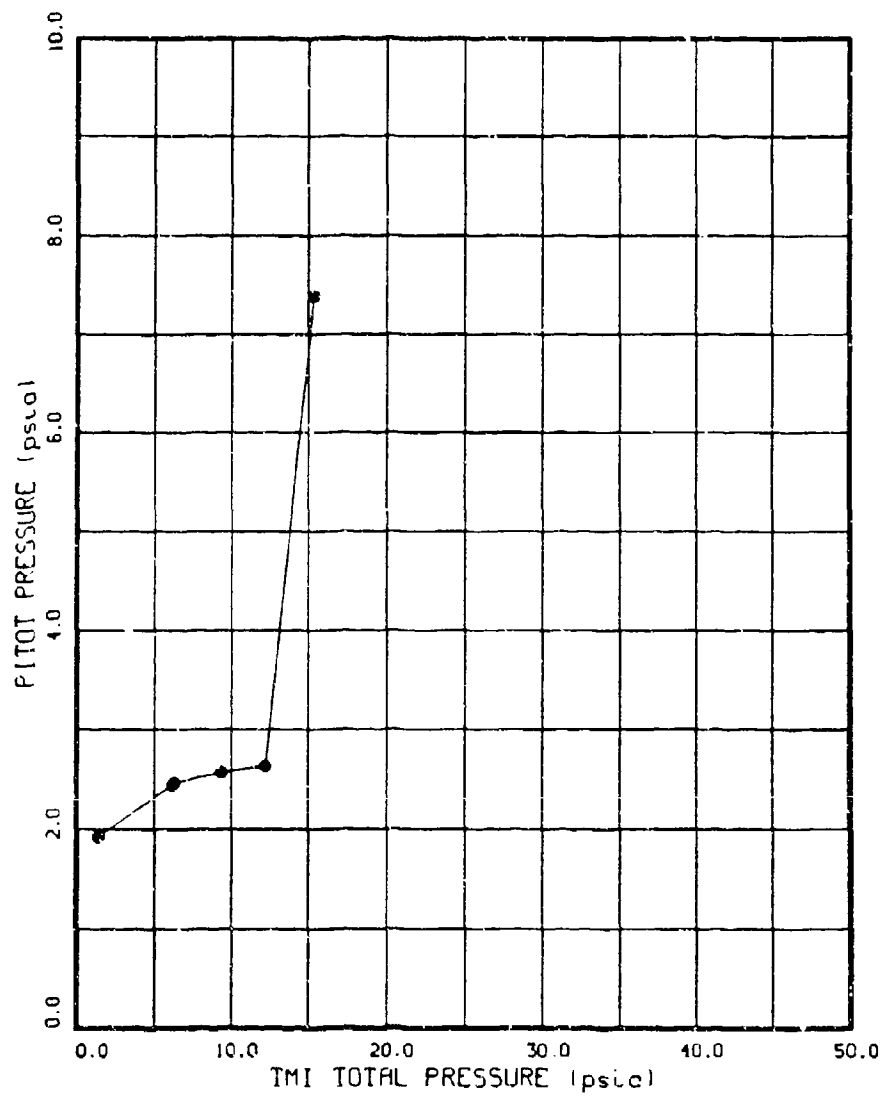


Figure 209. Run 60 Pitot Pressure vs. TMI Pressure

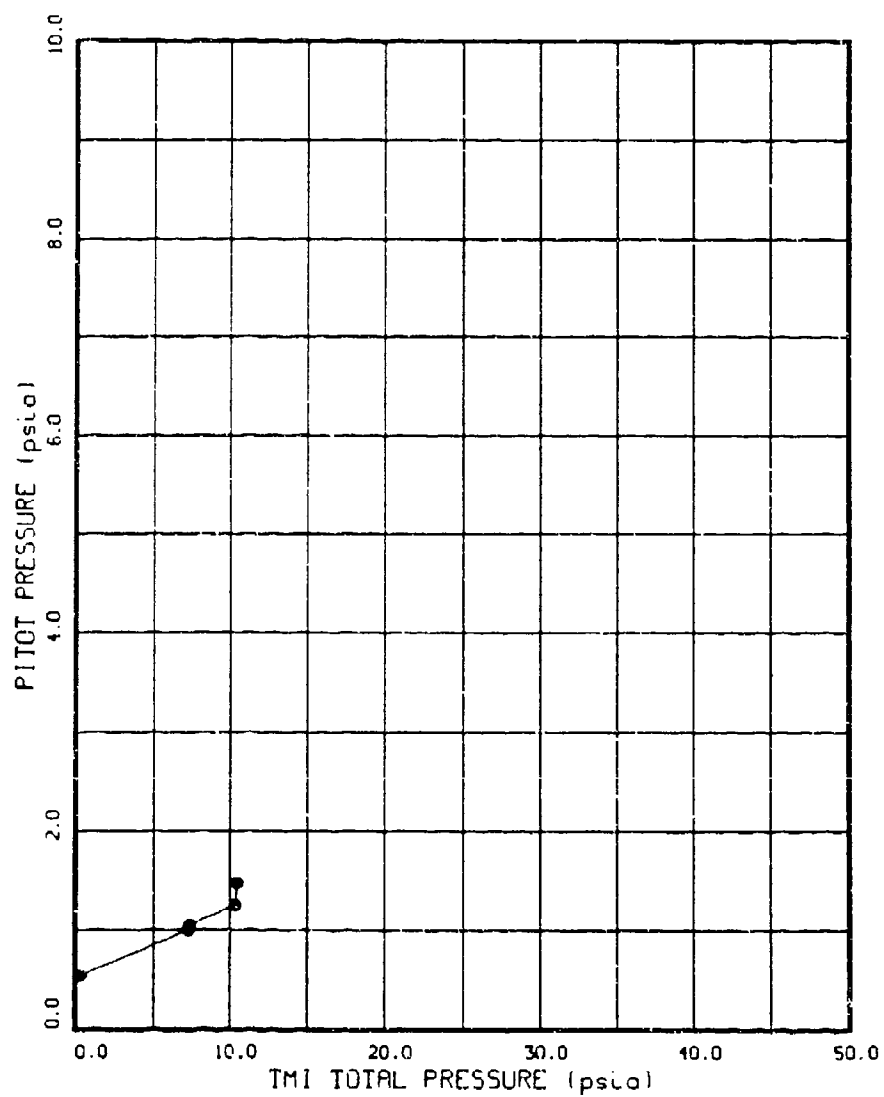


Figure 210. Run 61 Pitot Pressure vs. TMI Pressure

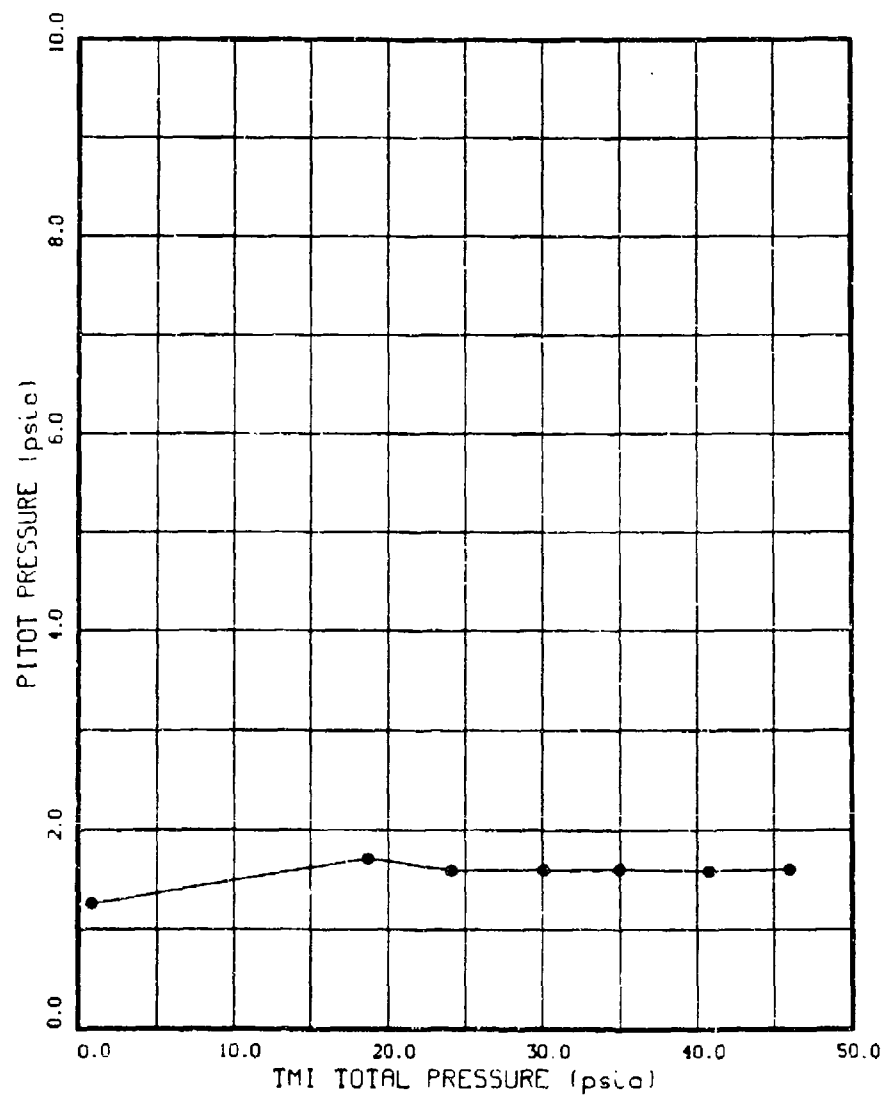


Figure 211. Run 62 Pitot Pressure vs. TMI Pressure

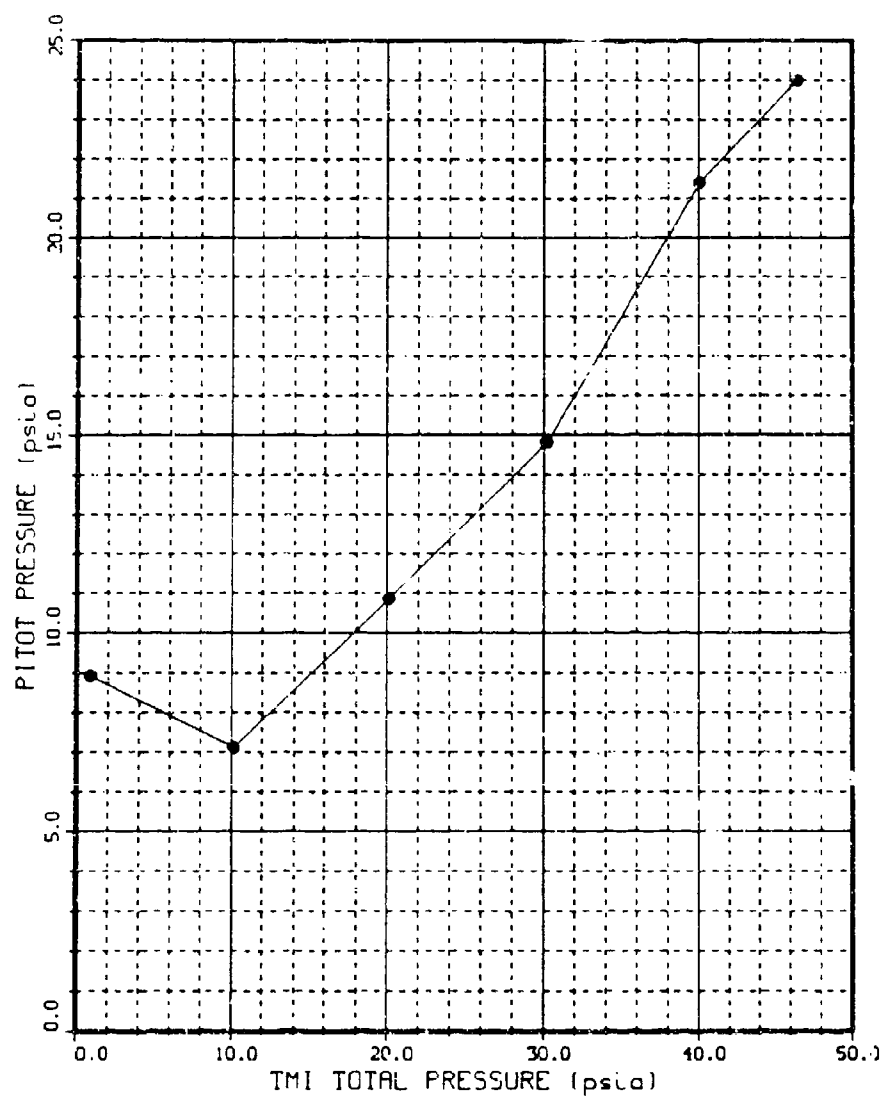


Figure 212. Run 40 Pitot Pressure vs. TMI Pressure

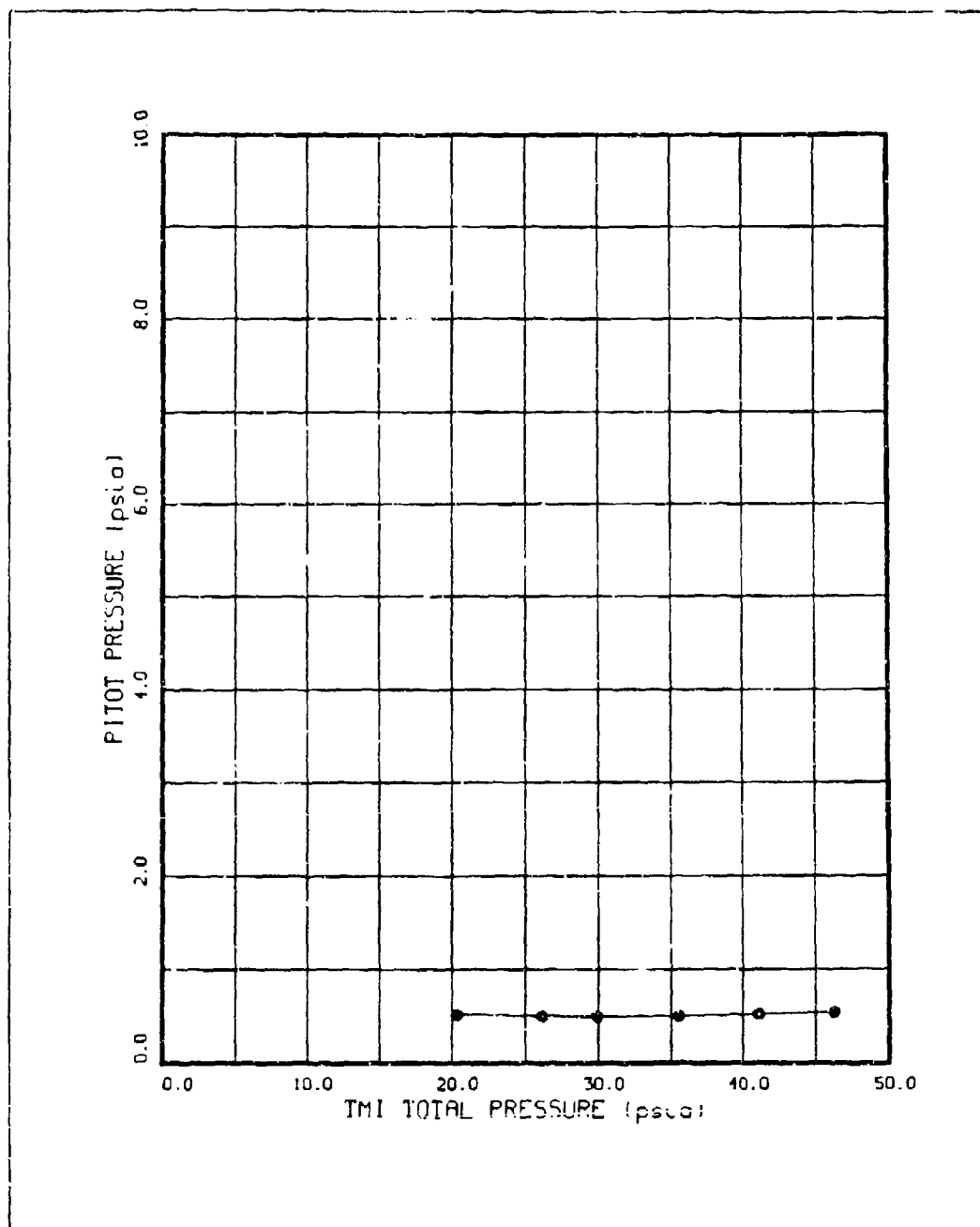


Figure 213. Run 54 Pitot Pressure vs. TMI Pressure

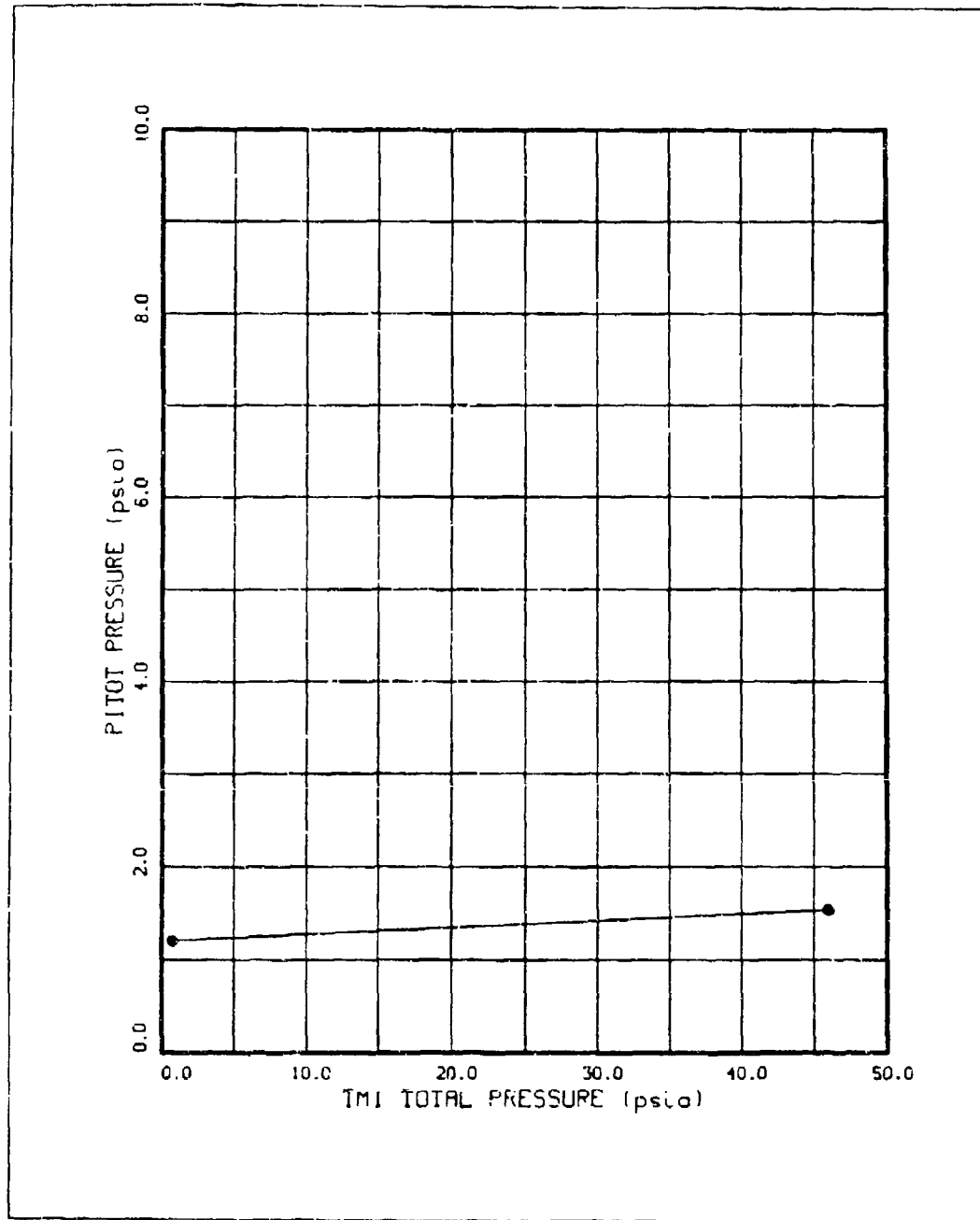


Figure 214. Run 55 Pitot Pressure vs. TMI Pressure

Vita

Richard J. Kacik was born on 11 August 1962 in Morgantown, West Virginia, the son of Robert and Anna Mae Kacik. He graduated summa cum laude from West Virginia University in 1984 with a Bachelor of Science degree in Aerospace Engineering. After graduation, he entered the Air Force Officer Training School at Lackland AFB TX and, upon completion, was commissioned a Second Lieutenant in the USAF.

His first assignment was to the Milstar Joint Program Office at HQ Space Systems Division, Los Angeles AFB CA. He was responsible for the acquisition management of the command and telemetry software for the Mission Control Element used to control the Milstar satellite constellation. Additionally, he had systems engineering responsibility for command, telemetry, and satellite interface areas. Later, he also assumed responsibility for the development of the Milstar System Simulator to be used for test and training.

Capt Kacik entered the Air Force Institute of Technology in May 1989 specializing in hypersonic aerodynamics and air-breathing propulsion. After completion of coursework, he was assigned as lead engineer on the COMBAT EDGE program at HQ Human Systems Division, Brooks AFB TX.

Current Address: 4406 Lakeway
San Antonio, TX 78244

Permanent Address: 115 Brookhaven Rd
Morgantown, WV 26505

REPORT DOCUMENTATION PAGE			Form Approved OMB No. 0704-0188	
<small>Public reporting burden for this collection of information is estimated to average 1 hour per response, including the time for reviewing instructions, searching existing data sources, gathering and maintaining the data needed, and completing and reviewing the collection of information. Send comments regarding this burden estimate or any other aspect of this collection of information, including suggestions for reducing this burden, to Washington Headquarters Services, Directorate for Information Operations and Reports, 1215 Jefferson Davis Highway, Suite 1204, Arlington, VA 22202-4302, and to the Office of Management and Budget, Paperwork Reduction Project (0704-0188), Washington, DC 20503.</small>				
1. AGENCY USE ONLY (Leave blank)	2. REPORT DATE December 1991	3. REPORT TYPE AND DATES COVERED Master's Thesis		
4. TITLE AND SUBTITLE Optimization of Tangential Mass Injection for Minimizing Flow Separation in a Scramjet Inlet		5. FUNDING NUMBERS		
6. AUTHOR(S) Richard J. Kacik, Capt, USAF				
7. PERFORMING ORGANIZATION NAME(S) AND ADDRESS(ES) Air Force Institute of Technology Wright-Patterson AFB OH 45433-6583		8. PERFORMING ORGANIZATION REPORT NUMBER AFIT/GAE/ENY/91D-2		
9. SPONSORING / MONITORING AGENCY NAME(S) AND ADDRESS(ES) Donald Stava Wright Laboratory, Flight Dynamics Directorate (WL/FIMM) Wright-Patterson AFB OH 45433-6553		10. SPONSORING / MONITORING AGENCY REPORT NUMBER		
11. SUPPLEMENTARY NOTES				
12a. DISTRIBUTION / AVAILABILITY STATEMENT Approved for public release; distribution unlimited		12b. DISTRIBUTION CODE		
13. ABSTRACT (Maximum 200 words) <p>The interaction of a shock wave with a boundary layer often results in its separation from the surface. In a scramjet inlet, a cowl lip shock may cause such flow separation near the shoulder (the corner between the forebody and combustor), potentially leading to reduced engine efficiency, inlet unstart, or even flameout. Recent proof-of-concept tests have demonstrated that tangential mass injection (TMI) upstream of the shock is effective in eliminating this separation. The objective of this investigation was to optimize the TMI slot location and other inlet geometric factors by determining the conditions which minimized the controlling TMI flow rate (that required to just eliminate separation). Experimental tests were conducted with an inlet freestream Mach number of 6 and an injection Mach number of 3 while varying such parameters as boundary layer thickness, cowl deflection and shoulder flow turning angles, distance from slot to cowl shock impingement, and slot to-shoulder distance. The controlling TMI rate was minimized at 3% of the captured inlet flow rate when the smallest values of the above parameters were tested. The optimum distance for the slot to be upstream of the shoulder was below the range tested, but it was estimated to be 5-6 slot heights.</p>				
14. SUBJECT TERMS Scramjet Inlet Hypersonic Diffuser Jet Mixing Flow Shock-Viscous Interaction Flow Separation Boundary Layer Control Secondary Injection Tangential Mass Injection Optimal Slot Location			15. NUMBER OF PAGES 292	
			16. PRICE CODE	
17. SECURITY CLASSIFICATION OF REPORT Unclassified	18. SECURITY CLASSIFICATION OF THIS PAGE Unclassified	19. SECURITY CLASSIFICATION OF ABSTRACT Unclassified	20. LIMITATION OF ABSTRACT UL	